Karlsruher Institut für Technologie

Simplified methods for transmission computation in 2D curved optical waveguides

Zur Erlangung des akademischen Grades eines

DOKTORS DER NATURWISSENSCHAFTEN

von der KIT-Fakultät für Mathematik des
Karlsruher Instituts für Technologie (KIT)
genehmigte

DISSERTATION

von

Mariia Sukhova

Tag der mündlichen Prüfung: 24. Juli 2024

1. Referent: Prof. Dr. Willy Dörfler
2. Referent: Prof. Dr. Roland Griesmaier

Contents

1. Introduction **6**

2. Multi-mode approximation **10**
2.1. Leaky modes . . . 12
2.1.1. Leaky modes in a straight open waveguide . . . 12
2.1.2. Leaky modes in an open waveguide with constant curvature. . . . 21
2.2. Existence and uniqueness of a solution in open waveguide . . . 24
2.2.1. Generalized Fourier transform associated with transverse differential operator . . . 25
2.2.2. Modal radiation condition . . . 29
2.3. Bends: Semi-analytic solution . . . 32
2.4. Features of the implementation of the cylindrical functions of complex order . . . 35
2.4.1. Asymptotic expansions of the cylindrical functions near the turning point. . . . 35
2.4.2. Methodology. . . . 39
2.5. Semi-analytic t-maps . . . 40
2.5.1. Orthogonality relation . . . 41
2.5.2. Overlap integral . . . 42
2.5.3. Resulting t-maps in MMA . . . 44

3. Numerical results **52**
3.1. FEM for open slab waveguides with constant thickness. . . . 52
3.1.1. Transformation optics. . . . 53
3.1.2. PML. . . . 55
3.1.3. Dirichlet to Neumann operator . . . 56
3.1.4. Variational formulation . . . 60
3.1.5. Transmission . . . 60
3.1.6. Convergence versus exact solution . . . 61
3.2. MMA for open slab waveguides with constant thickness . . . 62
3.2.1. Example 1: 90-degree bow . . . 62
3.2.2. Example 2: the curvature of the central trajectory of the waveguide is not constant . . . 69
3.2.3. Example 3: central trajectories from the experiment . . . 75

4. Thin waveguide model problem **84**
4.1. Quantum waveguide . . . 84
4.2. Closed planar waveguide . . . 87
4.3. Model problem 1D . . . 90
4.4. Numerical examples . . . 91
4.4.1. Example 1: 90-degree bow . . . 94
4.4.2. Example 2: $\mathcal{C}^1$-Hump . . . 97
4.4.3. Example 3: $\mathcal{C}^2$-Hump . . . 100

5. Application of simplified methods to the waveguide junction optimization 103
5.1. Application of asymptotically small waveguides model. 104
5.1.1. Optimization problem 105
5.1.2. Example: Shifted hump. 106
5.2. Application of MMA 108
5.2.1. Optimization problem 108
5.2.2. Optimization scheme 109
5.2.3. Numerical examples 110

A. Lamé coefficients 117

Acknowledgement

I want to thank my supervisor Prof. Dr. Willy Dörfler for his guidance and support through this journey. Your expertise and experience were essential. It has been a pleasure working with you.

As well as my second supervisor Prof. Dr. Roland Griesmaier. Thank you for your support and transparent feedback.

Also, I would like to thank Prof. Dr. Carsten Rockstuhl for the fruitful collaboration of our working groups that led to great results.

Big thank you goes to my fellow colleagues. My office neighbours Pascal Kraft and Stefan Karch. Colleagues from our working group and beyond Raphael Schoof, Zoltan Veszelka, Fabian Castelli, Jan Bohn (special thanks for going through struggles of handling teaching during the pandemic), Tim Laufer, Mehdi Elasmi, Fedor Bukreev and many others. Thank you all for your support, scientific discussions, nice and interesting lunch talks, and simply for being with me in the same boat throughout the years.

Speaking about "boats", special thank you goes to Maria Paszkiewicz, fellow sailor of "Open Waveguides" boat. Thank you for standing with me shoulder to shoulder during storms.

During this time I have met plenty of interesting and talented people. Professors, researchers, and students from various areas of science. This gave me a lot of fruitful insights and definitely influenced my perception of this World. In a positive way of course.

I want to thank KIT and specifically CRC 1173 for giving me an opportunity to conduct my research and being part of such a great place. It was an honour working with such talented people and being part of this group.

It was a journey with ups and downs, happy moments and difficult times, for being alongside me throughout the whole way, I would like to sincerely thank my family and especially my husband for their support and love they gave me during these times. You provided solid ground for me to conduct my research feeling safe and understood. Thank you. Not to mention our cat Afanasij, his support was indescribable, even though in some cases he was just asking for extra food.

1. Introduction

Motivation. This work is the result of participation in an interdisciplinary C4 project of the collaborative research center 1173 Wave Phenomena at KIT. In this project, as the subject of study, structures that allow signal transmission in an integrated photonic circuit were defined. Such a structure, which is called a *photonic wire bond* or an *optical waveguide*, transmits light between different components of a photonic integrated circuit, and optimization of its shape is necessary to minimize signal losses.

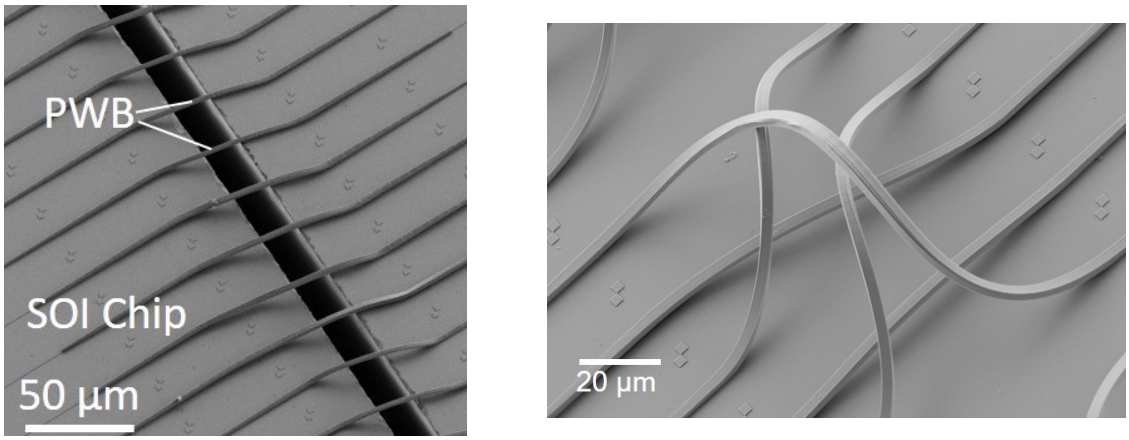

Figure 1: *Photonic wire bonds* or *optical waveguides* of various shapes in the design of the integrated circuit. **Left**: Structures without torsion [10]. **Right**: Structures with torsion [55].

In Figure 1, left, we have an example of optical waveguides connecting chips located at a distance of about 50 µm from each other. Taking into account the straight connecting parts of the photonic wire bond, in numerical simulation of light propagation in such a waveguide this leads to the computational domain size in the direction of signal propagation of approximately 100 µm.

Finding a numerical solution in structures of this size and subsequent calculation of the transmission with the full-wave solvers for 3D Maxwell's equations requires too much computational time and is not applicable for online calculations in the manufacturing process of optical integration circuits. Namely, the photonic integrated circuit mass production requires optical waveguide shape optimization within tens of seconds, while solvers for 3D Maxwell's equations carry out computations from several hours to several days [74]. This motivates the construction of simplified numerical methods for efficient transmission approximation for further utilization in optical waveguide shape optimization.

Subject of study. In Figure 1, left, photonic wire bonds have bending only in one direction and their central trajectories are represented by planar curves. 2D optical waveguides of constant thickness transmitting the optical signal generated by such a central curve are the subject of study of this work. An example of photonic wire bonds

of constant width with a spatial central trajectory is shown in Figure 1, right. These are optical waveguides with torsion, but we do not consider such structures here.

The aim of the thesis is to construct simplified numerical methods for efficient transmission computation for the Helmholtz equation in 2D *open slab waveguides* of constant width generated by planar central trajectories. We emphasize that these simplified methods should be efficient when applied to waveguides of the size corresponding to real-life structures.

Simplified methods. One such method is the *Multimode Approximation Method* [74], an extension of the *Fundamental Mode Approximation* [67]. This approach essentially divides the photonic wire bonds into tiny sections. Each section is characterized by a propagation loss because of the its finite curvature, and at the interface between consecutive sections, we encounter transmission losses. Tracing the fraction of light that propagates through the free-form waveguide allows for the fast computation of the light transmission.

In this work, we present a calculation of transmission coefficients for an interface between two bent waveguide sections of various radii of curvature using *Semi-Analytic solutions* [46], which are leaky modes. As a result, we obtain a *pre-calculated database of transmission coefficients*. The advantage of the semi-analytic approach lies in the sufficient accuracy of the obtained transmission coefficients, which allows the transmission approximation of a free-formed waveguide. The finite element method is used as a reference solution for evaluating the transmission of waveguides with varying curvature.

As a second simplified methodology for efficient optimization, we construct a 1D reduction model of a thin planar 2D closed waveguide based on works studying 3D-1D [14] and 2D-1D [2] convergence for the Laplace operator with the Dirichlet conditions on the cladding of a *quantum waveguide*. We apply the 1D model in the optimization of signal transmission in curved real-life-sized open waveguides to obtain a heuristic initial assumption.

Outline. The organization of the thesis is the following:

In Chapter 2 we construct a Multi-mode approximation method based on Semi-analytic solutions.

In Section 2.1, we consider leaky modes, starting with an overview of the infinite perfectly matched layer transformation applied to a straight waveguide.

In Section 2.2, we recall some results from the open waveguides well-posedness theory, namely the modal radiation condition constructed with the help of the Generalized Fourier transform.

In Sections 2.4, 2.5 we present the main result of the chapter, namely the computation of the transmission coefficients database. Such a database is obtained with the implementation methodology based on the uniform expansion method for cylindrical functions of large complex order. Furthermore, we define the overlap integral with a weighted biorthogonality relation for the leaky modes associated with two adjacent waveguide segments. At the end of the chapter, we describe the application of the MMA method to a waveguide with a planar central trajectory.

In Chapter 3 we validate the Multi-Mode approximation method with the help of the Finite Element Method (FEM) comparing the relative transmission difference obtained by both methods. We especially highlight the results of Section 3.2.3, where with Semi-analytic MMA we can observe the transmission drop characteristic of the benchmark [68] trajectories related to the real size structures.

In Chapter 4 we construct a 1D reduction model of the thin planar 2D waveguide and compare the numerical solutions of both problems. For the potential step equation, we observe the stable prediction of the reflection values for the 2D problem provided by the 1D problem.

In the last Chapter 5, we consider some examples of shape optimization related to real-life-sized open waveguides with the MMA method and the thin waveguide model used as an initial approximation in the open waveguide optimization procedure. Starting with the central trajectory providing 15% transmission, we end up with the trajectory, which ensures 99,7% transmission power on the end port of the structure. The optimization execution time is hundreds of seconds.

Prepublications. As of the date of submission (29.05.2024), parts of the results presented in this thesis are already published.

Namely, in this work, we extensively utilize the Multi-Mode Approximation method, which was developed by our project partners for Maxwell's equations based on the transmission coefficients database computed with a commercial solver, the results are published in [74].
In the joint work [74] the theoretical part, in particular the method development and the physical interpretation, was essentially contributed by M.Sc.Maria Paszkiewicz supervised by Prof. Dr. Carsten Rockstuhl.

In this thesis, this method appears in Chapters 2, 3, 5. The improved interpolation of the t-maps, regardless of the choice of method for transmission coefficients computation, was proposed by me supervised by Prof. Dr. Willy Dörfler for the Helmholtz equation and partially used in publication [74] implemented for Maxwell's equations in a commercial solver. In our case, in Chapters 2, 3, 5, the implementation of Multi-Mode approximation with improved interpolation of t-maps was done in Matlab [64] for the Helmholtz equation. In this work, we utilize the Multi-Mode approximation method with a choice of bending loss in Chapters 2, 3, and 5 different from the choice in the publication [74].

The theoretical development of the Semi-Analytic t-maps for the Helmholtz equation and numerical implementation done by me supervised by Prof. Dr. Willy Dörfler in Matlab [64], this result is not published, presented in this thesis in Chapter 2.

Furthermore, the project partners provided a set of central trajectories for the transmission benchmark published in [68], that we use in this work, in Chapter 2 to illustrate the benchmark, in Chapter 3, to compare the Finite Element Method and constructed Semi-Analytical MMA numerical results for the Helmholtz equation. In the joint work [68], the theoretical part, the physical interpretation, and the experimental part were essentially contributed by Dr.Aleksandar Nesic supervised by Prof. Dr. Christian Koos.

2. Multi-mode approximation

Motivation. We consider an open slab waveguide with fixed thickness in a setting where two straight parts are connected by a curved junction. The signal propagation in the structure is characterized by the wavelength and piecewise constant refractive index. The shape of the waveguide is characterized by its central trajectory.

The *Fundamental mode approximation* method (FMA) was proposed in [67] for the efficient transmission calculation in a 3D waveguide with rectangular cross-section without twisting supporting a single mode. It was further extended for the same type of waveguide to the *Multimode approximation* (MMA) method [74], where it was shown that the MMA method is reliable for $R^+ \geq 10$ µm for a sequence of bow structures when the junction is represented by a waveguide of constant radius of curvature R^+.

Another example for application of the MMA is a waveguide with an adiabatic change of curvature considered in [74], where the central trajectory is represented by a sinusoidal function and the method is reliable for the minimum radius of curvature greater than 20 µm.

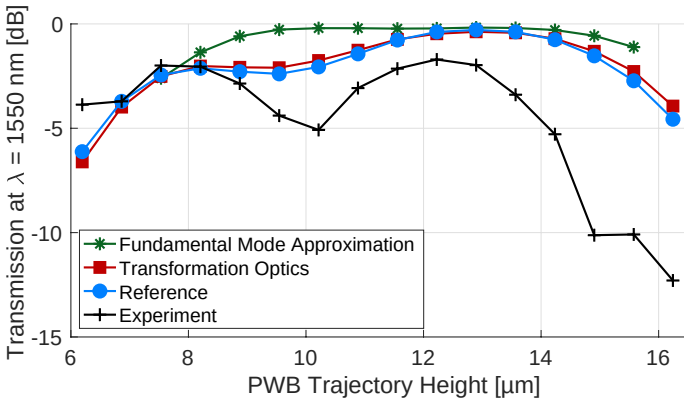

Figure 2: Benchmark of transmission calculated for slab 3D waveguides with different methods. The FMA method based on the database of transmission coefficients obtained with a commercial solver does not show the characteristic drop for the trajectory of height 10 µm. Reference computation is done via the time-domain finite-integration technique. Notation and figure are taken from [68].

To study more complex waveguide shapes, a set of central trajectories was considered. For them, within the framework of the CRC 1173 C4 project, real-life experiments were done to measure the transmission. As a result, the transmission benchmark related to such a set of trajectories (see Figures 2, 30) was obtained in [68]. One of the main characteristics of this benchmark is the local minimum in transmission for certain trajectories. The transmission drop was also confirmed by evaluations made with the time-domain finite-integration technique [68].

However, testing of the FMA method on this set of advanced trajectories did not show the characteristic transmission drop [68]. It was therefore assumed that the FMA method is not suitable for this set of trajectories since the corresponding waveguides from the real-life experiment support two modes.

With such waveguide parameters, even if initially only one mode is directed along the structure, the curvature of the central trajectory can cause interference, and therefore a second mode can be excited [77]. The interaction of the first and higher modes must be taken into account, which is done in the MMA method.

However, in the application of MMA to the set of real-life experiment-related trajectories using the FEM-based commercial solver for the transmission coefficients calculation, the transmission drop was also not visible.

The MMA method is based on the idea of dividing the central trajectory of an open waveguide into segments small enough such that the approximated curvature can be considered constant in each segment. Then we assume that the waveguide is approximated by the composition of the slices $\widehat{S}_j$, $j = 1, \ldots, n-1$.

In the setting that we are considering in this work, the single slice $\widehat{S}_j$ is a 2D open slab waveguide characterized by a constant outer radius of curvature R_j^+, also called a *bent* or *bend waveguide*. In case of such a shape of the waveguide and a piecewise constant refractive index of the core and cladding materials we can go to the cylindrical coordinates (r, θ) and we can represent the solution as a superposition of the longitudinal component $\mathrm{e}^{-\mathrm{i}\mu_j R_j^+ \theta}$ and complex amplitude $u_{2_j}(r)$, where $\mu_j \in \mathbb{C}, \mathfrak{Im}\mu_j \neq 0$ is the propagation constant. The complex amplitude u_{2_j} is a solution to the eigenvalue problem on the cross-section of the bend. The eigenfunctions corresponding to the discrete part of the spectrum of the related transverse operator are guided and leaky modes. They can be expressed via *cylindrical functions of complex order* $\nu = \mu_j R_j^+$.

At the interface of two waveguide slices $\widehat{S}_j$, $\widehat{S}_{j+1}$ with related radii of curvature R_j^+ and R_{j+1}^+ such that $R_j^+ \neq R_{j+1}^+$, a scattering problem arises since the guided and leaky modes are transmitted and coupled to each other. In MMA and FMA methods for an efficient approximation of the transmission in the entire waveguide such a scattering situation is taken into account.

The main component of the method is the evaluation of the overlap integral at the interface for all adjacent segments in which such an interference pattern occurs. The terms in the overlap integral are solutions on the cross-section of the corresponding adjacent segments $\widehat{S}_j$ and $\widehat{S}_{j+1}$. In [46] it was shown that modes on the bend cross-section can be found with the *Semi-analytic method*.

The advantage of the Semi-analytic approach lies in the sufficient accuracy of the obtained transmission coefficients, which allows the transmission approximation of a free-formed waveguide. However, an estimation of the individual cylindrical functions of large order and argument requires a special approach.

Therefore, the correct evaluation of cylindrical functions of complex and large order is the most important ingredient in the MMA method with transmission coefficients calculated by the Semi-analytic approach.

As a result, we obtain a *pre-calculated database* of transmission coefficients for various combinations of radii of curvature, which allows the fast approximation of the light transmission along the whole slab waveguide with a curved junction.

2.1. Leaky modes

In this section, we will consider the definition of *leaky modes* and show that those modes can also be presented in a waveguide of constant curvature.

The definition of leaky modes can be given with the help of spectral analysis in a waveguide. For example, in [40] a straight waveguide is observed, and how the transverse differential operator is affected by an *infinite Perfectly Matched Layer (PML)*. They apply a complex scaling technique in the context of 2D and 3D open straight waveguides. This method, also called *spectrum deformation* or *analytic dilation*, was originally used to study the problem of resonances (e.g. see [48] or [41]).

Indeed, with infinite PML it can be shown that the differential transverse operator is no longer self-adjoint. In this case, spectral analysis differs significantly from the case of a self-adjoint operator. In the first part of this section, we will present some definitions and results from spectral analysis for our waveguide setting, following Theorems 2.1-2.2 in [40] to consider the phenomenon of spectrum rotation even in this simple waveguide's geometry case, where it can be shown explicitly. We also give a definition of leaky modes depending on the characteristics of the transverse differential operator spectrum. For further details of the spectral operator theory, including non-self-adjoint ones, see e.g. [32].

In the second part we will consider a bent waveguide. Since modes in open waveguides with constant curvature are leaky modes, it is directly related to the Multi-Mode approximation method and it can be shown that the transverse differential operator indeed has complex eigenvalues for such a waveguide.

2.1.1. Leaky modes in a straight open waveguide

In the following subsection we will focus our attention on the mathematical description of leaky modes. We consider the approach from Chapter 2 in [40] slightly adapted to our case. There the occurrence of leaky modes is studied from the point of view of spectral theory for the case of a straight open waveguide.

Let us denote by x the direction of signal propagation along the waveguide, and by y the transverse direction. The problem under consideration is

$$-\Delta u - k^2 u = 0 \quad \text{in } \mathbb{R}^2, \tag{1}$$

where the wavenumber $k \in \mathbb{R}$ defined for all $x \in \mathbb{R}$ as

$$k(x,y) = \begin{cases} k_0 n_{\text{co}}, & \text{if } y \in (-d,d) \ , \\ k_0 n_{\text{cl}}, & \text{else} \ , \end{cases}$$

with given constant material values $k_0 = \omega/c_0 = \omega\sqrt{\mu_0 \varepsilon_0}$, refractive index in the core n_{co} and in the cladding n_{cl}. Since the values of the refractive indices are constant in the x-direction, the wave number actually depends only on y.

We denote $k_{\text{co}} := k_0 n_{\text{co}}$, $k_{\text{cl}} := k_0 n_{\text{cl}}$, and d relates to the core width, it is fixed and constant.

In a straight waveguide we can apply separation of variables ansatz and the solution is represented with

$$u(x, y) = u_1(x)u_2(y),$$

where the form of the solution in propagation direction $u_1(x)$ is known and $u_2(y)$ is the solution to the eigenvalue equation in the waveguide cross-section (which is whole $\mathbb{R}$ in open waveguide case)

$$-\frac{\mathrm{d}^2 u_2}{\mathrm{d}y^2} - k^2 u_2 = \lambda u_2. \tag{2}$$

Then the transverse operator $A\colon D(A) \subset L^2(\mathbb{R}) \to L^2(\mathbb{R})$ can be defined in the following way:

Definition 2.1 (The transverse operator A)**.** *The transverse operator A is an operator defined as*

$$Av := -\frac{\mathrm{d}^2 v}{\mathrm{d}y^2} - k^2 v, \quad \textit{for any} \quad v \in D(A) := \left\{ v \in H^1(\mathbb{R}),\ \frac{\mathrm{d}^2 v}{\mathrm{d}y^2} \in L^2(\mathbb{R}) \right\}. \tag{3}$$

Before we move on studying the structure of the spectrum of the transverse operator A, we list below some definitions from spectral theory that we will use further. More details can be found, for example, in [32].

Let X be the Hilbert space and consider an operator $B\colon X \to X$ with corresponding operator $B_\lambda := B - \lambda I$.

Definition 2.2 (Resolvent)**.** *The resolvent operator $R_B(\lambda)$ is a bounded operator defined by B_λ^{-1}.*

Definition 2.3 (Resolvent set)**.** $\rho(B) := \{\lambda \in \mathbb{C} :\ B_\lambda^{-1}\ \textit{exists}\}$.

Definition 2.4 (Spectrum)**.** $\sigma(B) := \mathbb{C} \setminus \rho(B)$ *and* $\sigma(B)$ *is open.*

Definition 2.5. *B is bounded holds*

$$\exists\, C > 0 :\ \textit{for any } u \in X \quad \|Bu\|_X \le C\|u\|_X.$$

Definition 2.6 (Adjoint operator)**.** *If for an operator B holds*

$$(Bu, v) = (u, B^* v), \qquad \textit{for any} \quad u \in D(B),\ v \in D(B^*),$$

then B^* is called adjoint operator of B.

Definition 2.7 (Self-adjoint operator)**.** *An operator B is self-adjoint if*

$$(Bu, v) = (u, Bv), \qquad \textit{for any} \quad u,\ v \in D(B).$$

Theorem 2.1. *The transverse operator A (3) is a self-adjoint operator for the scalar product $(\cdot, \cdot)_{L^2(\mathbb{R})}$*

Proof. Proposition 1.2 and 1.3 in [40], Theorem 2.2.3 in [72]. □

Theorem 2.2 (Spectrum $\sigma(A)$)**.** *The spectrum of self-adjoint transverse operator A (3) is real and consists of the discrete spectrum*

$$\sigma_d(A) \subset (-k_{\text{co}}^2,\, -k_{\text{cl}}^2) \tag{4}$$

and essential spectrum

$$\sigma_e(A) = [-k_{\text{cl}}^2, +\infty), \tag{5}$$

i.e. $\sigma(A) = \sigma_e(A) \cup \sigma_d(A)$.

Proof. Proposition 1.4 and 1.6 in [40], Lemma 2.4.4, Lemma 2.4.6 in [72]. □

Thus, the transverse operator A related to the problem (1) is self-adjoint and has the spectrum structure described above. Below we highlight some properties of the spectrum $\sigma(A)$:

- Isolated eigenvalues corresponding to the resolvent's $R_A(\lambda)$ poles are located in $\sigma_d(A)$ and characterize *guided modes*.
- Eigenvalues $\lambda \in \sigma_e(A)$ are associated with *radiation modes*.
- The residual spectrum of the transverse operator A is empty, which follows directly from Theorem 2.2.

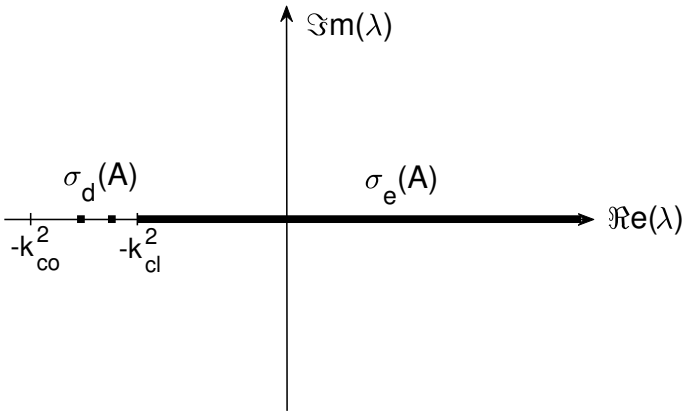

Figure 3: Spectrum of the self-adjoint transverse operator A (3)

The question arises whether there are any other modes besides the guided and radiation modes. It turns out [40] that if one introduces an infinite PML, it is possible to catch another type of modes that correspond to a discrete part of the spectrum, but the eigenvalues will no longer be real.

Thus, next we introduce the PML transformation in the direction y perpendicular to the propagation direction x, to consider later how this transformation will affect the structure of the spectrum $\sigma(A)$.

The parameterization can be given, for example, in the following way:

Definition 2.8 (Analytic continuation in the transverse direction via infinite PML)**.** *Let $\tilde{y} \in \mathbb{R}$. For $d \leq d_2 < d_3$ a* **Perfectly Matched Layer (PML)***, which starts in d_2, can be defined with parametrization*

$$C(\tilde{y}) := \begin{cases} \tilde{y}, & |\tilde{y}| < d_2, \\ d_2 + \dfrac{\tilde{y} - d_2}{\alpha_\infty}, & \textit{else}\ , \end{cases}$$

with $\alpha_\infty \in \mathbb{C} \setminus \{0\}$, or

$$C(\tilde{y}) := \begin{cases} \tilde{y}, & |\tilde{y}| < d_2, \\ \zeta(\tilde{y}), & d_2 \leq |\tilde{y}| < d_3, \\ \dfrac{\tilde{y}}{\alpha_\infty}, & \textit{else}\ , \end{cases}$$

with $\alpha_\infty \in \mathbb{C} \setminus \{0\}$ and ζ such that C is a twice continuously differentiable function. We assume that $\mathfrak{Re}(C)$ is strictly increasing and that $\mathfrak{Im}(C)$ is monotonically increasing with bounded derivatives.

Remark: The PML transformation, which we use later for implementing signal propagation in an open waveguide (76), is a special case of the example above.

Now, in order to construct a transformed operator, we consider

$$u_2 = R_A(\lambda) f, \quad f \in L^2(\mathbb{R}),\ \lambda \in \rho(A),\ u_2 \in D(A)$$

for $|y| > d$. Assuming that f has support in the waveguide's core $\operatorname{supp}(f) \subset (-d, d)$ we get

$$-\frac{\mathrm{d}^2 u_2}{\mathrm{d}y^2} - (k_{\mathrm{cl}}^2 + \lambda) u_2 = 0, \quad \text{for } |y| > d. \tag{6}$$

To extend this equation analytically, it has to be considered w.r.t. the complex variable $\hat{y}$

$$-\frac{\mathrm{d}^2 \hat{u}_2(\hat{y})}{\mathrm{d}\hat{y}^2} - (k_{\mathrm{cl}}^2 + \lambda) \hat{u}_2(\hat{y}) = 0. \tag{7}$$

This is done by introducing a virtual absorbent layer of material, using parameterization $\hat{y} := C(\tilde{y})$ from Definition 2.8, which forces the wave to decay in the transverse direction. Then with notation $\tilde{u}_2(\tilde{y}) := \hat{u}_2(C(\tilde{y}))$ and $\alpha := \dfrac{1}{C'(\tilde{y})}$, $C'(\tilde{y}) \neq 0$, we have the following equation

$$-\alpha \frac{\mathrm{d}}{\mathrm{d}\tilde{y}} \left(\alpha \frac{\mathrm{d}\tilde{u}_2}{\mathrm{d}\tilde{y}} \right) - (k_{\mathrm{cl}}^2 + \lambda) \tilde{u}_2 = 0 \quad \text{for all } \tilde{y} \in \mathbb{R},\ |\tilde{y}| > d.$$

Hence, for the whole cross-section, we have

$$-\alpha \frac{\mathrm{d}}{\mathrm{d}\tilde{y}} \left(\alpha \frac{\mathrm{d}\tilde{u}_2}{\mathrm{d}\tilde{y}} \right) - (k^2 + \lambda) \tilde{u}_2 = f \quad \text{for all } \tilde{y} \in \mathbb{R}.$$

Remark: In order not to visually overload the notations below, the tilde will be omitted.

Therefore the transverse operator A after application of the infinite PML becomes transverse transformed operator $A_\alpha \colon D(A_\alpha) \subset L^2(\mathbb{R}) \to L^2(\mathbb{R})$ which is defined as follows:

Definition 2.9 (The transverse transformed operator A_α)**.** *The PML-transformed transverse operator A_α is an operator defined as*

$$A_\alpha v := -\alpha \frac{\mathrm{d}}{\mathrm{d}y}\left(\alpha \frac{\mathrm{d}v}{\mathrm{d}y}\right) - k^2 v, \tag{8}$$

$$\text{for any} \quad v \in D(A_\alpha) := \left\{ v \in H^1(\mathbb{R}),\, \alpha \frac{\mathrm{d}}{\mathrm{d}y}\left(\alpha \frac{\mathrm{d}v}{\mathrm{d}y}\right) \in L^2(\mathbb{R}) \right\}. \tag{9}$$

The following theorems present results for the essential spectrum $\sigma_e(A_\alpha)$ and discrete spectrum $\sigma_d(A_\alpha)$ of the transformed operator A_α. We reproduce and sketch proofs from Chapter 2 in [40] slightly adapted to our case.

Remark: When determining the structure of spectrum A_α, it is necessary to take into account that it is no longer a self-adjoint operator, and techniques that work for a self-adjoint operator are not suitable here.

Let the branch cut for the complex square root function be the half-line $\mathrm{i}\mathbb{R}^+$ and we fix α_∞ (Def. 2.8) with assumption $-\frac{\pi}{2} < \arg_{\mathrm{i}\mathbb{R}^+}(\alpha_\infty) < 0$.

Theorem 2.3 (Essential spectrum $\sigma_e(A_\alpha)$)**.** *The essential spectrum of the transverse operator A_α (8) transformed according to parameterization C (Def. 2.8) is complex-valued and is rotated by an angle $2\arg_{\mathrm{i}\mathbb{R}^+}(\alpha_\infty)$ relative to the essential spectrum of the transverse operator A (3):*

$$\sigma_e(A_\alpha) = -k_{\mathrm{cl}}^2 + \alpha_\infty^2 \mathbb{R}^+.$$

Proof. First, let us introduce the auxiliary operator

$$A_\alpha^\infty v := -\alpha_\infty^2 \frac{\mathrm{d}^2 v}{\mathrm{d}y^2} - k_{\mathrm{cl}}^2 v, \quad \text{for any} \quad v \in H^2(\mathbb{R}). \tag{10}$$

We have from Lemma 2.1 in [40], that

$$\sigma(A_\alpha^\infty) = \sigma_e(A_\alpha^\infty) = -k_{\mathrm{cl}}^2 + \alpha_\infty^2 \mathbb{R}^+. \tag{11}$$

The main goal is to show that

$$\exists\, \xi \in \mathbb{C} : \ \xi \in \rho(A_\alpha) \cap \rho(A_\alpha^\infty)$$

and that for such ξ the corresponding resolvent can be represented as

$$R_{A_\alpha}(\xi) = R_{A_\alpha^\infty}(\xi) + K,$$

where K is a compact operator.

1. As a first step we seek for ξ such that $\exists\, R_{A_\alpha}(\xi) := (A_\alpha - \xi I)^{-1}$ and $\exists\, R_{A_\alpha^\infty}(\xi) := (A_\alpha^\infty - \xi I)^{-1}$.

We are looking for $\xi \in \mathbb{C}$ such that for $f \in L^2(\mathbb{R})$, $u_2 \in D(A_\alpha)$ following equation holds $R_{A_\alpha}(\xi) f = u_2$. Let us show that the corresponding sesquilinear form

$$\left(\frac{1}{\alpha}(A_\alpha - \xi)u_2,\, v\right)_{L^2(\mathbb{R})} = \int_{\mathbb{R}} \alpha \frac{\mathrm{d}u_2}{\mathrm{d}y}\frac{\mathrm{d}\overline{v}}{\mathrm{d}y} - \frac{1}{\alpha}(k^2 + \xi) u_2 \overline{v}\, \mathrm{d}y \tag{12}$$

is coercive. By assumption $-\frac{\pi}{2} < \arg_{\mathrm{i}\mathbb{R}^+}(\alpha_\infty) < 0$ and definition of α (Def. 2.8) we see that $-\frac{\pi}{2} < \arg_{\mathrm{i}\mathbb{R}^+}(\alpha) \leq 0$.

Let us take $\varepsilon > 0$ small enough such that $-\frac{\pi}{2} + \varepsilon < \arg_{\mathrm{i}\mathbb{R}^+}(\alpha) \leq 0$. Since $\arg_{\mathrm{i}\mathbb{R}^+}\left(\frac{1}{\alpha}\right) = -\arg_{\mathrm{i}\mathbb{R}^+}(\alpha)$ we have the following estimate:

$$0 \leq \arg_{\mathrm{i}\mathbb{R}^+}\left(\frac{1}{\alpha}\right) < \frac{\pi}{2} - \varepsilon.$$

And since wavenumber k^2 is real, we can find $\xi \in \mathbb{C}$ such that

$$-\frac{\pi}{2} + \frac{\varepsilon}{2} < \arg_{\mathrm{i}\mathbb{R}^+}(-(k^2+\xi)) < \frac{\varepsilon}{2}.$$

Hence, with $\arg_{\mathrm{i}\mathbb{R}^+}(\alpha_1\,\alpha_2) = \arg_{\mathrm{i}\mathbb{R}^+}(\alpha_1) + \arg_{\mathrm{i}\mathbb{R}^+}(\alpha_2)$, we have

$$-\frac{\pi}{2} + \frac{\varepsilon}{2} < \arg_{\mathrm{i}\mathbb{R}^+}\left(\frac{-(k^2+\xi)}{\alpha}\right) < \frac{\pi}{2} - \frac{\varepsilon}{2}.$$

With the help of these estimates, we can see, that the values taken by α, $-\dfrac{(k^2+\xi)}{\alpha}$ are all strictly in the half-plane $\{\tau \in \mathbb{C} : \ \mathfrak{Re}\,\tau > 0\}$. Therefore, $\exists\, C > 0$ such that

$$\begin{aligned}
\mathfrak{Re}\Big(\frac{1}{\alpha}(A_\alpha - \xi)u_2,\, u_2\Big)_{L^2(\mathbb{R})} &= \mathfrak{Re}\int_{\mathbb{R}} \alpha \frac{\mathrm{d}u_2}{\mathrm{d}y}\frac{\mathrm{d}\overline{u_2}}{\mathrm{d}y} - \frac{1}{\alpha}(k^2+\xi)u_2\overline{u_2}\,\mathrm{d}y \\
&= \mathfrak{Re}\int_{\mathbb{R}} \alpha\Big|\frac{\mathrm{d}u_2}{\mathrm{d}y}\Big|^2 + \frac{1}{\alpha}(-k^2-\xi)\big|u_2\big|^2\,\mathrm{d}y \\
&> C\|u_2\|^2_{H^1(\mathbb{R})}.
\end{aligned}$$

Thus, with the boundness of the sesqilinear form follows that such $\xi \in \rho(A_\alpha)$ exists [53], [5].

We see from (11) that $R_{A_\alpha^\infty}(\xi)$ exists for all $\xi \notin -k_{\mathrm{cl}}^2 + \alpha_\infty^2\mathbb{R}^+$. Hence, $\xi \in \rho(A_\alpha^\infty)$.

2. Next, we are going to show that $R_{A_\alpha}(\xi) = R_{A_\alpha^\infty}(\xi) + K$, where K is compact.

Let (f_n) be a bounded sequence in $L^2(\mathbb{R})$. In order not to complicate the notation, we will omit here the index 2 of the function u_2 defined in the y direction. Let us denote

$$u_n := R_{A_\alpha}(\xi)f_n \quad \text{and} \quad u_n^\infty := R_{A_\alpha^\infty}(\xi)f_n.$$

We want to show that from $w_n := u_n - u_n^\infty$ we can select a subsequence that strongly converges in $L^2(\mathbb{R})$. Further indexing with n is used for a subsequence notation as well.

The main trick that is used here is to consider the difference in variational formulations of problems

$$(A_\alpha - \xi)u_n = f_n \quad \text{and} \quad (A_\alpha^\infty - \xi)u_n^\infty = f_n :$$

$$\Big(\frac{1}{\alpha}(A_\alpha-\xi)u_n-\frac{1}{\alpha_\infty}(A^\infty_\alpha-\xi)u^\infty_n,\,v\Big)_{L^2(\mathbb{R})}=$$
$$\int_{\mathbb{R}}\Big(\alpha\frac{\mathrm{d}u_n}{\mathrm{d}y}\frac{\mathrm{d}\overline{v}}{\mathrm{d}y}-\frac{1}{\alpha}(k^2+\xi)u_n\overline{v}\Big)\,\mathrm{d}y-\int_{\mathbb{R}}\Big(\alpha_\infty\frac{\mathrm{d}u^\infty_n}{\mathrm{d}y}\frac{\mathrm{d}\overline{v}}{\mathrm{d}y}-\frac{1}{\alpha_\infty}(k^2_{\mathrm{cl}}+\xi)u^\infty_n\overline{v}\Big)\,\mathrm{d}y$$
$$=\int_{\mathbb{R}}\frac{1}{\alpha}f_n\overline{v}\,\mathrm{d}y-\int_{\mathbb{R}}\frac{1}{\alpha_\infty}f_n\overline{v}\,\mathrm{d}y.$$

Considering that $u_n=w_n+u^\infty_n$ we have

$$\int_{\mathbb{R}}\alpha\frac{\mathrm{d}w_n}{\mathrm{d}y}\frac{\mathrm{d}\overline{v}}{\mathrm{d}y}\,\mathrm{d}y-\int_{\mathbb{R}}\alpha_\infty\frac{\mathrm{d}u^\infty_n}{\mathrm{d}y}\frac{\mathrm{d}\overline{v}}{\mathrm{d}y}\,\mathrm{d}y+\int_{\mathbb{R}}\alpha\frac{\mathrm{d}u^\infty_n}{\mathrm{d}y}\frac{\mathrm{d}\overline{v}}{\mathrm{d}y}\,\mathrm{d}y$$
$$-\int_{\mathbb{R}}\frac{k^2+\xi}{\alpha}w_n\overline{v}\,\mathrm{d}y+\int_{\mathbb{R}}\frac{k^2_{\mathrm{cl}}+\xi}{\alpha_\infty}u^\infty_n\overline{v}\,\mathrm{d}y-\int_{\mathbb{R}}\frac{k^2+\xi}{\alpha}u^\infty_n\overline{v}\,\mathrm{d}y$$
$$=\int_{\mathbb{R}}\Big(\frac{1}{\alpha}-\frac{1}{\alpha_\infty}\Big)f_n\overline{v}\,\mathrm{d}y.$$

By taking $v=w_n$ we have

$$a_n=b_n+c_n+d_n, \tag{13}$$

where

$$a_n:=\int_{\mathbb{R}}\alpha\Big|\frac{\mathrm{d}w_n}{\mathrm{d}y}\Big|^2-\frac{1}{\alpha}(k^2+\xi)\big|w_n\big|^2\,\mathrm{d}y,$$
$$b_n:=\int_{\mathbb{R}}\Big(\frac{1}{\alpha}-\frac{1}{\alpha_\infty}\Big)f_n\overline{w_n}\,\mathrm{d}y,$$
$$c_n:=\int_{\mathbb{R}}(\alpha_\infty-\alpha)\frac{\mathrm{d}u^\infty_n}{\mathrm{d}y}\frac{\mathrm{d}\overline{w_n}}{\mathrm{d}y}\,\mathrm{d}y,$$
$$d_n:=\int_{\mathbb{R}}\Big(\frac{k^2+\xi}{\alpha}-\frac{k^2_{\mathrm{cl}}+\xi}{\alpha_\infty}\Big)u^\infty_n\overline{w_n}\,\mathrm{d}y.$$

By assumption (f_n) is a bounded sequence in $L^2(\mathbb{R})$, then by Theorem 3.18 in [17] there is a limit to which a subsequence (f_n) weakly converges in $L^2(\mathbb{R})$. Without loss of generality, we assume that $f_n\rightharpoonup 0$ in $L^2(\mathbb{R})$.

Resolvent $R_{A_\alpha}(\xi)$ is a bounded operator in $L^2(\mathbb{R})$ with values in $H^1(\mathbb{R})$ (9), and $R_{A^\infty_\alpha}(\xi)$ is a bounded operator in $L^2(\mathbb{R})$ with values in $H^2(\mathbb{R})$ (10). Then from the weak convergence of $f_n\rightharpoonup 0$ in $L^2(\mathbb{R})$ it follows $u_n\rightharpoonup 0$ in $H^1(\mathbb{R})$, $w_n\rightharpoonup 0$ in $H^1(\mathbb{R})$ and $u^\infty_n\rightharpoonup 0$ in $H^2(\mathbb{R})$.

We denote with $\Omega_d:=\operatorname{supp}(\alpha-\alpha_\infty)$. By assumption on α, Ω_d is compact.

Now consider each term in (13):

$$b_n=\int_{\Omega_d}\Big(\frac{1}{\alpha}-\frac{1}{\alpha_\infty}\Big)f_n\overline{w_n}\,\mathrm{d}y.$$

By Rellich-Kondrachov Compactness theorem (see e.g. section 5.7 Theorem 1 and remark after theorem in [34]) if $w_n\rightharpoonup 0$ in $H^1(\Omega_d)$ we have $w_n\to 0$ strongly in $L^2(\Omega_d)$ up to a subsequence. And since $(f_n)_n$ is bounded in $L^2(\Omega_d)$ we deduce that $b_n\to 0$.

Next term becomes

$$c_n = \int_{\Omega_d} (\alpha_\infty - \alpha) \frac{\mathrm{d}u_n^\infty}{\mathrm{d}y} \frac{\mathrm{d}\overline{w_n}}{\mathrm{d}y} \,\mathrm{d}y.$$

From weak convergence $u_n^\infty \rightharpoonup 0$ in $H^2(\Omega_d)$ we have $\frac{\mathrm{d}u_n^\infty}{\mathrm{d}y} \to 0$ strongly in $L^2(\Omega_d)$. Furthermore $\frac{\mathrm{d}w_n}{\mathrm{d}y}$ is bounded in $L^2(\Omega_d)$. Hence $c_n \to 0$.

Finally we consider the last term

$$d_n = \int_{\Omega_d} \Big(\frac{k^2 + \xi}{\alpha} - \frac{k_{\mathrm{cl}}^2 + \xi}{\alpha_\infty} \Big) u_n^\infty \overline{w_n} \,\mathrm{d}y.$$

u_n^∞ is bounded in $L^2(\Omega_d)$ and $w_n \to 0$ in $L^2(\Omega_d)$. Therefore $d_n \to 0$.

We can deduce that $d_n \to 0$. Based on the estimates obtained in the first step, we have $|a_n| \geq C\|w_n\|^2_{H^1(\mathbb{R})}$. Hence $w_n \to 0$ in $H^1(\mathbb{R})$.

In the second step we showed that if we assume that (f_n) tends to zero in $L^2(\mathbb{R})$, then $\|w_n\|_{H^1(\mathbb{R})} \to 0$, since $\alpha_\infty - \alpha$ has compact support. Thus, we have shown that the resolvent $R_{A_\alpha}(\xi) = R_{A_\alpha^\infty}(\xi) + K$, where K is a compact operator.

3. As the last step, we derive the expression for the essential spectrum of the transformed transverse operator A_α.

According to the result from the previous step and Theorem 2.1, Chapter 9 in [32], which is a generalization for not necessarily self-adjoint operators of Weyl's theorem, we have

$$\sigma_e(R_{A_\alpha^\infty}(\xi) + K) = \sigma_e(R_{A_\alpha^\infty}(\xi)),$$

hence

$$\sigma_e(R_{A_\alpha}(\xi)) = \sigma_e(R_{A_\alpha^\infty}(\xi)). \tag{14}$$

Next, according to Theorem 2.3 in Chapter 9 in [32], spectrum of the operator and the resolvent operator are related as follows:

$$\text{for} \quad \lambda \neq \xi,\, \lambda \in \sigma_e(A_\alpha^\infty) \quad \Leftrightarrow \quad \frac{1}{\lambda - \xi} \in \sigma_e(R_{A_\alpha^\infty}(\xi)).$$

Then together with (14) we observe that from

$$\lambda \in \sigma_e(A_\alpha^\infty) = -k_{\mathrm{cl}}^2 + \alpha_\infty^2 \mathbb{R}^+$$

follows that

$$\frac{1}{\lambda - \xi} \in \sigma_e(R_{A_\alpha^\infty}(\xi)).$$

Then

$$\frac{1}{\lambda - \xi} \in \sigma_e(R_{A_\alpha}(\xi)) \quad \text{with} \quad \lambda \in -k_{\mathrm{cl}}^2 + \alpha_\infty^2 \mathbb{R}^+$$

and finally

$$\frac{1}{\lambda - \xi} \in \sigma_e(R_{A_\alpha}(\xi)) \quad \Leftrightarrow \quad \lambda \in \sigma_e(A_\alpha),\ \sigma_e(A_\alpha) = -k_{\mathrm{cl}}^2 + \alpha_\infty^2 \mathbb{R}^+.$$

□

Remark: In the case of non-self-adjoint operators, several different definitions can be found in the literature. For example, according to the classification of Edmunds and Evans, Chapter 1, Section 4 in [32], the results presented above correspond to spectrum definitions σ_{e_k}, $k = 1, 2, 3, 4$. It is proven in Theorem 2.1 in [40], that $\sigma_e(A_\alpha) = -k_{\text{cl}}^2 + \alpha_\infty^2 \mathbb{R}^+$ is also valid for the remaining definitions of the essential spectrum.

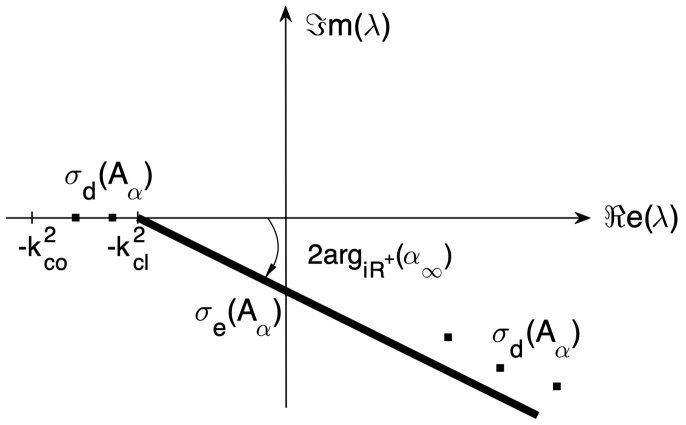

Figure 4: Spectrum of the non-self-adjoint transverse operator A_α (8): rotation of the essential spectrum $\sigma_e(A^\alpha)$ after transformation; values of the discrete spectrum $\sigma_d(A^\alpha)$ correspond now not only to the guided modes but also to the leaky modes.

Now we consider the structure of the discrete spectrum of the transverse transformed operator A_α. We assume again that $\alpha_\infty : -\dfrac{\pi}{2} < \arg_{\text{i}\mathbb{R}^+}(\alpha_\infty) < 0$.

Theorem 2.4 (Discrete spectrum $\sigma_d(A_\alpha)$)**.** *The discrete spectrum of the transformed transverse operator A_α (8) consists of the discrete spectrum of the transverse operator A (3):*

$$\sigma_d(A) \subset (-k_{\text{co}}^2,\, -k_{\text{cl}}^2)$$

as well as a countable set of values of finite multiplicity in the sector:

$$\{\lambda \in \mathbb{C} :\, 2\arg_{\text{i}\mathbb{R}^+}(\alpha_\infty) < \arg_{\text{i}\mathbb{R}^+}(k_{\text{cl}}^2 + \lambda) \leq 0\}.$$

Proof. Let $\lambda \in \sigma_d(A_\alpha)$ and $\tilde{u}_2$ to be a corresponding eigenfunction. The main idea of the proof is to consider the following equation which is satisfied by the function of a real variable $u_2(y) := \tilde{u}_2\big(C^{-1}(y)\big)$:

$$-\frac{\mathrm{d}^2 u_2}{\mathrm{d}y^2} - (k^2 + \lambda)u_2 = 0, \quad \text{for any } y \in \mathbb{R}.$$

In the case of a straight waveguide, the form of the solution and its behavior at infinity are known. Eigenvalues are examined for two cases. If λ such that

$$-\frac{3\pi}{2} < \arg_{\text{i}\mathbb{R}^+}(k_{\text{cl}}^2 + \lambda) < 2\arg_{\text{i}\mathbb{R}^+}(\alpha_\infty)$$

or

$$0 < \arg_{i\mathbb{R}^+}(k_{cl}^2 + \lambda) < \frac{\pi}{2},$$

then it can be shown [40] that the constructed functions u_2 are eigenfunctions of the transverse operator A. Hence, in this case, eigenfunctions are real with a finite number of $\lambda \in \sigma_d(A) \subset (-k_{co}^2, -k_{cl}^2)$.

Next, if λ is considered on the remaining sector of the complex plane, it can be shown that $\lambda \in \sigma_d(A_\alpha) \setminus \sigma_d(A)$ for

$$2\arg_{i\mathbb{R}^+}(\alpha_\infty) < \arg_{i\mathbb{R}^+}(k_{cl}^2 + \lambda) \leq 0.$$

For the details see Theorem 2.2 in [40]. □

Having considered the spectrum of an open waveguide, we can classify the leaky modes according to the structure of the spectrum as follows:

Definition 2.10 (Leaky modes)**.** *Eigenfunctions related to eigenvalues λ of the discrete spectrum of the transverse operator such that $\lambda \in \mathbb{C}$, $\mathfrak{Im}\lambda \neq 0$ are called leaky modes.*

Thus, if the differential operator defined on the waveguide cross-section is not self-adjoint, then in addition to guided modes and radiation modes, leaky modes can also be identified. Moreover, as can be seen from Theorem 2.3, in this case, the essential spectrum rotates according to the infinite PML transformation.

In the PML-transformed straight waveguides, leaky modes decay in the direction of propagation. But in the next subsection, we will show that this is not always the case.

2.1.2. Leaky modes in an open waveguide with constant curvature.

Now we will consider a more complex structure, the waveguide is no longer straight but has a bending of constant curvature in the direction of propagation. This case is discussed in detail in Section 2.3 since we will utilize solutions related to such a waveguide to calculate transmission coefficients for the Multi-Mode Approximation method (65).

Modeling bending losses in optical waveguides has been of particular interest for many years and in physical literature is directly linked to the concept of leaky mode. The approximation approaches for waveguides with large bending radii and, accordingly, small radiation losses can be found in the classical works on the optical physics of waveguides, for example, [77], [62], [61].

However, for bends with a small radius of curvature, such a simplification is not enough, and the leaky modes have to be considered as an exact solution of the Helmholtz equation for a cylindrical slab waveguide. In [46] it was shown that the solution in a waveguide with constant curvature can be represented semi-analytically using Bessel functions of complex order (35). The authors call such solutions leaky modes as well.

Despite the long history of leaky modes and open optical systems, for structure cases with more complex geometries than a straight waveguide (e.g. the bends considered here) the proof of the localization of the transverse operator spectrum has not been presented in the literature, to the best of our knowledge.

Helmholtz equation in a bend. The 2D bend or a waveguide with a constant curvature is a slab waveguide in a ring shape characterized by an outer radius of curvature R^+. We denote the core width by d and the material parameters of the structure are determined by the refractive indices n_{co} in the core and n_{cl} in the cladding (see Figure 7, left). It is suitable to consider differential equations with cylindrical symmetry in the cylindrical coordinates $(r,\, \theta)$:

$$x = r\sin(\theta),\ \ y = r\cos(\theta),\ \ r \in (0,\, \infty),\, \theta \in (0,\, 2\pi].$$

Then corresponding Lamé coefficients (150) are $h_r = 1$, $h_\theta = r$ and our leading equation

$$-\Delta u - k^2 u = 0, \quad (x, y) \in \mathbb{R}^2 \tag{15}$$

with

$$k(x,y) = \begin{cases} k_0 n_{\text{co}}, & \text{if } R^+ - d < \sqrt{x^2+y^2} < R^+ \ , \\ k_0 n_{\text{cl}}, & \text{else} \ , \end{cases}$$

where the refractive index $n(r) = n_{\text{co}}$ inside the core and $n(r) = n_{\text{cl}}$ in the cladding, $n_{\text{co}} > n_{\text{cl}} > 0$, $k_0 = 2\pi/\lambda_0$, becomes

$$r^2 \frac{\partial^2 u}{\partial r^2} + r\frac{\partial u}{\partial r} + \frac{\partial^2 u}{\partial \theta^2} + r^2 k^2 u = 0$$

for

$$k(r) = \begin{cases} k_0 n_{\text{co}}, & \text{if } R^+ - d < r < R^+ \ , \\ k_0 n_{\text{cl}}, & \text{else} \ . \end{cases}$$

With the separation of variables ansatz $u_1(\theta)u_2(r)$ we obtain in the longitudinal direction

$$-\frac{\mathrm{d}^2 u_1}{\mathrm{d}\theta^2} + \nu^2 u_1 = 0,$$

hence the component of the solution in fixed propagation direction is represented with $\mathrm{e}^{-\mathrm{i}\nu\theta}$, which together with $\nu = \mu R^+$ corresponds to the propagation along the bend. The constant μ is a propagation constant of the following form

$$\mu = \beta - \mathrm{i}\alpha, \quad \beta > 0,\, \alpha \geq 0, \tag{16}$$

where $\mathfrak{Re}\mu = \beta$ is a phase constant and α is an attenuation constant.

Then the components of the solution in the transverse direction are defined with

$$r^2 \frac{\mathrm{d}^2 u_2}{\mathrm{d}r^2} + r\frac{\mathrm{d}u_2}{\mathrm{d}r} + (k^2 r^2 - \mu^2 R^{+2}) u_2 = 0 \tag{17}$$

and we equip it with the following boundary conditions

$$\begin{aligned} &|u_2(r)| \to 0, \quad \text{as } r \to 0, \\ &|u_2(r)| \to 0, \quad \text{as } r \to +\infty, \quad u_2 \text{ is outgoing.} \end{aligned} \tag{18}$$

Definition 2.11 (The transverse operator A_{R^+})**.** *The transverse operator A_{R^+} is an operator in $L^2(0,\infty)$ defined as*

$$A_{R^+}v(r) := \frac{\mathrm{d}}{\mathrm{d}r}\Big(\frac{r}{R^+}\frac{\mathrm{d}v(r)}{\mathrm{d}r}\Big) + k^2(r)\frac{r}{R^+}v(r), \tag{19}$$

for any

$$v \in D(A_{R^+}) := \Big\{v \in H^1(0,\infty) : \frac{\mathrm{d}v}{\mathrm{d}r}\Big(\frac{r}{R^+}\frac{\mathrm{d}v}{\mathrm{d}r}\Big) \in L^2(0,\infty), \\ \textit{satisf. given boundary conditions}\Big\}.$$

Then the weighted eigenvalue problem with parameter R^+ on the cross-section of the waveguide can be written as

$$A_{R^+}u_2 = \frac{R^+}{r}\mu^2 u_2, \quad r \in (0,\infty). \tag{20}$$

It is shown in the previous subsection that in the case of a straight open waveguide in the absence of PML the transverse operator is self-adjoint and corresponding eigenvalues are real. For the more advanced waveguide shapes, we can observe with numerical

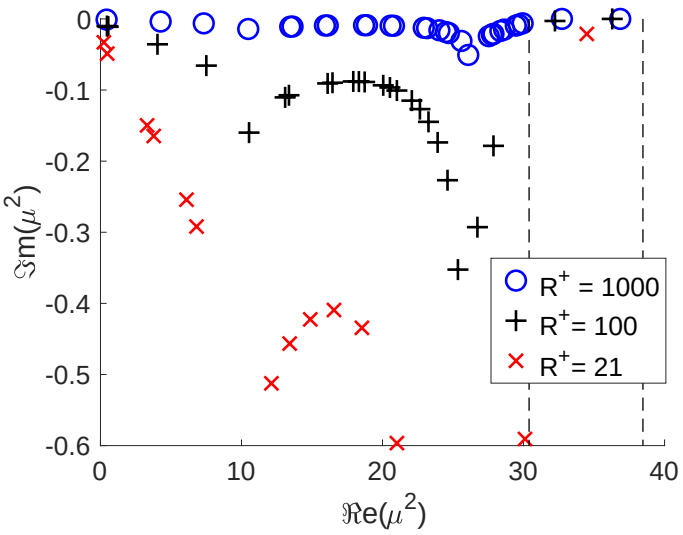

Figure 5: Location of the discrete spectrum in the complex plane for a bent waveguide of radius $R^+ = \{21, 100, 1000\}$. The black dashed lines correspond to $k_{\mathrm{cl}}^2 = n_{\mathrm{cl}}^2 k_0^2$ and $k_{\mathrm{co}}^2 = n_{\mathrm{co}}^2 k_0^2$. Values between them relate to guided modes, and to the left from k_{cl} correspond to leaky modes. Parameters: $d = 1.8$, $\lambda_{wave} = 1.55$, $n_{\mathrm{co}} = 1.53$, $n_{\mathrm{cl}} = 1.36$.

computations that the differential operator on the cross-section is characterized with eigenvalues μ^2 such that $\mathfrak{Im}(\mu^2) \neq 0$ even in the absence of PML, see Figure 5. Then the cross-section operator related to such a waveguide cannot be self-adjoint. The values μ^2 can be found by solving (40) for the order $\nu = \mu R^+$ of the cylindrical functions. They can be computed, for example, in Mathematica [51] utilizing `FindRoot` following the heuristic procedure described in [46].

Therefore, following Definition 2.10 we indeed can see, that solutions that are used in the Multi-Mode approximation method (65) are leaky modes if $\mathfrak{Im}(\mu^2) \neq 0$ and guided modes otherwise.

We observe in Figure 5 that the imaginary parts of the eigenvalues of the transverse differential operator of a bent waveguide decrease when the associated mode is mainly localized in the waveguide's core. For a waveguide with a large radius of curvature, they are almost zero, which corresponds to the fact that as the radius tends to infinity, the bent waveguide solutions behave as solutions in a straight waveguide.

One also can see in Figure 5, that the eigenvalues corresponding to the guided modes are located in the interval $(k_{\text{cl}}^2,\, k_{\text{co}}^2)$, and beyond k_{cl}^2 we can observe a distribution of eigenvalues of the leaky modes in a certain section of the complex plane.

2.2. Existence and uniqueness of a solution in open waveguide

Here we recall some results from open waveguides well-posedness theory.

In the previous Section 2.1, we considered the application of an infinite PML for the open straight waveguide. For a waveguide with a curved junction, showing the structure of the spectrum in this way is not an easy task, since, firstly, the shape is such that an explicit representation of the transverse operator may be impossible and, secondly, the structure of the spectrum before the introduction of the PML is also not known.

Therefore for waveguides with curved junction, in order to show existence and uniqueness, one should use another approach. In the case of waveguides with compact perturbation, as far as we know, well-posedness has been shown for 2D waveguides, where signal transmission is modeled by the Helmholtz equation.

The configuration of our interest is an open waveguide which is represented as endless straight parts connected by a junction. The signal facing the junction could be reflected and the different nature of the resulting reflected waves allows them to be classified into subtypes. The modal radiation condition proposed in [27] controls the propagation of such transmitted and reflected waves along the waveguide, that is, if the incident wave u^{inc} goes from left to right, then the wave reflected from the junction $u - u^{\text{inc}}$ propagates to the left, and the transmitted signal goes to the right.

The construction of this modal radiation condition was done via the *Generalized Fourier transform*. For Sturm–Liouville operators such a transformation was for the first time introduced in [80], the cases with semi-infinite and infinite layers were considered later in [84]. From among the numerous further applications, we highlight [43], where they constructed a distribution framework for the Generalized Fourier transform for a Sturm–Liouville operator on a half-space $\mathbb{R}^+$. This generalized Fourier transform framework was then applied in [27] to formulate the modal radiation condition, which was subsequently used in the proof of well-posedness in [28].

Below we recall the main results from [43], [27], [28]. First, we will consider the features of the generalized Fourier transform application in the case of an open waveguide on an example of a straight waveguide. Then we consider a problem with a junction and present the modal radiation condition, which utilizes the generalized Fourier transform associated with the transverse differential operator on semi-infinite straight waveguide sections. Then it is possible to show that the corresponding scattering problem, which

arises due to the junction, equipped with modal radiation condition is well posed (Theorem 2.3 and 4.1 in [28]).

2.2.1. Generalized Fourier transform associated with transverse differential operator

We consider again the problem (1), but in the setting proposed in the works mentioned above. The waveguide is considered now in a half-plane $\mathbb{R}^2_+ := \Big\{(x,y) \in \mathbb{R}^2,\, y > 0\Big\}$ with $u(x,0) = 0$ for $x \in \mathbb{R}$. The wave number k is real and depends on the transverse direction $y \in \mathbb{R}^+$ for all $x \in \mathbb{R}$ as

$$k = \begin{cases} k_{\mathrm{co}}, & \text{if } y \in (0,d)\ , \\ k_{\mathrm{cl}}, & \text{else}\ . \end{cases}$$

With the separation of variables, we have the following Sturm–Liouville eigenvalue problem in transverse direction: find $\lambda \in \mathbb{C}$ and $u_2 \in H^2(\mathbb{R}^+) \cap H^1_0(\mathbb{R}^+)$ s.th.

$$\begin{cases} -\dfrac{\mathrm{d}^2 u_2}{\mathrm{d}y^2} - k^2 u_2 &= \lambda u_2 \quad \text{in } \mathbb{R}^+, \\ u_2 &= 0 \qquad \text{for } y = 0. \end{cases} \tag{21}$$

For every fixed $\lambda \in \mathbb{C}$ an entire family of solutions to (21) is defined by the linear combination

$$\Phi_\lambda(y) := c_\lambda(0) s_\lambda(y) - s_\lambda(0) c_\lambda(y)$$

of the following functions

$$\begin{aligned} s_\lambda(y) &:= \frac{1}{\sqrt[\mathrm{i}\mathbb{R}^+]{k^2+\lambda}} \sin\Big(\sqrt[\mathrm{i}\mathbb{R}^+]{k^2+\lambda}\,(y-d)\Big), \\ c_\lambda(y) &:= \cos\Big(\sqrt[\mathrm{i}\mathbb{R}^+]{k^2+\lambda}\,(y-d)\Big), \end{aligned}$$

where the branch cut for the complex square root function is the half-line $\mathrm{i}\mathbb{R}^+$.

The associated transverse operator $A^+ \colon D(A^+) \subset L^2(\mathbb{R}^+) \to L^2(\mathbb{R}^+)$ is given as:

Definition 2.12 (The transverse operator A^+)**.** *The transverse operator A^+ is an operator defined as*

$$A^+ v := -\frac{\mathrm{d}^2 v}{\mathrm{d}y^2} - k^2 v, \quad \textit{for any} \quad v \in D(A^+) := \Big\{v \in H^2(\mathbb{R}^+) \cap H^1_0(\mathbb{R}^+)\Big\}. \tag{22}$$

This operator is an unbounded self-adjoint operator and, like in Section 2.1.1, Theorem 2.2, its spectrum consists of an essential and discrete spectrum

$$\sigma(A^+) = \sigma_e(A^+) \cup \sigma_d(A^+).$$

The corresponding modes can be classified w.r.t. these two parts of the spectrum:

- The discrete spectrum $\sigma_d(A^+) \subset (-k^2_{\mathrm{co}}, -k^2_{\mathrm{cl}})$ consists of a finite number of eigenvalues λ_j, $j = 1, 2, \ldots, N$, and the related eigenfunctions Φ_{λ_i} are guided modes, $\Phi_{\lambda_i} \in L^2(\mathbb{R}^+)$.

- For each eigenvalue from the essential spectrum $\lambda \in \sigma_e(A^+)$, $\sigma_e(A^+) = [-k_{\text{cl}}^2,\, +\infty)$, the corresponding Φ_λ is no longer an eigenfunction, but a *generalized eigenfunction* since $\Phi_\lambda \notin L^2(\mathbb{R}^+)$. Modes related to essential spectrum $\sigma_e(A^+)$ are radiation modes.

From this spectral decomposition, we can see that certain types of solutions correspond to certain values of the spectrum. Thus, with generalized Fourier transformation it is possible to show the isomorphism between "physical" space and "spectral" space, i.e. generalized Fourier transformation leads to unitary transformation from $L^2(\mathbb{R}^+)$ to some L^2 spectral space.

Spectral measure. To characterize this spectral space, we consider the definition of the spectral measure for the transverse operator A^+ (see [43], Section 3).

Definition 2.13. *The spectral measure E associated with the transverse operator A^+ is defined with the following expression: for every measurable function $f\colon \mathbb{R} \to \mathbb{C}$, the operator $f(A^+)$ can be expressed as*

$$f(A^+)\phi = \int_{\mathbb{R}} f(\lambda)\,\mathrm{d}E_\lambda\phi, \quad \text{for any } \phi \in D(f(A^+)),$$
$$D(f(A^+)) = \Big\{v \in L^2(\mathbb{R}^+) : \int_{\mathbb{R}} |f(\lambda)|^2\,\mathrm{d}\|E_\lambda v\|^2_{\mathbb{R}^+} < \infty\Big\}.$$

With the application of Stone's formula [75] for any $\phi \in L^2(\mathbb{R}^+)$ and $I = [\lambda_1,\, \lambda_2] \subset \mathbb{R}$ we have

$$\|E_I\phi\|^2_{\mathbb{R}^+} = \frac{1}{2\mathrm{i}\pi} \lim_{\delta\to 0+} \lim_{\varepsilon\to 0+} \int_{\lambda_1-\delta}^{\lambda_2+\delta} \Big(\big(R_{A^+}(\lambda+\mathrm{i}\varepsilon) - R_{A^+}(\lambda-\mathrm{i}\varepsilon)\big)\phi,\, \phi\Big)_{\mathbb{R}^+} \mathrm{d}\lambda.$$

In the case under consideration it is possible to explicitly express the Green's function. Therefore with the integral representation of the resolvent via the Green's function one can show the following explicit expression for the spectral measure related to the Sturm–Liouville problem (21):

Proposition 1. *For any function ϕ of $L^2(\mathbb{R}^+)$ with compact support $\phi \in L^2_{\text{comp}}(\mathbb{R}^+)$, the spectral measure can be expressed as*

$$\mathrm{d}\|E_\lambda\phi\|^2_{\mathbb{R}^+} = \big|\langle\phi,\, \Phi_\lambda\rangle_{\mathbb{R}^+}\big|^2 \rho_\lambda\,\mathrm{d}\lambda\Big|_{\sigma_e(A^+)} + \sum_{\lambda\in\sigma_d(A^+)} \big|(\phi,\, \Phi_\lambda)_{\mathbb{R}^+}\big|^2 \rho_\lambda\delta_\lambda$$

where $\mathrm{d}\lambda\big|_{\sigma_e(A^+)}$ is the Lebesgue measure for $\sigma_e(A^+)$, δ_λ is the Dirac measure for $\lambda \in \sigma_d(A^+)$, and

$$\rho_\lambda := \begin{cases} \dfrac{1}{\|\Phi_\lambda\|^2_{\mathbb{R}^+}}, & \text{if } \lambda \in \sigma_d(A^+)\,, \\[2ex] \dfrac{\sqrt{k_{\text{cl}}^2+\lambda}}{\pi\big(c_\lambda^2(0) + (k_{\text{cl}}^2+\lambda)s_\lambda^2(0)\big)}, & \text{if } \lambda \in \sigma_e(A^+)\,. \end{cases}$$

Proof. See Proposition 1 in [43]. □

Diagonalization of A^+ and distributions. Let us denote the measure on $\mathbb{R}$ with

$$\mathrm{d}\mu := \sum_{\lambda\in\sigma_d(A^+)} \rho_\lambda \delta_\lambda + \rho_\lambda \,\mathrm{d}\lambda\Big|_{\sigma_e(A^+)}. \tag{23}$$

The following theorem defines the generalized Fourier transform and describes how it can be applied.

Theorem 2.5 (Generalized Fourier transform F)**.** *The generalized Fourier transformation F related to the transverse operator operator A^+ (22)*

$$\begin{aligned}(F\phi)(\lambda) :&= \int_{\mathbb{R}^+} \phi(y)\,\overline{\Phi_\lambda(y)}\,\mathrm{d}y \\ &= \langle \phi,\, \Phi_\lambda\rangle_{\mathbb{R}^+}, \quad \textit{for any } \lambda\in\sigma(A^+),\, \phi\in L^2_{\mathrm{comp}}(\mathbb{R}^+)\end{aligned}$$

extends to a unitary operator from $L^2(\mathbb{R}^+)$ to $L^2(\sigma,\,\mathrm{d}\mu)$, which diagonalizes A in the sense that for every measurable function $f\colon \mathbb{R}\to\mathbb{C}$

$$f(A)\phi = F^{-1}f(\lambda)F\phi, \quad \textit{for any } \phi\in D(f(A)) = F^{-1}(L^2(\sigma,\,(1+|f(\cdot)|^2)\mathrm{d}\mu)), \tag{24}$$

where $f(\lambda)$ denotes multiplication by $f(\lambda)$ in $L^2(\sigma,\,\mathrm{d}\mu)$ and

$$\begin{aligned}(F^{-1}\widehat{\phi})(y) &= \int_{\sigma(A^+)} \Phi_\lambda(y)\,\widehat{\phi}(\lambda)\,\mathrm{d}\mu(\lambda) \\ &= \sum_{\lambda\in\sigma_d(A^+)} \rho_\lambda\widehat{\phi}(\lambda)\Phi_\lambda(y) + \lim_{m\to+\infty}\int_{-k_{\mathrm{cl}}^2+m^{-1}}^{m} \widehat{\phi}(\lambda)\Phi_\lambda(y)\rho_\lambda\,\mathrm{d}\lambda, \\ &\qquad\qquad \textit{for all } \widehat{\phi}\in L^2(\sigma,\,\mathrm{d}\mu).\end{aligned}$$

Proof. See Theorem 3 in [43]. □

Corollary 2.5.1. *For any $\phi\in L^2(\mathbb{R}^+)$ with help of (24) we have the following representation*

$$\begin{aligned}\phi &= F^{-1}F\phi \\ &= \sum_{\lambda\in\sigma_d(A^+)} \frac{(F\phi)(\lambda)}{\|\Phi_\lambda\|^2_{\mathbb{R}^+}}\Phi_\lambda + \int_{\lambda\in\sigma_e(A^+)} (F\phi)(\lambda)\,\Phi_\lambda\rho_\lambda\,\mathrm{d}\lambda.\end{aligned}$$

However, we cannot apply diagonalization to solve the open straight waveguide problem yet, since, as we mentioned earlier, solutions $u(x,\cdot)$ do not belong to $L^2(\mathbb{R}^+)$ in general. Hence, we need to extend the Fourier transform to a larger space – the space of distributions.

A generalized function (or distribution) φ is defined with a linear continuous functional over a space of "sufficiently good functions" – test functions. For example, $\varphi\in D'(\mathbb{R}^n)$ such that $\varphi\colon v\to(\varphi,\,v)$ for any $v\in D(\mathbb{R}^n)$. In other words, we can

consider test functions as a structure that allows to construct the space of generalized functions (the space of linear functionals).

A remarkable property of the class of generalized functions of slow growth is that the Fourier transform does not take them outside this class. The common choice as a test function space in this case is the *Schwartz space* $S(\mathbb{R}^n)$. These are infinitely smooth functions on $\mathbb{R}^n$, decaying for $|x| \to \infty$ faster than any $|x|^{-k}$, $k \in \mathbb{N}$, as well as all their derivatives [81].

If we consider the Fourier transform of a test function from such a space, it can be shown for $v \in S(\mathbb{R}^n)$ function $Fv \in S(\mathbb{R}^n)$ [81].

Now consider Fourier transform for generalized functions $S'(\mathbb{R}^n)$. For some measurable function f on $\mathbb{R}^n$ function $F\,f$ defines a generalized function of slow growth with the following expression

$$(Ff,\, v) = \int_{\mathbb{R}^n} (Ff)(\xi)\, v(\xi)\, \mathrm{d}\xi, \quad \text{for any } v \in S(\mathbb{R}^n).$$

It can be shown that $(Ff,\, v) = (f,\, F\,v)$, $v \in S(\mathbb{R}^n)$, $f \in S'(\mathbb{R}^n)$ and with this the Fourier transform for any distribution $f \in S'(\mathbb{R}^n)$ can be defined.

In the case of the open waveguide problem considered in the current section, in [43], a suitable Schwartz space corresponding to the transverse operator A^+ was constructed. With the following cutoff frequency assumption

$$k_{\mathrm{co}}^2 - k_{\mathrm{cl}}^2 \neq \left(n + \frac{1}{2}\right)^2 \frac{\pi^2}{d^2}, \quad \text{for any } n \in \mathbb{N} \tag{25}$$

it is defined as follows:

Definition 2.14 (Space of test functions $S_{A^+}(\mathbb{R}^+)$)**.**

$S_{A^+}(\mathbb{R}^+) := \{v \in C^\infty(\mathbb{R}^+\backslash\{d\}) :$ *decay to 0 for* $x \to +\infty$ *rapidly with all its derivatives and satisfy for any* $n \in \mathbb{N}$

$$\begin{aligned}
&\frac{\mathrm{d}^{2n} v(0)}{\mathrm{d}y} = 0, \\
&\lim_{\varepsilon \to 0+} \left[\left(\frac{\mathrm{d}^2}{\mathrm{d}y} + k^2 \right)^n \big(v(d+\varepsilon) - v(d-\varepsilon) \big) \right] \\
&\qquad = \lim_{\varepsilon \to 0+} \left[\frac{\mathrm{d}^2}{\mathrm{d}y} \left(\frac{\mathrm{d}^2}{\mathrm{d}y} + k^2 \right)^n \big(v(d+\varepsilon) - v(d-\varepsilon) \big) \right] = 0 \ \}.
\end{aligned}$$

The following chain of spaces was shown in [43], i.e. with generalized Fourier transform $\widehat{S}_{A^+}(\sigma) = F(S_{A^+}(\mathbb{R}^+))$ we can convert "physical" chain of spaces into a "spectral" chain:

$$\begin{array}{ccccc}
S_{A^+}(\mathbb{R}^+) & \subset & L^2(\mathbb{R}^+) & \subset & S'_{A^+}(\mathbb{R}^+) \\
\downarrow F & & \downarrow F & & \downarrow F \\
\widehat{S}_{A^+}(\sigma) & \subset & L^2(\sigma, \mathrm{d}\mu) & \subset & \widehat{S}'_{A^+}(\sigma)
\end{array}$$

Hence, we will assume that outside the waveguide (21) core $y \geq 0$, the function $u(x, \cdot)$ is in the distribution space $S'_{A^+}(\mathbb{R}^+)$ to be able to apply the generalized Fourier transform to it.

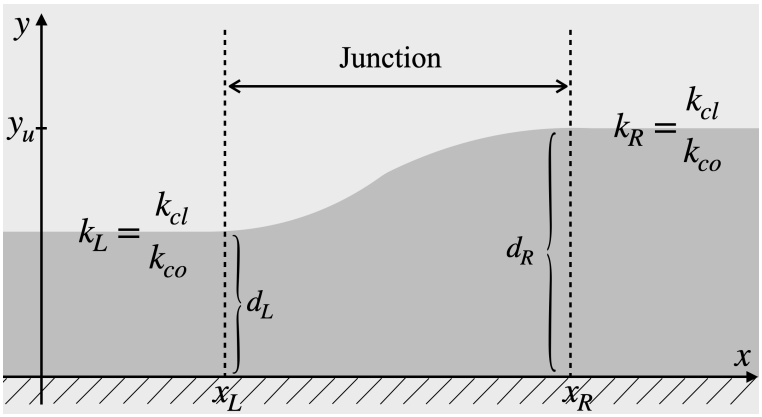

Figure 6: Open waveguide with a junction and semi-infinite straight parts. Transverse direction $y \in \mathbb{R}^+$.

2.2.2. Modal radiation condition

Now, with the generalized Fourier transform in hand, we can formulate the conditions for the open waveguide problem with a junction. The presence of a junction is illustrated by the local perturbation $\widetilde{k}(x, y)$ of the wave number without perturbation $k(x, y)$: $\widetilde{k}(x, y) - k(x, y)$ is assumed to be compactly supported in $[x_{\mathrm{L}}, x_{\mathrm{R}}] \times [0, y_{\mathrm{u}}]$, where $x_{\mathrm{L}} > 0$, $x_{\mathrm{R}} > 0$, $y_{\mathrm{u}} > 0$ are fixed.

To determine the radiation condition, consider the problem on semi-infinite parts of the waveguide. Let these parts of the waveguide, located to the left and right of the junction, have the core thickness d_{L} and d_{R}, respectively. Then the wavenumber becomes

$$k_{\mathrm{L,R}}(y) := \begin{cases} k_{\mathrm{co}}, & \text{if } 0 < y < \mathrm{d}_{\mathrm{L,R}}, \\ k_{\mathrm{cl}}, & \text{if } y > \mathrm{d}_{\mathrm{L,R}} \end{cases}$$

and then

$$k(x, y) := k_{\mathrm{L,R}}(y), \ x < x_{\mathrm{L}}, \ x > x_{\mathrm{R}}.$$

Now consider the problem on semi-infinite waveguide parts, see Figure 6

$$\begin{cases} -\Delta u - k^2_{\mathrm{L,R}} u &= 0 \quad \text{in } (x, y) \in \mathbb{R}^2 : y > 0, \, x < x_{\mathrm{L}}, \, x > x_{\mathrm{R}}, \\ u(x, 0) &= 0. \end{cases} \tag{26}$$

The corresponding unbounded self-adjoint transverse operator $A^{\mathrm{L,R}}$ is defined in $L^2(\mathbb{R}^2)$ in the same manner as operator A^+ (22) by

$$A^{\mathrm{L,R}} v := -\frac{\mathrm{d}^2 v}{\mathrm{d}y^2} - k^2_{\mathrm{L,R}} v, \quad \text{for any} \quad v \in D(A^{\mathrm{L,R}}) := \left\{ v \in H^2(\mathbb{R}^+) \cap H^1_0(\mathbb{R}^+) \right\} \tag{27}$$

and its spectrum has the usual structure for the transverse self-adjoint operator

$$\sigma_e(A^{\mathrm{L,R}}) = \sigma_e(A^{+}), \quad \sigma_d(A^{\mathrm{L,R}}) = \sigma_d(A^{+}),$$
$$\sigma(A^{\mathrm{L,R}}) = \sigma_e(A^{\mathrm{L,R}}) \cup \sigma_d(A^{\mathrm{L,R}}).$$

For the associated spectral family $\{\Phi_\lambda^{\mathrm{L,R}},\, \lambda \in \sigma(A^{\mathrm{L,R}})\}$ there is a corresponding generalized Fourier transform

$$\begin{aligned}(F_{\mathrm{L,R}}\phi)(\lambda) :&= \int_{\mathbb{R}^+} \phi(y)\, \overline{\Phi_\lambda^{\mathrm{L,R}}(y)}\, \mathrm{d}y \\ &= \langle \phi,\, \Phi_\lambda^{\mathrm{L,R}} \rangle_{\mathbb{R}^+}, \quad \text{for any } \lambda \in \sigma(A^{\mathrm{L,R}}),\, \phi \in L^2_{\mathrm{comp}}(\mathbb{R}^+).\end{aligned}$$

The spectral measure $\mathrm{d}\mu_{\mathrm{L,R}}$ is defined in the same way as in the straight waveguide case (23). Then the inverse generalized Fourier transform $F_{\mathrm{L,R}}^{-1}$ will be

$$(F_{\mathrm{L,R}}^{-1}\,\widehat{\phi})(y) = \int_{\sigma(A^{\mathrm{L,R}})} \Phi_\lambda^{\mathrm{L,R}}(y)\, \widehat{\phi}(\lambda)\, \mathrm{d}\mu_{\mathrm{L,R}}(\lambda) \tag{28}$$

$$= \sum_{\lambda \in \sigma_d(A^{\mathrm{L,R}})} \rho_\lambda^{\mathrm{L,R}} \widehat{\phi}(\lambda) \Phi_\lambda^{\mathrm{L,R}}(y) + \lim_{m\to+\infty} \int_{-k_{\mathrm{cl}}^2+m^{-1}}^{m} \widehat{\phi}(\lambda) \Phi_\lambda^{\mathrm{L,R}}(y) \rho_\lambda^{\mathrm{L,R}}\, \mathrm{d}\lambda, \tag{29}$$

$$\text{for all } \widehat{\phi} \in L^2(\sigma^{\mathrm{L,R}},\, \mathrm{d}\mu_{\mathrm{L,R}}).$$

Since by Theorem 2.5 we can diagonalize operator $A^{\mathrm{L,R}}$ (27)

$$A^{\mathrm{L,R}}\phi = F_{\mathrm{L,R}}^{-1}\, \lambda\, F_{\mathrm{L,R}}\, \phi, \quad \text{for any } \phi \in D(A^{\mathrm{L,R}}) \tag{30}$$

then, applying $F_{\mathrm{L,R}}$ to semi-infinite problem (26), we have

$$-\frac{\partial^2}{\partial x^2} F_{\mathrm{L,R}}\, u(x,\lambda) + \lambda F_{\mathrm{L,R}}\, u(x,\lambda) = 0, \quad x < x_{\mathrm{L}},\, x > x_{\mathrm{R}},\, \lambda \in \sigma^{\mathrm{L,R}},$$

whose solutions related to the right semi-infinite waveguide are

$$F_{\mathrm{R}}\, u(x,\lambda) = \alpha_{\mathrm{R}}(\lambda) \mathrm{e}^{-\sqrt{\lambda}(x-x_{\mathrm{R}})} + \beta_{\mathrm{R}}(\lambda) \mathrm{e}^{\sqrt{\lambda}(x-x_{\mathrm{R}})} \quad \text{for } x > x_{\mathrm{R}},\ \text{for all } \lambda \in \sigma^{\mathrm{R}}$$

and the solutions for the left side $x < x_{\mathrm{L}}$ are defined similarly by $F_{\mathrm{L}}\, u(x,\lambda)$. From (30) with inverse transform $F_{\mathrm{L,R}}^{-1}$ (28) we have the decomposition of u into guided and radiation modes. Hence with our fixed definition of the complex root, the modal radiation condition will be (Definition 2.4 in [27]).

Definition 2.15 (Modal radiation condition)**.** *A weak solution to the problem* (26) *satisfies the modal radiation condition if there exist* $\alpha_{\mathrm{L,R}} \colon \sigma(A^{\mathrm{L,R}}) \to \mathbb{C}$ *s.th.*

$$F_{\mathrm{R}}\, u(x,\lambda) = \alpha_{\mathrm{R}}(\lambda) \mathrm{e}^{-\sqrt{\lambda}(x-x_{\mathrm{R}})} \quad \textit{for } x > x_{\mathrm{R}},\ \lambda \in \sigma(A^{\mathrm{R}}), \tag{31}$$

$$F_{\mathrm{L}}\, u(x,\lambda) = \alpha_{\mathrm{L}}(\lambda) \mathrm{e}^{-\sqrt{\lambda}(x-x_{\mathrm{L}})} \quad \textit{for } x < x_{\mathrm{L}},\ \lambda \in \sigma(A^{\mathrm{L}}). \tag{32}$$

Modal radiation condition selects outgoing solutions, such that if the incident wave is coming from the left, then the scattering wave in the left semi-infinite side of the waveguide is left-going, and the total wave in the right semi-infinite side of the waveguide is right-going.

Now let us introduce several spaces to define the problem on the entire waveguide, and not in the just semi-infinite straight parts.

We have again a cutoff frequency assumption

$$k_{\mathrm{co}}^2 - k_{\mathrm{cl}}^2 \neq \left(n + \frac{1}{2}\right)^2 \frac{\pi^2}{d_{\mathrm{L,R}}^2}, \quad \text{for any } n \in \mathbb{N} \tag{33}$$

and with the following spaces of generalized Fourier transform coefficients

$$\widehat{V}_{\mathrm{L,R}} := \left\{\alpha \colon \sigma(A^{\mathrm{L,R}}) \to \mathbb{C} : \ |\lambda|^{\frac{1}{4}}\alpha \in L^2\big(\sigma(A^{\mathrm{L,R}}),\, \mathrm{d}\mu_{\mathrm{L,R}}\big)\right\},$$
$$\widehat{V}'_{\mathrm{L,R}} := \left\{\alpha \colon \sigma(A^{\mathrm{L,R}}) \to \mathbb{C} : \ |\lambda|^{-\frac{1}{4}}\alpha \in L^2\big(\sigma(A^{\mathrm{L,R}}),\, \mathrm{d}\mu_{\mathrm{L,R}}\big)\right\},$$

which are subspaces of spectral distributions $\widehat{S}'_{A^{\mathrm{L,R}}}(\sigma)$ [28], and since we can define

$$V_{\mathrm{L,R}} := F_{\mathrm{L,R}}^{-1}\big(\widehat{V}_{\mathrm{L,R}}\big), \quad V'_{\mathrm{L,R}} := F_{\mathrm{L,R}}^{-1}\big(\widehat{V}'_{\mathrm{L,R}}\big),$$

together with notations

$$H_{\mathrm{L}} := \big\{u \in H^1_{\mathrm{loc}}\big((-\infty, x_{\mathrm{L}}) \times \mathbb{R}^+\big) : u(x,\cdot)\big|_{x<x_{\mathrm{L}}} \in V_{\mathrm{L}}\big\},$$
$$H_{\mathrm{R}} := \big\{u \in H^1_{\mathrm{loc}}\big((x_{\mathrm{R}}, +\infty) \times \mathbb{R}^+\big) : u(x,\cdot)\big|_{x>x_{\mathrm{R}}} \in V_{\mathrm{R}}\big\}$$

the scattering problem can be formulated as:

For $f \in L^2(\mathbb{R}^2_+)$ find $u \in H^1_{\mathrm{loc}}(\mathbb{R}^2_+) : u(x,\cdot)\big|_{x<x_{\mathrm{L}}} \in H_{\mathrm{L}}, \quad u(x,\cdot)\big|_{x>x_{\mathrm{R}}} \in H_{\mathrm{R}}$ such that

$$\begin{cases} -\Delta u - \widetilde{k}^2 u = & f \quad \text{in } (x,y) \in \mathbb{R}^2 : y > 0, \\ u(x,0) = & 0, \\ u - u^{\mathrm{inc}} & \text{satisfies (32)} \\ u & \text{satisfies (31)}, \end{cases} \tag{34}$$

where the incident wave u^{inc} is coming from the left.

Theorem 2.6 (Well-posedness of the scattering problem)**.** *With assumption (33) for all $f \in L^2(\mathbb{R}^2_+)$ with $\mathrm{supp}(f) \subset [x_{\mathrm{L}}, x_{\mathrm{R}}] \times [0, y_u]$, $x_{\mathrm{L}} > 0$, $x_{\mathrm{R}} > 0$, $y_u > 0$ fixed, problem (34) has a unique solution which depends continuously on f and u^{inc}.*

Proof. Consider the non-abrupt junction of the waveguide as a perturbation of an abrupt junction of the same waveguide. Theorems 2.3 and 4.1 in [28]. □

The case considered above concerns open waveguide placed in $\mathbb{R} \times \mathbb{R}^+$. For 2D non-parallel open waveguides that are connected by a junction, well-posedness was shown in [72] by assuming the constant small absorption of the material. This approach is based on the half-space matching method, initially proposed in [13]. Since then, the half-space matching method application has been expanded to various cases, see, for example, [12]. It also uses a diagonalization of the transverse operator, similar to what we described in Section 2.2.1, but the generalized eigenfunctions were defined for the transverse operator in $\mathbb{R}$, and wavenumber is defined as

$$k(y) = \begin{cases} k_{\mathrm{cl}_1}, & \text{for } y < 0 \ , \\ k_{\mathrm{co}}, & \text{for } 0 < y < d \ , \\ k_{\mathrm{cl}_2}, & \text{for } y > d. \end{cases}$$

We would also like to mention the direction of the study of the 2D open waveguides and the related Green's function presented in [60], where the case with a constant refractive index in the cladding and a variable refractive index in the core was considered. These results led to the formulation of the radiation condition in [23], [24], [22].

Limitations The generalized Fourier transform, through which the modal radiation condition can be determined, is only possible if the waveguide geometry and wave number allow the generalized eigenfunctions to be expressed explicitly.

For the open waveguide scattering problem with a junction in the 3D waveguides case there is no well-posedness proof, as far as we know.

As well in the case when signal propagation is described with Maxwell's equations there are no results. Regarding the approach presented above, the authors [28] see certain technical obstacles in applying this framework to Maxwell's equations, since they are vector equations.

2.3. Bends: Semi-analytic solution

In this section, we will consider open waveguides of constant curvature and a semi-analytical method for obtaining a solution on the cross-section in a waveguide of such a shape.

Equation (17) related to the cross-section of the bend waveguide has solutions called cylindrical functions, namely *Bessel functions* $J_\nu(kr)$ of the first and $Y_\nu(kr)$ second kind. They are linearly independent for all ν. Another linearly independent pair of solutions are Hankel functions of the first $H_\nu^{(1)}(kr)$ and second $H_\nu^{(2)}(kr)$ kind [1], [46]. These special functions are characterized by their order $\nu \in \mathbb{C}$, $\nu = \mu R^+$. They have the following properties:

- $J_\nu(kr)$ is bounded as $r \to 0$.
- $H_\nu^{(2)}(kr)$ tends to zero as $r \to +\infty$, since (9.2.4 in [1])

$$H_\nu^{(2)} \sim \sqrt{\frac{1}{2\pi k_0 n_{\mathrm{cl}}\, r}} \mathrm{e}^{-\mathrm{i}(k_0 n_{\mathrm{cl}} r - \nu\pi/2 - \pi/4)} \quad \text{for } |r| \to \infty.$$

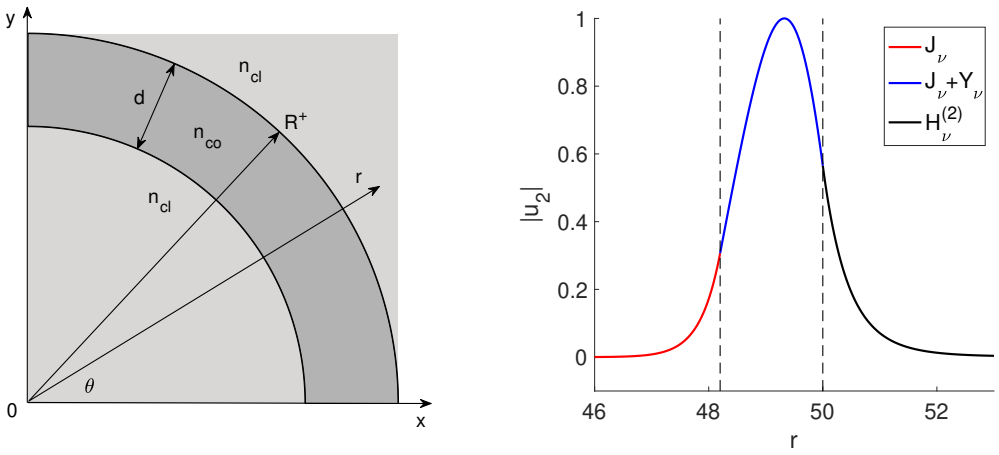

Figure 7: **Left**: Waveguide with constant curvature (bend). The cladding represented by the refractive index n_{cl} is light gray, the core represented by the refractive index n_{co} is dark gray. **Right**: Amplitude of the transverse solution u_2 in the bend with $R^+ = 50$ µm, first mode. Represented by Bessel function of the first kind (red line), Bessel function of the first and second kind (blue line) and Hankel function of the second kind (black line). Dashed black line indicates the waveguide's core.

The choice of cylindrical functions in the solution representation corresponds to each part of the waveguide such that the solution is physically correct [62], [46].

In the part of the waveguide cladding from the origin to the core, this is a Bessel function of the first kind, since it is limited at zero.

In the core, where the signal propagates and the wave has oscillatory behavior, the part of the solution to (17) is represented by a combination of Bessel functions of the first and second kinds.

In the outer part of the cladding, the solution decreases at infinity and is presented by a Hankel function of the second kind, see Figure 7, right.

Therefore, the piecewise solution for a slab open waveguide of constant radii of curvature R^+ is given by [62] [46] :

$$u_2(r) = \begin{cases} C_1 J_\nu(n_{\text{cl}} k_0 r) & \text{if } 0 < r \leq R^- \ , \\ C_2 J_\nu(n_{\text{co}} k_0 r) + C_3 Y_\nu(n_{\text{co}} k_0 r) & \text{if } R^- \leq r \leq R^+ \ , \\ C_4 H_\nu^{(2)}(n_{\text{cl}} k_0 r) & \text{for } r \geq R^+ \ . \end{cases} \tag{35}$$

where $|u_2| \to 0$ as $r \to 0$, $|u_2| \to 0$ as $r \to \infty$ and u_2 is outgoing, $R^- := R^+ - d$.

Remark: the solutions corresponding to (35) are guided modes and leaky modes. The radiation modes are not covered in this approach.

For the solution (35) the following method was proposed in [46]:

Method to find coefficients C_1, C_2, C_3, C_4:

Consider $\mathcal{C}^0$- and $\mathcal{C}^1$-regularity on the interface between the waveguide's cladding and

core at the inner radius R^-:

$$\begin{aligned} u_2(r)|_{r=R^-} &= C_1 J_\nu(n_{\text{cl}} k_0 R^-) \\ &= C_2 J_\nu(n_{\text{co}} k_0 R^-) + C_3 Y_\nu(n_{\text{co}} k_0 R^-), \qquad (36) \\ u_2'(r)|_{r=R^-} &= C_1 n_{\text{cl}} k_0 \; J_\nu'(n_{\text{cl}} k_0 r)|_{r=R^-} \\ &= C_2 n_{\text{co}} k_0 \; J_\nu'(n_{\text{co}} k_0 r)|_{r=R^-} + C_3 n_{\text{co}} k_0 \; Y_\nu'(n_{\text{co}} k_0 r)|_{r=R^-} \qquad (37) \end{aligned}$$

and at the outer radius R^+:

$$\begin{aligned} u_2(r)|_{r=R^+} &= C_2 J_\nu(n_{\text{co}} k_0 R^+) + C_3 Y_\nu(n_{\text{co}} k_0 R^+) \\ &= C_4 H_\nu^{(2)}(n_{\text{cl}} k_0 R^+), \qquad (38) \\ u_2'(r)|_{r=R^+} &= C_2 n_{\text{co}} k_0 \; J_\nu'(n_{\text{co}} k_0 r)|_{r=R^+} + C_3 n_{\text{co}} k_0 \; Y_\nu'(n_{\text{co}} k_0 r)|_{r=R^+} \\ &= C_4 n_{\text{cl}} k_0 \; H_\nu^{(2)'}(n_{\text{cl}} k_0 r)\Big|_{r=R^+}, \qquad (39) \end{aligned}$$

where the prime denotes the derivative with respect to r. These lead to the linear system of equations which has to be solved with respect to the amplitude coefficients C_1, C_2, C_3, C_4. And since this system is homogeneous, non-trivial solutions exist only if $\det\mathbf{A} = 0$, where $\mathbf{A}$ is the matrix of the system

$$\mathbf{A} = \begin{pmatrix} J_\nu(n_{\text{cl}} k_0 R^-) & -J_\nu(n_{\text{co}} k_0 R^-) & -Y_\nu(n_{\text{co}} k_0 R^-) & 0 \\ n_{\text{cl}} k_0 J_\nu'(n_{\text{cl}} k_0 R^-) & -n_{\text{co}} k_0 J_\nu'(n_{\text{co}} k_0 R^-) & -n_{\text{co}} k_0 Y_\nu'(n_{\text{co}} k_0 R^-) & 0 \\ 0 & J_\nu(n_{\text{co}} k_0 R^+) & Y_\nu(n_{\text{co}} k_0 R^+) & -H_\nu^{(2)}(n_{\text{cl}} k_0 R^+) \\ 0 & n_{\text{co}} k_0 J_\nu'(n_{\text{co}} k_0 R^+) & n_{\text{co}} k_0 Y_\nu'(n_{\text{co}} k_0 R^+) & -n_{\text{cl}} k_0 H_\nu^{(2)'}(n_{\text{cl}} k_0 R^+) \end{pmatrix}.$$

Hence, we can find the order $\nu = \mu R^+$ from

$$F(\nu) := F_1(\nu) F_2(\nu) - F_3(\nu) F_4(\nu) \stackrel{!}{=} 0, \qquad (40)$$

where

$$\begin{aligned} F_1 &= J_\nu(n_{\text{co}} k_0 R^-) J_\nu'(n_{\text{cl}} k_0 R^-) - q J_\nu(n_{\text{cl}} k_0 R^-) J_\nu'(n_{\text{co}} k_0 R^-), \\ F_2 &= Y_\nu(n_{\text{co}} k_0 R^+) H_\nu^{(2)'}(n_{\text{cl}} k_0 R^+) - q H_\nu^{(2)}(n_{\text{cl}} k_0 R^+) Y_\nu'(n_{\text{co}} k_0 R^+), \\ F_3 &= Y_\nu(n_{\text{co}} k_0 R^-) J_\nu'(n_{\text{cl}} k_0 R^-) - q J_\nu(n_{\text{cl}} k_0 R^-) Y_\nu'(n_{\text{co}} k_0 R^-), \\ F_4 &= J_\nu(n_{\text{co}} k_0 R^+) H_\nu^{(2)'}(n_{\text{cl}} k_0 R^+) - q H_\nu^{(2)}(n_{\text{cl}} k_0 R^+) J_\nu'(n_{\text{co}} k_0 R^+), \end{aligned}$$

with $q = n_{\text{co}}/n_{\text{cl}}$.

The main steps for finding semi-analytic solutions on the cross-section of the open waveguide with constant curvature are summarized in the Algorithm 1.

Remark: It was shown in [46] that equation (17) also provides the solution to 2D Maxwell equations on the cross-section of a waveguide with constant curvature.

The procedure for finding the amplitudes is similar to that described above, with the only difference that in the case of the transverse magnetic modes $u_2(r)$ and $\epsilon^{-1} u_2'(r)$ have to fulfill continuity condition at the interface, where $\epsilon = n^2$ is the relative permittivity.

Algorithm 1 Bend waveguide: semi-analytic solution

1. Define the linear system: apply continuity conditions for solution $u_2(r)$ to (35) in R^- and R^+.
2. Solve (40) to find true propagation constant $\mu = \nu/R^+$.
3. With ν find coefficients C_1, C_2, C_3, C_4 from the linear system (36) - (39).

And then in equation (40) $q = n_{\text{co}}/n_{\text{cl}}$ in the case of the electric field component and $q = n_{\text{cl}}/n_{\text{co}}$ in the case of the magnetic field.

Thus, given the suitable region of an order and argument pair (ν, kr) of the corresponding cylindrical function, a standard complex root finding solver can be used to establish the true order ν from the relation (40). Then solving the linear system we can find coefficients C_1, C_2, C_3, C_4 which do matching for different parts of the transversal solution (35).

We can see that μ^2 are eigenvalues to the transverse problem (20), where the largest value corresponds to the first mode, the next one to the second etc., see Figure 5.

Although the solution representation is straightforward, its application to waveguides with parameters corresponding to real-life experiments is not simple. In our case, due to the bending of the waveguide in the longitudinal direction, the order of the cylindrical functions is complex. Therefore, for numerical calculation of the Bessel and Hankel functions of complex order, certain obstacles must be taken into account.

2.4. Features of the implementation of the cylindrical functions of complex order

This section lists the difficulties of implementing cylindrical functions characterizing the transverse solution of the open waveguide with constant curvature.

2.4.1. Asymptotic expansions of the cylindrical functions near the turning point.

The first feature of the functions necessary for the solution representation (35) is that these are cylindrical functions of a complex order and standard solutions in most software packages are not supporting their implementation.

For example, the functions `besselj`, `bessely`, `besselh` in Matlab [64] are defined for a complex argument and based on work [3], however, no implementation is provided for a complex order with a non-zero imaginary part.

In Mathematica [51], cylindrical functions of complex order and argument are supported, but there is no access to the source code. Therefore there is no opportunity to understand, firstly, with what kind of method the cylindrical functions are calculated, and secondly, to make changes that may be necessary.

On the other hand, more control and capabilities are provided by the package [66] that was originally written for Octave and translated later for Matlab. It implements the *uniform expansion method* for cylindrical functions of large complex order and argument following [79].

Many differential equations whose solutions are special functions can be reduced to the form of the equation with a turning point (47) where the solutions are expressed in terms of *Airy functions* (see Chapter 11 in [70]). For example, the WKB or Liouville–Green method approximates solutions to the Schrödinger equation with a turning point utilizing Airy functions to relate the change in behavior from oscillating to exponentially decreasing [6], [11].

The uniform asymptotic expansions of the Bessel functions for large order ν in terms of Airy functions Ai, Bi (47) are given with [1]

$$J_\nu(\nu z) \sim \left(\frac{4\,\zeta}{1-z^2}\right)^{\frac{1}{4}} \left[\frac{\mathrm{Ai}(\nu^{\frac{2}{3}}\,\zeta)}{\nu^{\frac{1}{3}}}\,a_\nu \;+\; \frac{\mathrm{Ai}'(\nu^{\frac{2}{3}}\,\zeta)}{\nu^{\frac{5}{3}}}\,b_\nu\right], \tag{41}$$

$$Y_\nu(\nu z) \sim \left(\frac{4\,\zeta}{1-z^2}\right)^{\frac{1}{4}} \left[\frac{\mathrm{Bi}(\nu^{\frac{2}{3}}\,\zeta)}{\nu^{\frac{1}{3}}}\,a_\nu \;+\; \frac{\mathrm{Bi}'(\nu^{\frac{2}{3}}\,\zeta)}{\nu^{\frac{5}{3}}}\,b_\nu\right] \tag{42}$$

as $\nu \to \infty$ uniformly w.r.t. z, where $\nu \in \mathbb{C}$, $|\arg(\nu)| < \frac{1}{2}\pi$. In our case $z \in (0,\,\infty)$, but in general the expressions (41), (42) also hold for $z \in \mathbb{C}$, $|\arg(z)| < \pi - \varepsilon$, $\varepsilon > 0$.

The terms in (41), (42) are defined as following:

the parameter ζ is given by

$$\frac{2}{3}\zeta^{\frac{3}{2}} = \ln\left(\frac{1+\sqrt{1-z^2}}{z}\right) - 1 + \sqrt{1-z^2}, \quad 0 < z \le 1 \tag{43}$$

for a case when the argument of the Bessel function is less then order ν and

$$\frac{2}{3}\Big(-\zeta\Big)^{\frac{3}{2}} = \sqrt{z^2-1} - \arccos\left(\frac{1}{z}\right), \quad z \ge 1 \tag{44}$$

for a case when the argument of the Bessel function is larger then order ν.

The coefficient a_ν for $\nu \to \infty$ is

$$\begin{aligned} a_\nu &\sim \sum_{k=0}^{\infty} \frac{a_k(\zeta)}{\nu^{2k}}, \\ \text{with}\;\; a_k(\zeta) &= \sum_{s=0}^{2k} \mu_s \zeta^{-\frac{3s}{2}} u_{2k-s}\Big(\big(1-z^2\big)^{-\frac{1}{2}}\Big), \end{aligned} \tag{45}$$

another coefficient b_ν for $\nu \to \infty$ is

$$b_\nu \sim \sum_{k=0}^{\infty} \frac{b_k(\zeta)}{\nu^{2k}},$$
$$\text{with } b_k(\zeta) = -\zeta^{-\frac{1}{2}} \sum_{s=0}^{2k+1} \lambda_s \zeta^{-\frac{3s}{2}} u_{2k-s+1}\Big(\big(1-z^2\big)^{-\frac{1}{2}}\Big), \tag{46}$$

and

$$\lambda_s = \frac{(2s+1)(2s+3)\dots(6s-1)}{s!\,(144)^s}, \quad \lambda_0 = 1,$$
$$\mu_s = -\frac{6s+1}{6s-1}\lambda_s.$$

The terms u_k are defined with the following recursive expression

$$u_0(t) = 1,$$
$$u_{k+1} = \frac{1}{2}t^2(1-t^2)u_k'(t) + \frac{1}{8}\int_0^t (1-5t^2)u_k(t)\,\mathrm{d}t.$$

Here the Airy functions $\mathrm{Ai}(\nu^{\frac{2}{3}}\zeta)$ and $\mathrm{Bi}(\nu^{\frac{2}{3}}\zeta)$ are linearly independent solutions to the following differential equation [79], [70]

$$\frac{\mathrm{d}^2 w}{\mathrm{d}\zeta^2} = (\nu^2\zeta)w. \tag{47}$$

It is known [70] that Airy functions have a *turning point* when $\zeta = 0$, and hence when $z = 1$ (what follows from expressions (43) and (44)). That is, a point at which the oscillatory behavior of Airy functions of the first kind Ai changes to exponentially decreasing towards zero, and of the second kind Bi to exponentially increasing, see Figure 8. Moreover, the Airy functions themselves and their derivatives do not have singularities at zero

$$\mathrm{Ai}(0) = \frac{1}{3^{\frac{2}{3}}\Gamma(\frac{2}{3})}, \quad \mathrm{Ai}'(0) = \frac{1}{3^{\frac{1}{3}}\Gamma(\frac{1}{3})}, \quad \mathrm{Bi}(0) = \frac{1}{3^{\frac{1}{6}}\Gamma(\frac{2}{3})}, \quad \mathrm{Bi}'(0) = \frac{3^{\frac{1}{6}}}{\Gamma(\frac{1}{3})}, \tag{48}$$

where Γ is the Gamma function, see 1.01 in [70], Chapter 2.

With $\Big(4\,\zeta\,(1-z^2)^{-1}\Big)^{\frac{1}{4}}\Big|_{\zeta=0} = 2^{\frac{1}{3}}$ [79] and (48) the expressions for the Bessel functions of the first and second kind (41), (42) in the turning point $z = 1$ becomes

$$J_\nu(\nu) \sim \frac{a}{\nu^{\frac{1}{3}}}\,a_\nu - \frac{b}{\nu^{\frac{5}{3}}}\,b_\nu,$$
$$Y_\nu(\nu) \sim -\frac{3^{\frac{1}{2}}a}{\nu^{\frac{1}{3}}}\,a_\nu - \frac{3^{\frac{1}{2}}b}{\nu^{\frac{5}{3}}}\,b_\nu,$$

where a and b denote constants $a = 2^{\frac{1}{3}}\mathrm{Ai}(0)$ and $b = 2^{\frac{2}{3}}\mathrm{Ai}'(0)$.

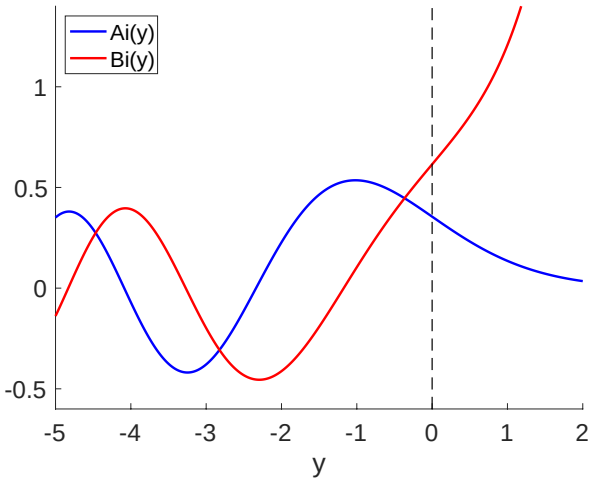

Figure 8: Airy functions of the first Ai and second Bi kind. The black dashed line corresponds to the turning point, where functions change their behavior from oscillating to exponentially decreasing and increasing, respectively.

However, the coefficients in the asymptotic formulas that approximate special functions through the Airy functions are well-known for the difficult evaluation near the turning point [79].

This problematic evaluation of the coefficients (45), (46) is relevant for the approximations we are considering for cylindrical functions (41), (42). For this case, for a large complex order, the following solution was proposed in [79]:

The aim is to evaluate the coefficients a_k, b_k (41), (42) in a_ν, b_ν, near the turning point. With the Maclaurin expansion of the inverse function $z = z(\zeta)$ (see [70], Chapter 11 Section 10.2 or [79])

$$z(\zeta) = \sum_{n=0}^{\infty} z_n \, (\zeta \, 2^{-\frac{1}{3}})^n = 1 - \zeta \, 2^{-\frac{1}{3}} + \frac{3}{10}(\zeta 2^{-\frac{1}{3}})^2 + \dots$$

consider the expansion of the coefficients a_k, b_k (45), (46)

$$a_k(\zeta) = \sum_{t=0}^{\infty} a_k^t \, (\zeta \, 2^{-\frac{1}{3}})^t, \quad b_k(\zeta) = 2^{\frac{1}{3}} \sum_{t=0}^{\infty} b_k^t \, (\zeta \, 2^{-\frac{1}{3}})^t,$$

where coefficients a_k^t, b_k^t are rational numbers. They can be found from recursion relations following (2.14) - (2.15) in [79]. The first few coefficients a_k, b_k expanded with the Maclaurin series are given in Table 2 in [79].

Similarly there is the expansion for the coefficient from the expressions (41), (42)

$$\left(4 \, \zeta \, (1 - z^2)^{-1}\right)^{\frac{1}{4}} = 2^{\frac{2}{3}} + \frac{1}{5}\zeta + \frac{9}{350}\zeta^2 + \dots .$$

Remark: Similar to (41), (42) expansions for the Hankel functions of the first and second kind $H_\nu^{(1)}$, $H_\nu^{(2)}$ and derivatives of the cylindrical functions we need in (40) and (35)

can be found in [1], 9.3.37, 9.3.43–9.3.45. All discussions above about the coefficients in the asymptotic expansion concern these functions as well. For the corresponding approximations at the turning point $z = 1$ see [79].

Thus, the method of uniform asymptotic expansions is suitable not only because it evaluates the cylindrical functions of complex order, but with additional expansions near the turning point, we can obtain correct evaluations for the transition region when the argument of the cylindrical function is approximately equal to its order.

Indeed, bends that we are considering have the outer radii of curvature R^+ in a range from 7 to 1000 µm. Therefore in the waveguide core at R^+ the argument of the cylindrical functions varies from 43.4 to 6.2e+03. At the same time, the real part $\mathfrak{Re}\nu$ of the order $\nu = (\beta - \mathrm{i}\alpha)R^+$ takes values from 42.5 to 6.07e+03 and $\mathfrak{Im}\nu$ goes to zero as R^+ increases (see Figure 9). Therefore argument and order of a cylindrical function related to the same bend with a large outer radius of curvature R^+ are roughly equal inside the waveguide's core.

Moreover, we also observe that the argument and order are large values, which is also covered by the uniform asymptotic expansions.

2.4.2. Methodology.

However, besides the turning point-adjusted uniform asymptotic expansion approach, we need an additional strategy.

We have implemented the semi-analytic solution (35) with evaluation to at least 32 significant digits since cylindrical functions of large complex order with large real and small imaginary parts are calculated incorrectly with usual precision.

Moreover, we need to redefine the Bessel function of the first kind J_ν in the core with the help of the Hankel functions of the first $H_\nu^{(1)}$ and second $H_\nu^{(2)}$ kinds. From the definitions [1]

$$H_\nu^{(2)}(n_{\mathrm{co}}k_0r) := J_\nu(n_{\mathrm{co}}k_0r) - \mathrm{i}Y_\nu(n_{\mathrm{co}}k_0r)$$

and

$$H_\nu^{(1)}(n_{\mathrm{co}}k_0r) := J_\nu(n_{\mathrm{co}}k_0r) + \mathrm{i}Y_\nu(n_{\mathrm{co}}k_0r)$$

we get

$$J_\nu(n_{\mathrm{co}}k_0R^\pm) = \frac{1}{2}\Big(H_\nu^{(1)}(n_{\mathrm{co}}k_0R^\pm) + H_\nu^{(2)}(n_{\mathrm{co}}k_0R^\pm)\Big). \tag{49}$$

We also utilize the following recurrence relations for the derivatives $J'_\nu(nk_0r)$ and $H_\nu^{(2)\prime}(nk_0r)$ (see 9.1.27 in [1])

$$J'_\nu(nk_0r) = \frac{1}{2}\Big(J_{\nu-1}(nk_0r) - J_{\nu+1}(nk_0r)\Big), \tag{50}$$

$$H_\nu^{(2)\prime}(nk_0r) = \frac{1}{2}\Big(H_{\nu-1}^{(2)}(nk_0r) - H_{\nu+1}^{(2)}(nk_0r)\Big), \tag{51}$$

for $n = n_{\mathrm{co}}$ in waveguide's core and $n = n_{\mathrm{cl}}$ in waveguide's cladding.

Finally, for the correct determination of the matching coefficients C_1, C_2, C_3, C_4 in (35), before solving the corresponding linear system it is necessary to scale each part of

the solution such that the maximum amplitude $|u_2| = 1$ in each part of the waveguide. Thus, to implement the algorithm of the semi-analytical solutions construction (Algorithm 1) corresponding to the entire range of outer radii of curvature 7 µm $\leq R^+ \leq$ 1000 µm that we need in the MMA method (65), the following methodology is required:

- Increase evaluation to at least 32 significant digits.
- To calculate cylindrical functions J_ν, Y_ν, Y'_ν, $H_\nu^{(1)}$, $H_\nu^{(2)}$ for given outer radius of curvature R^+ and fixed waveguide thickness d, refractive indices n_{co}, n_{cl} and wavelength λ_0 the method of the uniform asymptotic expansions for a large complex order ν is utilized. For the transit region $\nu - \varepsilon \leq n_{\text{co}} k_0 r \leq \nu + \varepsilon$, $\varepsilon > 0$ the precalculated coefficients of the related Maclaurin expansions near the turning point are used.
- Redefine the Bessel function of the first kind at the waveguide's core interface $R^\pm$ with Hankel functions by (49).
- Define Bessel and Hankel derivatives with recurrence relations (50) and (51).
- Scale each part of the solution before solving the system to determine the matching coefficients C_1, C_2, C_3, C_4 in (35).

Figure 10 shows examples of the resulting solution amplitudes along with the real and complex parts. We can observe that the field profile changes significantly depending on the outer radius of curvature R^+ as expected.

Figure 9 shows that the smaller the outer radius R^+ is, the larger the imaginary part α of the propagation constant μ becomes. That corresponds to leaky modes which "leak" more outside the waveguide's core.

At the same time, for the outer radius of curvature $R^+ = 1000$ µm, we see that the profile of the solution in the cross-section behaves like a guided mode and is symmetrically confined in the center of the waveguide core. In addition, we see that the second mode extends beyond the core more than the first mode, which corresponds to a larger part of the attenuation constant α in the propagation constant μ, see Figure 10 and Figure 9.

This corresponds to the Definition 2.10 of the leaky modes from the Section 2.1, as modes whose eigenvalues are part of the discrete spectrum of a transverse differential operator A_{R^+} (19) such that $\mathfrak{Im}\mu$ is not always equal to zero. In the physics literature, such modes of waveguides with constant curvature are also called leaky modes or *quasinormal modes*, see for example [77].

As the next step, we will normalize this resulting solution to the transverse problem (17) and will define and calculate the overlap integral, which plays a crucial role in the MMA method.

2.5. Semi-analytic t-maps

In this section, we will consider the main steps of how to obtain the pre-calculated database of transmission coefficients for the MMA method based on the semi-analytical solutions discussed in the previous section.

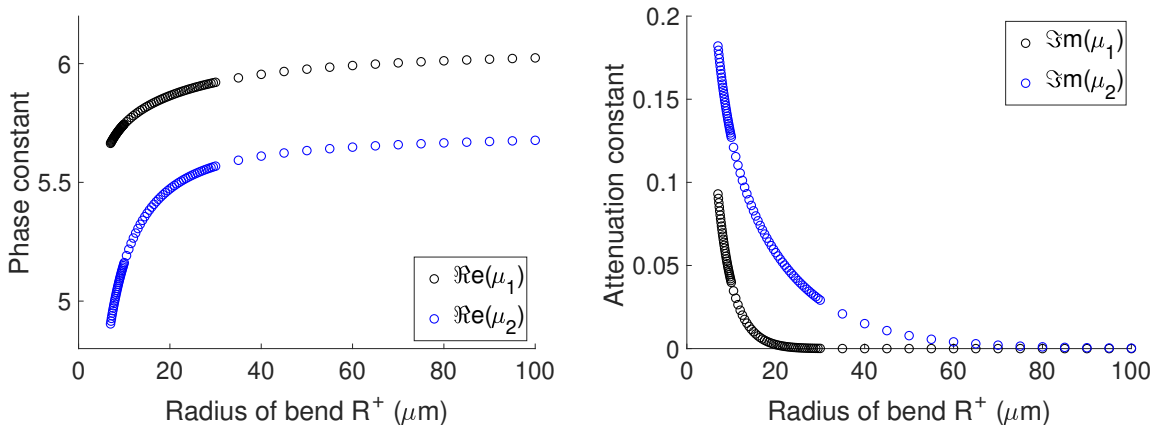

Figure 9: Real β (left) and imaginary α (right) parts of the propagation constant μ for the first and second mode depending on the outer radius of curvature R^+. Bends with parameters $d = 1.8$ µm, $\lambda_0 = 1.55$ µm, $n_{\text{co}} = 1.53$, $n_{\text{cl}} = 1.36$.

We have omitted subscript 2 for the cross-section solution (35) so as not to overwhelm the notation.

2.5.1. Orthogonality relation

The biorthogonality relation between transverse solutions related to the same bend of curvature R^+ is defined as follows

$$\int_0^\infty \frac{R^+}{r}\, u_m\, u_k \,\mathrm{d}r = \rho\, \delta_{m,k}, \qquad (52)$$

$$\text{with } \rho = \int_0^\infty \frac{R^+}{r}\, u_m^2 \,\mathrm{d}r \quad \text{for } m,\, k \in \{1, \ldots, M\},$$

where M is the number of modes. We have the weight in (52) since the corresponding transverse eigenvalue problem (20) is weighted. This expression holds also for guided and radiation modes [77], [59]. The biorthogonality relation for eigenfunctions corresponding to a non-self-adjoint transverse operator can also be found in [15].

The fulfillment of the relation (52) can be observed in Figure 11, with two fragments of t-maps related to the outer radii of curvature $R^+ \in [7, 30]$ µm. The diagonal elements of $\mathbf{t}_{11}$ are transmission coefficients between the first modes in the same bend. Such values correspond to

$$\int_0^\infty \frac{R_j^+}{r}\, \widehat{u}_{1,j}\, \widehat{u}_{1,j} \,\mathrm{d}r = 1, \quad \text{for } j = 1, \ldots, N.$$

The diagonal elements of $\mathbf{t}_{12}$ are transmission coefficients between the first and second modes in the same bend. They are related to

$$\int_0^\infty \frac{R_j^+}{r}\, \widehat{u}_{1,j}\, \widehat{u}_{2,j} \,\mathrm{d}r = 0, \quad \text{for } j = 1, \ldots, N,$$

where $\widehat{u}_{m,j}$ denotes mode scaled with respect to (52).

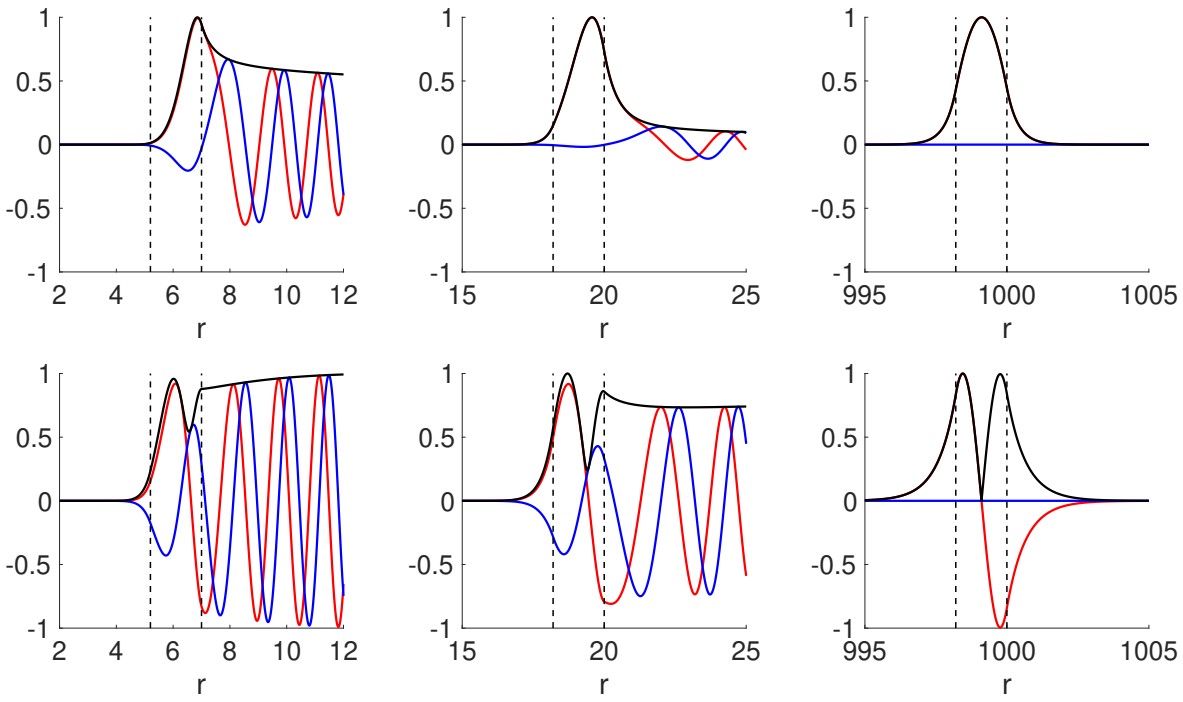

Figure 10: Semi-analytic transverse solution u_2 obtained following Section 2.4.2. The real part is shown in red, the imaginary in blue, and the absolute value in black. Dashed black line indicates the waveguide's core. **Top row**: first mode. Left to right: outer radius of curvature $R^+ = 7$ µm, $R^+ = 20$ µm, $R^+ = 1000$ µm. **Bottom row**: second mode. Left to right: outer radius of curvature $R^+ = 7$ µm, $R^+ = 20$ µm, $R^+ = 1000$ µm. **Right column**: the cylindrical functions used for the representation in the core have the large argument in a range [6.19e+03, 6.2e+03] and the large orders ν_1 =6.07e+03 − i4.92e-12, ν_2 =5.72e+03 − i1.22e-11.

2.5.2. Overlap integral

Following the MMA method [74], the transition losses between sections of waveguides of different curvature are specified with the help of an overlap integral.

Let us consider a set of N bend waveguides and denote:

- the transverse solution corresponding to the waveguide of constant curvature R_j^+ as $u_{m,j}$
- the related propagation constant as $\mu_m(R_j^+) = \beta_m(R_j^+) - \mathrm{i}\alpha_m(R_j^+)$
- the order of the corresponding cylindrical functions as $\nu_m(R_j^+) = R_j^+\mu_m(R_j^+)$.

Here $j = 1, \ldots, N$ and $m = 1, \ldots, M$, where M is the number of modes under consideration corresponding to the same waveguide of a fixed outer radius of curvature.

Let us assume that this set of waveguides is ordered with respect to the outer radii of curvature and there are no two identical waveguides in the set such that

$$0 < R_1^+ < R_2^+ < \ldots < R_N^+.$$

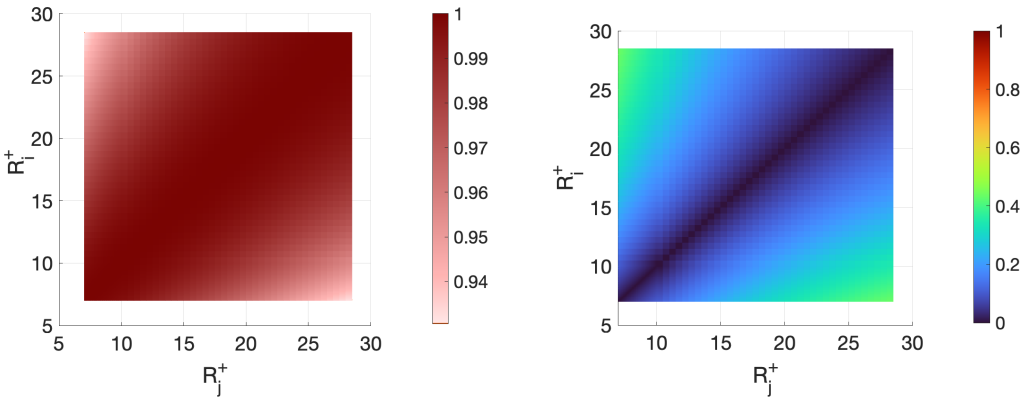

Figure 11: Example: top view of t-maps for $R^+ \in [7, 30]$ µm. **Left**: $|\mathbf{t}_{11}|$. **Right**: $|\mathbf{t}_{12}|$.

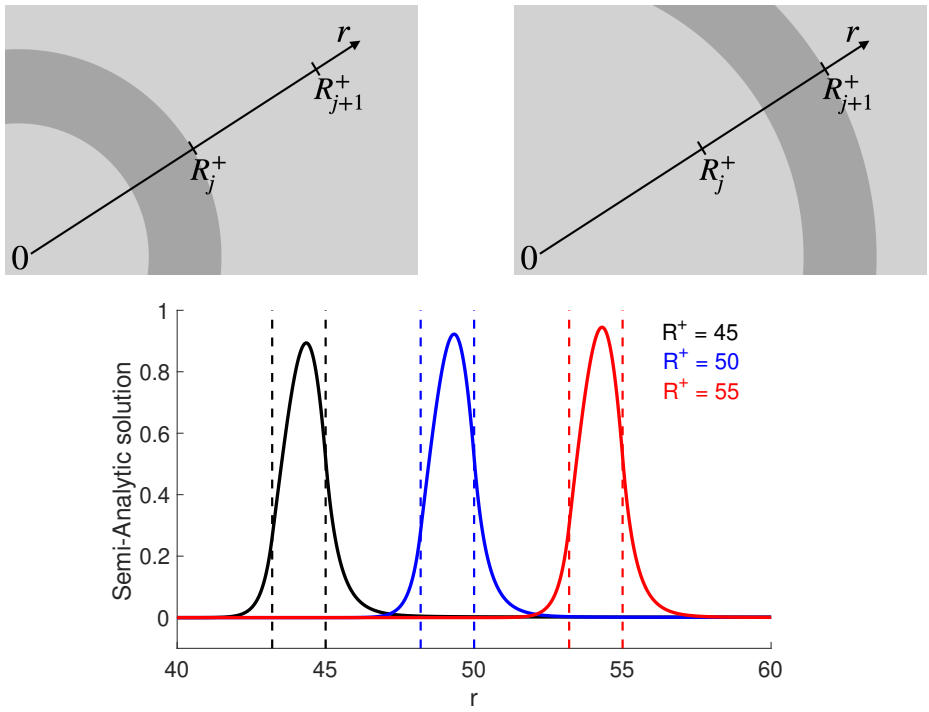

Figure 12: Semi-analytic transverse solutions u_2 related to different R^+ are all defined for $r \in (0, \infty)$. For a correct overlap integral definition the shift is required.

Shift. Consider a solution $u_{m,j}$ in a waveguide of constant curvature $1/R_j^+$. We know that it is defined for $r \in (0, \infty)$, however, we can see from the representation (35), that it is localized near the core of the waveguide $r \in (R^- - \varepsilon', R^+ + \varepsilon'')$, $\varepsilon', \varepsilon'' > 0$. Figure 12 shows cross-section solutions related to various radii of curvature.

The overlap integral must be determined for solutions located along the core of the free-form waveguide approximated by segments of different curvature. Therefore, for a

correct overlap integral definition, it is necessary to shift the solutions with respect to some fixed point on r, for example, zero.

Then the shift δ_j is defined as

$$\delta_j := R_j^+ - d/2. \tag{53}$$

However, the integration limits will change from $(0, \infty)$ to $(-\delta_j, \infty)$ as well. Therefore to shift $u_{m,j}(r)$ for all radii R_j^+, $j = 1, \dots, N$, simultaneously we have to choose a left-side cut. We can truncate the integration interval on the left side when the values of modes $u_{m,j}$ are less then a certain tolerance, for example ε = 10e-15 for all $m = 1, \dots, M$, $j = 1, \dots, N$.

Since the part of the solution $u_{m,j}$ for $r \in (0,\ R_j^-)$, represented by the Bessel function of the first kind $J_{\nu_{m,j}}$, has support only near the waveguide's core, then we can choose left-side truncation as r_L s.th. $|u_{m,j}(r_L)| \le \varepsilon$, $\varepsilon > 0$ small enough and $r_L \ge -R_1^+$.

Transmission coefficient. Then the overlap integral between two segments with radii of curvature R_i^+, R_j^+ for $i, j \in \{1, \dots, N\}$ is defined as

$$t_{mk}(R_i^+,\ R_j^+) = \int_{r_L}^{\infty} \sqrt{\frac{R_i^+}{r+\delta_i}} \sqrt{\frac{R_j^+}{r+\delta_j}}\, \widehat{u}_{m,i} \widehat{u}_{k,j}\, \mathrm{d}r \quad \text{for } m, k \in \{1, \dots, M\}, \tag{54}$$

where $\hat{u}_{m,i}$ and $\hat{u}_{k,j}$ are normalised with respect to (52) m-th and k-th modes of the bends characterized by outer radii of curvature R_i^+ and R_j^+, $\hat{u}_{m,i} = \hat{u}_m(r)\big|_{R^+=R_i^+}$, $\hat{u}_{k,j} = \hat{u}_k(r)\big|_{R^+=R_j^+}$. The shifts δ_i, δ_j are defined by the associated outer radii of curvature (53).

In practice, in addition to the left cut-off r_L, it is also necessary to set the integration limit on the right side far enough. We choose the cut-off $r_R = 500$ µm.

2.5.3. Resulting t-maps in MMA

To apply the MMA method for the waveguide configurations under consideration in this work, the *t-maps*

$$\begin{aligned} \mathbf{t}_{11} &= \big(t_{11}(R_i^+,\ R_j^+)\big)_{i=1,\,j=1}^{N,\,N}, \qquad & \mathbf{t}_{12} &= \big(t_{12}(R_i^+,\ R_j^+)\big)_{i=1,\,j=1}^{N,\,N}, \\ \mathbf{t}_{21} &= \big(t_{21}(R_i^+,\ R_j^+)\big)_{i=1,\,j=1}^{N,\,N}, & \mathbf{t}_{22} &= \big(t_{22}(R_i^+,\ R_j^+)\big)_{i=1,\,j=1}^{N,\,N} \end{aligned} \tag{55}$$

were obtained with (54) for a pre-selected set of radii I_{R^+} consisting of N elements $R_i^+ \in I_{R^+}$, $R_j^+ \in I_{R^+}$, $i = 1, \dots, N$, $j = 1, \dots, N$. To obtain the transmission coefficients database we choose the following set of radii

$$I_{R^+} = [7,\ 7.1,\ \dots,\ 10,\ 10.5,\ \dots,\ 30,\ 35,\ \dots,\ 200,\ 225,\ \dots 1000]\ \text{µm}.$$

The corresponding bends parameters are

$$d = 1.8\,\text{µm}, \quad n_{\text{co}} = 1.53, \quad n_{\text{cl}} = 1.36, \quad \lambda_0 = 1.55\,\text{µm}. \tag{56}$$

For the numerical evaluation of integrals Gauss–Kronrod quadrature from Matlab library `quadgk` was used [64]. The t-maps truncated for visual convenience to the range $I_{R^+} = [7,\ 100]$ µm are shown in Figures 13 and 14, the real and imaginary parts separately.

For example, the elements of $t_{12}(R_i^+,\ R_j^+)$ for $i \neq j$, refers to the coupling between the first mode in a bend with the outer radius of curvature R_i^+ and the second mode in another bend with an outer radius of curvature R_j^+.

As a result of the Sections 2.4 -2.5 we have a pre-calculated database of transmission coefficients for guided and leaky modes. Computing such a database is time-consuming. However, when applying the MMA method, calculating the transmission itself for a free-form waveguide takes a few seconds per central trajectory, see Tables 1, 2 and Figure 35.

Thus, a fast optimization of the waveguide shape with fixed parameters such as width d, wavelength λ_0, and refractive indices n_{co}, n_{cl} is possible (56). If one of these parameters changes, the database must be recalculated using all the steps listed in Sections 2.4 -2.5.

For numerical examples of the t-maps application for the transmission calculation, see Sections 3.2.1-3.2.3.

We highlight one more advantage of using semi-analytical solutions for the t-maps construction – the t-maps remain smooth even for small radii of curvature, see Figure 15. It allows the impact of leaky modes related to bends of small radii of curvature to be taken into account in the transmission calculation, see Section 3.2.3.

Transmission with MMA. Now we show how these overlap integrals are utilized in the MMA method. Consider a waveguide of fixed thickness d, whose shape is defined by a central $\mathcal{C}^2$-curve.

Let the central planar curve $\Gamma = (\Gamma_1,\ \Gamma_2)$ of length L_s be given in the parametric form by the graph of $y = f(x)$:

$$\Gamma := \big\{\ \big(x,\ f(x)\big),\ x \in [0,\ L_x]\big\}. \tag{57}$$

We assume that the curve $\Gamma \in \mathcal{C}^2$ has no self-intersections and its curvature

$$\kappa(x) = \frac{|\Gamma'(x) \times \Gamma''(x)|}{|\Gamma'(x)|^3} = \frac{|f''(x)|}{\big(1 + (f'(x))^2\big)^{\frac{3}{2}}}, \quad x \in [0,\ L_x] \tag{58}$$

has a compact support $\operatorname{supp}(\kappa) \subset [x_L,\ x_R]$, $x_L,\ x_R \in (0, L_x)$.

For natural parameterization, we find a parameter $s \in [0, L_s]$ such that $|v(s)| = 1$, where $v = (\Gamma_1',\ \Gamma_2')$ is the velocity vector [30]. For the graph parametrization (57) it has the form $v(x) = (1,\ f'(x))$.

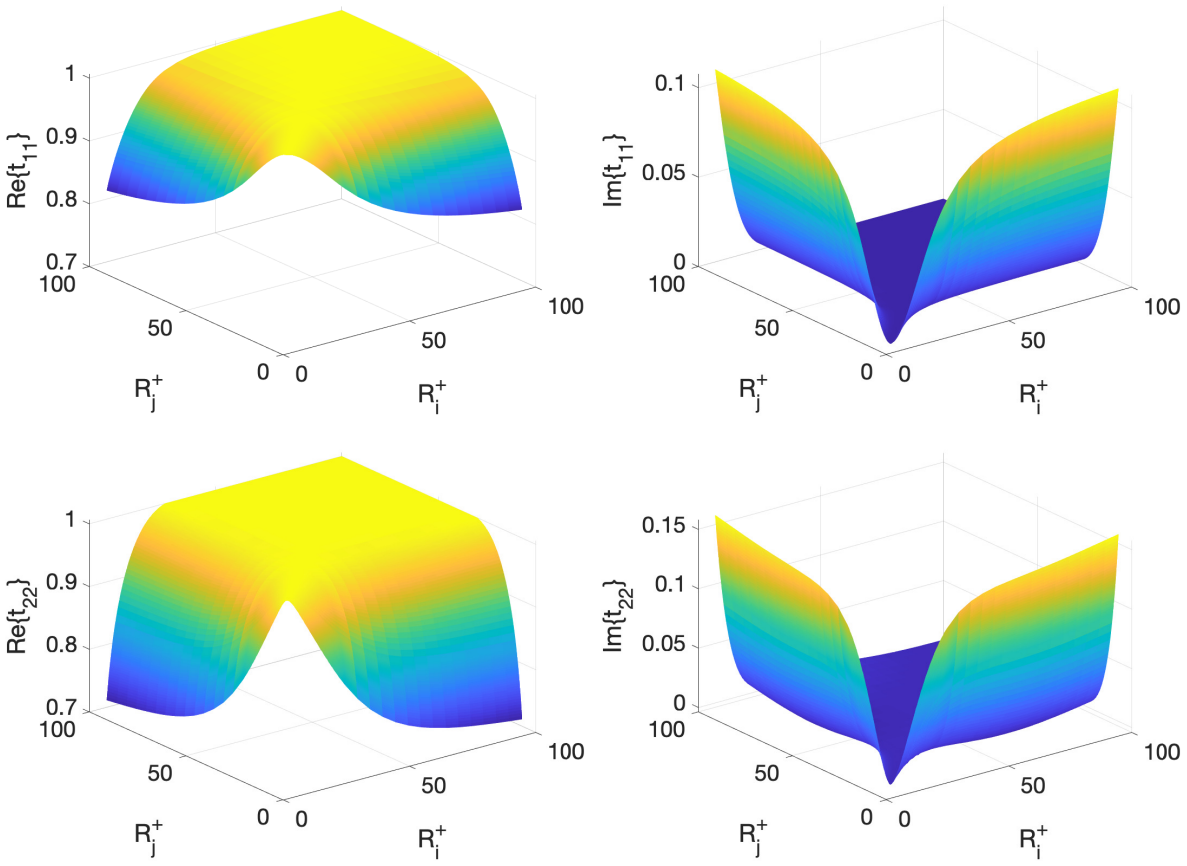

Figure 13: Real and imaginary parts of the t-maps $\mathbf{t}_{11}$, $\mathbf{t}_{22}$ between curved waveguide segments with radii of curvature $R_{\mathrm{i}}^{+} \in [7, 100]$ µm and $R_{\mathrm{j}}^{+} \in [7, 100]$ µm. The shown radii range is cut at 100 µm for readability.

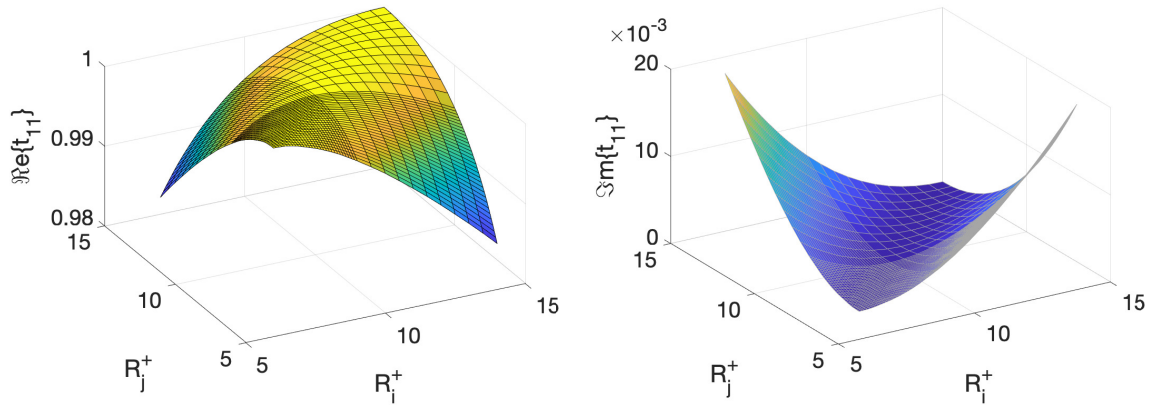

Figure 15: t-maps for small radii of curvature $R^{+} \in [7, 15]$ µm. Left: $\mathfrak{Re}(\mathbf{t}_{11})$. Right: $\mathfrak{Im}(\mathbf{t}_{11})$.

Since a natural parameter s is the length of the curve we can find it from the expression for the arclength of the curve $f(x)$ from 0 to x. For $s\colon [0, L_x] \to [0, L_s]$ we

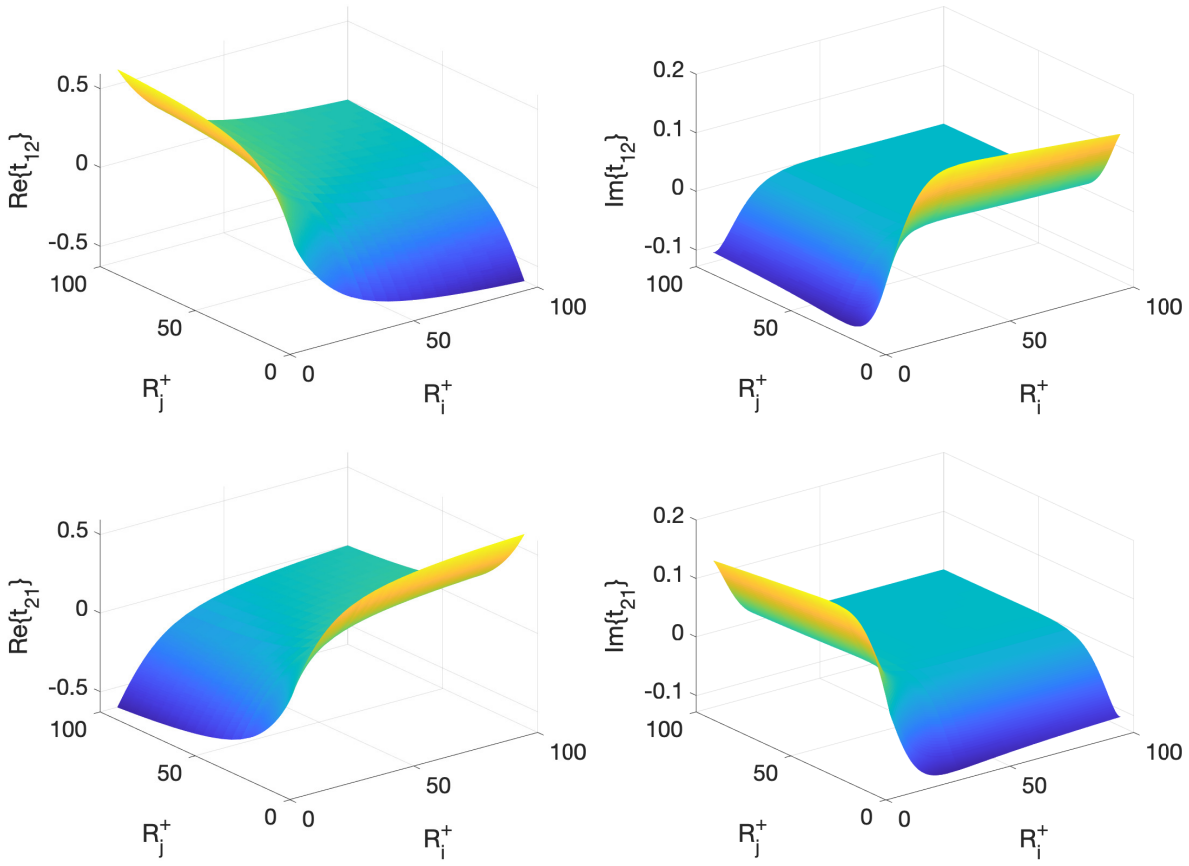

Figure 14: Real and imaginary parts of the t-maps $\mathbf{t}_{12}$, $\mathbf{t}_{21}$ between curved waveguide segments with radii of curvature $R_{\mathrm{i}}^{+} \in [7, 100]$ µm and $R_{\mathrm{j}}^{+} \in [7, 100]$ µm. The shown radii range is cut at 100 µm for readability

have

$$s(x) = \int_0^{x(s)} |v(\xi)| \, \mathrm{d}\xi = \int_0^{x(s)} \sqrt{1 + (f'(\xi))^2} \, \mathrm{d}\xi. \tag{59}$$

Since $\dfrac{\mathrm{d}s(x)}{\mathrm{d}x} = |v(x)|$, hence we can find the inverse $x\colon [0, L_s] \to [0, L_x]$ by solving ordinary differential equation $\dfrac{\mathrm{d}x(s)}{\mathrm{d}s} = \dfrac{1}{|v(x(s))|}$ numerically. Then we have the naturally parametrized curve

$$\widetilde{\Gamma}(s) = \Gamma\big(x(s)\big) = \big\{\big(\, x(s),\, f(x(s))\,\big),\ s \in [0,\, L_s]\big\}. \tag{60}$$

A slab open waveguide of small enough thickness d generated by such a central curve Γ is given by the following wave number which is defined in the locally orthogonal system (s, t) for all $s \in [0, L_s]$ and $t \in \mathbb{R}$ as

$$k(t) = \begin{cases} k_0 n_{\mathrm{co}}, & \text{if } t \in \Big(-\dfrac{d}{2}, \dfrac{d}{2}\Big), \\ k_0 n_{\mathrm{cl}}, & \text{else .} \end{cases}$$

We assume that the thickness d is such that the waveguide does not intersect itself.

For the MMA method with the partition $\triangle_n^s : 0 = s_1 < \ldots < s_n = L_s$ we divide the central curve such that $s_{j+1} - s_j = l_s$, for all $j = 1, \ldots, n-1$. That is, the arc length l_s of each segment is fixed. By $\triangle_n$ we denote the corresponding x-partition $\triangle_n : 0 = x_1 < \ldots < x_n = L_x$, where $x_j = x(s_j)$, $s_j \in \triangle_n^s$.

We find the mean curvature associated with each segment with

$$\widetilde{\kappa_j} = \frac{1}{x_{j+1} - x_j} \int_{x_j}^{x_{j+1}} \kappa(x)\,\mathrm{d}x, \quad x_j,\, x_{j+1} \in \triangle_n. \tag{61}$$

The arc length l_s has to be small enough to assume that the curvature of the central curve is approximated by $\widetilde{\kappa_j}$ on each interval of $\triangle_n^s$.

We choose $l_s = 1/2\pi$. Figure 16 shows the relative difference between FEM and MMA total transmission related to a fixed central trajectory with varying curvature versus $l_s \in \{1/4\pi, \ldots, 1/2\pi, \ldots, \pi/4, \pi/2, \pi\}$. For $l_s \le 1/2\pi$, the result does not differ by more than 0.01%. Moreover, a partition in radians (blue line) is more suitable than an arbitrary partition (black line).

Next, according to the partition $\triangle_n^s$, we divide the open slab waveguide generated with Γ by $n-1$ segments S_j, $j = 1, \ldots, n-1$, see Figure 18. We approximate each segment S_j by bend $\widehat{S}_j$ with a constant radius of curvature $R_j^+ = 1/\widetilde{\kappa_j}$ (61).

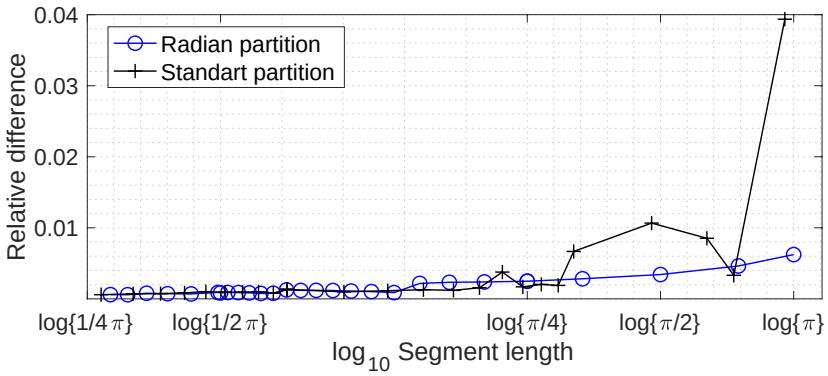

Figure 16: Relative difference between total transmission via FEM with pd = 2, $h = \lambda_0/20$ and via MMA versus segment length l_s. The central trajectory is Euler spiral (95) with $R_J = 38.63$ µm.

In the physical literature, several possible mechanisms of optical loss in open waveguides are defined [77], [62], [69], [63].

The first type of loss is *bending loss* – a loss that occurs for non-straight waveguides. For an open bend, it is defined with such parameters as the arc length and the attenuation constant.

The second source of optical losses are losses occurring by passing through the interface of two segments of different radii of curvature. The corresponding transmission is called a *transition transmission*. Transmission losses caused by a drastic change in the

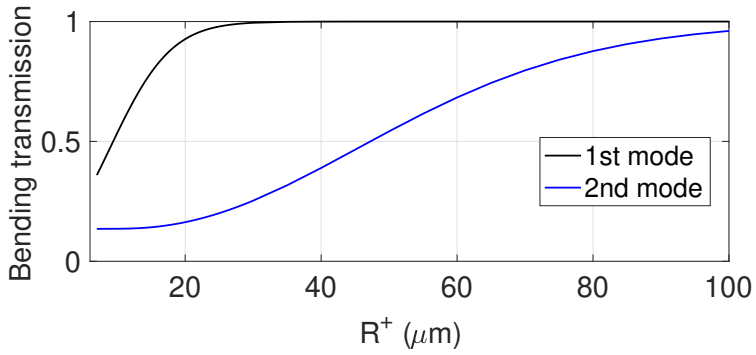

Figure 17: Influence of bending with arc length $l_s = \pi R^+/2$ on signal transmission by 1st and 2nd mode.

radius of curvature are associated with field mismatch. Therefore, the incoming wave excites not only guided and leaky modes, but also radiation modes. As of today, the MMA method does not take into account radiation modes in transition transmission and the approach used here utilizes the guiding and leaky modes.

The third possible source of losses is imperfections in the material. For example, caused by a production defect. However, in this work they are not taken into account and the material coefficients and the wavenumber are considered piecewise constant and real.

According to [67], the bending transmission $\widehat{\mathbf{p}}(R_j^+)$ related to two modes $u_{m,j}$, $m \in \{1, 2\}$ which are corresponding to the same segment $\widehat{S}_j$, is determined with the help of the attenuation constant $\alpha_m(R_j^+)$ (16) and its arc length l_j as

$$\widehat{\mathbf{p}}(R_j^+) = \begin{pmatrix} \exp\{-\alpha_1(R_j^+)\, l_j\} & 0 \\ 0 & \exp\{-\alpha_2(R_j^+)\, l_j\} \end{pmatrix}, \quad \text{for } j = 2, \ldots, n-1, \tag{62}$$

and the total transmission $\mathbf{T}$ for the entire waveguide will be approximated by [74]:

$$\begin{aligned} \mathbf{T}(R_1^+, \ldots, R_{n-1}^+) = \widehat{\mathbf{p}}(R_{n-1}^+)\, \widehat{\mathbf{t}}(R_{n-2}^+, R_{n-1}^+)\, \widehat{\mathbf{p}}(R_{n-2}^+) \\ \ldots\, \widehat{\mathbf{t}}(R_2^+, R_3^+)\, \widehat{\mathbf{p}}(R_2^+)\, \widehat{\mathbf{t}}(R_1^+, R_2^+)\, \mathbf{U_i}, \end{aligned} \tag{63}$$

where $\mathbf{U_i}$ is an amplitude distribution between incoming modes.

For example, if $\mathbf{U_i} = (1, 0)^\top$, then the incoming signal is represented with the first mode. The transition transmission here

$$\widehat{\mathbf{t}}(R_j^+,\, R_{j+1}^+) = \begin{pmatrix} t_{11}(R_j^+,\, R_{j+1}^+) & t_{12}(R_j^+,\, R_{j+1}^+) \\ t_{21}(R_j^+,\, R_{j+1}^+) & t_{22}(R_j^+,\, R_{j+1}^+) \end{pmatrix}, \quad \text{for } j = 1, \ldots, n-2, \tag{64}$$

is a matrix of mode overlaps between two segments of outer radii of curvature R_j^+ and R_{j+1}^+.

To simplify the notation, we denote $\widehat{\mathbf{p}}_{\mathbf{j-1}} = \widehat{\mathbf{p}}(R_j^+)$, $j = 2, \ldots, n-1$ and $\widehat{\mathbf{t}}_{\mathbf{j}} = \widehat{\mathbf{t}}(R_j^+,\, R_{j+1}^+)$, $j = 1, \ldots, n-2$. Then the total amplitude transmission (63) becomes

$$\mathbf{T}(R_1^+, \ldots, R_{n-1}^+) = \widehat{\mathbf{p}}_{\mathbf{n-2}}\, \widehat{\mathbf{t}}_{\mathbf{n-2}}\, \widehat{\mathbf{p}}_{\mathbf{n-3}}\, \ldots\, \widehat{\mathbf{t}}_{\mathbf{2}}\, \widehat{\mathbf{p}}_{\mathbf{1}}\, \widehat{\mathbf{t}}_{\mathbf{1}}\, \mathbf{U_i}. \tag{65}$$

We use this notation in the sketch of a waveguide divided into segments, see Figure 18.

Remark: Note, that by total transmission approximation with MMA method we will further mean the total power transmission, which is defined via the total amplitude transmission $\mathbf{T} = (T_1, T_2)^\top$ (65) as $T(R_1^+, \ldots, R_{n-1}^+) = |T_1|^2 + |T_2|^2$.

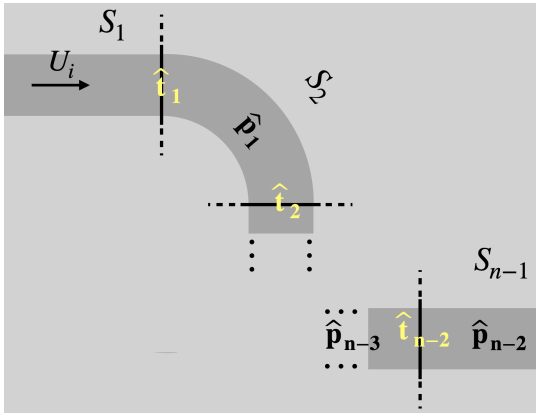

Figure 18: MMA method: an open waveguide divided into segments of approximately constant curvature each. Dark gray - waveguide core, light gray - waveguide cladding. Bending transmission (62) denoted $\hat{\mathbf{p}}$, transition transmission denoted $\hat{\mathbf{t}}$ (64).

The first and last segments are straight open waveguides since the curvature of the central curve has compact support. We approximate them by a curved waveguide with an outer radius of curvature $R^+ = 1000$ µm.

This choice was made as per two reasons. First, such a radius is large enough not to contradict the physical characteristics of the field in a straight waveguide with the same settings of parameters d, n_{co}, n_{cl} [74].

Second, it is not clear how to determine the overlap integral (54) for transverse solutions in straight and bent waveguides. The reason being that the transverse operator (3) for a straight open waveguide is self-adjoint and the corresponding eigenvalue problem (2) is not weighted, while the transverse operator corresponding to the bend (19) cannot be self-adjoint since some eigenvalues have non vanishing imaginary part and the related eigenvalue problem (20) is weighted.

3. Numerical results

We want to show the validity of the MMA method with the help of the finite element method (FEM) comparing the relative transmission difference obtained by both methods. In the first section, we derive a variational formulation of our problem of interest and verify the numerical solution obtained by FEM with a numerical test of convergence versus the exact solution inside the core of the straight waveguide. The main techniques that we use here for the successful implementation of such a reference numerical solution are PML, application of the Dirichlet to Neumann operator (DtN), and transformation optics (TO).

In the second part of the chapter, we verify numerically and qualitatively the simplified MMA method by comparing the computed transmission on several examples of open waveguides, including the experimental set corresponding to the benchmark used in the CRC 1173 C4 project, see Figure 2. We will show the advantages of the MMA method over the FMA method in the case where the waveguide can support more than one mode.

3.1. FEM for open slab waveguides with constant thickness.

The structure of our interest is the waveguide of constant thickness d generated by the central planar curve $\Gamma := \{\big(\gamma_1(x), \gamma_2(x)\big), x \in \mathbb{R}\}$. We assume that $\Gamma \in \mathcal{C}^2$ has no intersections, and the thickness d is small enough such that the waveguide does not intersect with itself. Such an open waveguide is represented as two infinite straight parts connected by a curved junction.

To validate the MMA method, we apply FEM for the numerical solution related to the following problem

$$\begin{cases} -\Delta u - k^2 u &= 0 \quad \text{in } (x,y) \in \mathbb{R}^2, \\ u - u^{\text{inc}}, &\text{is left-going, } x < x_{\text{L}} \\ u, &\text{is right-going, } x > x_{\text{R}}, \end{cases} \tag{66}$$

where the incident wave u^{inc} is coming from the left, $k = k_0\, n_{\text{co}}$ inside the core, $k = k_0\, n_{\text{cl}}$ in the cladding. We assume that the refractive indices satisfy $n_{\text{co}} > n_{\text{cl}} > 0$, and that $k \in \mathbb{R}$, $k_0 = 2\pi/\lambda_0$ for a wavelength λ_0.

As was shown (2.6) for the halfspace $\mathbb{R} \times \mathbb{R}_+$ case, the scattering problem will be well-posed if the modal radiation condition holds. Therefore, in order to find a numerical solution, we need to correctly truncate the computational domain such that the modal radiation condition for $x < x_{\text{L}}$ and $x > x_{\text{R}}$ is satisfied. That is, we will distinguish between the left and right going waves with the help of the Dirichlet to Neumann (DtN) operator and will equip the computational domain with absorbing layers, which we introduce via PML in the longitudinal and transverse directions.

In this section, we will show how the leading equation in (66) changes after TO application, then we will apply the PMLs in the longitudinal and transverse directions and, furthermore, construct DtN conditions at the transverse intervals related to the ends of the offset. Next, we will present a variational formulation for the boundary value problem we are considering (66), provide an expression for calculating transmission in

a waveguide, and also show with the convergence versus exact solution the validity of the FEM numerical solution to (66).

3.1.1. Transformation optics.

Now, we consider the waveguide of constant thickness represented by the central trajectory in a finite domain of computation, which we denote as $\Omega \subset \mathbb{R}^2$.

The TO method is based on the fact that Maxwell's equations in a slab waveguide (and, accordingly, the acoustic Helmholtz equation) preserve their structure under coordinate transformations [29], [44], [83]. Namely, the material parameter values are transformed, resulting in an additional material tensor in the differential operator.

We transform the curved waveguide in the original computational domain Ω into a straight waveguide in the transformed domain in the following way. Let the central curve Γ of length L_s be parametrised by arclength $\Gamma := \{\big(\gamma_1(s),\, \gamma_2(s)\big),\, s \in [0,\, L_s]\}$. We define the domain transformation $\Phi\colon [0,\, L_s] \times [-L_t/2,\, L_t/2] \to \Omega \subset \mathbb{R}^2$ with

$$\Phi(s,t) := \begin{bmatrix} \gamma_1(s) - t\gamma_2'(s) \\ \gamma_2(s) + t\gamma_1'(s) \end{bmatrix} = \begin{bmatrix} \Phi_1(s,t) \\ \Phi_2(s,t) \end{bmatrix}. \tag{67}$$

We require the transformation to be continuously differentiable and bijective for sufficiently small L_t. The Jacobian is

$$\mathrm{J}_\Phi(s,t) = \begin{bmatrix} \gamma_1' - t\gamma_2'' & -\gamma_2' \\ \gamma_2' + t\gamma_1'' & \gamma_1' \end{bmatrix}. \tag{68}$$

With the natural parametrization, we have

$$(\gamma_1')^2 + (\gamma_2')^2 = 1, \tag{69}$$

then the signed curvature $\kappa(s) = \big(\gamma_1''\gamma_2' - \gamma_1'\gamma_2''\big)\big((\gamma_1')^2 + (\gamma_2')^2\big)^{\frac{3}{2}}$ becomes

$$\kappa(s) = \gamma_1''\gamma_2' - \gamma_1'\gamma_2''. \tag{70}$$

We obtain

$$\det \mathrm{J}_\Phi = (\gamma_1')^2 + (\gamma_2')^2 + t(\gamma_1''\gamma_2' - \gamma_2''\gamma_1') = 1 + t\,\kappa(s). \tag{71}$$

We denote the transformed computational domain as $\Omega_h := I_s \times I_t$ with $I_s := [0,\, L_s]$, $I_t := [-L_t/2,\, L_t/2]$. With the change of variables

$$\int_{\Phi(\Omega_h)} u(x,y)\,\mathrm{d}x\,\mathrm{d}y = \int_{\Omega_h} u\big(\Phi(s,t)\big)\,\det \mathrm{J}_\Phi\,\mathrm{d}s\,\mathrm{d}t = \int_{\Omega_h} \widetilde{u}(s,t)\,\det \mathrm{J}_\Phi\,\mathrm{d}s\,\mathrm{d}t$$

and the chain rule $(\nabla u) \circ \Phi = (\mathrm{J}_\Phi^{-1})^\top \nabla(u \circ \Phi)$ we apply TO to the following volume integral which we obtain from our leading equation in (66) using Green's first identity

$$\begin{aligned} &\int_{\Phi(\Omega_h)} \nabla u \cdot \nabla \overline{v} - k^2\, u\, \overline{v}\,\mathrm{d}x\,\mathrm{d}y \\ &\qquad = \int_{\Omega_h} \Big\{ (\mathrm{J}_\Phi^{-1})^\top \nabla \widetilde{u} \cdot (\mathrm{J}_\Phi^{-1})^\top \nabla \overline{\widetilde{v}} - \widetilde{k}^2\, \widetilde{u}\, \overline{\widetilde{v}} \Big\}\, \det \mathrm{J}_\Phi\,\mathrm{d}s\,\mathrm{d}t. \end{aligned} \tag{72}$$

We have

$$\begin{aligned}\mathrm{J}_\Phi^{-1}\mathrm{J}_\Phi^{-\top} &= \frac{1}{(\det \mathrm{J}_\Phi)^2}\begin{bmatrix}(\gamma_1')^2+(\gamma_2')^2 & \gamma_1'(-\gamma_2'-t\gamma_1'')+\gamma_2'(\gamma_1'-t\gamma_2'')\\ (-\gamma_2'-t\gamma_1'')\gamma_1'+(\gamma_1'-t\gamma_2'')\gamma_2' & (-\gamma_2'-t\gamma_1'')^2+(\gamma_1'-t\gamma_2'')^2\end{bmatrix}\\ &= \frac{1}{(\det \mathrm{J}_\Phi)^2}\begin{bmatrix}1 & -t(\gamma_2'\gamma_2''+\gamma_1'\gamma_1'')\\ -t(\gamma_2'\gamma_2''+\gamma_1'\gamma_1'') & 1+2t(-t(\gamma_2'\gamma_1''-\gamma_1'\gamma_2'')+t^2|\gamma''|^2)\end{bmatrix}\end{aligned}$$

where we used (69).

Since the velocity $[\gamma_1', \gamma_2']$ and acceleration $[\gamma_1'', \gamma_2'']$ vectors are orthogonal under natural parameterization (see Lemma 1, Chapter 1, §5 in [30]) and (70) holds, we obtain

$$\mathrm{J}_\Phi^{-1}\mathrm{J}_\Phi^{-\top} = \frac{1}{(\det \mathrm{J}_\Phi)^2}\begin{bmatrix}1 & 0\\ 0 & 1+2\,t\,\kappa(s)+t^2\,|\gamma''|^2\end{bmatrix}$$

and (72) becomes

$$\int_{\Omega_h} \widetilde{A}(s,t)\nabla\widetilde{u}\cdot\nabla\overline{\widetilde{v}} - \widetilde{c}(s,t)\,\widetilde{u}\,\overline{\widetilde{v}}\;\mathrm{d}s\,\mathrm{d}t. \tag{73}$$

With (71) the coefficients are

$$\widetilde{A}(s,t) = \frac{1}{1+t\kappa(s)}\begin{bmatrix}1 & 0\\ 0 & 1+2\,t\,\kappa(s)+t^2\,|\gamma''|^2\end{bmatrix} \tag{74}$$

and

$$\widetilde{c}(s,t) = k^2(t)(1+t\kappa(s)). \tag{75}$$

Further, we omit the tilde so as not to overload the notation.

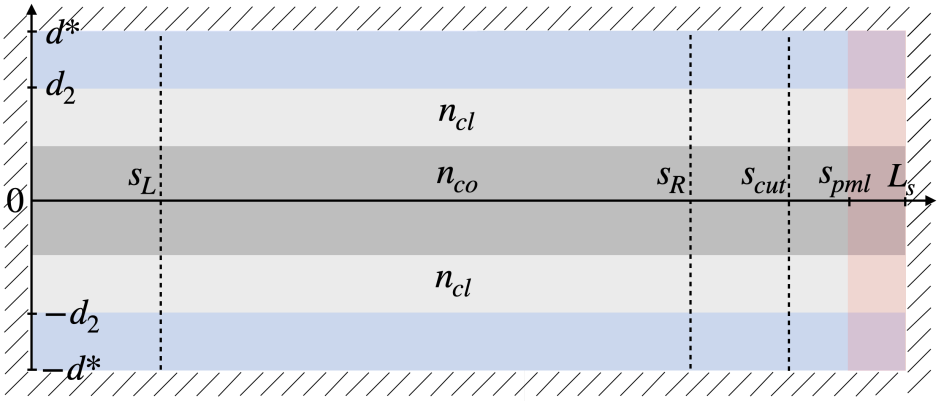

Figure 19: Sketch of a waveguide after TO application. PMLs in the transverse direction in blue, in the longitudinal direction in red. DtN applied at interfaces $\{s_{\mathrm{L,R}}\} \times I_t$. Transmission is evaluated at $\{s_{\mathrm{cut}}\} \times I_t$

Example: 90-degree bow. In the case of the 90-degree bow setting (see Section 3.2.1) the central trajectory Γ of the waveguide is parameterized with

$$\gamma_1(s) := \begin{cases} s, & \text{if } 0 \le s < s_{\mathrm{L}}\ ,\\ R_\Phi^+ \sin\left(\dfrac{s}{R_\Phi^+}\right), & \text{if } s_{\mathrm{L}} \le s < s_{\mathrm{R}},\\ R_\Phi^+ + \delta_{s_{\mathrm{L}}}, & \text{else}\ , \end{cases}$$

$$\gamma_2(s) := \begin{cases} R_\Phi^+ + \delta_{s_\mathrm{L}}, & \text{if } 0 \le s < s_\mathrm{L} \ , \\ R_\Phi^+ \cos\left(\dfrac{s}{R_\Phi^+}\right), & \text{if } s_\mathrm{L} \le s < s_\mathrm{R}, \\ s_\mathrm{R} - s, & \text{else} \ , \end{cases}$$

where we denote $R_\Phi^+ := R^+ - \dfrac{1}{2}d$ for the junction with the outer radius of curvature R^+, $s_\mathrm{L} := \delta_{s_\mathrm{L}}$ and $s_\mathrm{R} := L_s - \delta_{s_\mathrm{R}}$ correspond to the left and right straight parts of the waveguide of length δ_{s_L} and δ_{s_R} respectively.

We can see that the signed curvature is piecewise constant and equal to

$$\kappa(s) = \frac{1}{R_\Phi^+}\sin^2\left(\frac{s}{R_\Phi^+}\right) + \frac{1}{R_\Phi^+}\cos^2\left(\frac{s}{R_\Phi^+}\right) = \frac{1}{R_\Phi^+}, \quad s \in [s_\mathrm{L},\, s_\mathrm{R})$$

in the junction and zero in the straight offsets.

We can define the related coordinate transform $\Phi(s,t) = (\Phi_1,\, \Phi_2)$ as

$$\Phi_1 := \begin{cases} s, & 0 \le s < s_\mathrm{L} \ , \\ R_\Phi^+ \sin\left(\dfrac{s}{R_\Phi^+}\right) + t\sin\left(\dfrac{s}{R_\Phi^+}\right), & s_\mathrm{L} \le s < s_\mathrm{R}, \\ R_\Phi^+ + t, & s_\mathrm{R} \le s \le L_s, \end{cases}$$

$$\Phi_2 := \begin{cases} R_\Phi^+ + t + \delta_{s_\mathrm{L}}, & 0 \le s < s_\mathrm{L} \ , \\ R_\Phi^+ \cos\left(\dfrac{s}{R_\Phi^+}\right) + t\cos\left(\dfrac{s}{R_\Phi^+}\right), & s_\mathrm{L} \le s < s_\mathrm{R}, \\ s_\mathrm{R} - s, & s_\mathrm{R} \le s \le L_s, \end{cases}$$

for all $t \in [-L_t/2,\, L_t/2]$.

3.1.2. PML.

PMLs were considered in Section 2.1.1 from the point of view of their influence on the transverse differential operator and corresponding spectrum transformation in the straight open waveguide. In addition, they have extensive practical applications in the electromagnetic design. PMLs were first introduced in [7]. Their equivalence to complex scaling was shown in [21].

The main idea behind the method is to introduce an artificial layer with such properties that the solution decays as it propagates through such a layer. This method is called the "perfectly matched layer" since the signal reaching the boundary with the PML fits perfectly with it and does not produce spurious reflections if the PML is infinitely large. In practice, the truncated PML cannot completely absorb the signal, and it is needed to define the size of the PML area in the computational domain large enough to avoid the significant influence of reflections from external boundaries with Dirichlet or Neumann conditions on the calculation result. In the context of open waveguides, truncating the computational domain with PMLs is equivalent to replacing an open waveguide with a closed one.

To introduce a PML of finite depth we use the following transformation in the transverse direction t and the longitudinal direction s

$$\Phi^{\text{pml}}(s,\, t) = [s + \mathrm{i}\sigma(s),\, t + \mathrm{i}\sigma(t)] \tag{76}$$

with

$$\sigma(t) := \begin{cases} 0, & |t| < d_2, \\ -\dfrac{\sigma_0}{k_0}(-d_2 - t)^p, & -d_2 \le t \le -d^*, \\ \dfrac{\sigma_0}{k_0}(t - d_2)^p, & d_2 \le t \le d^*, \end{cases}$$

$$\sigma(s) := \begin{cases} 0, & 0 \le s < s_{\text{pml}}, \\ \dfrac{\sigma_0}{k_0}(s - s_{\text{pml}})^p, & s_{\text{pml}} \le s \le L_s, \end{cases}$$

where $p \in \mathbb{N}$, $p \ge 1$ and parameter $\sigma_0 > 0$ is real-valued. In this work we choose $p = 1$, then the Jacobian of the transformation is

$$\mathrm{J}_{\Phi^{\text{pml}}}(s,t) = \begin{bmatrix} 1 + \mathrm{i}\sigma'(s) & 0 \\ 0 & 1 + \mathrm{i}\sigma'(t) \end{bmatrix}.$$

For the choice $p = 1$, we can express the PML parametrization in the form presented in Section 2.1, Definition 2.8

$$\alpha^t := \begin{cases} 1, & |t| < d_2, \\ \alpha^t_\infty & \text{else}, \end{cases} \qquad \alpha^s := \begin{cases} 1, & s < s_{\text{pml}}, \\ \alpha^s_\infty & \text{else}, \end{cases} \tag{77}$$

where $\alpha^t_\infty = (1+\mathrm{i}\sigma'(t))^{-1}$, $\alpha^s_\infty = (1+\mathrm{i}\sigma'(s))^{-1}$. Then our leading equation in variational form (73) after TO and PML application becomes

$$\int_{\Omega_h} A(s,t)\nabla u \cdot \nabla \overline{v} - c(s,t)\, u\, \overline{v}\ \mathrm{d}s\, \mathrm{d}t = 0 \tag{78}$$

with the modified refraction coefficient

$$c(s,t) = \frac{k^2(t)}{\alpha^s \alpha^t}(1 + t\kappa(s)) \tag{79}$$

and diffusion matrix

$$A(s,t) = \frac{1}{1 + t\kappa(s)} \begin{bmatrix} \dfrac{\alpha^s}{\alpha^t} & 0 \\ 0 & \dfrac{\alpha^t}{\alpha^s}\big(1 + 2\,t\,\kappa(s) + t^2\,|\gamma''|^2\big) \end{bmatrix}. \tag{80}$$

3.1.3. Dirichlet to Neumann operator

Dirichlet to Neumann condition is applied at the interface between the straight parts of the waveguide and the junction. With this condition, we can distinguish between left-going and right-going waves in the left and right waveguide straight offsets. Therefore,

to construct DtN operator we start with the straight waveguide consideration. We construct DtN operator following [15] and [40].

In Section 2.1.1 we considered the transverse differential operator A_α (8) after the infinite PML application related to the problem $-\Delta u - k^2 u = 0$ in $\mathbb{R}^2$ with $k = k_0 n_{\text{co}}$ in the waveguide core and $k = k_0 n_{\text{cl}}$ in the cladding. Now we consider the straight waveguide problem with the leading equation $-\Delta u - k^2 u = 0$ in the truncated computational domain Ω_h.

For the PML to work correctly, we have to choose the thickness of PMLs large enough and impose Dirichlet or Neumann boundary conditions on the boundary of the computational domain. In the transverse direction, we choose Dirichlet boundary conditions. Let the PML in the transverse direction occupy the segments $[d_2, d^*]$ and $[-d_2, -d^*]$, see Figure 19.

The truncated PML-transformed operator $\widetilde{A}_\alpha \in L^2(I_t)$ is defined with parameter α^t (77) as

$$\widetilde{A}_\alpha v := -\alpha^t \frac{\mathrm{d}}{\mathrm{d}t}\Big(\alpha^t \frac{\mathrm{d}v}{\mathrm{d}t}\Big) - k^2 v,$$
$$\text{for any} \quad v \in D(\widetilde{A}_\alpha) := \Big\{ v \in H^1(I_t),\ \alpha^t \frac{\mathrm{d}}{\mathrm{d}t}\Big(\alpha^t \frac{\mathrm{d}v}{\mathrm{d}t}\Big) \in L^2(I_t),\ v(-d^*) = v(d^*) = 0 \Big\}.$$

The truncation of PML changes the structure of the spectrum – according to Theorem 3.1 in [40], the operator $\widetilde{A}_\alpha$ has a compact resolvent. That is, the spectrum $\sigma(\widetilde{A}_\alpha)$ consists only of a discrete spectrum. The main difference with $\sigma_d(A_\alpha)$, is that the continuous spectrum related to the infinite PML is now also discretized [15]. However, despite the fact that the spectrum is discrete, the transverse operator $\sigma(\widetilde{A}_\alpha)$ is not self-adjoint and we cannot use the spectral theorem to show the completeness of the system of eigenfunctions as in the case of a closed waveguide. However, for DtN operator construction, we need only the modal decomposition, and here, we do not need to show the completeness of eigenfunctions [15], [40].

Hence, for the truncated problem with the PML of finite size, we use the expression for the mode expansion which is inspired by the closed waveguide case and has (see (109) or [71] for more details) the following form

$$u(s,t) = \sum_m (a_m^{\mathrm{R}} \mathrm{e}^{\mathrm{i}\sqrt{-\lambda_m} s} + a_m^{\mathrm{L}} \mathrm{e}^{-\mathrm{i}\sqrt{-\lambda_m} s}) \Phi_m(t), \tag{81}$$

where a_m^{L}, $a_m^{\mathrm{R}} \in \mathbb{C}$, $m \in \mathbb{N}$ are modal expansion coefficients, $\Phi_m(t)$ are eigenfunctions of the transverse operator $\widetilde{A}_\alpha$ and $\sqrt{-\lambda_m}$ is the propagation constant in the longitudinal direction with $\sqrt{-\lambda_m} = \mathrm{i}\sqrt{\lambda_m}$ if $\lambda_m > 0$. We choose $\mathfrak{Re}\sqrt{-\lambda_m} \geq 0$, $\mathfrak{Im}\sqrt{-\lambda_m} \geq 0$. For the fixed time dependency $\mathrm{e}^{-\mathrm{i}wt}$ we characterize the incoming and outgoing waves as follows:

- $\mathrm{e}^{\mathrm{i}\sqrt{-\lambda_m} s}\Phi_m(t)$ is right-going if $\mathfrak{Im}\sqrt{-\lambda_m} = 0$ and decays exponentially to the right if $\mathfrak{Im}\sqrt{-\lambda_m} \neq 0$.
- $\mathrm{e}^{-\mathrm{i}\sqrt{-\lambda_m} s}\Phi_m(t)$ is left-going if $\mathfrak{Im}\sqrt{-\lambda_m} = 0$ and decays exponentially to the left if $\mathfrak{Im}\sqrt{-\lambda_m} \neq 0$.

We need the following biorthogonality result for the transverse operator in case of truncated PML for the DtN operator construction:

Theorem 3.1. *Asume that $\lambda_n \in \sigma(\widetilde{A}_\alpha)$ with the algebraic multiplicity 1 and the eigenfunctions Φ_n are such that for all $n \in \mathbb{N}$*

$$\int_{I_t} \frac{1}{\alpha^t} \Phi_n^2 \, \mathrm{d}t \neq 0.$$

Then if $\lambda_n \neq \lambda_m$, $\lambda_m \in \sigma(\widetilde{A}_\alpha)$, $m \in \mathbb{N}$ we have the following biorthogonality relation

$$(\Phi_n, \, \Phi_m^*)_{L^2(I_t)} = \int_{I_t} \frac{1}{\alpha^t} \Phi_n \, \Phi_m \, \mathrm{d}t = 0,$$

where Φ_n is the eigenfunction related to the eigenvalue λ_n, Φ_m^* is the eigenfunction related to the eigenvalue λ_m of the adjoint to $\widetilde{A}_\alpha$ operator $\widetilde{A}_\alpha^*$.

Proof. See Theorem 3.2 in [40], Proposition 3.1 in [15]. □

Hence, the projection onto its own subspace has the form

$$P_{\lambda_n} v := \frac{(v, \, \Phi_n^*)_{L^2(I_t)}}{(\Phi_n, \, \Phi_n^*)_{L^2(I_t)}} \Phi_n. \tag{82}$$

Then with a fixed definition of the left and right-going and evanescent waves, we can construct exact boundary conditions at the interfaces between the straight parts of the waveguide and the junction $\{s_{\mathrm{L,R}}\} \times I_t$.

Let us consider the left straight part of the waveguide $s \leq s_{\mathrm{L}}$. The incoming wave u^{inc} is right-going, therefore with (81) we have

$$u^{\mathrm{inc}}(s,t) = \sum_m a_{0_m}^{\mathrm{R}} \mathrm{e}^{\mathrm{i}\sqrt{-\lambda_m^{\mathrm{L}}}(s_L - s)} \Phi_m^{\mathrm{L}}(t),$$

where Φ_m^{L} is the eigenfunction corresponding to the transverse operator of the left straight part of the waveguide with PML in the transverse direction, $\sqrt{-\lambda_m^{\mathrm{L}}}$ associated longitudinal propagation constant. Then on the left interface we have

$$\frac{\partial u^{\mathrm{inc}}}{\partial s}\Big|_{\{s_{\mathrm{L}}\} \times I_t} = -\sum_m a_{0_m}^{\mathrm{R}} \, \mathrm{i}\sqrt{-\lambda_m^{\mathrm{L}}} \Phi_m^{\mathrm{L}}.$$

With (81) we have left-going

$$u(s,t) - u^{\mathrm{inc}}(s,t) = \sum_m a_m^{\mathrm{L}} \mathrm{e}^{-\mathrm{i}\sqrt{-\lambda_m^{\mathrm{L}}}(s_L - s)} \Phi_m^{\mathrm{L}}(t)$$

and on the left interface, we have

$$\frac{\partial u}{\partial s}\Big|_{\{s_{\mathrm{L}}\} \times I_t} - \frac{\partial u^{\mathrm{inc}}}{\partial s}\Big|_{\{s_{\mathrm{L}}\} \times I_t} = -\sum_m a_m^{\mathrm{L}} \, \mathrm{i}\sqrt{-\lambda_m^{\mathrm{L}}} \Phi_m^{\mathrm{L}}.$$

The coefficients a_{0_m}, a_m are the projection of the solution on the slice corresponding to the beginning of the left offset onto the subspace associated with the eigenfunction Φ^{L}_m. Hence, for left-side coefficients with (82) we have

$$a^{\mathrm{R}}_{0_m} + a^{\mathrm{L}}_m = P^{\mathrm{L}}_{\lambda_m} u\Big|_{\{s_{\mathrm{L}}\}\times I_t} = \Big(\int_{I_t} \frac{1}{\alpha^t}(\Phi^{\mathrm{L}}_m)^2\,\mathrm{d}t\Big)^{-1} \int_{I_t} \frac{1}{\alpha^t} u\Big|_{\{s_{\mathrm{L}}\}\times I_t} \Phi^{\mathrm{L}}_m\,\mathrm{d}t.$$

Now we consider the right offset $s \geq s_{\mathrm{R}}$. the waveguide is straight and, by our assumption, the wave here is only right-going. Therefore with (81) we have

$$u(s,t) = \sum_m a^{\mathrm{R}}_m \mathrm{e}^{\mathrm{i}\sqrt{-\lambda^{\mathrm{R}}_m}(s-s_{\mathrm{R}})}\Phi^{\mathrm{R}}_m(t),$$

where Φ^{R}_m is the corresponding transverse operator eigenfunction related to the truncated problem. $\sqrt{-\lambda^{\mathrm{R}}_m}$ is the associated longitudinal propagation constant. Then on the right interface we have

$$\frac{\partial u}{\partial s}\Big|_{\{s_{\mathrm{R}}\}\times I_t} = \sum_m a^{\mathrm{R}}_m\,\mathrm{i}\sqrt{-\lambda^{\mathrm{R}}_m}\Phi^{\mathrm{R}}_m.$$

Therefore, for the right-side coefficients with (82), we obtain

$$a^{\mathrm{R}}_m = P^{\mathrm{R}}_{\lambda_m} u\Big|_{\{s_{\mathrm{R}}\}\times I_t} = \Big(\int_{I_t} \frac{1}{\alpha^t}(\Phi^{\mathrm{R}}_m)^2\,\mathrm{d}t\Big)^{-1} \int_{I_t} \frac{1}{\alpha^t}\, u\Big|_{\{s_{\mathrm{R}}\}\times I_t} \Phi^{\mathrm{R}}_m\,\mathrm{d}t.$$

Thus, on the left side interface $\{s_{\mathrm{L}}\}\times I_t$, we have

$$-\frac{\partial u}{\partial s}\Big|_{\{s_{\mathrm{L}}\}\times I_t} = -2\Lambda_{\mathrm{L}} u^{\mathrm{inc}}\Big|_{\{s_{\mathrm{L}}\}\times I_t} + \Lambda_{\mathrm{L}} u\Big|_{\{s_{\mathrm{L}}\}\times I_t}, \tag{83}$$

where DtN operator on the left side is defined as

$$\Lambda_{\mathrm{L}}\colon H^{\frac{1}{2}}\big(\{s_{\mathrm{L}}\}\times I_t\big) \to H^{-\frac{1}{2}}\big(\{s_{\mathrm{L}}\}\times I_t\big),$$

$$\begin{aligned}\Lambda_{\mathrm{L}} v :&= \sum_m (P^{\mathrm{L}}_{\lambda_m} v)\,\mathrm{i}\sqrt{-\lambda^{\mathrm{L}}_m}\Phi^{\mathrm{L}}_m \\ &= \sum_m \Big(\int_{I_t} \frac{1}{\alpha^t}(\Phi^{\mathrm{L}}_m(t))^2\,\mathrm{d}t\Big)^{-1}\Big(\int_{I_t} \frac{1}{\alpha^t} v(t)\,\Phi^{\mathrm{L}}_m(t)\,\mathrm{d}t\Big)\,\mathrm{i}\sqrt{-\lambda^{\mathrm{L}}_m}\Phi^{\mathrm{L}}_m(t).\end{aligned}$$

The space $H^{-\frac{1}{2}}\big(\{s_{\mathrm{L}}\}\times I_t\big)$ denotes topological dual space of $H^{\frac{1}{2}}\big(\{s_{\mathrm{L}}\}\times I_t\big)$. For the right side interface $\{s_{\mathrm{R}}\}\times I_t$, we have

$$\Lambda_{\mathrm{R}}\colon H^{\frac{1}{2}}\big(\{s_{\mathrm{R}}\}\times I_t\big) \to H^{-\frac{1}{2}}\big(\{s_{\mathrm{R}}\}\times I_t\big),$$

$$\begin{aligned}-\frac{\partial u}{\partial s}\Big|_{\{s_{\mathrm{R}}\}\times I_t} &= \Lambda_{\mathrm{R}} u\Big|_{\{s_{\mathrm{R}}\}\times I_t} \\ &:= \sum_m \Big(P^{\mathrm{R}}_{\lambda_m} u\Big|_{\{s_{\mathrm{R}}\}\times I_t}\Big)\,\mathrm{i}\sqrt{-\lambda^{\mathrm{R}}_m}\Phi^{\mathrm{R}}_m \\ &= \sum_m \Big(\int_{I_t} \frac{1}{\alpha^t}(\Phi^{\mathrm{R}}_m(t))^2\,\mathrm{d}t\Big)^{-1}\Big(\int_{I_t} \frac{1}{\alpha^t} u(s_{\mathrm{R}},t)\Phi^{\mathrm{R}}_m(t)\,\mathrm{d}t\Big)\,\mathrm{i}\sqrt{-\lambda^{\mathrm{R}}_m}\Phi^{\mathrm{R}}_m(t).\end{aligned} \tag{84}$$

The space $H^{-\frac{1}{2}}\big(\{s_{\mathrm{R}}\}\times I_t\big)$ denotes topological dual space of $H^{\frac{1}{2}}\big(\{s_{\mathrm{R}}\}\times I_t\big)$.

3.1.4. Variational formulation

We need a variational formulation of the problem for discretization by the finite element method. Taking into account approaches introduced above for sorting outgoing and incoming waves, the problem of our interest (66) after truncation and TO application has the following variational formulation: find $u \in H^1_\partial(\Omega_h)$, where

$$H^1_\partial(\Omega_h) := \Big\{ v \in H^1(\Omega_h) : v(\cdot, -d^*)\Big|_{I_s} = 0,\ v(\cdot, d^*)\Big|_{I_s} = 0, \qquad (85)$$
$$\frac{\partial v}{\partial \nu}(0,\cdot)\Big|_{I_t} = 0,\ \frac{\partial v}{\partial \nu}(L_s,\cdot)\Big|_{I_t} = 0 \Big\},$$

such that for any $v \in H^1_\partial(\Omega_h)$

$$\begin{aligned} \int_{\Omega_h} A(s,t)\nabla u \cdot \nabla \overline{v} - c\, u\, \overline{v}\ \mathrm{d}s\,\mathrm{d}t - \Big\langle \Lambda_{\mathrm{L}} u,\, v \Big\rangle_{H^{-\frac{1}{2}}(\{s_{\mathrm{L}}\}\times I_t),\, H^{\frac{1}{2}}(\{s_{\mathrm{L}}\}\times I_t)} \\ - \Big\langle \Lambda_{\mathrm{R}} u,\, v \Big\rangle_{H^{-\frac{1}{2}}(\{s_{\mathrm{R}}\}\times I_t),\, H^{\frac{1}{2}}(\{s_{\mathrm{R}}\}\times I_t)} \\ = -2\Big\langle \Lambda_{\mathrm{L}} u^{\mathrm{inc}},\, v \Big\rangle_{H^{-\frac{1}{2}}(\{s_{\mathrm{L}}\}\times I_t),\, H^{\frac{1}{2}}(\{s_{\mathrm{L}}\}\times I_t)}. \end{aligned} \qquad (86)$$

Here coefficients A, c are defined with (80) and (79). In addition to PMLs, we use DtN conditions on the left and right interfaces $\{s_{\mathrm{L,R}}\} \times I_t$, therefore the dual products correspond to DtN conditions (84) and (83) obtained by construction for the truncated problem. Condition (83) selects the propagation in the longitudinal direction of reflected wave $u - u^{\mathrm{inc}}$ to the left, and of the incoming wave u^{inc} to the right in the left offset. Condition (84) fixes the propagation of the wave to the right in the longitudinal direction. The sum in these terms is truncated for practical purposes according to the finite number of modes considered in the implementation.

DtN terms on the interfaces are related to the straight parts of the waveguide, therefore Jacobian J_Φ (68) does not appear here.

3.1.5. Transmission

In the simplified MMA method, we utilize the pre-calculated database of transmission coefficients, and no numerical solution to the boundary value problem is required to compute the signal transmission. In the case of FEM, we first seek the numerical solution to the truncated problem (86), then evaluate the transmission over the interval I_t in the transverse direction at the end of the right offset for $s < s_{\mathrm{pml}}$. Energy flow coming out through the section $\{s\} \times I_t$ for an acoustic wave equation is given by

$$\mathfrak{Im}\Big(\int_{I_t} \frac{\partial u(s,t)}{\partial \nu}\, \overline{u}(s,t)\, \mathrm{d}t \Big), \qquad (87)$$

which, together with the DtN operator for the right-going modes (84) and the parameters we have chosen for the PML (77), provides the following expression

$$\mathfrak{Im}\Big(\int_{I_t} \Lambda_{\mathrm{R}} u(s,t)\, \overline{u}(s,t)\, \mathrm{d}t \Big) = \sum_m \frac{\sqrt{-\lambda^{\mathrm{R}}_m}}{\int_{I_t} (\Phi^{\mathrm{R}}_m(t))^2\, \mathrm{d}t} \int_{I_t} u(s,t)\, (\Phi^{\mathrm{R}}_m(t))\, \mathrm{d}t \int_{I_t} (\Phi^{\mathrm{R}}_m(t))\, \overline{u}(s,t)\, \mathrm{d}t.$$

Let us introduce the amplitude functional $F_m\colon H^1_\partial(\Omega_h) \to \mathbb{R}$ of the m-th mode [72]

$$F_m(u) := \int_{I_t} \Phi^{\mathrm{R}}_m(t)\,\overline{u}\,\mathrm{d}t,$$

then the power transmission related to the right-going m-th mode of the truncated problem (86) is

$$|T_m|^2 = \frac{\sqrt{-\lambda^{\mathrm{R}}_m}}{\int_{I_t}(\Phi^{\mathrm{R}}_m(t))^2\,\mathrm{d}t}|F_m|^2.$$

3.1.6. Convergence versus exact solution

We consider the straight waveguide case of the problem (66), for which the exact solution is known. Our computational domain is defined as

$$\Omega_h = [0,\, L_s] \times [-L_t/2,\, L_t/2],$$

where $L_s = 8\lambda_0$ with wavelength $\lambda_0 = 1.55$ µm is the length related to the longitudinal propagation direction, $L_t = 9$ µm is the length related to the transverse direction.

We choose the following waveguide's parameters

$$d = 1.8\,\mu\mathrm{m}, \quad n_{\mathrm{co}} = 1.53, \quad n_{\mathrm{cl}} = 1.36.$$

We denote the m-th eigenvalue as $\mu_m := -\lambda_m$. Then the chosen waveguide parameters together with wavelength λ_0 provides the eigenvalue related to the fundamental eigenmode $\mu_1 = 36.9178$. The PMLs parameters are

$$\sigma = 8, \quad p = 1, \quad \delta^{\mathrm{pml}}_s = \lambda_0, \quad \delta^{\mathrm{pml}}_t = 1.5\,\mu\mathrm{m},$$

where δ^{pml}_s, δ^{pml}_t are PML thicknesses in the direction of longitudinal propagation and along the transverse direction, respectively.

For the straight waveguide problem solution related to the eigenvalue problem in the transverse direction is known and has the following form [72]

$$\Phi_m(t) := \begin{cases} c_1\,\mathrm{e}^{\sqrt{\mu_m - k_0^2 n_{\mathrm{cl}}^2}\,t}, & t < -d/2, \\ c_2\,\mathrm{e}^{\mathrm{i}\sqrt{k_0^2 n_{\mathrm{co}}^2 - \mu_m}\,t} + c_3\,\mathrm{e}^{-\mathrm{i}\sqrt{k_0^2 n_{\mathrm{co}}^2 - \mu_m}\,t}, & -d/2 < t < d/2, \\ c_4\,\mathrm{e}^{-\sqrt{\mu_m - k_0^2 n_{\mathrm{cl}}^2}\,t}, & t > d/2. \end{cases}$$

With $\mathcal{C}^1$-continuity we can determine the linear system of equations for the coefficients $c_1, \ldots, c_4$ which has nontrivial solutions only if the determinant of the system is zero. If the eigenvalues of the m-mode are unknown, then initial guess μ^0_m has to be provided. The exact solution for the straight waveguide has the form of the incoming right-going mode $u_m(s,t) = \mathrm{e}^{\mathrm{i}\sqrt{\mu_m}s}\,\Phi_m(t)$.

We use mesh sizes $h = \lambda_0/10 = 0.155\,\mu\mathrm{m}, \ldots, \lambda_0/40 = 0.03875\,\mu\mathrm{m}$ [50]. The discrete solutions converge to the exact solution inside the waveguide's core when we distribute the second order $\mathrm{pd} = 2$ finite elements with the second order in the H^1-norm and the third order in the L^2-norm, see Figure 20.

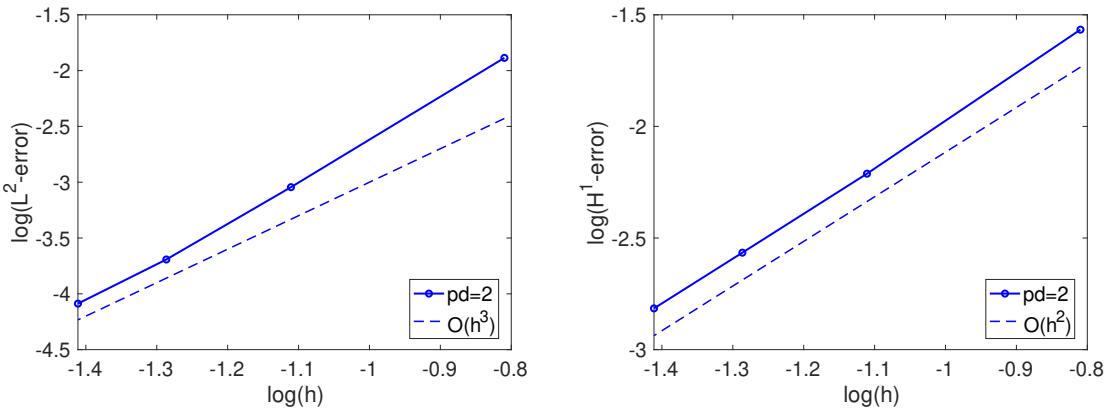

Figure 20: Convergence analysis for the straight slab waveguide with respect to the waveguide core. L^2- and H^1-errors for pd $= 2$ are plotted against the mesh size $h = \lambda_0/(10n)$, $n = 1, \ldots, 4$. The dashed reference line indicates the optimal order.

3.2. MMA for open slab waveguides with constant thickness

In this section, we compare the signal transmission values for three cases:

(i) Waveguides with the junction represented by part of the ring. The curvature of the central trajectory has exact constant values for each segment.

(ii) Waveguides with varying curvature. The central trajectory is given by a formula.

(iii) Waveguides with central trajectories and parameters from an experiment.

As a reference solution to MMA, we use the Finite Element Method formulated in the curvilinear coordinate system transformation optics (TO) approach (67).

3.2.1. Example 1: 90-degree bow

In the field of waveguide studies, bends with constant curvature are usually the next most complex case after a straight waveguide. In addition to theoretical interest, they have practical value, since bends are important parts of integration schemes and are used, for example, to change the direction of signal propagation [33], [4], [49], [65], [67]. This type of waveguide is characterized by signal losses at bending, and there is a dependence of the power transmitted along the waveguide on the bending radius – the smaller the radius, the greater the losses.

At the same time, bends of the smallest radius are of the greatest practical interest in integrated photonics. Therefore, the question of their fast shape optimization and, as a consequence, a method for an efficient transmission calculation, is interesting in itself. However, in this section, we are interested in a waveguide with constant curvature as a basic example of the Multi-Mode Approximation method application.

In Section 2.3, we considered the semi-analytic solution for the ring-shaped waveguide and now study an example of a waveguide in which segments of different curvature can

be distinguished. In it, one straight part is connected to another with the help of an arch of constant curvature. Let us call this type of waveguide a *90-degree bow*.

2-D bent structure. The 90-degree bow waveguide setting consists of two straight slab waveguides and a curved junction Ω_J between them, represented by a bent slab waveguide characterized by an outer radius of curvature R^+. The core width d is assumed to be constant for all parts of the waveguide. The material parameters of the structure are determined by the refractive indices n_{co} in the core and n_{cl} in the cladding for the vacuum wavelength λ_0 (see Figure 21, left). The choice of these values is

$$R^+ \in [7, 100]\,\mu\text{m}, \quad d = 1.8\,\mu\text{m}, \quad n_{\text{co}} = 1.53, \quad n_{\text{cl}} = 1.36, \quad \lambda_0 = 1.55\,\mu\text{m}. \tag{88}$$

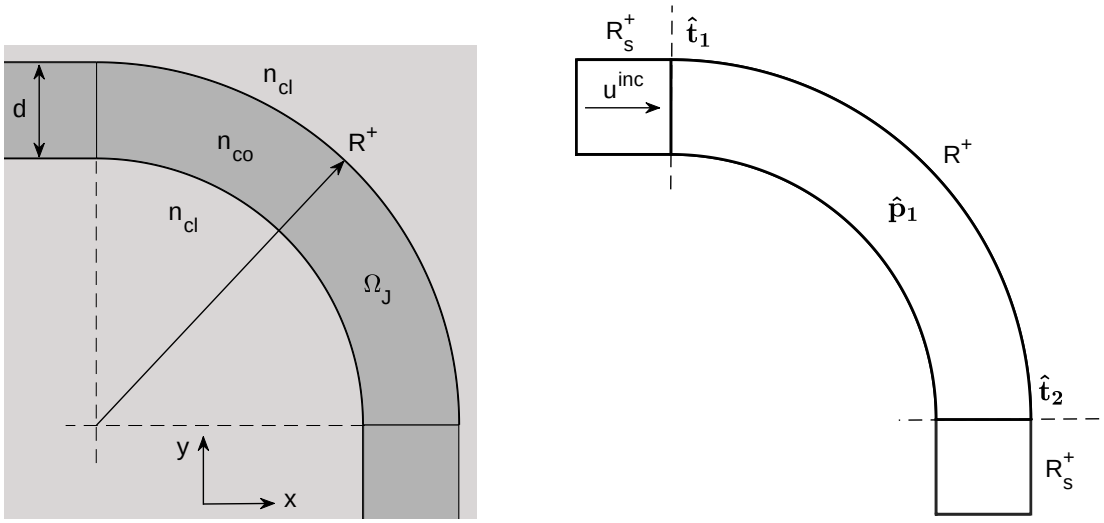

Figure 21: **Left**: a sketch of a 90-degree bow waveguide with the core thickness d, and refractive indices n_{cl}, n_{co}. The junction Ω_J has an outer radius of curvature R^+. **Right**: how bending $\hat{\mathbf{p}}$ and transition $\hat{\mathbf{t}}$ transmission are related to each part of the 90-degree bow. We set $R_s^+ = 1000$ µm for the straight parts of the waveguide.

Implementation details of the reference solution. For the FEM reference solution, we take mesh sizes $h = \lambda_0/(10\,n)$ with $n \in \{1, 2, 3, 4\}$ for polynomial degree $\text{pd} = 2$ and $n \in \{1, 2\}$ for $\text{pd} = 3$, to confirm the choice of parameters that was made based on the results for the straight waveguide in Section 3.1.6.

We consider the central curve Γ_J in $\mathbb{R}^2$ of the 90-degree bow junction Ω_J in parametric form

$$\Gamma_J = \{\gamma_1(s),\, \gamma_2(s),\, s \in \mathbb{R}\}, \quad \gamma_1(s) = R^+ \sin\big(s/R^+\big),\ \gamma_2(s) = R^+ \cos\big(s/R^+\big). \tag{89}$$

Then, after applying the transformation optics approach (see Section 3.1.1 for the details), our computational domain is defined as

$$\Omega_h = [0,\, L_s] \times [-L_t/2,\, L_t/2], \quad L_s = R^+\pi/2 + \delta_{s_{\text{L}}} + \delta_{s_{\text{R}}},$$

where L_s is the total length related to the longitudinal propagation direction, $R^+\pi/2$ is the arclength of the junction Ω_J, and δ_{s_L}, δ_{s_R} are lengths of offsets related to the left and right straight parts of the waveguide. We fix $\delta_{s_\mathrm{L}} = 1$ µm and the length δ_{s_R} to be adjusted such that $h = \lambda_0/(10\,n)$ holds, see Section 3.1.6. L_t is the thickness in the transverse direction, $L_t > d$ and we set $L_t = 9$ µm for all radii of curvature R^+.

For example, in case $R^+ = 70$ µm, the computational domain is $[0,\ 114.7]\times[-4.5,\ 4.5]$. With a choice of the mesh size $h = 0.0775$ µm and quadratic finite elements pd $= 2$, the domain is discretized with $N_\mathrm{cells} = 1\,065\,600$ cells.

To truncate the computational domain, we use the PML defined by (76) with parameters

$$\sigma = 8, \quad p = 1, \quad \delta_s^\mathrm{pml} = \lambda_0, \quad \delta_t^\mathrm{pml} = 1.5\,\mu\mathrm{m}, \tag{90}$$

where δ_s^pml, δ_t^pml are PML thicknesses in the direction of longitudinal propagation and along the transverse direction, respectively. The transmission is measured on the cross-section at $s_\mathrm{cut} = L_s - 2\lambda_0$, on the right offset before the start of PML (see Figure (19)):

$$L_s - \delta_{s_R} < s_\mathrm{cut} < L_s - \delta_s^\mathrm{pml}.$$

The eigenvalues for the considered set of parameters (88) related to the first and second guided modes of the corresponding straight waveguide are

$$\mu_1 = 36.9178, \quad \mu_2 = 34.4569. \tag{91}$$

We denote the outer radius in the 90-degree bow structure as R^+, but in (89), we mean the outer radius of the central curve. To not overload the visual clarity, we do not introduce additional notation for this, but it is necessary to take values $R^+ - d/2$ for the computation of the reference solution with FEM.

Examples of the calculated field for radii $R^+ \in \{7,\ 30,\ 100\}$ µm for $h = \lambda_0/20$ are shown in Figure 22, top row. The row at the bottom corresponds to the distribution of energy between the first (black solid line) and second (blue solid line) guided modes transferred along the waveguide.

Let us consider the emergence of the second mode in a 90-degree bow. As can be clearly seen from Figure 22, bottom left, the first mode passes through the straight part of the waveguide, transferring all the power $|T_1|^2 = 1$. At the same time, the second mode does not transfer energy at the left offset, and its transmission is zero $|T_2|^2 = 0$. Since, in this example, the radius of curvature is small $R^+ = 7$ µm, when the first mode encounters the junction Ω_J, most of the power transmitted by it is spent on exciting the radiating waves and the second mode. The bottom middle and bottom right Figures 22 show that with increasing radius of curvature, the amount of energy transferred by the second mode decreases, and for $R^+ = 100$ µm almost all the energy is carried by the first mode along the entire waveguide.

Therefore, a 90-degree bow waveguide is characterized by large losses due to the occurrence of radiation modes, if its radius of curvature is such that the amount of energy transmitted by the second mode, exceeds the amount of energy transmitted by the first mode.

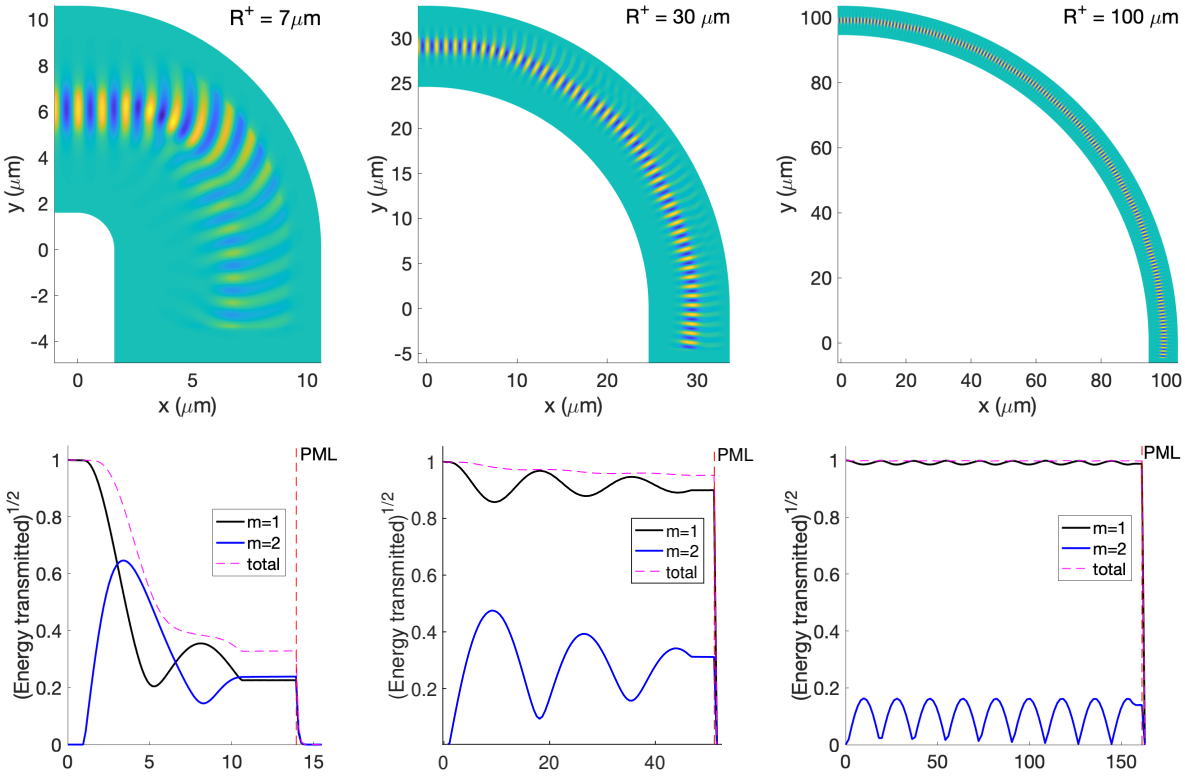

Figure 22: 90-degree bow example with $d = 1.8$ µm, $\lambda_0 = 1.55\,\mu\text{m}$, $n_{\text{co}} = 1.53$, $n_{\text{cl}} = 1.36$. **Top row**: FEM numerical solution with pd $= 2$, $h = \lambda_0/20$ µm, the outer radius of curvature $R^+ = 7$ µm, $R^+ = 30$ µm, $R^+ = 100$ µm. **Bottom row**: transmission carried by the first and second guiding modes along the direction of the light propagation; **Left**: $R^+ = 7$ µm, most of the energy is dissipated; **Center**: $R^+ = 30$ µm, most of the energy is confined near the core of the waveguide; **Right**: $R^+ = 100$ µm, most of the energy is transmitted by the first guiding mode.

MMA for three segments. Now, we apply the multi-mode approximation method to this example. Following the expression for the general case (65), bending transmission related to a certain waveguide's segment of a radius of curvature R^+ and arclength l should be defined with an attenuation constant $\mathfrak{Im}\beta$ as:

$$\hat{\mathbf{p}}_{\mathbf{1}} = \begin{pmatrix} \exp\{-\mathfrak{Im}\,\beta_1(R^+)l\} & 0 \\ 0 & \exp\{-\mathfrak{Im}\,\beta_2(R^+)l\} \end{pmatrix}, \tag{92}$$

then, the total transmission $\mathbf{T}$ for the 90-degree bow setting will be:

$$\mathbf{T} = \begin{pmatrix} T_1 \\ T_2 \end{pmatrix} = \hat{\mathbf{t}}_{\mathbf{2}}\,\hat{\mathbf{p}}_{\mathbf{1}}\,\hat{\mathbf{t}}_{\mathbf{1}} \begin{pmatrix} 1 \\ 0 \end{pmatrix}, \quad \text{where } \hat{\mathbf{t}}_{\mathbf{2}} = \begin{pmatrix} \mathbf{t}_{11} & \mathbf{t}_{12} \\ \mathbf{t}_{21} & \mathbf{t}_{22} \end{pmatrix} \tag{93}$$

is the transmission along the junction between bent and straight waveguide parts. Similarly, $\hat{\mathbf{t}}_{\mathbf{1}}$ is the transition transmission between the straight part and the bending junction. See the sketch in Figure 21.

The basic steps of the transmission computation with MMA in a 90-degree bow are summarized in Algorithm 2.

We also compare the MMA method with the fundamental mode approximation (FMA) method. The steps of FMA algorithm for a waveguide of three segments of constant curvature are described in Algorithm 3.

Algorithm 2 MMA, 90-degree bow.

Given: t-maps $\mathbf{T}_{pq} = (t_{pq,ij})_{1\le i,j\le N}$, $p, q \in \{1, 2\}$

characterized by $\mathbf{I}_{R^+} = [R_1^+, R_2^+, \ldots, R_N^+]$ with $R_N^+ = R_s^+ = 1000$ µm.

First and second leaky modes in a segment with constant radii of curvature $R_k^+ \in \mathbf{I}_{R^+}$ have propagation constants $\beta_1(R_k^+)$ and $\beta_2(R_k^+)$.

1. With arclength $l_k = \pi R_k^+/2$ find bending transmission $\hat{\mathbf{p}}_\mathbf{1}$ (92).
2. Define transition transmission between straight and bent parts

   $\hat{\mathbf{t}}_\mathbf{1} = [t_{11,Nk},\, t_{12,Nk}\,;\, t_{21,Nk},\, t_{22,Nk}]$

   and transition transmission between bent and straight parts

   $\hat{\mathbf{t}}_\mathbf{2} = [t_{11,kN},\, t_{12,kN}\,;\, t_{21,kN},\, t_{22,kN}]$ (93).
3. Find total transmission $\mathbf{T}$ (93).

Algorithm 3 FMA, 90-degree bow.

Given: t-maps $\mathbf{T}_{11} = (t_{11,ij})_{1\le i,j\le N}$,

characterized by $\mathbf{I}_{R^+} = [R_1^+, R_2^+, \ldots, R_N^+]$ with $R_N^+ = R_s^+ = 1000$ µm.

The solution in a segment with constant radii of curvature $R_k^+ \in \mathbf{I}_{R^+}$, has propagation constant $\beta_1(R_k^+)$.

1. With arclength $l_k = \pi R_k^+/2$, find bending transmission $\hat{p} = \exp\{-2\Im\mathfrak{m}\,\beta_1(R_k^+)l_k\}$.
2. Define transition transmission $\hat{t} = |t_{11,Nk}|^2\,|t_{11,kN}|^2$.
3. Find total transmission power $|T| = \hat{p}\,\hat{t}$.

MMA versus FEM and FMA. Now, we consider the difference in output power for the approximation methods and FEM. Since 90-degree bows of small radius are of greater interest, we use $R^+ = 7, 7.1, \ldots, 10$ µm and $R^+ = 10, 10.5, \ldots, 30$ µm. For large radii, we take $R^+ = 35, 40, \ldots, 100$ µm.

We see in Figure 23 bottom, that the relative difference reaches 3% at $R^+ = 9.9$ µm. For visual clarity, the results for pd $= 2$, $h \in \{\lambda_0/20,\, \lambda_0/30\}$ are shown, but for small radii $7\mu\text{m} \le R^+ \le 10\mu\text{m}$ for $h = \lambda_0/40$ and pd $= 3$ $h \in \{\lambda_0/10,\, \lambda_0/20\}$ the outcome is the same.

In Figure 24 left, we observe that the FMA method becomes reliable for $R^+ \ge 50$ µm. The absolute relative difference for FMA reaches 1% for $R^+ \ge 100$µm. We also see

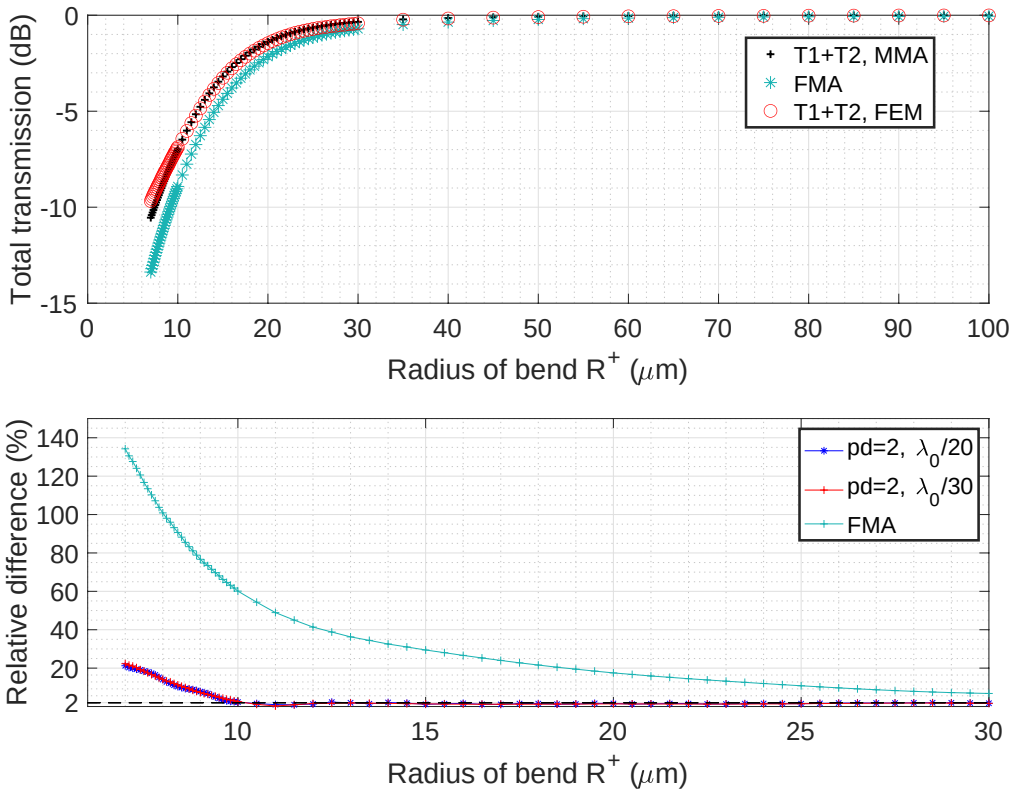

Figure 23: 90-degree bow example with $d = 1.8$ µm, $\lambda_0 = 1.55$ µm, $n_{\text{co}} = 1.53$, $n_{\text{cl}} = 1.36$. **Top**: total power transmission calculated by MMA, FMA, and FEM versus radii of curvature $R^+ \in [7, 100]$ µm. **Bottom**: relative difference between power transmission found by MMA and by FEM for radii of curvature $R^+ \in [7, 30]$ µm and different sizes of FEM mesh (blue and red lines). Relative difference between power transmission found by FMA and by FEM for $R^+ \in [7, 30]$ µm with pd $= 2$, $h = \lambda_0/20$ µm (turquoise line).

that for large radii, the difference between MMA, FMA, and FEM is less than 1%. This is due to the fact that the signal transmission occurs practically without losses, and all the energy is transferred by the first mode. This result is true for any choice of mesh size and polynomial degree indicated in the Figure 24 left, except pd $= 2$, $h = \lambda_0/10$.

Limitations. As we can see in Figure 23, this approximation method is reliable for a waveguide supporting two modes when applied to bends with a radius of curvature $R^+ \geq 9.9$ µm. In the case of waveguides supporting only the fundamental mode, the FMA is also suitable for $R^+ \geq 10$ µm [67].

For bends with small radii of curvature most of the energy is dissipated in the direction away from the waveguide core as radiation modes transfer it. The dominance of energy transfer of the second mode over the first indicates the occurrence of radiation modes, which we can observe from the transmission distribution between the first and second modes in Figure 24, right.

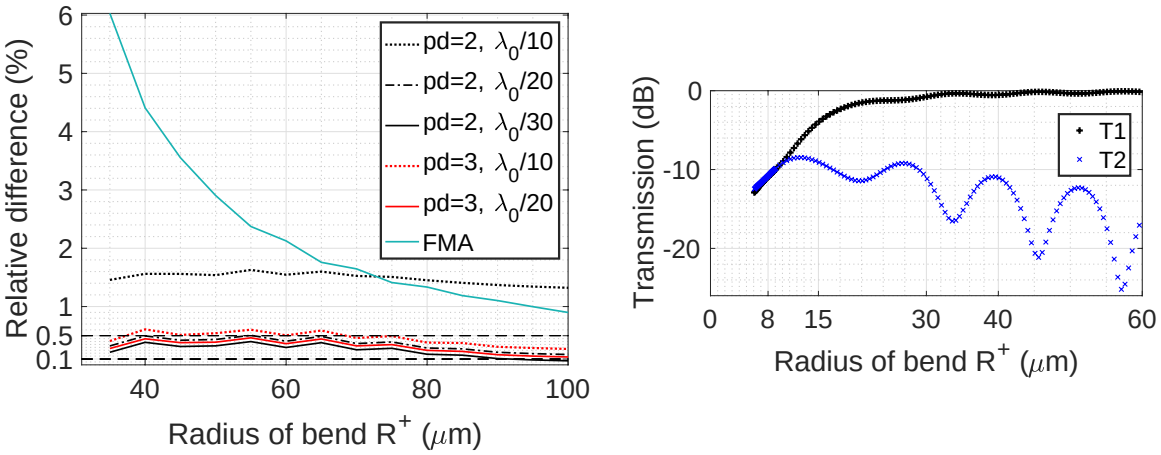

Figure 24: 90-degree bow example with $d = 1.8$ µm, $\lambda_0 = 1.55\,\mu\text{m}$, $n_{\text{co}} = 1.53$, $n_{\text{cl}} = 1.36$. **Left**: relative difference between power transmission found by MMA and by FEM for radii of curvature $R^+ \in [30, 100]$ µm and different sizes of FEM mesh (black and red lines). Relative difference between power transmission found by FMA and by FEM for $R^+ \in [30, 100]$ µm with pd $= 2$, $h = \lambda_0/20$ µm (turquoise line). **Right**: first and second mode transmission calculated by FEM with pd $= 2$, $h = \lambda_0/20$ versus radii of curvature $R^+ \in [7, 60]$ µm.

The significant signal losses characterize a 90-degree bow with $R^+ < 9.9$ µm as expected. Therefore, since the MMA method does not consider radiation modes, the relative transmission difference is large for very sharp bends.

Efficiency. Table 1 shows examples of the efficiency of transmission calculations with MMA and FEM. For example, if $R^+ = 70$ µm MMA computational time is 2.1e−2 seconds.

The relative difference $\triangle T$ for various choices of mesh size h and polynomial degree pd for $R^+ = 70$ µm is: $\triangle T = 0.23\%$ for pd $= 2$, $h = \lambda_0/30$, $\triangle T = 0.37\%$ for pd $= 2$, $h = \lambda_0/20$, $\triangle T = 1.5\%$ for pd $= 2$, $h = \lambda_0/10$, $\triangle T = 0.46\%$ for pd $= 3$, $h = \lambda_0/10$, and $\triangle T = 0.33\%$ for pd $= 3$, $h = \lambda_0/20$. The relative difference with FMA is $\triangle T = 1.5\%$ for pd $= 2$, $h = \lambda_0/20$.

Therefore, for our choice of polynomial degree pd and mesh size h, the relative transmission difference between MMA and FEM is less than 1% with a calculation time of less than a second for MMA. For FMA, the difference is more than 1%.

Table 1: Comparison of computational time FEM versus MMA, 90-degree bow.

R^+ [µm]	15	30	50	70
MMA, Time [s]	2.4e−02	2.1e−02	2.2e−02	2.1e−02
FEM, pd $= 2$, $h = \lambda_0/20$, Time [s]	5.7e+01	1.1e+02	2.1e+02	2.87e+02
FEM, pd $= 3$, $h = \lambda_0/10$, Time [s]	2.5e+01	4.3e+01	7.0e+01	1.0e+02

3.2.2. Example 2: the curvature of the central trajectory of the waveguide is not constant

In construction engineering, connecting blocks with an Euler spiral as a central curve are basic junctions. For example, they are used when designing any bend in a highway. This type of waveguide junction is also studied in theoretical and applied optics and photonics [82].

The use of this example can be explained by the remarkable property of the Euler spiral – its curvature varies linearly along the curve [9]. In application to waveguide research, this means that losses due to excitation of radiation modes are lower since there are no abrupt curvature changes. Therefore, a derivative of the Euler spiral for advantageous comparison with a standard junction is also studied in the context of a 90-degree bow as a structure that provides better signal transmission [4], [52].

2D slab waveguide with varying curvature. The Euler spiral structure consists of two straight slab waveguides and a curved junction Ω_J between them, determined by an Euler spiral with a minimum radius of curvature R_J and the core width d. The waveguide has a constant thickness. The refractive indices n_{co} in the core and n_{cl} in the cladding for the vacuum wavelength λ_0 are material parameters of the structure (see Figure 25). We use the following parameter values

$$R_J \in [8, 450]\,\mu\text{m}, \quad d = 1.8\,\mu\text{m}, \quad n_{\text{co}} = 1.53, \quad n_{\text{cl}} = 1.36, \quad \lambda_0 = 1.55\,\mu\text{m}. \tag{94}$$

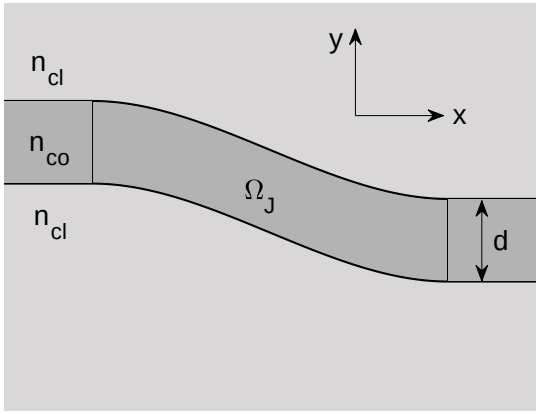

Figure 25: the geometry of a waveguide with thickness d, the minimum radius of curvature R_J, and refractive indices n_{cl}, n_{co}. The central trajectory of the junction Ω_J has a varying curvature.

Implementation details of the reference solution. For the FEM reference solution, we take mesh sizes $h = \lambda_0/(10n)$ with $n = 6$ for polynomial degree pd $= 1$, $n \in \{1, 2, 3, 4\}$ for polynomial degree pd $= 2$, and $n \in \{1, 2\}$ for pd $= 3$, to confirm the

choice of parameters that was made based on the results for the straight waveguide in Section 3.1.6.

For the Euler spiral interpolation, we use the MATLAB software package [8], which is described in detail in [9]. We use there

$$x_0 = \delta_{s_\mathrm{L}}, \quad y_0 = \mathrm{H_J}, \quad x_1 = 10\,\mu\mathrm{m}, \quad y_1 = 0\,\mu\mathrm{m}, \quad \theta_0 = \theta_1 = 0, \quad N_s = 400, \tag{95}$$

where (x_0, y_0), (x_1, y_1) are coordinates of the initial and final points, $\mathrm{H_J}$ is the height of the left offset, $0.03\,\mu\mathrm{m} \leq \mathrm{H_J} \leq 1.6\,\mu\mathrm{m}$, θ_0, θ_1 are angles of the Euler spiral at the initial and final points, N_s is number of points along the curve.

With this, we can define the central trajectory curve Γ_J of the junction Ω_J in parametric form as described in Section 2.5.3, and after applying transformation optics (67), our domain is defined as

$$\Omega_h = [0,\, L_s] \times [-L_t/2,\, L_t/2], \quad L_s = L_J + \delta_{s_\mathrm{L}} + \delta_{s_\mathrm{R}}, \tag{96}$$

where L_s is the total length related to the longitudinal propagation direction, L_J is the arclength of the junction Ω_J, and the length of the right straight part of the waveguide δ_{s_R} is adjusted such that $h = \frac{\lambda_0}{10\,n}$ holds, see Section 3.1.6.

The left offset length $\delta_{s_\mathrm{L}} = 1$ µm. L_t is the thickness in the transverse direction, $L_t > d$, and we set $L_t = 9$ µm.

For example, in case $R_J = 33.8$ µm, the computational domain is $[0,\, 18.6] \times [-4.5,\, 4.5]$. With a choice of the mesh size $h = 0.0775$ µm and quadratic finite elements $\mathrm{pd} = 2$, the domain is discretized with $N_\mathrm{cells} = 172\,800$ cells.

To truncate the computational domain, we use the PML (76) with the same parameters as in the first example (90). Since d, n_co, n_cl, λ_0 in Examples 1 (88) and 2 (94) are the same, we have eigenvalues μ_1 and μ_2 from Example 1 (88).

Results of FEM computation with $h = \lambda_0/20$, $\mathrm{pd} = 2$ for some R_J can be found in Figure 26. In the top row is the numerical solution of the waveguide field. In the bottom row is the corresponding transmission distribution between the first and second modes along the waveguide.

MMA for a waveguide with varying curvature. In the Algorithm 4 we follow formulas for MMA (62), (64), (65) and describe its application to a waveguide of constant thickness generated by a central trajectory which curvature varies along the propagation direction.

As an assumption, we approximate the straight waveguide with a waveguide of constant curvature with $R_s^+ = 1000$ µm. Therefore, R_s^+ is the largest radius of curvature in MMA. The minimum radius of curvature considered is 7 µm.

For t-maps calculation we do not take into account cases when there is a change in the sign of curvature. Hence, in implementation, we take absolute values of mean radii of curvature. As another assumption, the partition $\triangle_n : x_1 < \ldots < x_n$ is chosen such that arc length l_s of the central curve is the same for all $n-1$ waveguide segments.

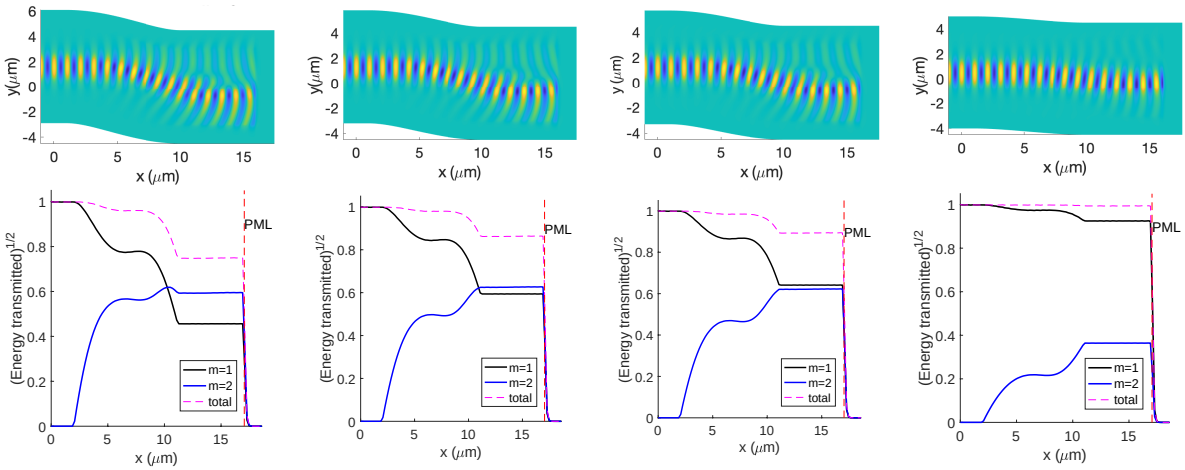

Figure 26: Euler spiral case with $d = 1.8$ µm, $\lambda_0 = 1.55$ µm, $n_{\text{co}} = 1.53$, $n_{\text{cl}} = 1.36$. **Top row**: FEM numerical solution with pd $= 2$, $h = \lambda_0/20$ µm, the minimum radius of curvature $R_J = 8.7$ µm, $R_J = 10.6$ µm, $R_J = 11.4$ µm, $R_J = 27$ µm. **Bottom row**: transmission carried by the first and second guiding modes along the direction of the light propagation; **left**: $R_J = 8.7$ µm, a significant part of the energy is dissipated; **right**: $R_J = 27$ µm, most of the energy is transmitted by the first guiding mode.

MMA versus FEM and FMA. Now, following (65) and Algorithm 4, we apply the multi-mode approximation method to this example with segment length $l_s = 1/2\pi$ µm, radii range

$$R^+ \in \{7,\, 7.1,\, \ldots,\, 10,\, 10.5,\, \ldots,\, 30,\, 35,\, \ldots,\, 200,\, 225,\, \ldots 1000\}\,\mu\text{m} \tag{97}$$

and compare the resulting relative transmission with the reference values obtained with FEM. The choice for segment length l_s is explained in Section 2.5.3.

Figure 27 top shows the relative difference in transmission for waveguides with the left offset height in the range

$$\mathrm{H_J} \in \{0.5,\, 0.6,\, \ldots,\, 1.6\}\,\mu\text{m}$$

with corresponding minimum junction radii R_J in a range

$$R_J \in \{22.5943,\, 19.3958,\, 17.0008,\, \ldots,\, 8.6889\}\,\mu\text{m}. \tag{98}$$

We see in this Figure 27 top, that the relative difference between MMA and FEM reaches 3% for $R_J \geq 12.4456$ µm.

For visual clarity, the results for pd $= 2$, $h \in \{\lambda_0/20,\, \lambda_0/30\}$ are shown, however, for pd $= 2$ with $h = \lambda_0/40$ and pd $= 3$ with $h \in \{\lambda_0/10,\, \lambda_0/20\}$ the outcome is the same.

FMA method does not reach the confidence level in this range (98) and is unreliable in it.

Algorithm 4 MMA, waveguide with varying curvature.

Given: t-maps $\mathbf{T}_{pq} = (t_{pq,ij})_{1\le i,j\le N},\ \ p,q \in \{1,2\}$

characterized by $\mathbf{I}_{R^+} = [R_1^+,\, R_2^+,\, \ldots,\, R_N^+],\ \ 7 = R_1^+ < \ldots < R_N^+ = 1000.$

Corresponding sets of propagation constants for the first and second leaky modes

$\boldsymbol{\beta}_p = [\beta_p(R_1^+),\, \beta_p(R_2^+),\, \ldots,\, \beta_p(R_N^+)],\ \ p \in \{1,2\}.$

Central trajectory coordinates $\mathbf{z} = [(x_1,\, y_1)^\top,\, \ldots,\, (x_n,\, y_n)^\top].$

1. W.r.t. partition $\triangle_n : x_1 < \ldots < x_n$ approximate central trajectory with complete cubic spline $z_{\triangle_n} \in \mathcal{C}^2([x_1, x_n])$.

2. For $\triangle_n$ with $z_{\triangle_n}$ find approximation $\boldsymbol{\kappa_n} = [\kappa_1,\, \ldots,\, \kappa_n]$ of the curvature κ of the central trajectory (58) and then

for $k = 1, 2, \ldots, n-1$ **do**

find mean curvature $\tilde{\kappa}_k$ on $[x_k,\, x_{k+1}]$.

end for

3.With the mean curvature of each segment $\tilde{\boldsymbol{\kappa}}_n$ define the mean radii of curvature $\mathbf{I}_{\tilde{R}^+} = [\tilde{R}_1^+,\, \ldots,\, \tilde{R}_{n-1}^+]$ for $n-1$ segments.

Adjust $\mathbf{I}_{\tilde{R}^+}$ to the assumptions $\max\limits_{1\le k\le n-1} |\tilde{R}_k^+| = 1000,\ \min\limits_{1\le k\le n-1} |\tilde{R}_k^+| = 7.$

4. For sorted $\mathbf{I}_{\tilde{R}^+}$ with unique elements , interpolate t-maps $\tilde{\mathbf{T}}_{pq} = (\tilde{t}_{pq,ij})_{1\le i,j\le M}$, $p,q \in \{1,2\}$, $M \le n-1$.

5. W.r.t. $\mathbf{I}_{R^+}$ and $\boldsymbol{\beta}_1$, $\boldsymbol{\beta}_2$ approximate propagation constants with cubic splines.

Define approximate $\tilde{\boldsymbol{\beta}}_p = [\tilde{\beta}_{p,1}, \ldots,\, \tilde{\beta}_{p,n-1}]$, $p \in \{1,2\}$ for the set $\mathbf{I}_{\tilde{R}^+}$.

6. **for** $k = 1, 2, \ldots, n-2$ **do**

With segment arclength $l_{s,k}$ (59) and propagation constants $\tilde{\beta}_{1,k}$, $\tilde{\beta}_{2,k}$ related to the segment k find bending transmission $\hat{\mathbf{p}}_k$ (62).

Find transition transmission $\hat{\mathbf{t}}_k$ (64) between segments k and $k+1$.

end for

7. Find total transmission $\mathbf{T}$ (65) .

Figure 28 shows the relative difference in transmission for waveguides with the left offset height $\mathrm{H_J}$ and minimum junction radii R_J in the ranges

$$\mathrm{H_J} \in \{0.03,\, 0.06,\, \ldots,\, 0.4\}\ \mu\mathrm{m}, \quad R_J \in \{450,\, 337.5,\, 270,\, 225,\, \ldots,\, 33.8\}\ \mu\mathrm{m}.$$

In Figure 28 we observe that the FMA method becomes reliable for $R_J \gtrsim 64$ µm. The absolute relative difference for FMA reaches 1% for $R_J \ge 96.5$ µm.

For the same radius value for pd = 2 with $h = \lambda_0/20$, pd = 3 with $h \in \{\lambda_0/10,\, \lambda_0/20\}$ relative difference with MMA is less the 0.5%. For pd = 2, $h = \lambda/30$ it reaches 0.1%. The corresponding transmission in dB for each method is shown in Figure 29.

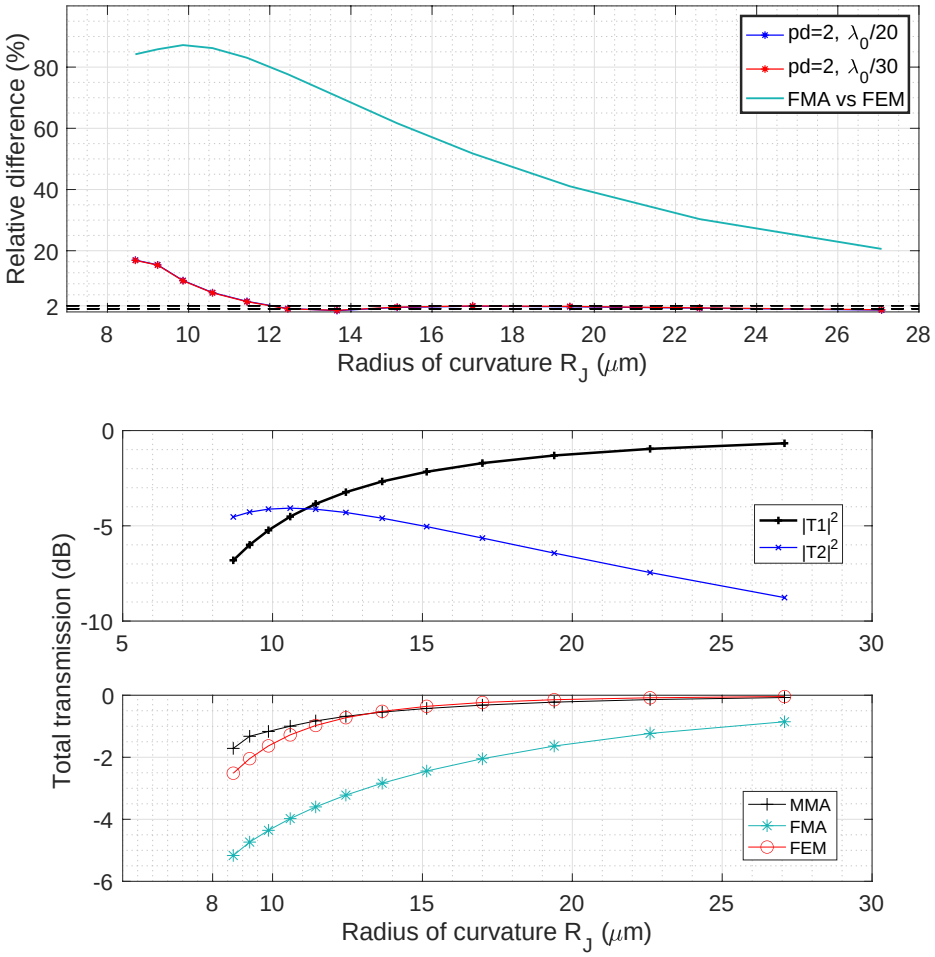

Figure 27: Euler example with $d = 1.8$ µm, $\lambda_0 = 1.55\,\mu$m, $n_{\text{co}} = 1.53$, $n_{\text{cl}} = 1.36$. **Top**: relative difference between power transmission found by MMA and by FEM for minimal junction radii of curvature $R_J \in [8.6889, 22.5943]$ µm and different sizes of FEM mesh (blue and red lines). The relative difference between power transmission found by FMA and by FEM with pd $= 2$, $h = \lambda_0/40$ µm (turquoise line). **Center**: first and second mode transmission calculated by FEM with pd $= 2$, $h = \lambda_0/40$ versus radii $R_J \in [8.6889, 22.5943]$ µm. **Bottom**: total transmission computed with MMA, FMA and FEM versus radii $R_J \in [8.6889, 22.5943]$ µm. FEM with pd $= 2$, $h = \lambda_0/40$.

Interference pattern. The Euler spiral is a good example for testing the reliability of the MMA method compared to FMA. By definition of the Euler spiral, its curvature changes linearly with its curve length. This slow change in curvature of the central trajectory allows us to observe the second mode propagation along the structure and avoid regimes, where the advantage of MMA over FMA is not so obviously observed.

For example, the *mode beating* is a regime of signal transmission in a waveguide when the interference pattern represents a redistribution of power between the guided modes in such a way, that the power dissipated on inhomogeneities is transferred not only

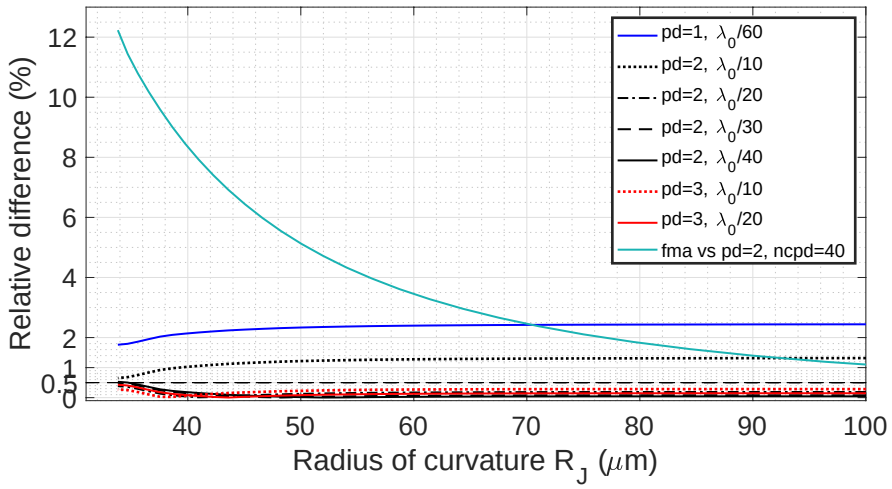

Figure 28: Euler example with $d = 1.8\mu m$, $\lambda_0 = 1.55\,\mu m$, $n_{co} = 1.53$, $n_{cl} = 1.36$. Relative difference between power transmission found by MMA and by FEM for minimal junction radii of curvature $R_J \in [33.8, 96.5]$ µm and different sizes of FEM mesh (black, blue and red lines). Relative difference between power transmission found by FMA and by FEM with pd $= 2$, $h = \lambda_0/40$ µm (turquoise line).

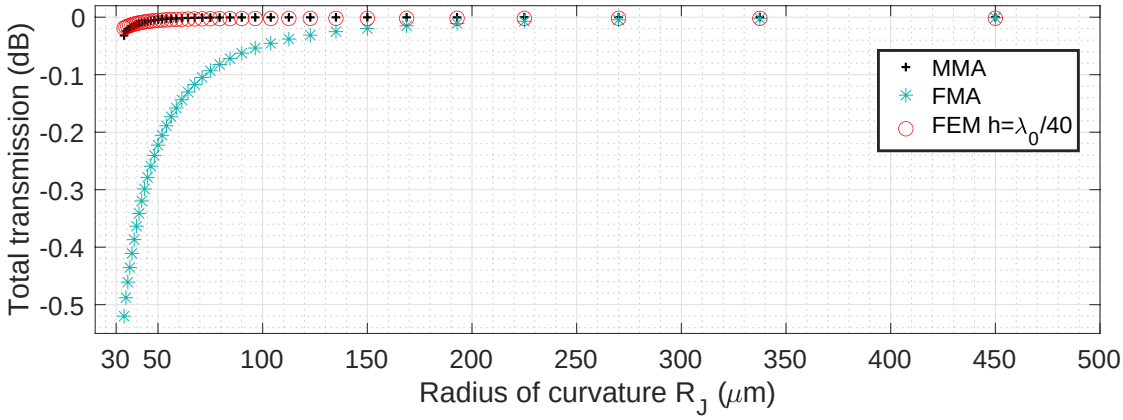

Figure 29: Euler example with $d = 1.8$ µm, $\lambda_0 = 1.55\,\mu m$, $n_{co} = 1.53$, $n_{cl} = 1.36$. Total transmission computed with MMA, FMA and FEM versus radii $R_J \in [33.8, 450]$ µm. FEM with pd $= 2$, $h = \lambda_0/40$.

into radiation power, but is also redistributed between forward and backward reflected modes, as well as leaky modes of higher orders [77]. That is, due to a sharp change in curvature, a mismatch of fields occurs, as a result, interference leads to mode *cross-talk*.

Euler waveguides are notable for the fact that even in cases of small bend radii, due to the linear change in curvature along its path length, the mode beating regime does not usually occur in them [52], [85], [20].

This can be observed for our setting. In the Figure 26, bottom row, the first guided mode, after being scattered at the junction, is transmitted further by the second mode.

At the same time, the second mode does not constantly interact with the first mode as it propagates along the core, and transfers a considerable amount of energy without coupling back into the fundamental mode.

Thus, we see a significant advantage of the MMA method over FMA in such waveguides with a clear interference pattern, as expected.

Limitations. As in the 90-degree bow Example 3.2.1, MMA has a limited range of applications in the case of redistribution of most of the transmitted power into power carried by radiation modes. With the given structure size (95) and parameters (94) MMA is not reliable for minimum junction radii $R_J \lesssim 12$ µm. This corresponds to considered Euler waveguides with height of $\mathrm{H_J} > 1.1$ µm.

Efficiency. A comparison of computational time for some Euler spiral waveguides is given in Table 2.

For MMA with arc length $l_s = 1/2\pi$, the average calculation time for one waveguide is less than one second. FEM with parameters pd $= 2$, $h = \lambda_0/20$ computes the transmission in about a minute, and FEM with parameters pd $= 3$, $h = \lambda_0/10$ in about half a minute.

The high accuracy of the MMA approximation method in the considered case makes this method quite suitable and reliable for calculating the power transmission for blocks of integration circuits in the shape generated by an Euler spiral.

Table 2: Comparison of computational time FEM versus MMA, Euler spiral.

R_J [µm]	12.4456	17.0008	33.8	450
MMA, Time [s]	6.1e−01	7.6e−01	6.1e−01	4.3e−01
FEM, pd $= 2$, $h = \lambda_0/20$, Time [s]	6.4e+01	6.6e+01	6.4e+01	6.6e+01
FEM, pd $= 3$, $h = \lambda_0/10$, Time [s]	2.8+01	2.7e+01	2.7e+01	3.1e+01

3.2.3. Example 3: central trajectories from the experiment

Waveguides have a direct practical purpose, therefore their numerical modeling in the case of shapes and parameters used in produced photonic integration circuits is of great interest. Fortunately for us, we have the opportunity to rely on real-life experimental results – as we mentioned earlier, within the framework of the CRC 1173 C4 project, an experimental study of the trajectory-dependent losses of arbitrarily shaped waveguides was done in [68]. As a result, a benchmark was obtained for a certain set of central waveguide trajectories. Namely, a series of central trajectories were modeled, and, according to this set, free-form silicone waveguides were produced with 3D printing. These free-formed junctions connect straight silicon photonic chip strip waveguides. The signal is sent using a laser from one end and the transmission is measured at the other end of the structure. A photo of the set of waveguides from the experiment is shown in Figure 30.

In this section, we compare the transmission corresponding to the 2D experimental trajectories obtained, as in Examples 3.2.1 and 3.2.2, with the finite element method and MMA method based on semi-analytical solutions. We will show that both of these methods show a local minimum in transmission that is characteristic of this benchmark.

This simplification and consideration of 2D slab waveguides instead of 3D free-formed structures is possible since the waveguides in the real-life experiment from [68] have a constant thickness and height. That is, there are no twists and the bending is in one direction. The key role of 2D results for 3D problem regarding waveguides of constant height and width can be found, for example, in [78] and [47], where the identity of 2D and 3D formalisms is used.

Setting. The structure consists of two straight slab waveguides connected by a curved junction Ω_J, which is defined by one of the central trajectories. Coordinates of these 2D trajectories set, including cases corresponding to the benchmark from the experiment, were kindly provided by M.Sc.Maria Paszkiewicz from the CRC 1173 C4 project.

We will call the waveguide generated by such curves as *hump*. Examples of some central curves are presented in Figure 30, where it can be seen that the humps in this case are characterized not only by the height $\mathrm{H_J}$ but also by different shapes.

As in previous examples, the waveguide has a constant thickness d, refractive indices n_{co} in the core and n_{cl} in the cladding, vacuum wavelength λ_0. The parameter values also correspond to the experiment [68]

$$6.7\,\mu\mathrm{m} \le \mathrm{H_J} \le 16\,\mu\mathrm{m}, \quad d = 1.8\,\mu\mathrm{m}, \quad n_{\mathrm{co}} = 1.53, \quad n_{\mathrm{cl}} = 1.36, \quad \lambda_0 = 1.55\,\mu\mathrm{m}. \tag{99}$$

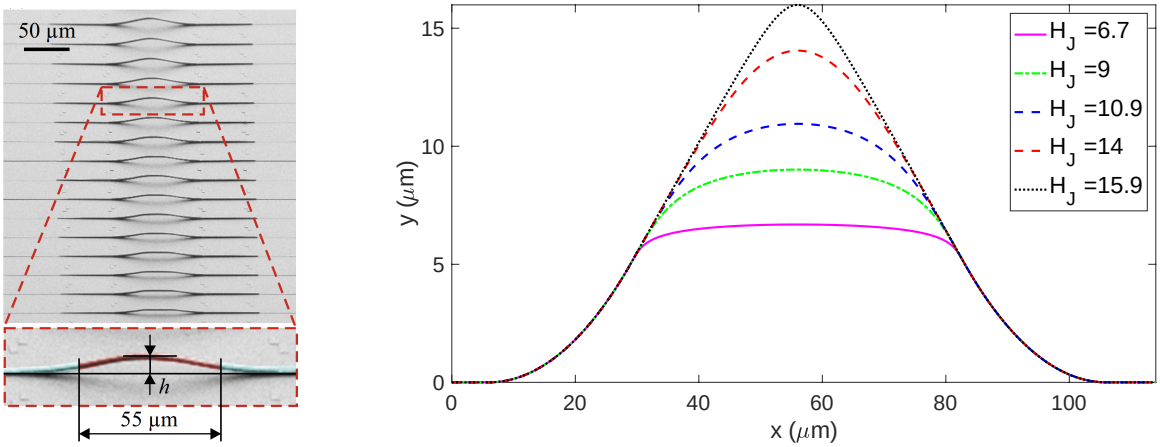

Figure 30: Experimental setup. **Left**: series of freeform waveguides fabricated on a silicon photonic chip. The image was taken with a scanning electron microscope. Here h denotes the apex height of a trajectory; notation and figure are taken from [68]. **Right**: examples of several central trajectories on one plot corresponding to humps of different shapes with heights $\mathrm{H_J} \in \{6.7, 9, 10.9, 14, 15.9\}$ µm.

Implementation details of the reference solution. To obtain the FEM reference solution, we take mesh sizes $h = \frac{\lambda_0}{10\,n}$ with $n = 2$ for polynomial degree pd $= 2$ and $n = 1$ for pd $= 3$.

We use cubic spline interpolation to the given central trajectory coordinates and define the central curve Γ_J of the junction Ω_J with the natural parametrization (60). Next, after transformation optics (67) application, the domain Ω_h is defined as in the previous example (96), where the width L_t in the transversal direction and the left offset δ_{s_L} also take the values

$$L_t = 9\,\mu\mathrm{m}, \quad \delta_{s_\mathrm{L}} = 1\,\mu\mathrm{m}$$

and the right offset δ_{s_R} is adjusted s.th. wavelength λ_0 is the multiple of mesh size h.

We apply PML (76) with parameters defined in the first example (90). The given eigenvalues μ_1 and μ_2 correspond to parameters d, n_{co}, n_{cl}, λ_0 defined above (99).

Depending on the trajectory, the total length L_s in propagation direction takes values from $L_s = 116.25$ µm to $L_s = 120.9$ µm. Then for pd $= 3$, $h = 0.155$ µm, the number of unknowns is about 1 240 000, and for pd $= 2$, $h = 0.0775$ µm, it is about 2 200 000.

Examples of FEM simulations with $h = \lambda_0/10$, pd $= 3$ for two trajectories from the experimental setting can be found in Figure 31. In the top and central rows is the computed magnitude of the field for humps with apex heights $\mathrm{H_J} = 9.9$ µm and $\mathrm{H_J} = 11.8$ µm. In the bottom row is the related transmission distribution between the first and second modes along the propagation direction x.

Let us recall that the signal is transmitted from left to right and consider the interference of the first and second modes in a waveguide with a height of $\mathrm{H_J} = 9.9$ µm. As can be seen in the bottom left Figure 31, the fundamental mode, having passed the straight section of the waveguide, encounters a junction Ω_J, which causes only a slight transmitted energy loss due to a smooth transition between straight and curved waveguide parts. We also observe the emergence of a second mode for $x > \delta_{s_\mathrm{L}}$. Then, due to a significant change in curvature in $x = 32$ µm, the second mode is excited stronger, and part of the transmitted energy is dissipated.

This also corresponds to oscillations, which can be observed in top Figure 31 with the computed field amplitude for 32 µm $< x <$ 72 µm. Further, for $x \geq 72$ µm, the second mode fades away, and most of the remaining energy is transferred by the first mode.

Similar oscillations were described for the waveguides with $\mathrm{H_J} = 9.54$ µm in [68] and [73], where numerical simulations were done for the 3D hump. We also can, in addition to the numerical results for the field amplitude, observe this mode interaction through the calculation of the energy transmitted by first and second guided modes along the waveguide, as we described above.

MMA versus FEM and FMA. Now we will compare the results of the transmission power calculation obtained via FEM, MMA, and FMA for a series of waveguides with the trajectories from the setting.

For MMA and FMA applications, we follow formulas (65) and Algorithm 4. Each curve from the given trajectory set is discretized such that the arc length of each segment

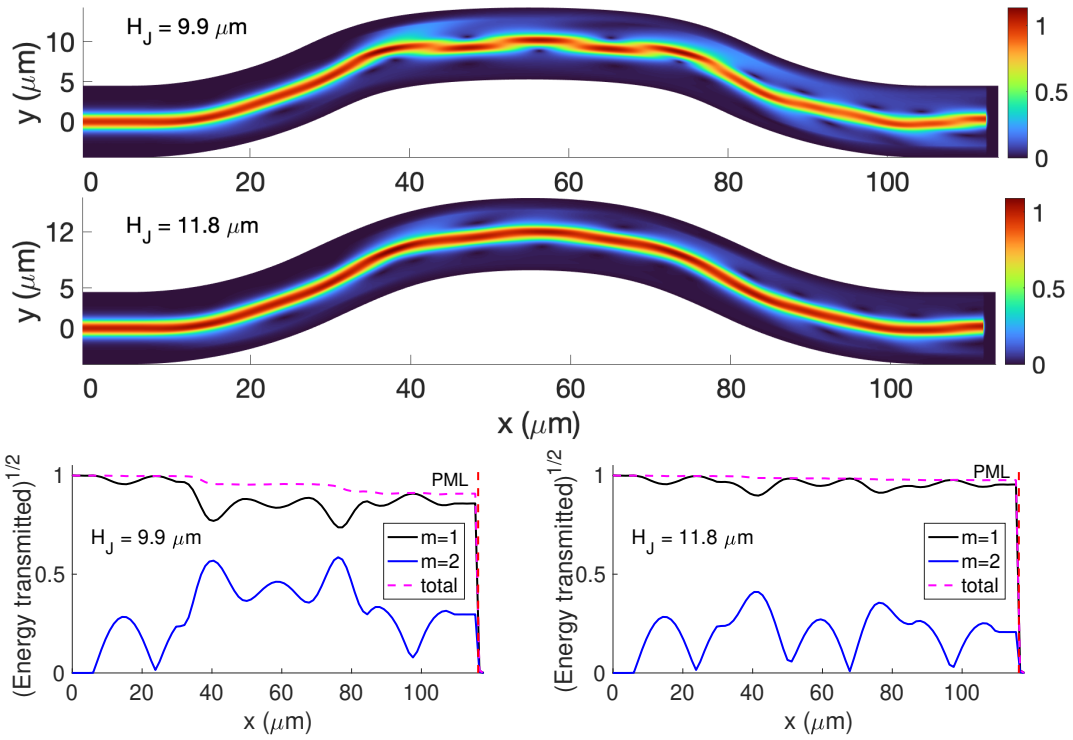

Figure 31: Hump example with $d = 1.8$ µm, $\lambda_0 = 1.55\,\mu\text{m}$, $n_{\text{co}} = 1.53$, $n_{\text{cl}} = 1.36$. Central trajectories from the experimental setting. **Top and Center**: magnitude of the field obtained with FEM with pd $= 3$, $h = \lambda_0/10$ µm for humps with apex height $\text{H}_\text{J} = 9.9$ µm and $\text{H}_\text{J} = 11.8$ µm. **Bottom row**: transmission obtained with FEM carried by the first (black line) and second (blue line) guiding modes along the direction of the light propagation x. The start of the PML region in x direction is indicated by the red dashed line; **Left**: for hump with apex height $\text{H}_\text{J} = 9.9$ µm; **Right**: for hump with apex height $\text{H}_\text{J} = 11.8$ µm.

is $l_s = \frac{1}{2\pi}$. The remark about the choice of segment length can be found in Section 2.5.3. Radii set for pre-calculated t-maps $\mathbf{T}_{11}$, $\mathbf{T}_{12}$, $\mathbf{T}_{21}$, $\mathbf{T}_{22}$ is again

$$\mathbf{I}_{R^+} = \{7,\, 7.1,\, \ldots,\, 10,\, 10.5,\, \ldots,\, 30,\, 35,\, \ldots,\, 200,\, 225,\, \ldots 1000\}\,\mu\text{m}.$$

Hence, mean radius of curvature for each segment $\tilde{R}^+$ should not take values outside the range $7\,\mu\text{m} \leq \tilde{R}^+ \leq 1000\,\mu\text{m}$.

Figure 32 shows the transmission power computed for a sequence of trajectories from the experimental setup by three methods: FEM with pd $= 2$, $h = \lambda_0/20$, MMA, and FMA. FEM with pd $= 3$, $h = \lambda_0/10$ is also given to compare the choice of parameters for the reference solution simulation.

The losses in a waveguide from the setting with constant thickness d, fixed refractive indices $n_{\text{co}}, n_{\text{cl}}$, and wavelength λ_0 depend on the curvature of the central trajectories. An abrupt change of curvature can lead to significant interference of the fundamental

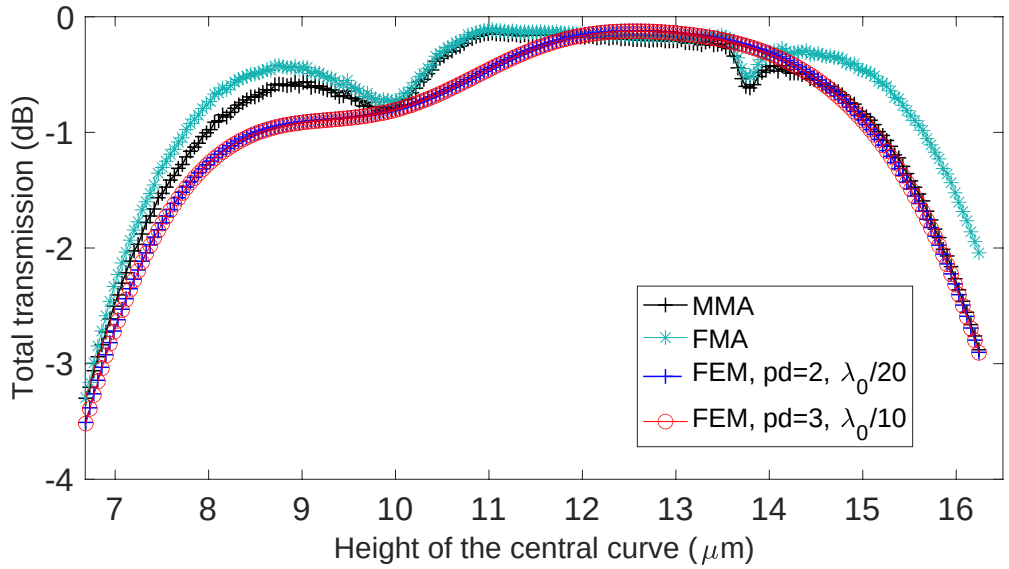

Figure 32: Power transmission computed with MMA, FMA, and FEM for series of humps with 223 central trajectories from the experimental setting versus humps apex height H_J. Waveguides parameters are $d = 1.8$ µm, $\lambda_0 = 1.55$ µm, $n_{co} = 1.53$, $n_{cl} = 1.36$. FEM with pd $= 2$, $h = \lambda_0/20$ and pd $= 3$, $h = \lambda_0/10$. For MMA and FMA, the arclength of a segment is $l = 1/2\pi$. Local transmission minimum for a trajectory with a height of about $H_J = 10$ µm.

mode with the radiation modes in the case of very sharp bends.

Consider, for example, one of the highest humps $H_J = 15.9$ µm from the experiment. For such a waveguide shape, the transmission calculated with FEM is 0.591 (or -2.28 dB) and MMA is 0.594 (or -2.26 dB). That is, about 60% of the signal is transmitted along such a waveguide, and the losses are explained by the sharp bend at the top of the hump (see Figure 30, black line). There, the minimum mean radius of curvature is $\tilde{R}^+ = 10.8$ µm, see Figure 33, right top.

As we can see in Figure 33, right bottom, from the interaction of the first and second guided modes, the transmission decreases when approaching the point on x axes related to the apex of this hump, while the amount of energy transmitted by the second mode increases. Then, propagating away from this point, a part of the transmitted energy remaining after dissipation is decoupled back into the fundamental mode and is carried mainly by the first mode. We can assume that for this case, the interference pattern is clear, therefore the power transmission calculated by MMA and FEM are in good agreement.

Now consider a waveguide with a smooth change in curvature. For the trajectory with $H_J = 12.1$ µm, the minimum mean radius of curvature is $\tilde{R}^+ = 41.8$ µm, see Figure 33, left top. For this hump, most of the energy is transferred by the first mode, and there is practically no interference with the second mode, as we can see in Figure 33, left

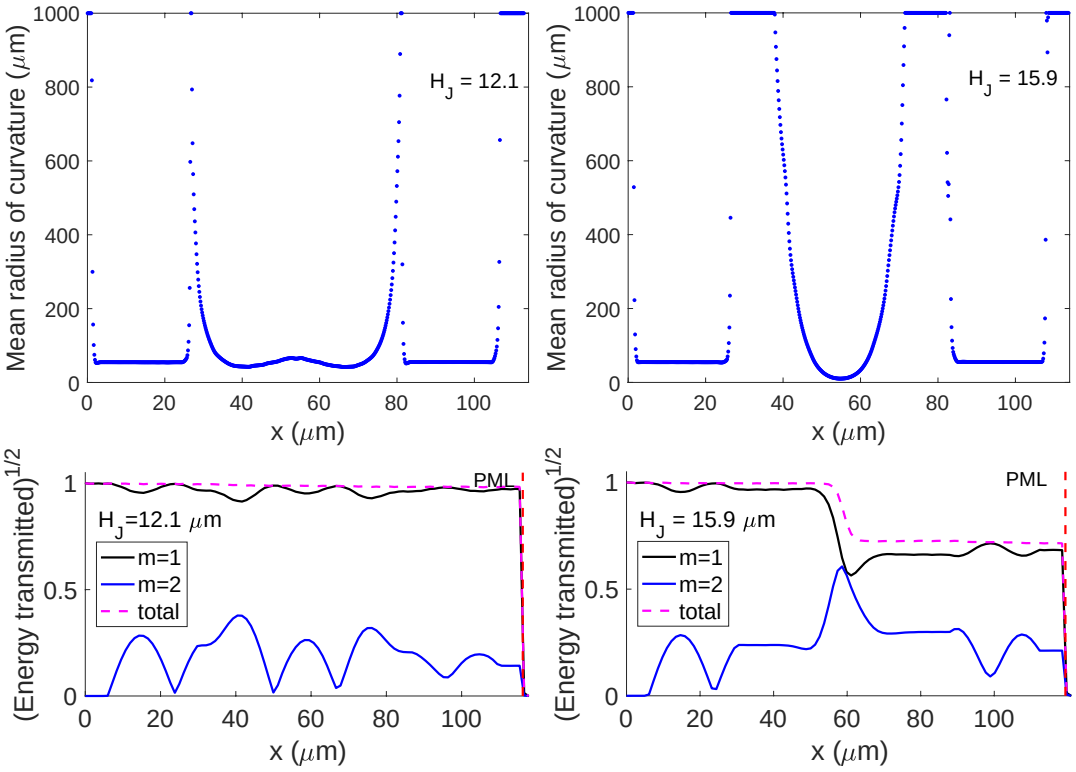

Figure 33: **Top row**: Absolute values of mean radii of curvature $\tilde{R}^+$ of a central waveguide's trajectory from Example 3.2.3 against the longitudinal direction of propagation x, µm; **Left**: trajectory with maximum apex height $H_J = 12.1$ µm and $\min \tilde{R}^+ = 41.8$ µm; **Right**: trajectory with maximum apex height $H_J = 15.9$ µm and $\min \tilde{R}^+ = 10.8$ µm. **Bottom row**: Computed with FEM pd $= 3$, $h = \lambda_0/10$ transmission carried by the first and second guiding modes along the direction of the light propagation; **Left**: the central curve with maximum apex height $H_J = 12.1$ µm; **Right**: trajectory with maximum apex height $H_J = 15.9$ µm

bottom. In this hump, there are no sharp bends and radiation losses are small, therefore most of the signal is transmitted along it. This corresponds to the transmission values obtained by FEM 0.9673 (or −0.145 dB) and MMA 0.9605 (or −0.183 dB).

Both methods show good agreement for this trajectory. An example of field visualization for a waveguide with a smooth change in curvature and low losses can be found in Figure 31, center.

Now let us have a look at a waveguide with a more complex interference pattern. In the experimental setting, some trajectories have such curvature that the signal propagates in the modes beating regime, which was discussed in the previous example as well, see Section 3.2.2.

In [68], the local minimum near $H_J = 10$ µm is explained by this regime. We can also observe this interference pattern for the corresponding trajectory with $H_J = 9.9$ µm. See Figure 31 for visualization of the mode beating field and interaction of the

transmission of the 1st and 2nd guided modes.

Previously, it was assumed [68] that due to the occurrence of the second mode, the FMA method may not indicate this local minimum. In the case of FMA calculated with the semi-analytical t-map for 2D waveguides, the method indicates this transmission drop. A similar regime of mode beating holds in neighboring trajectories, where the agreement between FEM and MMA and FMA is less than in the local minimum, see Figure 34. From this, we assume that for the beating regime for trajectories of a certain curvature, the interaction between the 1st and 2nd modes utilized in the MMA method is not sufficient, since, due to the emerging interferential pattern, it is necessary to take into account the interaction with the resulting higher order modes and radiation modes.

Although FMA also shows a local minimum near $H_J = 10$ µm, MMA more accurately approximates the transmission. At the point of this local minimum, the relative difference with FEM, pd $= 3$ is less than 0.5%, and with FMA more than 1.5%. For trajectories with a sharp apex, the difference with FMA reaches 22%, and for MMA, it is less than 1%.

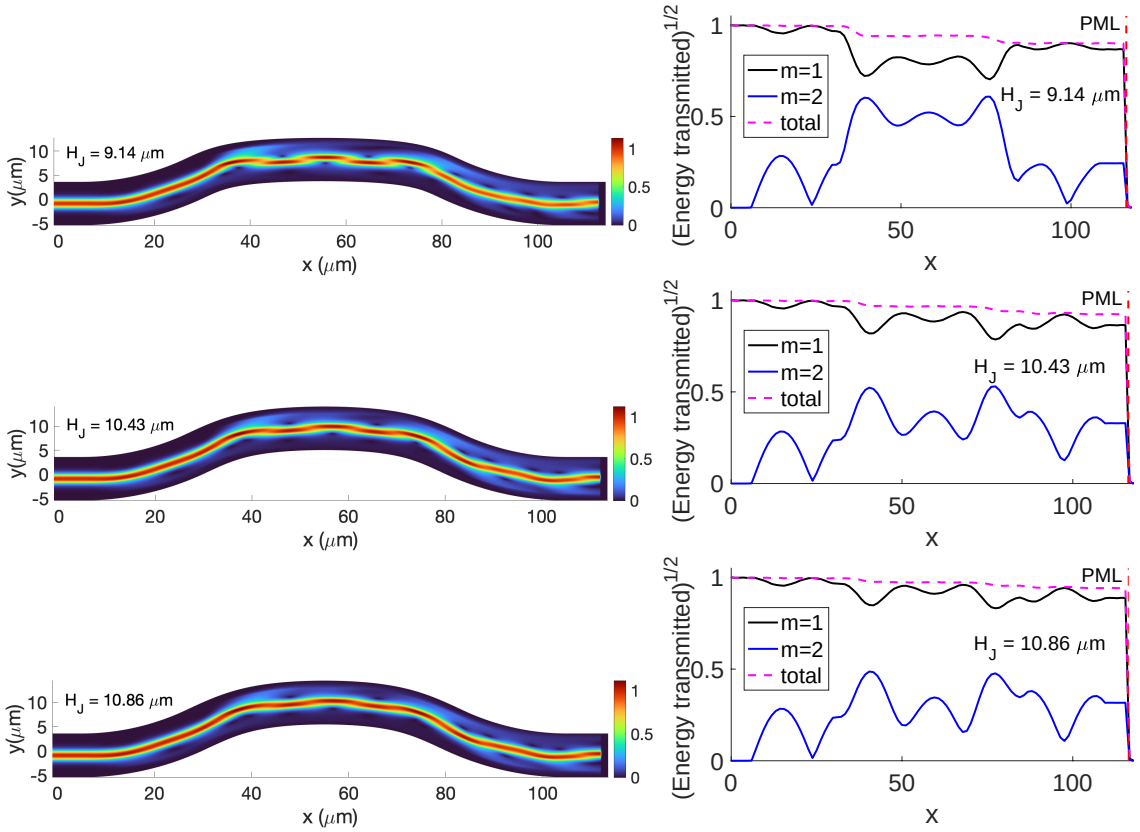

Figure 34: Mode beating regime in humps from the experimental setting with $H_J \in \{9.14, 10.43, 10.86\}$ µm. **Left column**: magnitude of the field, FEM with pd $= 3$, $h = \lambda_0/10$. **Right column**: corresponding mode interaction between 1st and 2nd mode.

Limitations. The reliable application of the MMA approximation method for mode beating requires further research and an introduction of additional limiting assumptions. For example, in [77], the beating regime is also considered as a special case in the description of the local modes approximation method. There, to ensure sufficient accuracy of approximation by local modes, they introduce a restriction on changes in waveguide parameters, for example, depending on the difference in the propagation constants of each mode.

At the same time, as we can see from the Euler spiral case and some trajectories from the experimental setting, in the absence of a mode-beating regime, MMA is a reliable and more accurate approximation method than FMA for a waveguide supporting more than one mode.

Efficiency. Based on the fact that the transmission power calculated by FEM with pd $= 3$, $h = \lambda_0/10$ is in excellent agreement with the choice pd $= 2$, $h = \lambda_0/20$ (see Figure 32), we will compare the transmission calculation time with more advantageous option, i.e. cubic finite elements pd $= 3$, mesh size $h = \lambda_0/10$.

Figure 35 shows the calculation time in seconds for each hump from the experimental setting. The computational time using FEM for each waveguide is about 155 seconds (for about 1 240 000 unknowns). The MMA method requires about 1.5 seconds for each trajectory from the considered example.

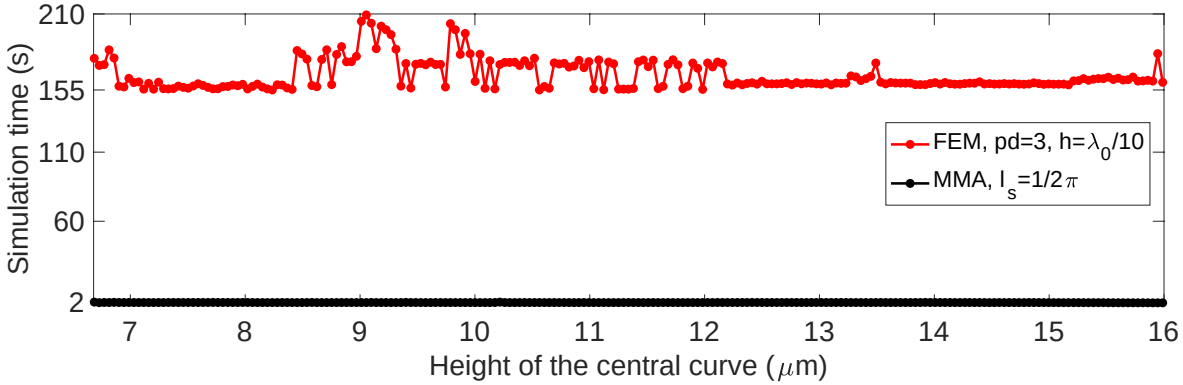

Figure 35: Comparison of computational time FEM versus MMA, central trajectories from the experiment.

Because of its execution speed, the MMA method is well suited for optimizing the shape of a waveguide with constant width, see Section 5.2.3.

4. Thin waveguide model problem

The structures that we study in this work are planar waveguides of uniform width generated by central curves Γ with compact support. Furthermore, these are waveguides which length is much larger than their thickness. Similar objects have been studied in the field of *quantum waveguides*, starting with [35], [31], where the norm resolvent convergence of the Dirichlet Laplacian on a domain with a scaled cross-section was shown when its width tends to zero. The smoothness of the curve is assumed to be $\Gamma \in \mathcal{C}^4$.

3D-1D reduction analysis is carried out in work [14] for the scaled Laplace operator with the Dirichlet conditions on the entire boundary of a thin tube. It showed that the original problem without potential, when the cross-section is shrinking, becomes a problem determined by the 1D operator on the central curve, where the potential, besides the curvature, includes a component of possible twisting. There, the weaker regularity condition for the central curve $\Gamma \in \mathcal{C}^3$ is assumed, and convergence in the strong resolvent sense was shown.

In [2], a quantum waveguide is approximated by a *quantum graph* – a geometric graph with a differential operator specified on it. They consider 2D-1D convergence at its vertices for the Laplace operator with the Dirichlet conditions on the cladding of a waveguide, which is infinite in the longitudinal direction. The quantum graph that approximates such a quantum waveguide is represented by a vertex corresponding to a junction located between two infinitely straight parts. The central curve is assumed to be $\Gamma \in \mathcal{C}^4$ piecewise.

Despite the fact that interest in this topic has been going on for several decades, due to the need to use non-standard methods of modern operator theory, examples of practical applications of quantum waveguides are mainly heuristic [56]. We focused in this interdisciplinary work on developing simplified and efficient methods for transmission computation in waveguides with parameters corresponding to real-life structures. Therefore, we do not prove here a convergence result similar to [2].

We will present in this section the methodology, which consists of a 1D reduction model of thin planar 2D waveguide based on works [14] and [2]. We consider the result as a heuristic initial assumption for effective optimization of signal transmission in curved real-life-sized structures.

4.1. Quantum waveguide

Consider a curved planar strip $\Omega \subset \mathbb{R}^2$ of constant width d. We want to change the variables in the same manner as in Section 3.1.1 and define points (x, y) of the strip Ω in the curvilinear coordinates $(s, t) \in \mathbb{R} \times [-d/2, d/2]$ with

$$x(s,t) = \gamma_1(s) - t\,\gamma_2'(s), \qquad y(s,t) = \gamma_2(s) + t\,\gamma_1'(s), \tag{100}$$

where γ_1 and γ_2 are smooth functions that characterize the central curve of the strip $\Gamma = \{\big(\gamma_1(s), \gamma_2(s)\big),\ s \in \mathbb{R}\}$. We assume the natural parametrization (69) of the curve Γ, that is s is the arclength of Γ. Furthermore, we assume that Γ is $\mathcal{C}^4$ piecewise smooth

curve, which curvature has compact support. Hence, Γ is represented by infinitely straight lines outside the support.

We denote with κ the signed curvature (70) of Γ and assume that the thickness d is small enough such that $\sup_s |\kappa(s)|\, d/2 < 1$ is satisfied, to ensure that the curvature $\kappa_\Omega(s,\, t) := |\kappa(s)|\big(\,|1 + t\,\kappa(s)|\,\big)^{-1}$ of a curve inside the strip at a point $(s,\, t)$ for fixed t is defined. The Jacobian of the coordinate transformation $\mathbb{R} \times [-d/2,\, d/2] \to \mathbb{R}^2$ (100) is

$$\mathrm{J}_{x,y}(s,t) := \begin{bmatrix} \gamma_1' - t\gamma_2'' & -\gamma_2'' \\ \gamma_2' + t\gamma_1'' & \gamma_1' \end{bmatrix}$$

with $\det \mathrm{J}_{x,y} = 1 + t\,\kappa(s)$.

Such Ω-type structures described above are called quantum waveguides. Let us consider the motion of a free particle along such a waveguide, which is described with the Hamiltonian without a potential. For effective mass chosen such that $\hbar = 2m = 1$ and Dirichlet boundary conditions at $\partial\Omega$ the Hamiltonian in this case is the Dirichlet Laplacian $-\Delta_\Omega^D$ in $L^2(\Omega)$.

The following result [35], [31] shows that $-\Delta_\Omega^D$ in quantum waveguide after the transition to the curvilinear coordinates is unitarily equivalent to Hamiltonian with a potential.

Theorem 4.1. *Let the central curve Γ of a planar quantum waveguide Ω be $\mathcal{C}^4$ piecewise smooth without intersections, which curvature κ is bounded $\|\kappa\|_{L^\infty(\mathbb{R})} < \infty$ and has compact support. Let $g(s,t) := \Gamma(s) + t\mathrm{N}(s)$, where $\mathrm{N} := \Gamma''/\|\Gamma''\|_{\mathbb{R}^2}$ denotes the normal to the central curve. Then the operator $-\Delta_\Omega^D$ in $L^2(\Omega)$ under the transformation $U\,v := (1 + t\,\kappa)^{\frac{1}{2}} v \circ g$ is unitarily equivalent to Friedrichs extension of the following operator*

$$H_0\, v := -\frac{\partial}{\partial s}\Big(\big(1 + t\kappa(s)\big)^{-2}\frac{\partial v}{\partial s}\Big) - \frac{\partial^2 v}{\partial t^2} + V(s,t)\, v, \qquad s \in \mathbb{R},\ t \in (-d/2,\, d/2) \quad (101)$$

with

$$V(s,t) = -\frac{1}{4}\frac{\kappa(s)^2}{\big(1 + t\kappa(s)\big)^2} + \frac{1}{2}\frac{t\kappa''(s)}{\big(1 + t\kappa(s)\big)^3} - \frac{5}{4}\frac{t^2\big(\kappa'(s)\big)^2}{\big(1 + t\kappa(s)\big)^4}$$

for any $v \in D(H_0) := \big\{v \in L^2(\mathbb{R} \times [-d/2,\, d/2]) :\ H_0 v \in L^2(\mathbb{R} \times [-d/2,\, d/2]),$
$v \in \mathcal{C}^\infty(\mathbb{R} \times [-d/2,\, d/2]),\ v(s,\, d/2) = v(s,\, -d/2) = 0\big\}.$

Proof. See Theorem 3.1 in [35]. □

We rescale the quantum waveguide in the transverse direction by setting thickness equal to $\varepsilon^{-1}d,\ \varepsilon > 0$ and with (101) for $t = \varepsilon\,\xi,\ \xi \in (-1/2,\, 1/2)$ we obtain

$$H_{0\varepsilon} := -\frac{\partial}{\partial s}\Big(\big(1 + \varepsilon\xi\,\kappa(s)\big)^{-2}\frac{\partial}{\partial s}\Big) - \frac{1}{\varepsilon^2}\frac{\partial^2}{\partial \xi^2} + V_\varepsilon(s,\xi)\,, \qquad s \in \mathbb{R},\ \xi \in (-1/2,\, 1/2)$$

with the rescaled potential

$$V_\varepsilon(s,\xi) = -\frac{1}{4}\frac{\kappa(s)^2}{\big(1 + \varepsilon\xi\kappa(s)\big)^2} + \frac{1}{2}\frac{\varepsilon\xi\kappa''(s)}{\big(1 + \varepsilon\xi\kappa(s)\big)^3} - \frac{5}{4}\frac{\varepsilon^2\xi^2\big(\kappa'(s)\big)^2}{\big(1 + \varepsilon\xi\kappa(s)\big)^4}.$$

We assume that for small $\varepsilon > 0$ we can consider the following approximation

$$H_{0\varepsilon} \approx \widetilde{H}_{0\varepsilon} := -\frac{\partial^2}{\partial s^2} - \frac{1}{\varepsilon^2}\frac{\partial^2}{\partial \xi^2} - \frac{1}{4}\kappa^2(s), \qquad s \in \mathbb{R},\ \xi \in (-1/2, 1/2). \tag{102}$$

Next, we consider the properties of the spectrum of a quantum waveguide, additionally bounded in the direction of signal propagation and equipped with Dirichlet boundary conditions. We report the result [14] for the quantum waveguide $\Omega \subset \mathbb{R}^3$ bounded in the transverse and longitudinal directions adapted to our case of study in the current section. The central simple $\mathcal{C}^3$ curve Γ parametrized by the arclength s is given by $\Gamma\colon [0, L] \to \mathbb{R}^3$.

We assume that Γ has zero torsion and bounded curvature $\kappa\colon [0, L] \to \mathbb{R}$, $\kappa \in L^\infty(0, L)$, $\Gamma' = \kappa N$, $N' = -\kappa T$, where N, B are are the components of the Frenet frame $(T,\, N,\, B)$ [30] with the tangent vector $T := \Gamma'$, the normal unit vector $N := T'/\|T'\|_{\mathbb{R}^3}$ and the binormal unit vector $B := T \times N$.

Then the quantum waveguide with cross-section $\omega \subset \mathbb{R}^2$ parameterized by the small $\varepsilon > 0$ generated via the central curve Γ is defined as

$$\Omega_\varepsilon := \{\Gamma(s) + \varepsilon\, t_1 N + \varepsilon\, t_2 B,\ s \in [0, L],\ t = (t_1,\, t_2) \in \omega\}. \tag{103}$$

Theorem 4.2. *Let the sequence of the quantum waveguides $\Omega_\varepsilon \subset \mathbb{R}^3$ for a cross-section parameter $\varepsilon > 0$ be defined with (103).*

(i) The eigenvalues associated with the problem

$$-\Delta u_\varepsilon = \lambda^\varepsilon u_\varepsilon, \quad u_\varepsilon \in H_0^1(\Omega_\varepsilon) \tag{104}$$

have the following asymptotical behavior

$$\lambda_m^\varepsilon = \frac{\lambda_1}{\varepsilon^2} + \mu_m + r(\varepsilon), \quad \lim_{\varepsilon \to 0} r(\varepsilon) = 0, \tag{105}$$

where μ_m, $m \in \mathbb{N}$ are the eigenvalues of the one-dimensional Sturm-Liouville problem

$$-\varphi'' - \frac{\kappa(s)^2}{4}\varphi = \mu\varphi, \quad \varphi \in H_0^1(0, L) \tag{106}$$

and λ_1 is the first eigenvalue on the cross-section $\omega \subset \mathbb{R}^2$ associated with the problem $-\Delta\theta_1 = \lambda_1\theta_1$, $\theta_1 \in H_0^1(\omega)$, $\|\theta_1\|_{L^2(\omega)} = 1$.

(ii) Let u_m^ε be a normalized eigenfunction of the problem (104) and λ_m^ε the related eigenvalue. Let $g_\varepsilon\colon [0, L] \times \omega \to \Omega_\varepsilon$, $g_\varepsilon(s, t) := \Gamma(s) + \varepsilon\, t_1 N + \varepsilon\, t_2 B$. Then $v_m^\varepsilon := u_m^\varepsilon \circ g_\varepsilon$ converges strongly in $L^2(\omega \times (0, L))$ to $v_m(s, t) = \varphi_m(s)\theta_1(t)$, where φ_m is the eigenfunction of the problem (106) associated with the eigenvalue μ_m, $\|\varphi_m\|_{L^2(0,L)} = 1$. Vice versa, any such v_m is the limit of the sequence $u_m^\varepsilon \circ g_\varepsilon$ where u_ε is an eigenfunction of the problem (104) associated with λ_m^ε.

Proof. See Theorem 4.4 and Theorem 3.1 in [14]. □

Remark: In the general case of Theorem 4.2, torsion is taken into account, see Theorem 4.4 in [14]. As a result, the 3D problem without a potential in the interior of the domain can be approximated with the 1D problem. There the particle sees the curvature and torsion as the following potential $q \in L^\infty(0, L)$

$$q(s) := \big(\tau(s) + \alpha'(s)\big)^2 C(\omega) - \frac{1}{4}\kappa(s)^2,$$

where $\alpha(s)$ is rotation angle, $\tau \in L^\infty(0, L)$ is a torsion, $C(\omega) := \int_\omega |\nabla_t \theta_1 \cdot Rt|^2 \, \mathrm{d}t$ is the geometrical parameter, R is the radius of the cross-section ω. In the case without torsion, the effective potential is $q(s) = -\frac{1}{4}\kappa(s)^2$ (106).

For example, consider the case when ω is a circle of constant curvature $\kappa = 1/R$, then $C(\omega) = 0$. By Theorem (4.2) we have in the longitudinal direction

$$\begin{aligned} -\varphi''(s) - \frac{1}{4}\kappa^2 \varphi(s) &= \mu\varphi(s) \qquad \text{for } s \in (0, L), \\ \varphi(0) = \varphi(L) &= 0. \end{aligned} \tag{107}$$

The Dirichlet Laplacian has eigenvalues $(m\pi/L)^2$ on $(0, L)$ for $m \in \mathbb{N}$, hence it holds $\mu_m = (m\pi/L)^2 - \frac{1}{4}\kappa^2$. The eigenvalues thus satisfy

$$\lambda_m^\varepsilon = \frac{\lambda_1}{\varepsilon^2} + \left(\frac{m\pi}{L}\right)^2 - \frac{1}{4}\kappa^2 \qquad \text{for } \varepsilon \to 0.$$

In the next sections, we apply the adapted from the field of quantum waveguides operator (102) in the context of closed waveguides.

4.2. Closed planar waveguide

We define the closed waveguide $\Omega \subset \mathbb{R}^2$ in the same manner as the quantum waveguide, namely Ω is a curved planar strip of finite width d small enough generated by the central curve Γ which has no self-intersections. The curvature of the central curve Γ has compact support $\mathrm{supp}(\kappa) \subset [x_L, x_R]$, $x_L, x_R \in \mathbb{R}$.

The signal propagation in such a structure is described via the scattering problem of a given incoming right-going wave u^{inc} at the junction of two semi-infinite straight waveguide parts

$$\begin{cases} -\Delta u - k^2 u &= 0 & \text{in } \Omega, \\ u &= 0 & \text{on the cladding}, \\ u - u^{\mathrm{inc}} & \text{is left-going} & \text{for } x \le x_{\mathrm{L}}, \\ u & \text{is right-going} & \text{for } x \ge x_{\mathrm{R}}, \end{cases} \tag{108}$$

with the given wave number $k = k_0 n_{\mathrm{co}}$, $k \in \mathbb{R}$, refractive index n_{co}, and $k_0 = 2\pi/\lambda_0$ for a wavelength λ_0.

The closed waveguide has the unbounded longitudinal direction of propagation x and is bounded in the transverse direction y. Unlike the other scattering problem at the junction of the open waveguide (66), here, the field is concentrated only in the core which is bounded by the cladding equipped with the Dirichlet boundary condition.

In this case, extensive studies of well-posedness have been conducted (see e.g. [71] and literature in it), and existence and uniqueness are ensured due to the radiation condition determined using the DtN operator on the transverse sections $\{x_{\mathrm{L,R}}\} \times I_y$, $I_y := (-d/2,\, d/2)$.

Radiation condition. In order to construct the condition for the outgoing wave at the junction interfaces $\{x_{\mathrm{L,R}}\} \times I_y$, in the same manner as in Section 3.1.3, we consider semi-infinite left and right parts of the closed waveguide $\Omega \subset \mathbb{R}^2$, which are straight waveguides $(-\infty, x_{\mathrm{L}}] \times I_y$ and $[x_{\mathrm{R}}, \infty) \times I_y$.

Applying separation of variables to the leading equation $-\Delta u - k^2 u = 0$, we obtain, on the one hand, the equation $u_1'' - \lambda u_1 = 0$ in the longitudinal direction x, the solution of which is a linear combination of $\mathrm{e}^{\pm \mathrm{i}\beta x}$, where β is the longitudinal propagation constant.

On the other hand, we obtain the equation $-u_2'' - k^2 u_2 = \lambda u_2$, $y \in I_y$ on the cross-section of the closed waveguide $u(x, -d/2) = u(x, d/2) = 0$. We can define the corresponding transverse operator $A^D v := -v'' - k^2 v$, for any $v \in D(A^D) := H^2(I_t) \cap H_0^1(I_t)$, which is a self-adjoint with a compact resolvent.

The associated eigenfunctions $\Phi_m \in D(A^D)$, $\Phi_m(y) = 1/\sqrt{2} \sin(m\pi y/d)$ form a complete orthonormal system $(\Phi_m)_{m\in\mathbb{N}}$ in $L^2(I_y)$. The eigenvalues related to the operator A^D are $\lambda_m = -k^2 + m^2\pi^2/d^2$, $m \in \mathbb{N}$. The longitudinal propagation constant is related to the eigenvalues of the transverse operator as $\lambda_m = -\beta_m^2$, $\sqrt{-\lambda_m} = \mathrm{i}\sqrt{\lambda_m}$ if $\lambda_m > 0$. We choose $\mathfrak{Re}\sqrt{-\lambda_m} \geq 0$, $\mathfrak{Im}\sqrt{-\lambda_m} \geq 0$.

There is a finite number of λ_m such that $\lambda_m < 0$. In this case, for a fixed time dependence $\mathrm{e}^{-\mathrm{i}\omega t}$, we have right $\mathrm{e}^{\mathrm{i}\sqrt{-\lambda_m}x}\Phi_m(y)$ and left $\mathrm{e}^{-\mathrm{i}\sqrt{-\lambda_m}x}\Phi_m(y)$ going modes. For the case when there are infinitely many eigenvalues $\lambda_m > 0$, these modes will be right and left evanescent modes, since the behavior along the direction of propagation will change from oscillating to exponentially decreasing.

Since $(\Phi_m)_{m\in\mathbb{N}}$ form a complete orthonormal system in $L^2(I_y)$, the solution of the Helmholtz equation in a closed straight waveguide with constant material coefficients can be represented in the form

$$u(x,y) = \sum_{m\in\mathbb{N}} u_{1,m}(x)\Phi_m(y) = \sum_{m\in\mathbb{N}} (a_m^{\mathrm{R}} \mathrm{e}^{\mathrm{i}\sqrt{-\lambda_m}x} + a_m^{\mathrm{L}} \mathrm{e}^{-\mathrm{i}\sqrt{-\lambda_m}x})\Phi_m(y), \tag{109}$$

where $u_{1,m}$ satisfy $u_{1,m}'' - \lambda_m u_{1,m} = 0$, $x \leq x_{\mathrm{L}}$, $x \geq x_{\mathrm{R}}$. With the modal expansion (109), we can distinguish between left and right going modes, which is required to determine the radiation condition for $x \leq x_{\mathrm{L}}$, $x \geq x_{\mathrm{R}}$ in the model problem (108).

For example, for $x \leq x_{\mathrm{L}}$ the $u - u^{\mathrm{inc}}$ is left-going, hence with (109) we have

$$u(x,y) - u^{\mathrm{inc}}(x,y) = \sum_{m\in\mathbb{N}} a_m^{\mathrm{L}} \mathrm{e}^{-\mathrm{i}\sqrt{-\lambda_m}x}\Phi_m(y) \quad \text{for any } x \leq x_{\mathrm{L}}.$$

The coefficient $a_m^{\mathrm{L}} \in \mathbb{C}$, $a_m^{\mathrm{L}} = \big(u(x_{\mathrm{L}}, \cdot), \Phi_m\big)_{L^2(I_y)}$ is a projection of $u(x_{\mathrm{L}}, \cdot)$ onto its own space associated with the eigenfunction of the transverse operator A^D. Similar expressions can be obtained for the right-going $u^{\mathrm{inc}}(x,y)$, $x \leq x_{\mathrm{L}}$ and u, $x \geq x_{\mathrm{R}}$.

For numerical implementation, we need to truncate the computational domain Ω. We replace it with

$$\Omega_J := \{(x,y) \in \Omega,\, x \in (x_{\mathrm{L}}, x_{\mathrm{R}})\} \tag{110}$$

and construct the boundary conditions utilizing the DtN operator. In order to impose transparent boundary conditions on the interfaces $\{x_{\mathrm{L,R}}\} \times I_y$, it is necessary to match the Dirichlet data $u(x_{\mathrm{L}}, \cdot)$ with the Neumann data $\partial_x u(x_{\mathrm{L}}, \cdot)$. In the same manner, as in Section 3.1.3, we define the expression for the DtN operator

$$\Lambda \colon H^{\frac{1}{2}}\big(\{x_{\mathrm{L,R}}\} \times I_y\big) \to H^{-\frac{1}{2}}\big(\{x_{\mathrm{L,R}}\} \times I_y\big), \qquad \Lambda v := \sum_{m \in \mathbb{N}} \mathrm{i}\sqrt{-\lambda_m}\big(v, \Phi_m\big)_{L^2(I_y)} \Phi_m(y) \tag{111}$$

by differentiating left and right going waves represented via (109) at the interfaces $\{x_{\mathrm{L,R}}\} \times I_y$ with respect to x.

Then we have the following variational formulation of the closed waveguide problem in the truncated domain Ω_J. For the given right-going incident wave u^{inc} and material parameters $k = k_0 n_{\mathrm{co}}$, $k \in \mathbb{R}$, $k_0 = 2\pi/\lambda_0$ we seek a variational solution $u \in H^1(\Omega_J)$ to the following problem

$$\begin{cases} -\Delta u - k^2 u &= 0 & \text{in } \Omega_J, \\ u &= 0 & \text{on } \partial\Omega_J \backslash \big(\{x_{\mathrm{L}}\} \times I_y \cup \{x_{\mathrm{R}}\} \times I_y\big), \\ -\partial_x u &= \Lambda u - 2\Lambda u^{\mathrm{inc}} & \text{on } \{x_{\mathrm{L}}\} \times I_y, \\ \partial_x u &= \Lambda u & \text{on } \{x_{\mathrm{R}}\} \times I_y. \end{cases} \tag{112}$$

Scaled 2D closed waveguide. As can be seen from the previous paragraph, the presence of the guiding modes in the closed straight waveguide is equivalent to the fulfillment of the condition $m^2\pi^2/d^2 - k^2 < 0$, $m \in \mathbb{N}$. Namely, the ratio of material parameters $k = k_0 n_{\mathrm{co}}$, where k_0 is determined with the wavelength λ_0, and waveguide thickness d, determines whether the signal will propagate or attenuate along the waveguide. We want to verify how well the 1D model (117) approximates solutions in a 2D closed waveguide (112), therefore we need to coordinate the geometric parameters of the 2D waveguide and wavelength λ_0 such that for each waveguide in such a sequence of 2D shrinking waveguides the ratio between parameters of the waveguide remains the same and the number of supported modes will not change after scaling.

We denote the reference length in the longitudinal direction x as ℓ_1, the reference length in the orthogonal direction y as ℓ_2. With this scaling, the non-dimensionalized form of the Helmholtz equation in the straight waveguide $[0,\, \ell_1] \times [0,\, \ell_2]$ is

$$-\partial_{\widehat{x}}^2 u(\widehat{x}, \widehat{y}) - \frac{1}{\delta^2}\partial_{\widehat{y}}^2 u(\widehat{x}, \widehat{y}) - \widehat{k}_0^2 n_{\mathrm{co}}^2 u(\widehat{x}, \widehat{y}) = 0, \quad \widehat{x} = \frac{x}{\ell_1},\ \widehat{y} = \frac{y}{\ell_2}, \quad x \in (0,\, \ell_1),\ y \in (0,\, \ell_2), \tag{113}$$

where $\widehat{k}_0 = k_0 \ell_1$ is the dimensionless wavenumber and $\delta := \ell_2/\ell_1$.

In the same way, as in the previous paragraph, we apply separation of variables and obtain equation $-u_2'' - \delta^2 \widehat{k}_0^2 n_{\mathrm{co}}^2 u_2 = \delta^2 \widehat{\lambda} u_2$ on the cross-section. With boundary conditions on the cladding $u(\widehat{x}, 0) = u(\widehat{x}, 1) = 0$ corresponding to the closed waveguide problem, we have the following eigenvalues associated with the transverse problem

$$\widehat{\lambda}_m = \frac{1}{\delta^2}(-\delta^2 \widehat{k}_0^2 n_{\mathrm{co}}^2 + \ell_2^2 \frac{m^2\pi^2}{d^2}) = \ell_1^2(-k_0^2 n_{\mathrm{co}}^2 + \frac{m^2\pi^2}{d^2}), \quad m \in \mathbb{N}. \tag{114}$$

Hence, $\widehat{\lambda}_m$ is scaled with respect to ℓ_1 as $\widehat{\lambda}_m = \ell_1^2 \lambda_m$, $m \in \mathbb{N}$ and we have the original physical combination, which defines the number of guiding modes. Therefore, the number of guiding modes remains the same after scaling.

For example, let $\ell_1 = 1$, $\delta = 1$, cross-section $\widehat{I}_y =: [0,1]$, $n_{\text{co}} = 1.5$, $\lambda_0 = 1.5$ µm $= 1.5\ell_1$, $k_0\ell_1 = 2\pi\ell_1/\lambda_0 = 2\pi/1.5$. Therefore the guiding mode condition for the propagation constant in the longitudinal direction $\widehat{\beta}_m^2 = -\widehat{\lambda}_m$ is

$$\widehat{\beta}_m^2 = \big(\frac{2\pi}{1.5}\big)^2 1.5^2 - (m^2)\pi^2 = \pi^2(2 - m^2) > 0, \quad m \in \mathbb{N}.$$

We can see, there is only one guiding mode for such a set of parameters. If, with all other fixed parameters, we set the oscillation frequency higher $\lambda_0 = 1.5/\sqrt{2}$, then the waveguide will additionally support the second mode.

4.3. Model problem 1D

We consider the operator of the governing equation of the closed waveguide problem (108) with a thin cross-section in the context of quantum waveguides. Utilizing the separation of variables $u(s,\xi) = u_1(s)u_2(\xi)$ and the expression (102) with small $\varepsilon > 0$ in the Helmholtz equation with constant $k = k_0 n_{\text{co}}$ we obtain

$$\begin{aligned}
0 &= \widetilde{H}_{0\varepsilon} u(s,\xi) - k^2 u(s,\xi) \\
&= -\partial_s^2 u_1(s) u_2(\xi) - \frac{1}{\varepsilon^2} u_1(s) \partial_\xi^2 u_2(\xi) - \big(\frac{1}{4}\kappa^2(s) + k^2\big) u_1(s) u_2(\xi) \\
&= \Big(- \frac{\partial_s^2 u_1(s)}{u_1(s)} - \big(\frac{1}{4}\kappa^2(s) + k^2\big) - \frac{1}{\varepsilon^2} \frac{\partial_\xi^2 u_2(\xi)}{u_2(\xi)} \Big) u_1(s) u_2(\xi), \qquad s \in \mathbb{R},\ \xi \in (-1/2, 1/2).
\end{aligned}$$

We modify our approach now by considering $\xi \in (0,1)$ which does not change the spectrum. After the separation of variables, on one hand, we obtain in the transverse direction $\partial_\xi^2 u_2(\xi) - \lambda u_2(\xi) = 0$ for all $\xi \in (0,1)$, and on the other hand we have in the longitudinal direction $-\partial_s^2 u_1(s) - \frac{1}{4}(\kappa^2(s) + k^2) u_1(s) = \frac{1}{\varepsilon^2}\lambda u_1(s)$, for all $s \in \mathbb{R}$.

We consider the first equation on closed waveguide cross-section characterized by the Dirichlet Laplacian $\Delta\colon H^2(0,1) \cap H_0^1(0,1) \to L^2(0,1)$. The eigenfunctions of such transverse operator form a complete orthonormal system $u_{2,m}(\xi) = 1/\sqrt{2}\sin(m\pi\xi)$ in $L^2(0,1)$, $m \in \mathbb{N}$. The corresponding eigenvalues are $\lambda_m = m^2\pi^2$, $m \in \mathbb{N}$.

The equation in the longitudinal direction s becomes

$$-\partial_s^2 u_1(s) - \big(k^2 + \frac{1}{4}\kappa^2(s)\big) u_1(s) = \frac{\lambda_m}{\varepsilon^2} u_1(s), \qquad \text{for all} \quad s \in \mathbb{R}. \tag{115}$$

Here we can see the connection with the result [14]. By the Theorem 4.2 we consider $-\Delta u = \lambda^\varepsilon u$ on waveguide junction with Dirichlet boundary conditions. With the associated one-dimensional Sturm-Liouville problem (105)

$$-\partial_s^2 u_1 - \frac{1}{4}\kappa^2 u_1 = \mu_m u_1, \qquad \text{for} \quad u_1 \in H_0^1(0,L),\ m \in \mathbb{N}$$

and wavenumber $k = 0$ it follows that $\lambda^\varepsilon u = \widetilde{H}_{0\varepsilon} u = (\mu_m + \lambda_m/\varepsilon^2)u$, where λ_m is related to the transverse operator on the cross-section $(0,1)$. Hence $\lambda^\varepsilon = \mu_m + \lambda_m/\varepsilon^2$.

This is also shown for the example of a circle of constant curvature, where μ_m can be determined explicitly (107).

For 2D closed straight waveguides of thickness d we have as a condition for signal propagation without attenuation $m^2\pi^2/d^2 - k^2 < 0$, $m \in \mathbb{N}$, which is satisfied by finitely many eigenvalues. For the thin waveguides with thickness defined via small parameter ε, there is undamped transmission whenever $\lambda_m/\varepsilon^2 - k^2 < 0$. However, the potential with curvature term gives rise to the reflection behavior.

Now we assume that there is one guiding mode with the normalized first mode $u_{2,1}$ on the waveguide cross-section, λ_1 is the related eigenvalue, $-\beta_1^2 = \lambda_1/\varepsilon^2 - k^2$ denotes propagation constant in the longitudinal direction. Then from (115) we obtain

$$-\partial_s^2 u_1(s) - \big(\frac{1}{4}\kappa^2(s) + \beta_1^2\big)u_1(s) = 0, \qquad \text{for all} \quad s \in \mathbb{R}. \tag{116}$$

Following the Section 4.2 we can construct conditions at the interfaces $\{s_{\mathrm{L,R}}\} \times (0,1)$ between semi-infinite straight parts of the waveguide and the junction. We consider a right-going incoming wave u^{inc}. With (111) for $\xi \in (0,1)$ we have

$$\begin{aligned}\Lambda u(s_{\mathrm{L}}, \xi) &= \mathrm{i}\beta_1 (u_{2,1}, u_{2,1})_{L^2(0,1)} u_1(s_{\mathrm{L}}) u_{2,1}(\xi) \\ &= \mathrm{i}\beta_1 u_1(s_{\mathrm{L}}) u_{2,1}(\xi).\end{aligned}$$

We replace in the longitudinal direction domain $\mathbb{R}$ by the interval $(s_{\mathrm{L}}, s_{\mathrm{R}})$ related to the waveguide junction and obtain the transparent boundary conditions

$$\begin{aligned}-u_1'(s_{\mathrm{L}})u_{2,1}(\xi) = \partial_\nu u(s_{\mathrm{L}}, \xi) = \Lambda u(s_{\mathrm{L}}, \xi) - 2\Lambda u^{\mathrm{inc}}(s_{\mathrm{L}}, \xi) = \mathrm{i}\beta_1\big(u_1(s_{\mathrm{L}}) - 2\big)u_{2,1}(\xi), \\ u_1'(s_{\mathrm{R}})u_{2,1}(\xi) = \partial_\nu u(s_{\mathrm{R}}, \xi) = \Lambda u(s_{\mathrm{R}}, \xi) = \mathrm{i}\beta_1 u_1(t_{\mathrm{L}}) u_{2,1}(\xi)\end{aligned}$$

for all $\xi \in (0,1)$. Then with (116) we have the following boundary value problem for $u_1 \in H^1(s_{\mathrm{L}}, s_{\mathrm{R}})$

$$\left\{\begin{array}{rcl} -u_1''(s) - \Big(\frac{1}{4}\kappa^2(s) + \beta_1^2\Big)u_1(s) &=& 0 \quad \text{for all } s \in (s_{\mathrm{L}}, s_{\mathrm{R}}), \\ -u_1'(s_{\mathrm{L}}) &=& \mathrm{i}\beta_1(u_1(s_{\mathrm{L}}) - 2), \\ u_1'(s_{\mathrm{R}}) &=& \mathrm{i}\beta_1 u_1(s_{\mathrm{R}}). \end{array}\right. \tag{117}$$

4.4. Numerical examples

In this section, we compare the numerical solution of the 1D waveguide model problem (117), where the curvature of the central trajectory is included in the potential of the leading equation, and the numerical solution to the 2D curved closed waveguide problem (112). We find numerical solutions to each problem with FEM for three examples of waveguides with constant thickness generated by distinct central curves.

For the numerical solution of the 2D closed waveguide problem (112) with FEM, we apply the TO described in detail in Section 3.1.1. With the domain transformation (67) we map the curved waveguide Ω_J (110) of constant thickness δ generated by the central trajectory $\Gamma\colon [s_{\mathrm{L}},\, s_{\mathrm{R}}] \to \mathbb{R}^2$ into a straight (in terms of shape) waveguide

$$\Omega_h := I_s \times I_t \subset \mathbb{R}^2 \quad \text{with} \quad I_s := [s_{\mathrm{L}},\, s_{\mathrm{R}}],\, I_t := [0,\, \delta].$$

The weak formulation which we need for the FEM implementation is derived analogously to the open waveguide case, without taking into account the transformations related to the truncated PML (76), since in the case of the closed waveguide, we utilize only the DtN operator (111) to satisfy the radiation condition in the scattering problem (108).

For a given right-going incoming wave $u^{\mathrm{inc}} \in H^1_{\mathrm{loc}}\big((-\infty, s_{\mathrm{L}}] \times I_t\big)$ [71] satisfying Dirichlet boundary conditions $u^{\mathrm{inc}}(\cdot, 0) = 0$, $u^{\mathrm{inc}}(\cdot, \delta) = 0$ on the cladding, we seek $u \in H^1_{\mathrm{cl}}(\Omega_h)$, where

$$H^1_{\mathrm{cl}}(\Omega_h) := \{v \in H^1(\Omega_h) : v(s, 0) = 0,\ v(s, \delta) = 0,\ \text{for all}\, s \in I_s\}$$

such that

$$\begin{aligned}\int_{\Omega_h} A(s,t)\nabla u \cdot \nabla \overline{v} - c\, u\, \overline{v}\ \mathrm{d}s\,\mathrm{d}t &- \Big\langle \Lambda_{\mathrm{L}} u,\, v \Big\rangle_{H^{-\frac{1}{2}}(\{s_{\mathrm{L}}\} \times I_t),\, H^{\frac{1}{2}}(\{s_{\mathrm{L}}\} \times I_t)} \\ &- \Big\langle \Lambda_{\mathrm{R}} u,\, v \Big\rangle_{H^{-\frac{1}{2}}(\{s_{\mathrm{R}}\} \times I_t),\, H^{\frac{1}{2}}(\{s_{\mathrm{R}}\} \times I_t)} \\ &= -2\Big\langle \Lambda_{\mathrm{L}} u^{\mathrm{inc}},\, v \Big\rangle_{H^{-\frac{1}{2}}(\{s_{\mathrm{L}}\} \times I_t),\, H^{\frac{1}{2}}(\{s_{\mathrm{L}}\} \times I_t)} \end{aligned} \tag{118}$$

holds for any $v \in H^1_{\mathrm{cl}}(\Omega_h)$. The coefficients A and c are defined with (74) and (75). The infinite sum in the DtN terms is truncated for the numerical implementation with respect to the number of guiding modes.

According to the problem (117), (112) geometry, the curvature of the central curve Γ has compact support $\mathrm{supp}(\kappa) \subset [s_L,\, s_R]$. In order to ensure that the central curve is represented by a straight line close to the interfaces defined by $s_{\mathrm{L,R}}$, we additionally define the connecting parts of length $\delta_{s_{\mathrm{L}}}$, $\delta_{s_{\mathrm{R}}}$, which are represented by straight lines. For the 2D closed waveguide the left and right connection parts are defined with [71]

$$(s_{\mathrm{L}},\, s_{\mathrm{L}} + \delta_{s_{\mathrm{L}}}) \times I_t = \{(s,t) \in \Omega_h :\ s \in (s_{\mathrm{L}},\, s_{\mathrm{L}} + \delta_{s_{\mathrm{L}}})\} \tag{119}$$

$$(s_{\mathrm{R}} - \delta_{s_{\mathrm{R}}},\, s_{\mathrm{R}}) \times I_t = \{(s,t) \in \Omega_h :\ s \in (s_{\mathrm{R}} - \delta_{s_{\mathrm{R}}},\, s_{\mathrm{R}})\} \tag{120}$$

accordingly.

For the numerical examples in the current section, we choose the following values for the refractive index n_{co} and the vacuum wavelength λ_0

$$n_{\mathrm{co}} = 1.5, \qquad \lambda_0 = 1.5/\sqrt{2}\,\mu\mathrm{m}. \tag{121}$$

Remark: For the comparison of 2D and 1D models, it is necessary to take into account the scaling with respect to the length and thickness of the associated 2D waveguide (113), (114). The scaling, in addition to wavelength, is also used in the argument of the eigenfunctions related to the straight waveguide cross-section, which must be taken into account for the implementation of the DtN terms in (118).

Reflection. As the first criterion for validating the results of simulations related to both models, we compute the reflected power. We obtain scattered energy terms from

the acoustic wave equation expression for the energy flow (87) utilizing DtN operator (111).

Consider the case when there is one guiding mode transmitted along the waveguide with propagation constant $\beta_1 = \sqrt{-\lambda_1}$, $\lambda_1 < 0$. In the 2D closed waveguide for the right-going incoming wave the energy flow is measured at the right interface $\{s_{\mathrm{R}}\} \times I_t$ for the transmitted energy

$$E^{\mathrm{trm}} = \beta_1 \left| (u, \Phi(s_{\mathrm{R}}))_{L^2(\{s_{\mathrm{R}}\}\times I_t)} \right|^2 \tag{122}$$

and at the left interface $\{s_{\mathrm{L}}\} \times I_t$ for the reflected energy

$$E^{\mathrm{rfl}} = \beta_1 \left| (u - u^{\mathrm{inc}}, \Phi(s_{\mathrm{L}}))_{L^2(\{s_{\mathrm{L}}\}\times I_t)} \right|^2. \tag{123}$$

The energy conservation $E^{\mathrm{inc}} = E^{\mathrm{sca}}$ holds for the incoming

$$E^{\mathrm{inc}} = \beta_1 \left| (u^{\mathrm{inc}}, \Phi(s_{\mathrm{L}}))_{L^2(\{s_{\mathrm{L}}\}\times I_t)} \right|^2 \tag{124}$$

and the scattered energy $E^{\mathrm{sca}} = E^{\mathrm{trm}} + E^{\mathrm{rfl}}$.

The transmitted, reflected, and incoming energy related to the solutions of the 1D waveguide problem (117) can be found with expressions

$$E^{\mathrm{trm}} = \beta_1 |u_1(s_{\mathrm{R}})|^2, \quad E^{\mathrm{rfl}} = \beta_1 |1 - u_1(s_{\mathrm{L}})|^2, \quad E^{\mathrm{inc}} = \beta_1 |u_1(s_{\mathrm{L}})|^2 \tag{125}$$

accordingly. The scattered energy is $E^{\mathrm{sca}} = \beta_1 \Big(|1-u_1(s_{\mathrm{L}})|^2 + |u_1(s_{\mathrm{R}})|^2 \Big)$ and $E^{\mathrm{inc}} = E^{\mathrm{sca}}$ must be satisfied.

We are especially interested in the relative transmitted $T \in [0,1]$ and the relative reflected $R \in [0,1]$ power

$$T = \frac{E^{\mathrm{trm}}}{E^{\mathrm{inc}}}, \qquad R = \frac{E^{\mathrm{rfl}}}{E^{\mathrm{inc}}}.$$

Asymptotic solution. As an additional measure of success, we compare L^2-norm and H^1- norm of the obtained solutions of 1D and 2D problems. Let us denote the asymptotic solution $u_A(s,t) = u_1(s)\sin(\pi t/\delta)$ for $s,t \in \Omega_h$. We can derive the relation between the L^2-norms of such asymptotic solution in Ω_h and the 1D solution u_1 in I_s

$$\begin{aligned} \|u_A\|^2_{L^2(\Omega_h)} &= \int_{s_{\mathrm{L}}}^{s_{\mathrm{R}}} |u_1(s)|^2 \,\mathrm{d}s \int_0^{\delta} \sin\left(\frac{\pi}{\delta}t\right)^2 \mathrm{d}t \\ &= \|u_1\|^2_{L^2(s_{\mathrm{L}},s_{\mathrm{R}})} \delta \int_0^1 \sin(\pi t)^2 \,\mathrm{d}t = \frac{\delta}{2}\|u_1\|^2_{L^2(s_{\mathrm{L}},s_{\mathrm{R}})}, \end{aligned} \tag{126}$$

or $\|u_A\|_{L^2(\Omega_h)} = \sqrt{\delta/2}\|u_1\|_{L^2(s_{\mathrm{L}},s_{\mathrm{R}})}$. Similarly we can relate $\|\nabla u_A\|_{L^2(\Omega_h)}$ to $\|u_1'\|_{L^2(s_{\mathrm{L}},s_{\mathrm{R}})}$ by

$$\begin{aligned} \|\nabla u_A\|^2_{L^2(\Omega_h)} &= \int_{s_{\mathrm{L}}}^{s_{\mathrm{R}}} |u_1'(s)|^2 \,\mathrm{d}s \int_0^{\delta} \sin\left(\frac{\pi}{\delta}t\right)^2 \mathrm{d}t + \int_{s_{\mathrm{L}}}^{s_{\mathrm{R}}} |u_1(s)|^2 \,\mathrm{d}s \,\frac{\pi^2}{\delta^2} \int_0^{\delta} \cos\left(\frac{\pi}{\delta}t\right)^2 \mathrm{d}t \\ &= \|u_1'\|^2_{L^2(s_{\mathrm{L}},s_{\mathrm{R}})} \delta \int_0^1 \sin(\pi t)^2 \,\mathrm{d}t + \|u_1\|^2_{L^2(s_{\mathrm{L}},s_{\mathrm{R}})} \delta \frac{\pi^2}{\delta^2} \int_0^1 \cos(\pi t)^2 \,\mathrm{d}t \\ &= \frac{\delta}{2}\|u_1'\|^2_{L^2(s_{\mathrm{L}},s_{\mathrm{R}})} + \frac{\pi^2}{2\delta}\|u_1\|^2_{L^2(s_{\mathrm{L}},s_{\mathrm{R}})}. \end{aligned} \tag{127}$$

4.4.1. Example 1: 90-degree bow

The central curve $\Gamma\colon [s_{\mathrm{L}}, s_{\mathrm{R}}] \to \mathbb{R}^2$ is represented by two segments of length $\delta_{s_{\mathrm{L}}}$, $\delta_{s_{\mathrm{R}}}$ connected by an arc of constant curvature $\kappa = 1/R^+$, $\delta_{s_{\mathrm{L}}} = \delta_{s_{\mathrm{R}}} = 0.25\,\mu\mathrm{m}$, $R^+ = 1\,\mu\mathrm{m}$. The arc Γ_J in $\mathbb{R}^2$ of constant curvature is parametrized with

$$\Gamma_J = \{(\gamma_1(s),\, \gamma_2(s)), s \in (s_{\mathrm{L}} + \delta_{s_{\mathrm{L}}},\, s_{\mathrm{R}} - \delta_{s_{\mathrm{R}}})\},$$
$$\gamma_1(s) = R^+ \sin\big(s/R^+\big),\ \ \gamma_2(s) = R^+ \cos\big(s/R^+\big).$$

2D thin waveguide. The computational domain after TO application (67) is

$$\Omega_h = [0,\, L_s] \times [0,\, \delta], \quad L_s = \pi/2 + \delta_{s_{\mathrm{L}}} + \delta_{s_{\mathrm{R}}},$$

where L_s is the total length related to the longitudinal propagation direction, $\pi/2$ is the arclength of the curved part of the waveguide with the radius of curvature $R^+ = 1\mu\mathrm{m}$, $\delta_{s_{\mathrm{L}}}$, $\delta_{s_{\mathrm{R}}}$ are lengths of the connection parts (119). The material parameters before scaling are given in (121). We scale the wavelength by λ_0/δ, and the thickness δ in the transverse direction is scaled accordingly. Then we obtain the scaled propagation constant in the longitudinal direction with (114).

1D waveguide. The 1D waveguide is represented by the central trajectory of the 2D waveguide and has piecewise constant curvature. For $R^+ = 1$ the arclength related to the curved part of the structure parametrized with $s \in (s_{\mathrm{L}} + \delta_{s_{\mathrm{L}}},\, s_{\mathrm{R}} - \delta_{s_{\mathrm{R}}})$ is $\pi/2$. Then in this case the 1D problem (117) for u_1 becomes

$$-u_1''(s) - \Big(\frac{1}{4}\chi_{[s_{\mathrm{L}}+\delta_{s_{\mathrm{L}}},\, s_{\mathrm{L}}+\delta_{s_{\mathrm{L}}}+\pi/2]}(s) + \beta_1^2\Big)u_1(s) = 0 \qquad \text{for all } s \in (s_{\mathrm{L}},\, s_{\mathrm{R}}),$$

together with the Robin boundary conditions in $s_{\mathrm{L,R}}$. The longitudinal propagation constant β_1 is δ-scaled according to (114). An example of the 1D numerical solution obtained with FEM for the scaling parameter $\delta = 0.0398$ and corresponding potential can be found in Figure 36.

Remark: In [57], it was shown that the central trajectory Γ can have milder continuity conditions than in Theorems (4.1) and (4.2). Specifically, for Γ such that its curvature is non-continuous and possibly vanishing, the Laplacian in a 3D quantum waveguide with bending and possible torsion converges to a one-dimensional potential problem with curvature terms in the resulting potential after the dimension reduction.

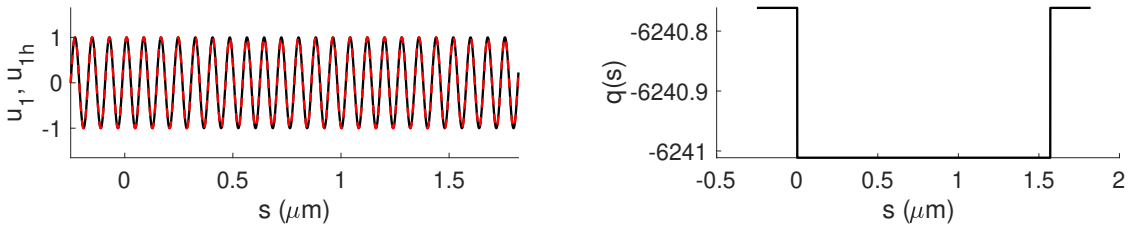

Figure 36: **Left**: exact and numerical 1D solution for the 90-degree bow; **Right**: the corresponding potential.

We consider a bow with the angle $\theta \in [0, \pi/2]$ and piecewise constant curvature with values κ_1, κ_2 outside and inside the interval $[s_{\mathrm{L}} + \delta_{s_{\mathrm{L}}},\ s_{\mathrm{R}} - \delta_{s_{\mathrm{R}}}]$ respectively. This corresponds to the *potential step* equation and we know the exact solution for this case [58]. We denote $k_1 = \sqrt{\kappa_1^2/4 + \beta^2}$, $k_2 = \sqrt{\kappa_2^2/4 + \beta^2}$, then the exact relative transmission $T \in [0, 1]$ is

$$T(\beta, \kappa_1, \kappa_2) = \left(1 + \frac{1}{4}\left(\frac{k_1}{k_2} - \frac{k_2}{k_1}\right)^2 (\sin(k_2 \ell))^2\right)^{-1}. \tag{128}$$

In our case we have $\kappa_1 = 0$, $\kappa_2 = 1/R^+$, $\ell = \theta\kappa_2$ and the propagation constant $\beta = \beta_1$ is δ-scaled (114). From the energy conservation law we obtain the relative reflection $R = 1 - T$.

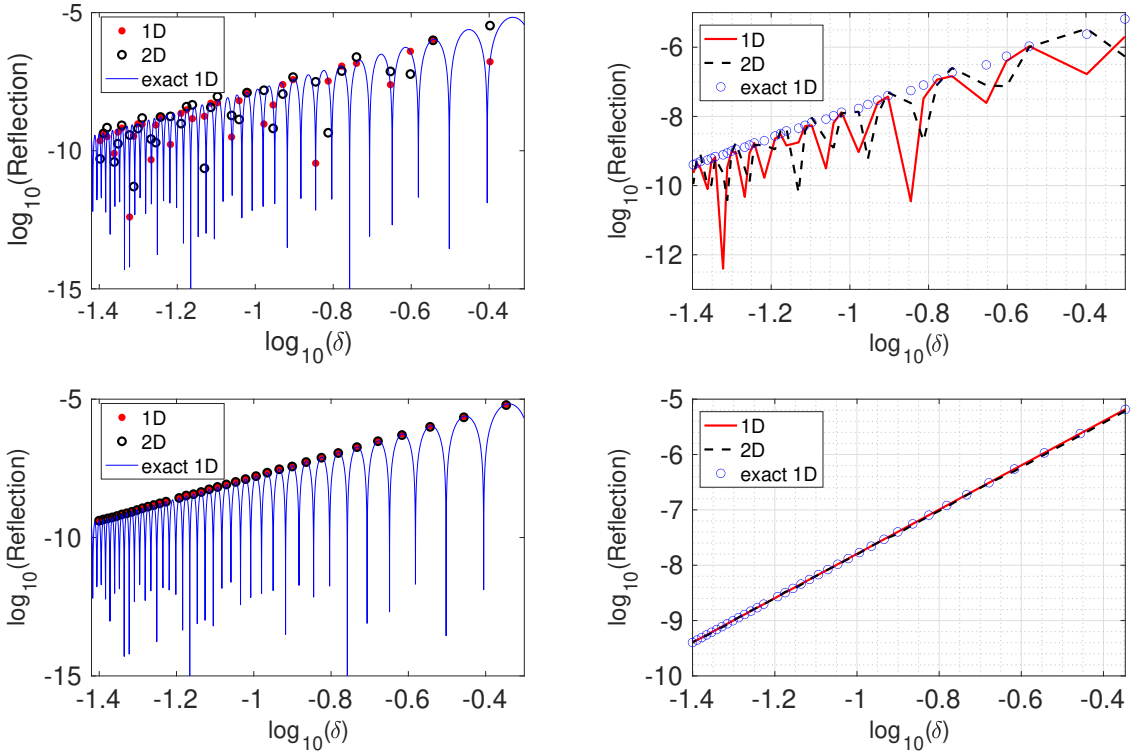

Figure 37: The relative reflection $R \in [0, 1]$ as a function of δ, 90-degree bow case. 1D (red), 2D (black) FEM simulation and the exact values (blue). **Top row**: R related to 1D and 2D numerical solutions evaluated at a sequence of δ that are not local maxima. **Bottom row**: R evaluated at a sequence of δ that are local maxima, the slope yields $R \sim \kappa^4$.

FEM numerical solution for the 1D problem computed in $[-1/4,\ 1/4 + \pi/2]$ with pd $= 3$, the number of cells is 64 considering δ-scaling to keep a fixed resolution per wavelength in the tested sequence of shrinking waveguides. For the 2D thin waveguide problem, we set the number of cells as 18 per dimension, taking into account δ-scaling in the longitudinal direction, pd $= 3$.

The reflection power values obtained with 2D, 1D FEM numerical solution utilizing (123), (124), (125) and the exact reflection calculated via (128) against the waveguide

thickness δ are presented in Figure 37. In the left column, the exact reflection values are computed for $\delta \in \{0.0385, 0.0386, \ldots, 0.45\}$ µm. In the top row, the reflection power for 1D and 2D problems was computed for $\delta \in \{1/25.5, 1/25, \ldots, 1/2\}$ µm, the exact values measured at points of local maxima. For the exact reflection values, we observe strong oscillations with respect to variation of the scale parameter δ. Therefore, the relative reflection values for $\delta \in \{1/25.5, 1/25, \ldots, 1/2\}$ µm related to the 1D model and the 2D model do not match as a consequence of the observed sensitivity of R to small changes in the cross-sectional width parameter δ.

In Figure 37, bottom row, the relative reflection is computed for 1D and 2D problems for the sequence of scale parameters δ, that are local maxima of the reflection curve (128). In this case, we observe the stable prediction of the reflection values for the 2D problem provided by the 1D problem. Furthermore, if we substitute such local maxima δ into the exact relative reflection formula for our case (128) for $\kappa \ll \beta_1 \sim 1/\delta$ we get $R \approx \kappa^4/16\beta_1^4 \sim \kappa^4\delta^4$.

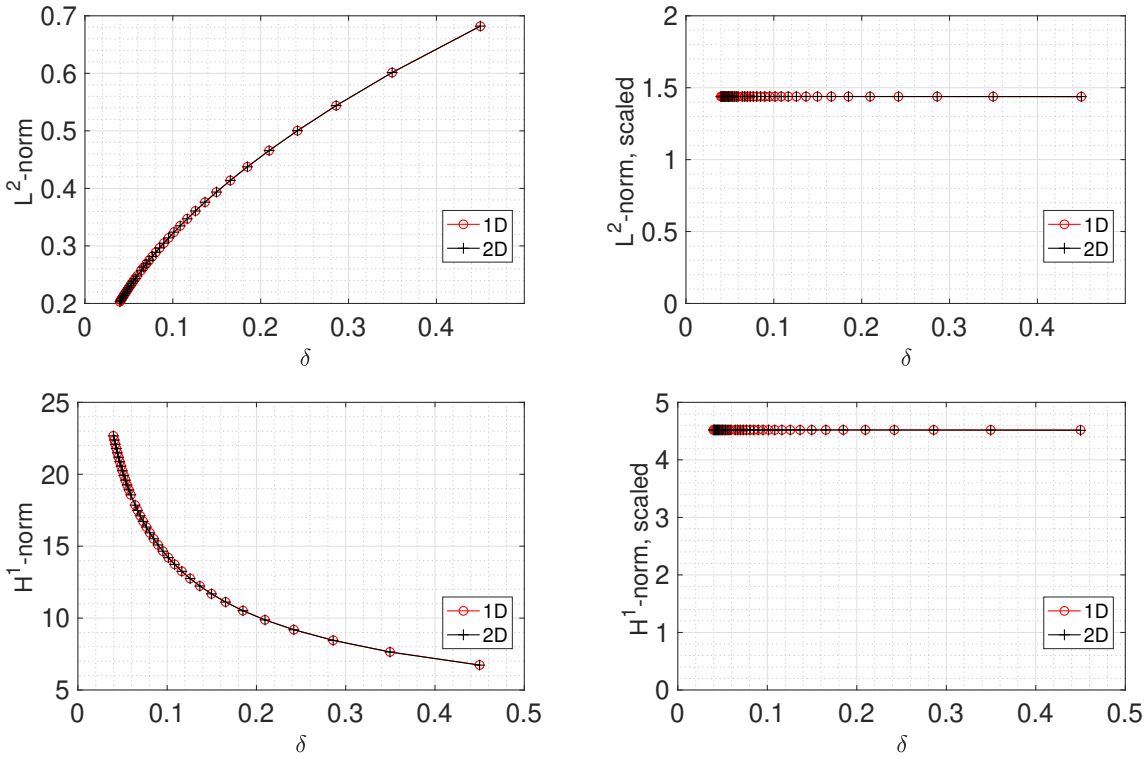

Figure 38: L^2, H^1-norm for numerical solution u_h in thin closed 90-degree bow (2D) and asymptotical approximation u_A. **Left column**: not-scaled. **Right column**: scaled.

In Figure 38 the L^2- and H^1-norms for u_h, u_A are shown. In the top right, we see that the relation between scaled L^2-norm of 2D solution and L^2-norm of the asymptotic solution according to (126) $\sqrt{2/\delta}\|u\|_{L^2(\Omega_h)} \approx \|u_1\|_{L^2(s_L,s_R)}$ is obtained. Indeed, by the numerical calculation for the 1D problem computed in $[-1/4, 1/4 + \pi/2]$ with the

number of cells equal to 64 considering δ-scaling and pd = 3 we have

$$\|u_1\|_{L^2(s_\mathrm{L},s_\mathrm{R})} \approx 1.44, \quad \|u_1'\|_{L^2(s_\mathrm{L},s_\mathrm{R})} \approx 4.52\frac{1}{\delta}.$$

Then with (127) we see that following relation for the scaled H^1-norm is satisfied $\sqrt{\delta}\|\nabla u\|_{L^2(\Omega_h)} \approx \sqrt{\delta}\|\nabla u_A\|_{L^2(\Omega_h)} \approx 4.52$, see Figure 38, right bottom. For the 2D FEM computations, pd = 3 and the number of cells 18 per dimension with respect to the scaling was chosen.

4.4.2. Example 2: $\mathcal{C}^1$-Hump

The central curve $\Gamma\colon [s_\mathrm{L}, s_\mathrm{R}] \to \mathbb{R}^2$ is represented by two segments of length δ_{s_L}, δ_{s_R}, connected by the $\mathcal{C}^1$-Hump of height H_J. The hump $\Gamma_J \in \mathbb{R}^2$ of length L_J is parametrized with

$$\Gamma_J = \big\{\big(x(s),\, f(x(s))\,\big),\, x(s) \in (0,\, 1)\big\}, \quad f(x(s)) = 16\, H_\mathrm{J}\, x(s)^2\, \big(1 - x(s)\big)^2. \tag{129}$$

The natural parameterization of the curve $s(x)$ can be found with (59).

2D thin waveguide. The computational domain after TO application (67) is

$$\Omega_h = [0,\, L_s] \times [0,\, \delta], \quad L_s = L_J + \delta_{s_\mathrm{L}} + \delta_{s_\mathrm{R}},$$

where L_s is the total length related to the longitudinal propagation direction, L_J is the arclength of the curved part of the waveguide, δ_{s_L}, δ_{s_R} are lengths of the connection parts (119). We choose $\delta_{s_\mathrm{L}} = \delta_{s_\mathrm{R}} = 0.25\,\mu\mathrm{m}$, $H_\mathrm{J} = 0.2\,\mu\mathrm{m}$. The material parameters before scaling are given in (121). The wavelength and the thickness are scaled with respect to δ. Then, we obtain the scaled propagation constant in the longitudinal direction β_1 (114), which relates the 2D and 1D problems by the δ parameter.

An example of the 2D numerical solution obtained with FEM for the scaling parameter $\delta = 0.0226$ µm and potential of the corresponding 1D problem can be found in Figure 39.

1D waveguide. The central curve is parameterized by the graph $s \mapsto f(s)$ (59) and we reformulate the problem (117) with (58) accordingly

$$\begin{cases} -\Big(\dfrac{1}{\sqrt{1+|f'|^2}}u_1'(s)\Big)' - \Big(\dfrac{1}{4}\dfrac{|f''|^2}{(1+|f'|^2)^3} + \beta_1^2\Big)u_1(s) &= 0 \quad \text{for all } s \in (s_\mathrm{L}, s_\mathrm{R}), \\ -u_1'(s_\mathrm{L}) &= \mathrm{i}\beta_1(u_1(s_\mathrm{L}) - 2), \\ u_1'(s_\mathrm{R}) &= \mathrm{i}\beta_1 u_1(s_\mathrm{R}). \end{cases} \tag{130}$$

For the FEM implementation, we need the weak formulation of the problem (130). For the given right-going incoming wave u_inc we seek $u_1 \in H^1(s_\mathrm{L}, s_\mathrm{R})$ satisfying

$$\int_{s_\mathrm{L}}^{s_\mathrm{R}} \frac{1}{\sqrt{1+|f'|^2}}u_1'v' - \Big(\frac{1}{4}\frac{|f''|^2}{(1+|f'|^2)^3} + \beta_1^2\Big)\sqrt{1+|f'|^2}\, u_1 v \,\mathrm{d}s$$
$$- \mathrm{i}\beta_1 u_1(s_\mathrm{R})v(s_\mathrm{R}) - \mathrm{i}\beta_1 u_1(s_\mathrm{L})v(s_\mathrm{L}) + 2\mathrm{i}\beta_1 u_\mathrm{inc}(s_\mathrm{L})v(s_\mathrm{L}) = 0,$$

for any $v \in H^1(s_L, s_R)$. The longitudinal propagation constant β_1 is δ-scaled (114).

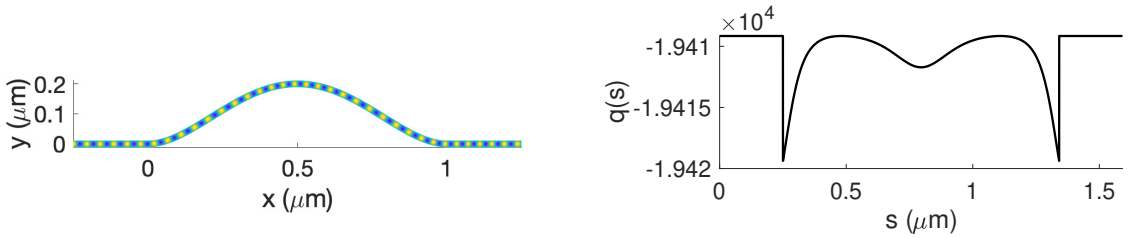

Figure 39: Left: 2D numerical solution for the thin $\mathcal{C}^1$-hump. Right: the potential of the associated 1D problem (130)

The numerical solution obtained with FEM for the 1D problem is computed in $[0, 1.5915]$ with pd $= 3$, the number of cells 64 with respect to the δ-scaling was chosen. For the 2D problem implementation, we set the number of cells equal to 18 per dimension, taking into account δ-scaling in the longitudinal direction, pd $= 2$. For the central trajectory, we use the complete cubic spline approximation (132).

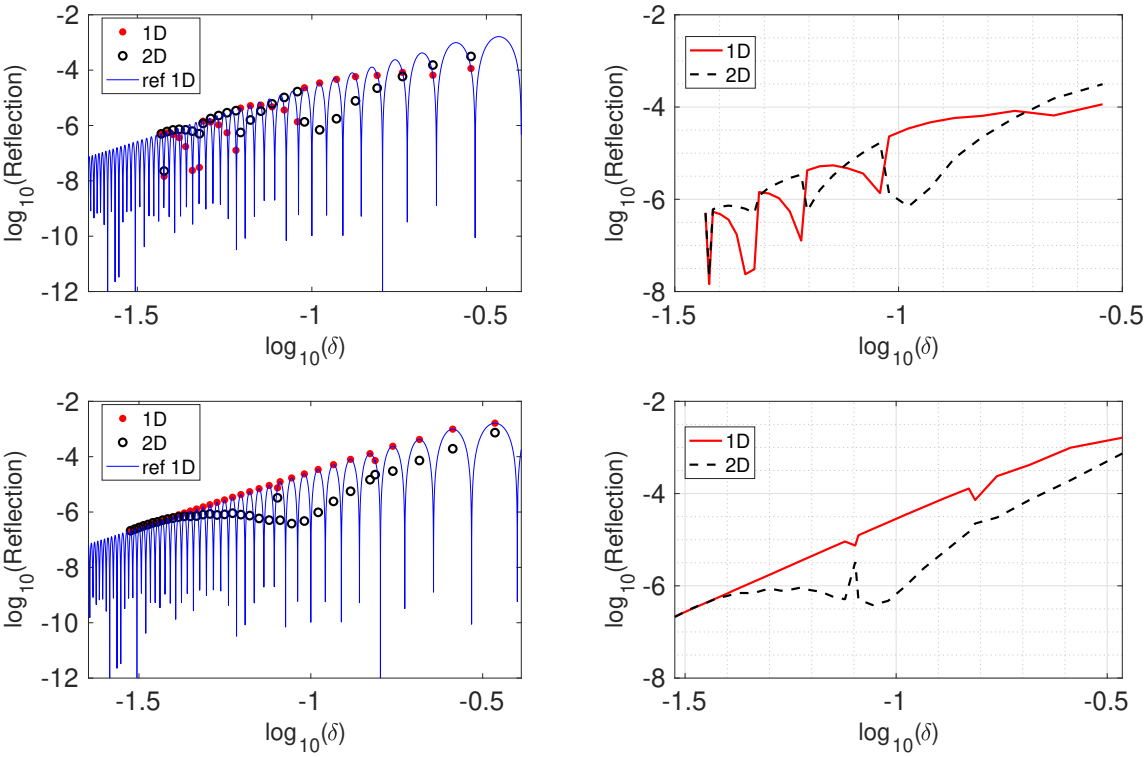

Figure 40: The relative reflection $R \in [0, 1]$ as a function of δ in the $\mathcal{C}^1$-hump case. 1D (red), 2D (black) FEM simulation, 1D reference via FEM (blue). **Top row**: R related to 1D and 2D numerical solutions evaluated at a sequence of δ that are not local maxima. **Bottom row**: R evaluated at a sequence of δ that are approximated local maxima.

With (123), (124), (125) we can find the reflection power values for the 2D and 1D

FEM numerical solution. The computed reflection coefficients versus the waveguide thickness δ are shown in Figure 40. In the left column, the 1D reference reflection values are computed for $\delta \in \{0.023, 0.0231, \ldots, 0.35\}$ µm, blue line. In the top row, the reflection power for 1D and 2D problems was calculated for $\delta \in \{1/27, 1/26.5, \ldots, 2/7\}$ µm.

For the 1D reference reflection values, same as in the previous example, we observe strong oscillations with respect to the scale parameter δ. Nevertheless, we can see that for the waveguide width $\delta < 0.04$ µm, the 1D and 2D relative reflections are in good agreement even in the case of an arbitrary choice of the thickness δ sequence.

In Figure 40, bottom row, the relative reflection for 1D and 2D problems is shown for the sequence of thickness δ, that are numerically approximated local maxima of the 1D reference reflection. With such a choice of δ we observe a more stable behavior for the relative reflected power of the 2D problem. Furthermore, we can see that for sufficiently thin 2D waveguides $\delta < 0.04$ µm represented by $\mathcal{C}^1$-Hump (129), the corresponding 1D model (130) can predict the values of the reflected energy.

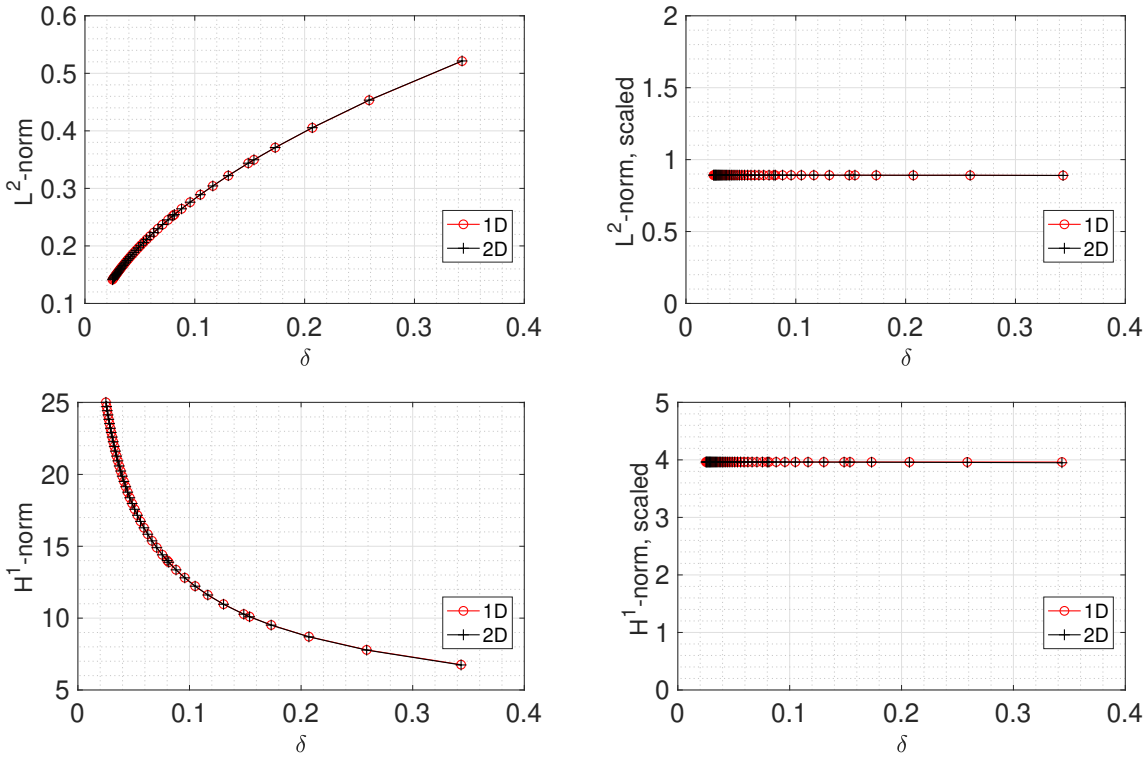

Figure 41: L^2, H^1-norm for numerical solution u_h in the thin closed $\mathcal{C}^1$-hump (2D) and asymptotical approximation u_A. **Left column**: not-scaled. **Right column**: scaled.

In Figure 41 the L^2- and H^1-norms for numerical FEM solution for the 2D problem u_h and asymptotic solution u_A are shown. In Figure 41, top right, we see that the relation between scaled L^2-norm of 2D solution and scaled L^2-norm of the asymptotic solution according to (126) $\sqrt{1/\delta}\|u\|_{L^2(\Omega_h)} \approx \sqrt{1/2}\|u_1\|_{L^2(s_L,s_R)}$ is obtained. We have

$\sqrt{1/2}\|u_1\|_{L^2(s_L,s_R)} \approx 0.89$ computed for the 1D problem in [0, 1.5915] with pd = 3 and the number of cells equal to 64 with respect to the δ scaling.

Then substituting $\|u_1'\|_{L^2(s_L,s_R)} \approx 3.9633/\delta$ and $\sqrt{1/2}\|u_1\|_{L^2(s_L,s_R)}$ in the expression (127), we see that relation for the scaled H^1-norm is satisfied

$$\sqrt{\delta}\|\nabla u\|_{L^2(\Omega_h)} \approx \sqrt{\delta}\|\nabla u_A\|_{L^2(\Omega_h)} \approx 3.96,$$

see Figure 41, right bottom. For the 2D FEM computations, pd = 3 and the number of cells 18 per dimension with respect to the scaling was chosen.

4.4.3. Example 3: $\mathcal{C}^2$-Hump

The central curve $\Gamma\colon [s_L, s_R] \to \mathbb{R}^2$ is represented by two straight segments of length $\delta_{s_L} = \delta_{s_R} = 0.25$ µm, connected by the $\mathcal{C}^2$-Hump of height H_J=0.2 µm. We denote the $\mathcal{C}^2$-Hump trajectory with $\Gamma_J \in \mathbb{R}^2$, it is parametrized with

$$\Gamma_J = \big\{\big(x(s),\, f(x(s))\big),\, x(s) \in (0,\, 1)\big\}, \quad f(x(s)) = 64\, H_J\, x(s)^3\, \big(1 - x(s)\big)^3. \tag{131}$$

The natural parameterization of the curve $s(x)$ can be found with (59).

The 2D and 1D problems for the closed waveguides generated by such a central curve are defined in the same manner as in the previous example, see Section 4.4.2.

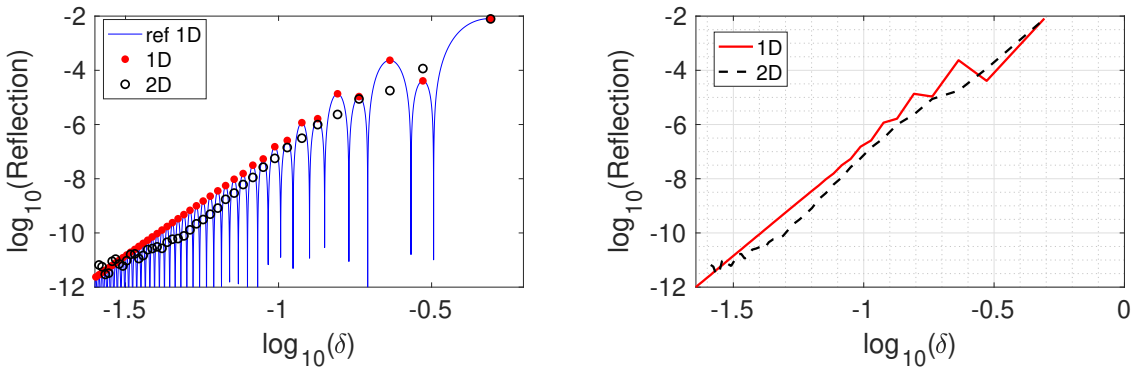

Figure 42: The relative reflection $R \in [0, 1]$ as a function of δ in the $\mathcal{C}^2$-Hump case. 1D (red), 2D (black) FEM simulation, 1D reference values via FEM (blue). R evaluated at a sequence of δ that are approximated local maxima.

The reflection power values obtained with 2D and 1D FEM numerical solution by the expressions (123),(124), (125) and the reference reflection values for the 1D problem against the sequence of the waveguide thickness δ are presented in Figure 42. For the 1D problem computed with FEM in [0, 1.5985], we set pd = 3 and take the number of cells as 64 considering δ-scaling to keep a fixed resolution per wavelength. For the 2D thin waveguide problem, we set the number of cells as 18 per dimension, taking into account δ-scaling in the longitudinal direction as well, pd = 2. In the Figure 42, left, the reference reflection values are computed for $\delta \in \{0.0255, 0.026, \ldots, 0.3\}$ µm. For the reference reflection values, same as we observed in previous examples, we

have strong oscillations with respect to the scale parameter δ. Therefore, the relative reflection power was computed for 1D and 2D problems for the sequence of thickness δ, which are local maxima of the 1D reference relative reflection. The results of such evaluation are shown in Figure 42. In this case, we observe that the reflection coefficients computed with the 1D problem numerical solution are in stable agreement with the relative reflection related to the 2D problem for the entire sequence of such scaling parameters δ.

The L^2- and H^1-norm for the numerical solution u_h of the 2D problem and for the asymptotic solution u_A are shown in Figure 43. For the 2D FEM implementation, we set pd = 3, and the number of cells per dimension with respect to the scaling of the longitudinal direction is 18. For the 1D problem computed in $[0, 1.5985]$ with FEM parameters chosen as pd = 3, number of cells is 64, we get

$$\frac{1}{\sqrt{2}}\|u_1\|_{L^2(s_\mathrm{L},s_\mathrm{R})} \approx 0.894, \quad \|u_1'\|_{L^2(s_\mathrm{L},s_\mathrm{R})} \approx 3.972\frac{1}{\delta}.$$

Hence with (127) the relation $\sqrt{\delta}\|\nabla u\|_{L^2(\Omega_h)} \approx \sqrt{\delta}\|\nabla u_A\|_{L^2(\Omega_h)} \approx 3.972$ for the scaled H^1-norm is satisfied, see Figure 43, right.

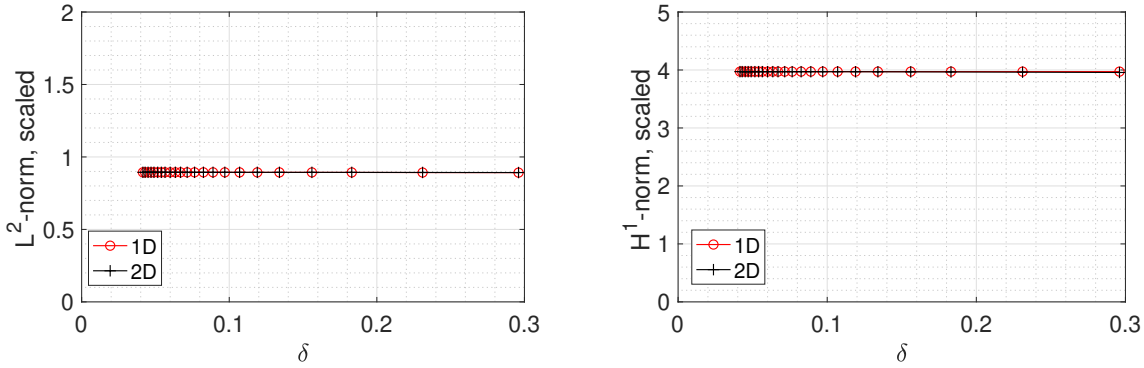

Figure 43: Scaled L^2, H^1-norm for numerical solution u_h in the thin closed $\mathcal{C}^2$-hump (2D) and for the related asymptotical approximation u_A.

5. Application of simplified methods to the waveguide junction optimization

In this chapter, we consider some examples of shape optimization utilizing the thin waveguides model for the transmission computation. Furthermore, we study the application of the MMA method to optimize a junction of an open slab waveguide of constant thickness. In the last Section 5.2.3 of this Chapter, we show how the asymptotically small waveguide model can be used as an initial approximation in the open waveguide optimization procedure.

For both simplified methods, the optimization goal is to change the shape of the central trajectory such that the signal transmission is maximized. For the choice of the optimization scheme, we took into account that we are interested in unconditional optimization since possible constraints are added to the objective function as penalty terms. Accordingly, the optimization method from the family of Newton optimization methods should be well suited [37], [38].

Different choices of the Hessian matrix approximation give rise to different types of quasi-Newton methods. To experience the simplified transmission approximation methods on some examples of waveguide junction optimization, we choose the BFGS approach [18][36][39][76]. In addition, examples of the successful application of BFGS in combination with penalty functionals, defined depending on the formulation of the objective function, can be found in other works related to trajectory optimization. To minimize our unconstrained minimization problem, we follow the idea in [19]. There, a quasi-Newton regularized iterative scheme approach was utilized for an inverse problem reconstruction. We apply the classical quasi-Newton scheme with line search and decrease the regularization parameter in the objective function with the suitable penalty term iteratively as well.

Choice of the optimization method. For a given function $f\colon I_x \to \mathbb{R}$ and partition $\triangle_n : x_1 < \ldots < x_n,\ \triangle_n \subset I_x$, we can construct [42] a unique interpolating cubic spline function $f_{\triangle_n} \in \mathcal{C}^2([x_1,\, x_n])$ which coincides on each subinterval with cubic polynomial p_i

$$f_{\triangle_n}(x) = p_i(x), \quad x \in [x_i,\, x_{i+1}],\ i = 1,\, \ldots,\, n-1. \tag{132}$$

The constructed spline and its derivatives satisfy $p_i^{[l]}(x_i) = f^{[l]}(x_i)$, $p_i^{[l]}(x_{i+1}) = f^{[l]}(x_{i+1})$ for inner knotes $i = 2,\, \ldots,\, n-2$, $l \in \{0,\, 1,\, 2\}$ and called *complete* [25] if the following boundary conditions hold: $f'_{\triangle_n}(x_1) = f'(x_1)$, $f'_{\triangle_n}(x_n) = f'(x_n)$.

Let an objective function $\mathcal{T}\colon \mathbb{R}^N \to \mathbb{R}$, $N \in \mathbb{N}$ be two times continuously differentiable. Consider its quadratic approximation near $\mathbf{f}_J \in \mathbb{R}^N$

$$\mathcal{T}(\mathbf{f}_J + \mathbf{d}) \approx \mathcal{T}(\mathbf{f}_J) + \nabla\mathcal{T}(\mathbf{f}_J)^\top \mathbf{d} + \frac{1}{2}\mathbf{d}^\top \nabla^2\mathcal{T}(\mathbf{f}_J)\mathbf{d}.$$

Then the problem of minimizing $\mathcal{T}(\mathbf{f}_J + \mathbf{d})$ in the direction $\mathbf{d}$ for a given $\mathbf{f}_J$ in the quadratic approximation is replaced by the problem

$$\min_{\mathbf{d}} \left\{ \nabla\mathcal{T}(\mathbf{f}_J)^\top \mathbf{d} + \frac{1}{2}\mathbf{d}^\top \nabla^2\mathcal{T}(\mathbf{f}_J)\mathbf{d} \right\}$$

which has a solution $\mathbf{d} = -\big(\nabla^2\mathcal{T}(\mathbf{f}_J)\big)^{-1}\nabla\mathcal{T}(\mathbf{f}_J)$. If we consider $\mathbf{f}_J + \mathbf{d}$ as an approximation $\mathbf{f}_J^{(k+1)}$ at the kth, $k \in \mathbb{N}_0$ iteration of the optimization method, then

$$\mathbf{f}_J^{(k+1)} = \mathbf{f}_J^{(k)} - \big(\nabla^2\mathcal{T}(\mathbf{f}_J^{(k)})\big)^{-1}\nabla\mathcal{T}(\mathbf{f}_J^{(k)}),$$

which is the classical iterative Newton method to seek a zero of $\nabla\mathcal{T}(\mathbf{f}_J)$.

It is known that Newton's method converges to a local minimizer $\mathbf{f}_J^*$ only with a sufficiently good initial approximation $\mathbf{f}_J^{(0)}$. Moreover, we need to assume that Hessian $\nabla^2\mathcal{T}(\mathbf{f}_J^*)$ is positive definite, that the $\nabla^2\mathcal{T}(\cdot)$ is continuous in the neighborhood of the local minimizer $\mathbf{f}_J^*$, and satisfies the Lipschitz condition there (see, for example, Theorem 3.1.1 in [37] or Theorem 5.2.1 in [26]). The classical Newton method also requires the calculation and storage of the Hessian, as well as solutions to the related system of linear equations.

To get around some of the above difficulties with the Hessian, consider the kth iteration update reminiscent of Newton's method

$$\mathbf{f}_J^{(k+1)} = \mathbf{f}_J^{(k)} + h_k\mathbf{d}^{(k)}, \qquad \mathbf{d}^{(k)} = -\mathbf{H}_k\nabla\mathcal{T}(\mathbf{f}_J^{(k)}), \tag{133}$$

where matrix $\mathbf{H}_k$ replaces $\big(\nabla^2\mathcal{T}(\mathbf{f}_J^{(k)})\big)^{-1}$, and the step parameter h_k satisfies

$$\mathcal{T}(\mathbf{f}_J^{(k+1)}) \approx \min_h \mathcal{T}(\mathbf{f}_J^{(k)} + h\mathbf{d}^{(k)}). \tag{134}$$

Replacing the Hessian with something more suitable is the main idea of quasi-Newton methods. In order for the replacement matrix $\mathbf{H}_k$ of the inverse Hessian to satisfy the descent property the quasi-Newtonian conditions

$$\mathbf{H}_k\big(\nabla\mathcal{T}(\mathbf{f}_J^{(i+1)}) - \nabla\mathcal{T}(\mathbf{f}_J^{(i)})\big) = \mathbf{f}_J^{(i+1)} - \mathbf{f}_J^{(i)}, \quad i = 0,\, 1,\, \ldots,\, k-1,$$

must be satisfied. Such a sequence can be constructed in different ways, which in general can be formulated as

$$\mathbf{H}_{k+1} = \mathbf{H}_k + \mathbf{c}_k,$$

where $\mathbf{c}_k$ is some correction matrix. The choice of $\mathbf{c}_k$ generates a class of quasi-Newtonian optimization methods. In this work, we use the BFGS method, in which the update is defined for $\mathbf{B}_k := \mathbf{H}_k^{-1}$ by the following expression [18][36][39][76]

$$\mathbf{B}_{k+1} = \mathbf{B}_k + \frac{\mathbf{q}_k\mathbf{q}_k^\top}{\mathbf{q}_k^\top\mathbf{y}_k} - \frac{\mathbf{B}_k\mathbf{y}_k\mathbf{y}_k^\top\mathbf{B}_k^\top}{\mathbf{q}_k^\top\mathbf{y}_k\mathbf{q}_k}, \tag{135}$$

where

$$\mathbf{y}_k = \mathbf{f}_J^{(k+1)} - \mathbf{f}_J^{(k)}, \quad \mathbf{q}_k = \nabla\mathcal{T}(\mathbf{f}_J^{(k+1)}) - \nabla\mathcal{T}(\mathbf{f}_J^{(k)}). \tag{136}$$

5.1. Application of asymptotically small waveguides model.

In this section, we consider the trajectory optimization of the 1D closed waveguides (130). As was shown in Section 4.4, when computing the reflection coefficients, there

is an intense oscillatory behavior of the reflection power depending on the scaling parameter δ. The trajectory optimization problem is to minimize the reflected energy, the waveguide will be ideally conductive when there are no reflections $R = 0$. Consequently, when optimizing the shape of a 1D waveguide, the objective function oscillates, making it challenging for the optimization method to avoid getting trapped in the local minimum close to the initial guess and reach good solutions.

We will show that the BFGS, in combination with an iterative reduction of the regularization parameter until the reflection error dominates, allows us to find the local minimum of the regularized transmission minimization problem for structures of the shapes represented in the practical optical integration circuits application.

5.1.1. Optimization problem

In order to determine the objective functional for our optimization problem, we introduce a solution operator. Let us denote the set of admissible parameterizations of the central curve in a closed 1D waveguide as

$$\Upsilon := \big\{\Gamma \in \mathcal{C}^2\big([s_{\mathrm{L}},\, s_{\mathrm{R}}],\, \mathbb{R}^2\big) : \Gamma \text{ has no self-intersections,} \\ \operatorname{supp}(\kappa) \subset (s_{\mathrm{L}} + \delta_{s_{\mathrm{L}}}, s_{\mathrm{R}} - \delta_{s_{\mathrm{R}}}) \text{ is compact}\big\}.$$

For the given propagation constant in longitudinal direction $\beta_1 \in \mathbb{R}$ and parametrization of the central curve $\Gamma \in \Upsilon$ we define the trajectory-solution operator

$$\mathcal{S}_\kappa \colon \Upsilon \to H^1(s_{\mathrm{L}}, s_{\mathrm{R}}), \quad \Gamma \mapsto \mathcal{S}_\kappa(\Gamma) := u_1,$$

where u_1 is a solution to (130). In this section, we will consider the graph parameterization of the central curve $\Gamma = \big\{\big(s,\, f(s)\,\big),\, s \in [s_{\mathrm{L}},\, s_{\mathrm{R}}]\big\} \in \Upsilon$. In this case, we can define the solution operator with respect to f as $\mathcal{S}_\kappa(f, s) = u_1(s)$, $s \in [s_{\mathrm{L}}, s_{\mathrm{R}}]$. Then according to (125), the output reflection functional associated with the 1D problem (130) is

$$R \colon \Upsilon \to \mathbb{R}, \quad R(f) = \Big(\beta_1 |1 - \mathcal{S}_\kappa(f, s_{\mathrm{L}})|^2\Big)\Big(\beta_1 |\mathcal{S}_\kappa(f, s_{\mathrm{L}})|^2\Big)^{-1}. \tag{137}$$

To evaluate the relative reflection we compute a numerical solution to (130) with FEM. We consider the following decomposition of the 1D computational domain

$$\triangle_n := \{s_{\mathrm{L}} = s_1 < \ldots < s_{\mathrm{L}} + \delta_{\mathrm{L}} < \ldots < s_{\mathrm{R}} - \delta_R < \ldots < s_n = s_{\mathrm{R}}\}.$$

For the trajectory update in the optimization method we introduce the subgrid of the decomposition $\triangle_n$

$$\triangle_p := \{s_{\mathrm{L}} = s_1 < \ldots < s_{\mathrm{L}} + \delta_{\mathrm{L}} < \ldots < s_{\mathrm{R}} - \delta_R < \ldots < s_p = s_{\mathrm{R}}\},\ \triangle_p \subset \triangle_n. \tag{138}$$

Let us denote the indices in the partition (138) indicating the knots supporting the curved part of the waveguide $s_{\mathrm{L}} + \delta_L < s_j < s_{\mathrm{R}} - \delta_R$, $s_j \in \triangle_p$ as $s_{\mathrm{L}_J} := s_{\mathrm{L}} + \delta_L$ and $s_{\mathrm{R}_J} := s_{\mathrm{R}} - \delta_R$. We construct the spline approximation $f_{\triangle_p}$ of the central trajectory with respect to the uniform decomposition $\triangle_p$ (132).

Due to the strong oscillatory behavior of the relative reflection in the 1D closed waveguide model (see Section 4.4.3, 4.4.2, 4.4.1), we will utilize the following curvature regularization term in the unconstrained optimization procedure

$$\mathcal{R}\colon \mathcal{S}_{\triangle} \to \mathbb{R}, \quad \mathcal{R}(f_{\triangle p}) := \Big(\int_{s_1}^{s_p} \frac{|f''_{\triangle_p}(s)|^2}{\big(1 + (f'_{\triangle_p}(s))^2\big)^3} \, \mathrm{d}s \Big)^{\frac{1}{2}}, \tag{139}$$

where $\mathcal{S}_{\triangle}$ denotes the space of complete cubic splines (132) constructed for the $\triangle_p$ partition.

We fix the points $\triangle_p$ and the values $f_j = f(s_j) : j \le \mathrm{L}_J, j \ge \mathrm{R}_J$, $s_j \in \triangle_p$ corresponding to the straight connecting parts of the waveguide (119) to ensure that during the optimization process the trajectories of the central curves always have zero curvature on the connecting parts, and the structure of the scattering problem in the sense of the correctness of the constructed radiation conditions does not change.

Hence we can readjust the approximation of the central trajectory defined by the graph parametrization varying the values of $\mathbf{f}_J := (f_{\mathrm{L}_J+1}, \ldots, f_{\mathrm{R}_J-1})^{\top}$ at the points $s_j \in \triangle_p$ associated with the waveguide junction.

Then with (139) the problem of minimizing the signal loss along the 1D conducting optical structure (130) is to find

$$\min_{\mathbf{f}_J} \{ R(f_{\triangle_p}) + \rho \, \mathcal{R}(f_{\triangle p}) \} \tag{140}$$

the values $\mathbf{f}_J$ related to the curved part of the waveguide such that the approximate relative reflection power $R(f_{\triangle_p})$, $R\colon \mathcal{S}_{\triangle} \to \mathbb{R}$ (137) will be locally minimized. Here $\rho\mathcal{R}(f_{\triangle p})$ is the penalty term with some regularization parameter $\rho \in (0, 1]$. The reflection term $R(f_{\triangle_p})$ utilizes the central trajectory approximation by spline, which is constructed for the set of values $\mathbf{f}_J$ and for the fixed values related to the straight connecting parts $f_j = f(s_j) : j \le \mathrm{L}_J, j \ge \mathrm{R}_J$, $s_j \in \triangle_p$ with respect to the knots $\triangle_p$, that are all fixed during the optimization.

5.1.2. Example: Shifted hump.

In this work we utilize the same optimization scheme for the 1D closed waveguides and 2D slab open waveguides with constant thickness. Therefore, the steps of BFGS via MMA application for the 2D slab waveguide described in Section 5.2.2 can also be applied to the 1D waveguide optimization with BFGS via FEM for $\min_{\mathbf{f}_J} \mathcal{T}(\mathbf{f}_J)$, where $\mathcal{T}(\mathbf{f}_J) := R(f_{\triangle_p}) + \rho \, \mathcal{R}(f_{\triangle p})$ (140).

We shift the right-side straight connection part of the $\mathcal{C}^2$-hump in the orthogonal direction to propagation and lift up one of the ends of the hump (131), calling this type of trajectory a *shifted hump*.

$$f(s) = \begin{cases} 0, & s_{\mathrm{L}} \le s \le s_{\mathrm{L}_J}, \\ 64 \, \mathrm{H_J} \, s^3 \Big(1 - s\Big)^3 + \mathrm{D} \, s^2 \Big(3 - 2\,s\Big), & s_{\mathrm{L}_J} < s < s_{\mathrm{R}_J}, \\ \mathrm{D}, & s_{\mathrm{R}_J} \le s \le s_R, \end{cases} \tag{141}$$

where $\mathrm{H_J} > 0$ is the height, $\mathrm{D} < \mathrm{H_J}$ is prescribed shift. We take $\mathrm{H_J} = 1$ µm, $\mathrm{D} = 0.5$ µm. We set the following waveguide parameters

$$n_{\mathrm{co}} = 1.5, \qquad \lambda_0 = 1.8/\sqrt{2}\,\mu\mathrm{m}, \qquad s_{\mathrm{L}} = -0.5\mu\mathrm{m},\ s_{\mathrm{R}} = 1.5\mu\mathrm{m}, \qquad \delta_{s_{\mathrm{L}}} = \delta_{s_{\mathrm{R}}} = 0.5\mu\mathrm{m}.$$

In order to compute reflection values, we seek a numerical solution to the 1D waveguide problem (130) with FEM in the computational domain $[-0.5,\ 1.5]$. We decompose the computational domain to obtain $\triangle_n$ partition, $n = 77$. For the subgrid $\triangle_p$ we choose $p = 21$. We fix 6 points in $\triangle_p$ related to the left and right straight connection parts in which corresponding values f_i remain unchanged during the optimization.

The trajectory (141) is interpolated via a complete cubic spline (132) with respect to the subgrid $\triangle_p \subset [-0.5,\ 1.5]$. For $s \in [-0.5,\ 0]$, $s \in [1,\ 1.5]$ the curve (141) is represented by straight line, we choose the complete cubic spline slopes $f'(s_1) = f'(s_p) = 0$ and define the related polynomials of zero degree over left and right straight connection parts $p_1\Big|_{[-0.5,\,0]} = 0,\ p_n\Big|_{[1,\,1.5]} = \mathrm{D}$ explicitly.

The initial trajectory (141) provides relative reflection power R =8.12e−01 for the 1D problem by computations via FEM with pd = 3, h = 0.026 µm. The relative reflection in a thin 2D waveguide of width $\delta = 0.04$ µm generated by the same trajectory is R =8.2e−05. We computed it with the TO method applying FEM in the computational domain $\Omega_h = [0,\ 3.36] \times [-0.02,\ 0.02]$ with parameters pd = 2, h =0.0075 µm.

Optimization of the 1D waveguide with the regularization parameter $\rho = 1$ provides reflection power R = 2.49e−10, and $\|\nabla\mathcal{T}(\mathbf{f}_j^*)\|_\infty$ =1.82e−06. BFGS computational time via 1D FEM is 77 sec.

The relative reflection power in the corresponding 2D closed waveguide with thickness $\delta = 0.04$ µm is R =1.92e−08, computed via FEM in the computational domain $[0,\ 2.15] \times [-0.02,\ 0.02]$ with piecewise polynomial functions of second order pd = 2 and mesh size h = 0.0048 µm.

We can observe that the optimized trajectories provide lower relative reflection power than the initial trajectories (141) in 1D and 2D cases as expected.

Figure 44 shows the dependence of relative reflection R on the scaling parameter δ for the sequence of shrinking 2D waveguides generated by the initial (blue) and optimized (black) trajectory. The reflection corresponding to the optimized trajectory is less than the values provided by the initial trajectory for the entire set of δ parameters. The oscillating character of the relative reflection is typical for the closed waveguide. The reference value obtained as a result of the 1D waveguide optimization is marked in red.

Despite the fact that we need to find a numerical solution to the boundary value problem (130) during the optimization process, considering that this is a 1D problem, this minimization is quite efficient.

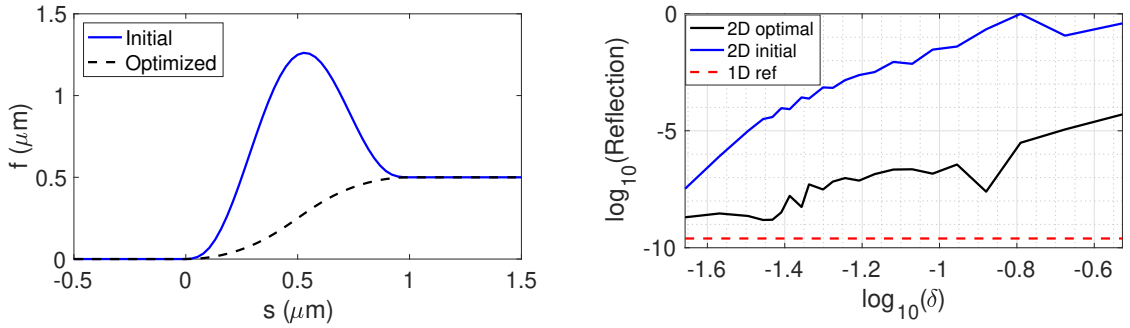

Figure 44: 1D optimization. **Left**: initial and optimized trajectories with BFGS via FEM pd = 3, h = 0.026 μm for (130). Regularization parameter $\rho = 1$. **Right**: The relative reflection $R \in [0, 1]$ as a function of δ in the 2D $\mathcal{C}^2$-shifted hump (blue) and in the 2D waveguide generated by the optimized trajectory (black), FEM pd = 2, 18 cells per dimension w.r.t scaling. R provided by the optimized 1D trajectory (red).

5.2. Application of MMA

We emphasize that the optimization scheme described in this section does not require a numerical solution of the boundary value problem (66), since the transmission computation with the MMA method (65) is based on the pre-calculated database of transmission coefficients (55). Furthermore, the size of open waveguides that need to be optimized corresponds to the structures built on real-life silicon photonic chips.

We consider the same slab waveguide parameters as in the previous chapters 2 and 3

$$d = 1.8\,\mu\text{m}, \quad n_{\text{co}} = 1.53, \quad n_{\text{cl}} = 1.36, \quad \lambda_0 = 1.55\,\mu\text{m}.$$

Here d is the thickness, n_{co} and n_{cl} are the refractive indices in the core and the cladding, λ_0 is the vacuum wavelength.

5.2.1. Optimization problem

Let the central trajectory of the waveguide be given via the graph parameterization $\Gamma := \{ (x, f(x)),\ x \in [0, L_x] \}$ with straight offsets defined with $\text{supp}(\kappa) \subset [x_L, x_R]$, $x_L, x_R \in (0, L_x)$. For the optimization problem, we introduce a partition

$$\triangle_p := \{0 = x_1 < \ldots < x_{\text{L}} < \ldots < x_{\text{R}} \ldots < x_p = L_x\}, \tag{142}$$

where x_{L} denotes the end of the left straight waveguide offset and x_{R} denotes the beginning of the right straight waveguide offset. Then $x_j \in \triangle_p$ with $\text{L} < j < \text{R}$ are the points associated with the waveguide junction.

Next we construct a spline approximation $f_{\triangle_p}$ of the given central curve with respect to the partition $\triangle_p$ (132). We want to find the total transmission associated with $f_{\triangle_p}$ via MMA method. Therefore, to define the segments for the MMA method, we divide the approximated by $f_{\triangle_p}$ curve with respect to the refined partition

$$\triangle_n := \{0 = x_1 < \ldots < x_n = L_x\}, \quad \triangle_p \subset \triangle_n. \tag{143}$$

Then with (61) we can find the mean curvature of each MMA segment

$$\widetilde{\kappa}_i = \frac{1}{x_{i+1} - x_i} \int_{x_i}^{x_{i+1}} \frac{|f''_{\triangle_p}(x)|}{\left(1 + (f'_{\triangle_p}(x))^2\right)^{\frac{3}{2}}} \,\mathrm{d}x, \quad x_i,\, x_{i+1} \in \triangle_n \tag{144}$$

and approximate the waveguide with a sequence of segments of constant radii of curvature $R_i^+ = 1/\widetilde{\kappa}_i$, $i = 1, \ldots, n-1$. According to (63) we can compute the total transmission with the resulting sequence of radii of curvature R_i^+, $i = 1, \ldots, n-1$.

If we fix all knots $\triangle_p$ and the values $f_j = f(x_j)$, $j \le \mathrm{L}$, $j \ge \mathrm{R}$, $x_j \in \triangle_p$ corresponding to the straight offsets, then we can change the shape of the central curve by varying the values of $\mathbf{f}_J := (f_{\mathrm{L}+1}, \ldots, f_{\mathrm{R}-1})^\top$ at the knots $x_j \in \triangle_p$ associated with the waveguide junction. Then the related curvature sequence (144) can be found by constructing the new spline $f_{\triangle_p}$ corresponding to the fixed partition $\triangle_p$ and the new values $\mathbf{f}_J$ at the junction knots.

From (144) and (63) we can see that the total power transmission depends on the trajectory of the central curve approximated by splines $T = T(f_{\triangle_p})$. Therefore, the MMA transmission maximization problem can be formulated as follows

$$\min_{\mathbf{f}_J} \{1 - T(f_{\triangle_p})\}. \tag{145}$$

The waveguide is ideally conductive when the total power transmission is $T(f_{\triangle_p}) = 1$. Accordingly, the problem (145) is the problem of minimizing losses by changing the shape of the curve connecting the straight offsets.

Based on observations of the dependence of the transmission on the curvature of the central curve in Section 3.2, we ensure that the central trajectory curvature is not highly oscillating. We denote by $\mathcal{S}_{\triangle_p}$ the space of complete cubic splines (132) constructed for the $\triangle_p$ partition. The regularization term $\mathcal{R}\colon \mathcal{S}_\triangle \to \mathbb{R}$ is defined by

$$\mathcal{R}(f_{\triangle_p}) := \Big(\int_{x_1}^{x_p} \frac{|f''_{\triangle_p}(x)|^2}{\left(1 + (f'_{\triangle_p}(x))^2\right)^3} \,\mathrm{d}x \Big)^{\frac{1}{2}}.$$

Then instead of (145) we consider the following unconstrained optimization problem

$$\min_{\mathbf{f}_J} \{1 - T(f_{\triangle_p}) + \rho\, \mathcal{R}(f_{\triangle_p})\}, \tag{146}$$

where $\rho\mathcal{R}(f_{\triangle_p})$ is the penalty term with some regularization parameter $\rho \in (0, 1]$.

5.2.2. Optimization scheme

Next, we describe the steps of the quasi-Newton BFGS optimization scheme (135) applied to maximize the amount of the transmitted energy in a slab waveguide with constant width. With the fixed $(x_j,\, f_j)$ associated with straight offsets we can denote $\mathcal{T}(\mathbf{f}_J) := 1 - T(f_{\triangle_p}) + \rho\, \mathcal{R}(f_{\triangle_p})$, and consider the minimization problem (146) $\min_{\mathbf{f}_J} \mathcal{T}(\mathbf{f}_J)$.

1. The initial guess $\mathbf{f}_J^{(0)}$ is given by function (e.g. (148) or (149)) evaluated in the knots associated with the waveguide junction

$$\mathbf{f}_J^{(0)} = (f_j^{(0)})_{\mathrm{L}<j<\mathrm{R}}, \quad f_j^{(0)} := f(x_j),\ x_j \in \triangle_p,\ x_{\mathrm{L}} < x_j < x_{\mathrm{R}}. \tag{147}$$

   The initial guess of the Hessian matrix is $\mathbf{B}_0 := \mathbf{I}$.

2. At the kth iteration of the BFGS method, $k \in \mathbb{N}_0$
   (i) The direction $\mathbf{d}^{(k)}$ is defined with (133)

$$\mathbf{B}_k \mathbf{d}^{(k)} = -\nabla \mathcal{T}(\mathbf{f}_J^{(k)}),$$

   where we approximate the gradient of the objective function with the help of finite differences $\nabla \mathcal{T}(\mathbf{f}_J^{(k)}) \approx (1/\varepsilon)\Big(\mathcal{T}[(f_j^{(k)} + \varepsilon)_{\mathrm{L}<j<\mathrm{R}}] - \mathcal{T}[(f_j^{(k)})_{\mathrm{L}<j<\mathrm{R}}]\Big)$. We take ε =1e−06.

   (ii) To determine the step parameter h_k in (133), the (134) minimization subproblem is solved $h_k = \arg\min_h \mathcal{T}(\mathbf{f}_J^{(k)} + h\mathbf{d}^{(k)})$. The standard libraries solve this problem with an indirect linear search method [37].

   (iii) Next, with updated h_k and $\mathbf{d}^{(k)}$ we can update the argument of the objective function $\mathbf{f}^{(k+1)} = \mathbf{f}^{(k)} + h_k \mathbf{d}^{(k)}$. Hence, by (136) we can update $\mathbf{y}_{k+1} = h_k \mathbf{d}^{(k)}$, $\mathbf{q}_k = \nabla \mathcal{T}(\mathbf{f}_J^{(k+1)}) - \nabla \mathcal{T}(\mathbf{f}_J^{(k)})$. Then, these terms are utilized in the update for the BFGS expression for the Hessian (135).

3. We terminate the optimization procedure when the relative bound of the step size $|\mathbf{f}_J^{(k)} - \mathbf{f}_J^{(k+1)}|/|\mathbf{f}_J^{(k)}| < \texttt{Tol}$ holds. We choose $\texttt{Tol}$ =1e−06. Then with the resulting values associated with the junction-related knots $\mathbf{f}_J^* := \mathbf{f}_J^{(k)}$ together with the fixed values related to the offset knots, we can construct the spline function $f^*_{\triangle p}$. The resulting $f^*_{\triangle_p}$ generates the locally optimal central trajectory of the slab waveguide, which provides maximized transmission between input and output offsets of the waveguide.

4. If the impact of the regularization term $\rho \mathcal{R}(f^*_{\triangle n})$, dominates the residual value of the objective function $\mathcal{T}(\mathbf{f}_J^*)$, then we decrease the value of the regularization parameter $\rho_{l+1} = \rho_l/10$, $l \in \mathbb{N}_0$. Next, we repeat the optimization procedure taking optimal $\mathbf{f}_J^*$ obtained with regularization parameter ρ_l as the initial guess $\mathbf{f}_J^{(0)} := \mathbf{f}_J^*$.

5.2.3. Numerical examples

We consider in this section two examples of the MMA and other simplified methods application to our optimization problem (146).

Example: Hump. We consider a slab open waveguide with the central trajectory $\Gamma := \{ (x,\, f(x)),\ x \in [0,\, L_x]\}$, $\mathrm{supp}(\kappa) \subset [x_L,\, x_R]$ defined by hump of height $\mathrm{H_J} > 0$

$$f(x) = \begin{cases} 64\,\mathrm{H_J}\dfrac{x^3}{L^3}\Big(1-\dfrac{x}{L}\Big)^3, & x_\mathrm{L} < x < x_\mathrm{R}, \\ 0, & \text{otherwise}, \end{cases} \tag{148}$$

where $L = |x_\mathrm{R} - x_\mathrm{L}|$. In order to evaluate $\mathcal{T}(\mathbf{f}_J)$ with MMA in the optimization scheme, we define the arclength partition $\triangle_n^s : 0 = s_1 < \ldots < s_n = L_s$ such that $s_{j+1} - s_j = 2/\pi$. We determine the related $\triangle_n^x$ partition (143) by (59) and choose $p = 16$ to obtain the subgrid $\triangle_p$. We fix 4 points corresponding to the ends of the left and right straight offsets.

We interpolate the central trajectory with the help of the cubic spline (132) for the partition $\triangle_p \subset [0,\, L_x]$. For $x \in [0,\, x_\mathrm{L}]$, $x \in [x_\mathrm{R},\, L_x]$ the central curve (148) is represented by a straight line. Therefore for the spline construction we choose the complete cubic spline slopes $f'(x_1) = f'(x_p) = 0$ and define corresponding polynomials of zero degree over left and right straight offsets $p_1\Big|_{[0,\,x_\mathrm{L}]} = 0$, $p_n\Big|_{[x_\mathrm{R},\,L_x]} = 0$ explicitly. With this redefinition of the polynomials on the offsets, we now have $f_{\triangle_p} \in \mathcal{C}^2([x_\mathrm{L},\, x_\mathrm{R}])$ instead of the entire interval $[x_1,\, x_p]$.

We study the application of the optimization scheme for a hump of height $\mathrm{H_J}$=42 µm and length $L_x = 100$ µm. Transmission associated with such central trajectory is given by FEM with pd = 3, h = $\lambda_0/10$ is 3.33e−01 (-4.7756 dB). This is a waveguide in which the interaction of the second mode with the first generates large losses. See Figure 45 top row.

Optimization with regularization parameter $\rho = 0.5$ provides transmission 0.9972 (-0.0122 dB). In Figure 45, we can see that the signal loss $\mathcal{T}(\mathbf{f}_J^{(k)})$ decreases with each iteration of the optimization method. As expected for this case, the optimized waveguide is a straight waveguide. All energy is transferred by the fundamental mode, see Figure 45, center row. BFGS computational time via MMA is 1.36e+03 sec, approximated $\|\nabla\mathcal{T}(\mathbf{f}_J^*)\|_\infty$ =4.92e−07.

Example: Shifted hump. Now, we consider a more advanced example where the optimized junction is not represented by a straight line. We will shift one of the straight offsets in y-direction and hence lift up one of the ends of the hump (148).

The central trajectory when the junction is represented by the shifted hump of height $\mathrm{H_J} > 0$ with prescribed shift $\mathrm{D} < \mathrm{H_J}$ is defined with

$$f(x) = \begin{cases} 0, & 0 \le x \le x_\mathrm{L}, \\ 64\,\mathrm{H_J}\dfrac{x^3}{L^3}\Big(1-\dfrac{x}{L}\Big)^3 + \mathrm{D}\dfrac{x^2}{L^2}\Big(3-2\dfrac{x}{L}\Big), & x_\mathrm{L} < x < x_\mathrm{R}, \\ \mathrm{D}, & x_\mathrm{R} \le x \le L_x, \end{cases} \tag{149}$$

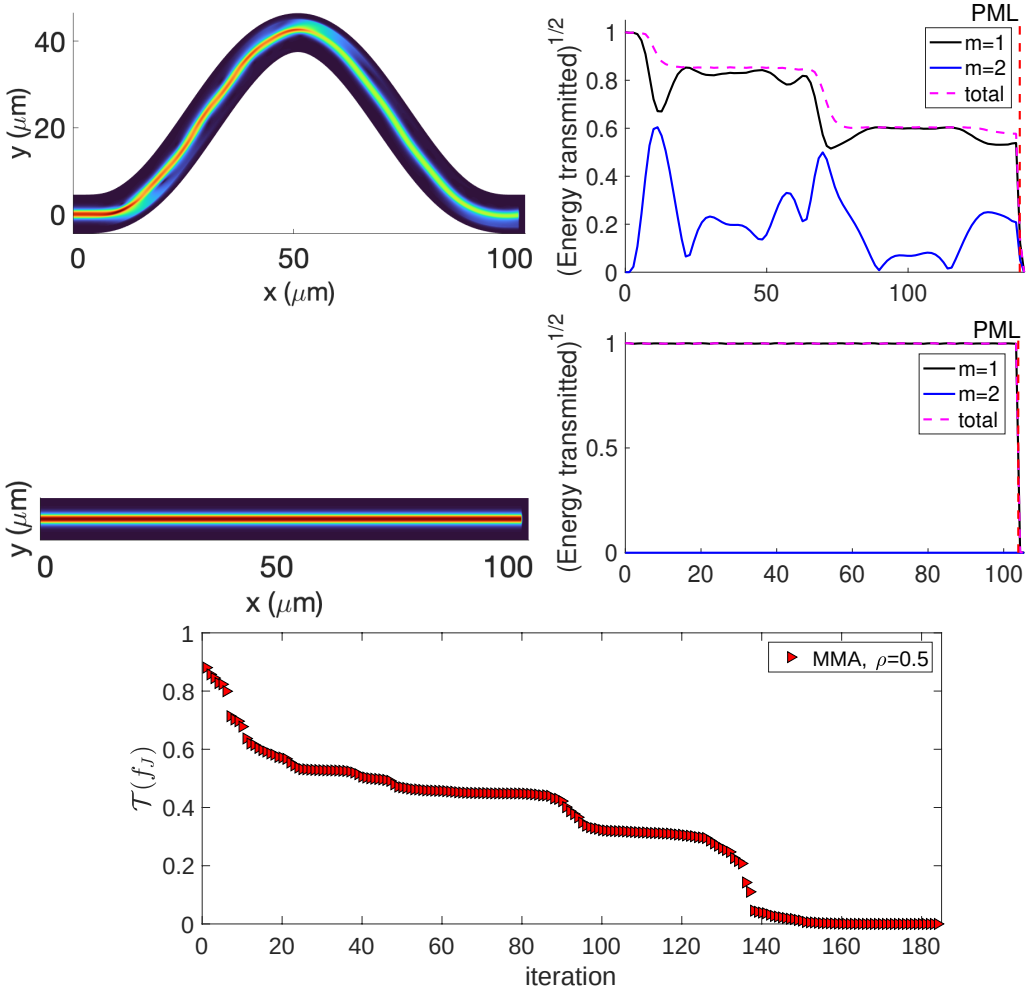

Figure 45: Optimization of the hump of height H_J=42 µm, open waveguide. **Top row**: field magnitude corresponding to the initial curve (148), significant amount of the energy is dissipated. Corresponding transmission distribution between two modes along the propagation direction. **Center row**: field magnitude of the waveguides generated by optimal central trajectory found with BFGS via MMA, $\rho = 0.5$, and corresponding mode interaction along the propagation direction. **Bottom**: signal loss $\mathcal{T}(\mathbf{f}_J^{(k)})$ with penalty term $\rho = 0.5$ computed with MMA versus BFGS iteration k.

where $L = |x_{\mathrm{R}} - x_{\mathrm{L}}|$.

In order to approximate transmission to evaluate $\mathcal{T}(\mathbf{f}_J)$ in the optimization scheme via the MMA method, we choose the arclength partition $\triangle_n^s : 0 = s_1 < \ldots < s_n = L_s$ such that $s_{j+1} - s_j = 2/\pi$. We compute the corresponding $\triangle_x$ partition (143) by (59). For the subgrid $\triangle_p$ we choose $p = 16$. We fix 4 points related to the ends of the left and right straight offsets in which corresponding values f_i do not change during the minimization process.

We interpolate (149) with the help of the cubic spline (132) for the partition $\triangle_p \subset [0, L_x]$. Since we know that for $x \in [0, x_{\mathrm{L}}]$, $x \in [x_{\mathrm{R}}, L_x]$ the central curve (149)

is represented by straight line, we choose the complete cubic spline slopes $f'(x_1) = f'(x_p) = 0$ and define corresponding polynomials of zero degree over left and right straight offsets $p_1\Big|_{[0,\,x_{\mathrm{L}}]} = 0$, $p_n\Big|_{[x_{\mathrm{R}},\,L_x]} = \mathrm{D}$ explicitly. With this redefinition of the polynomials on the offsets, we now have $f_{\triangle_p} \in C^2([x_{\mathrm{L}},\, x_{\mathrm{R}}])$ instead of the entire interval $[x_1,\, x_p]$.

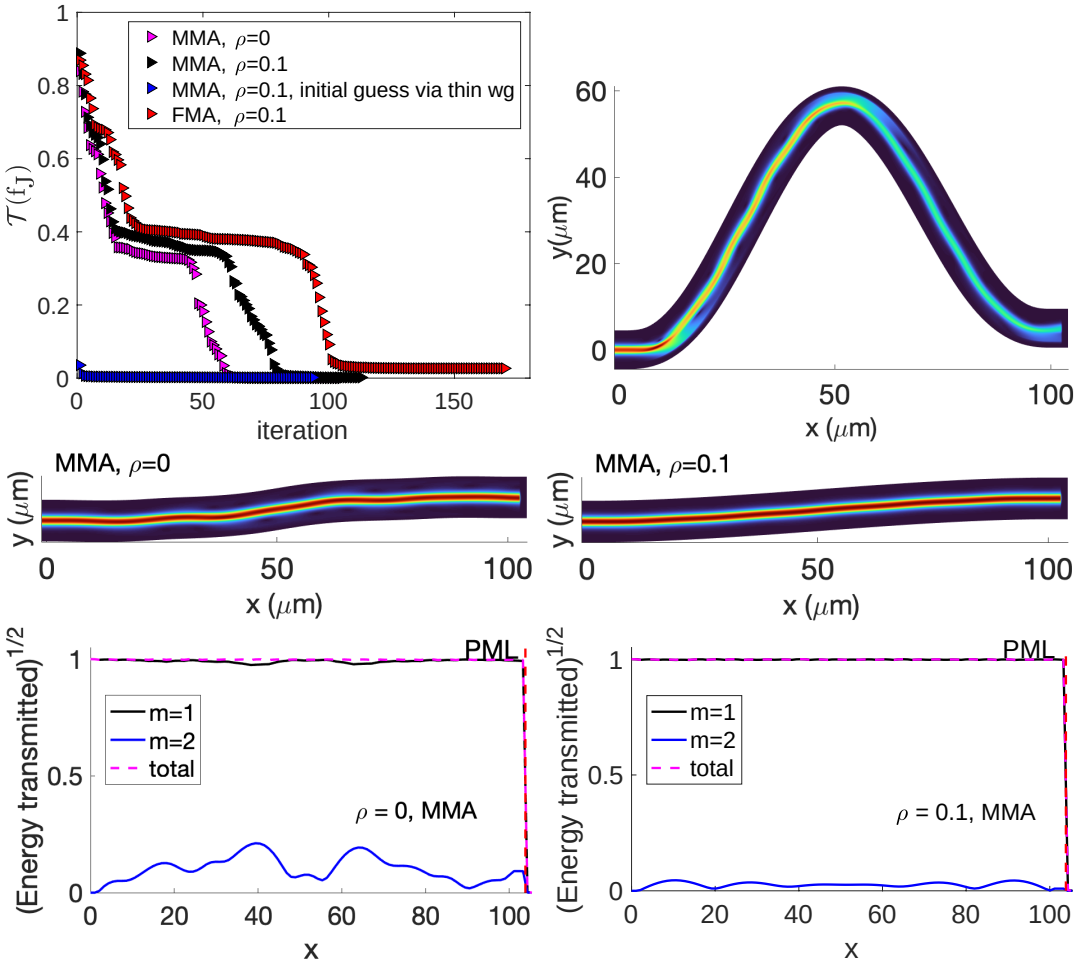

Figure 46: Optimization of the shifted hump of height $\mathrm{H_J}$=55 μm, open waveguide. **Top left**: signal loss $\mathcal{T}(\mathbf{f}_J^{(k)})$ with possible penalty term computed with MMA and FMA versus BFGS iteration k. **Top right**: field magnitude corresponding to the initial curve (149), most of the energy is dissipated. **Center row**: field magnitude of the waveguides generated by optimal central trajectory found with BFGS via MMA. On the left without regularization ($\rho = 0$), on the right with the starting regularization parameter $\rho = 0.1$. **Bottom row**: Corresponding transmission distribution between two modes along the propagation direction.

Application of regularized MMA, FMA, and MMA with thin waveguide model initial guess. Next, we will compare different simplified approaches for the transmis-

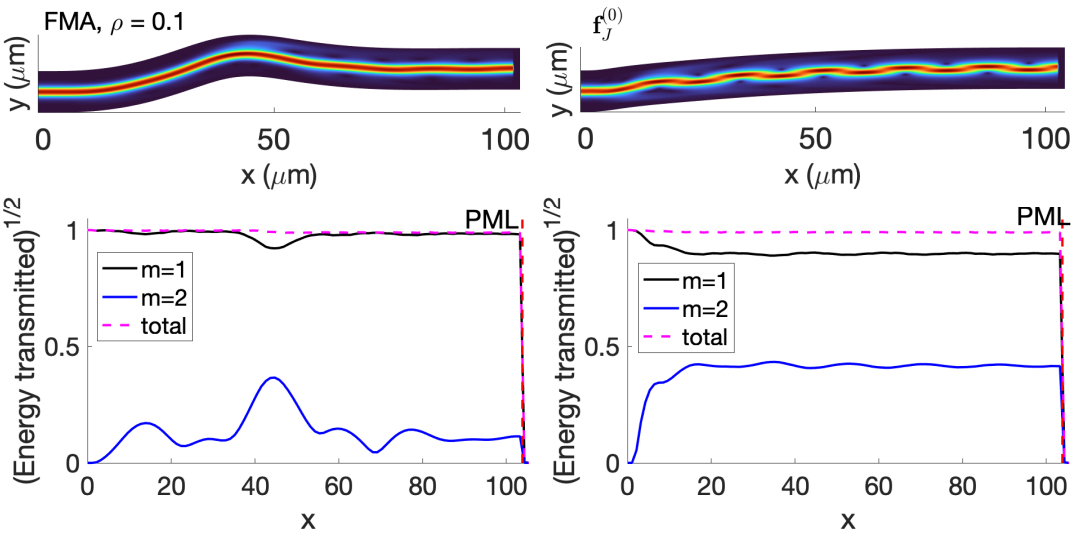

Figure 47: Optimization of the shifted hump of height H_J=55 µm, open waveguide. **Left top**: field magnitude of the waveguide generated by optimal central trajectory found with BFGS via FMA, with the starting regularization parameter $\rho = 0.1$. The magnitude of the fields obtained with FEM, pd = 3, $h = \lambda_0/10$. **Left bottom**: the distribution of transmitted energy along the waveguide associated with $\mathbf{f}_J^*$ obtained with BFGS via FMA, $\rho = 0.1$. **Right top**: field magnitude computed with FEM, pd = 3, $h = \lambda_0/10$ for the waveguide generated by initial guess $\mathbf{f}_J^0$ trajectory found with BFGS via thin waveguides approach. **Right bottom**: the distribution of transmitted energy along the waveguide associated with $\mathbf{f}_J^{(0)}$.

sion computation used in the optimization scheme 5.2.2 for a shifted hump of height H_J = 55 µm, L_x=100 µm, D=5 µm (149). The waveguide is called ideally conducted if the transmission is 1 (0 dB). The transmitted energy obtained with FEM pd = 3, $h = \lambda_0/10$ associated with the initial trajectory is 0.1579 (-8.0162 dB). Such a central curve corresponds to the initial guess, which is far from an optimal solution. See Figure 46, top right.

First we consider MMA without regularisation, i.e. $\rho = 0$ in (146). We can see in Figure (46) that the signal loss $\mathcal{T}(\mathbf{f}_J^{(k)})$ decreases with each iteration of the optimization method. The approximated first-order optimality measure is $\|\nabla\mathcal{T}(\mathbf{f}_J^*)\|_\infty$ = 4.01e−05. The transmitted energy of the optimized trajectory computed with FEM is 0.89 (0.5061 dB). BFGS computational time is 8.74e+02 sec.

In case of MMA with $\rho = 0.1$, BFGS converges slower, but the transmission of the optimized trajectory 0.997 (-0.0122 dB) is much better. The approximated first-order optimality measure is $\|\nabla\mathcal{T}(\mathbf{f}_J^*)\|_\infty$ =3.68e−06. Optimization computational time is 1.1784e+03.

The magnitude of the fields of slab open waveguides generated by trajectories optimized with $\rho = 0$ and $\rho = 0.1$ computed with FEM can be found in Figure 46, central row. The corresponding distribution of the transmitted signal along the propagation

direction x between two modes, which can be seen in the bottom row of Figure 46, also indicates that the energy associated with the curve optimized with regularization is transmitted by the first mode. While in a waveguide corresponding to the curve optimized without regularization, the variability of the curvature gives rise to the excitation of the second mode, which leads to a lower value of transmitted energy, as expected.

The impact of the second mode on the optimization process can also be seen from the optimization results for FMA. The waveguide of the corresponding trajectory optimized with the regularization parameter $\rho = 0.1$ is shown in Figure 47, left. The transmitted energy in the resulting structure is 0.97 (-0.1323 dB), which is less than obtained with the regularized optimization via MMA discussed above. BFGS computational time is 1.657e+03, $\|\nabla\mathcal{T}(\mathbf{f}_J^*)\|_\infty = 1.96\text{e}{-04}$.

Now we consider regularized optimization via MMA with initial guess $\mathbf{f}_J^{(0)}$ obtained by the thin waveguide approach with $\|\nabla\mathcal{T}(\mathbf{f}_J^*)\|_\infty = 1.4\text{e}{-04}$. In Figure 47, bottom right, we can see the energy distribution between modes in the waveguide generated by such $\mathbf{f}_J^{(0)}$. Although a significant part of the signal is transmitted by the second mode there, signal losses are low since the second mode transfers it without coupling back into the fundamental mode. The transmitted energy before and after regularized optimization with $\rho = 0.1$ is 0.98 (-0.0877 dB) and 0.997 (-0.0122 dB). $\|\nabla\mathcal{T}(\mathbf{f}_J^*)\|_\infty = 3.09\text{e}{-06}$. Total optimization computational time is 8.45e+02 sec, including 3.83e+02 sec for the computation of the initial guess $\mathbf{f}_J^{(0)}$ and 4.62e+02 sec for BFGS optimization via MMA with $\rho = 0.1$.

Hence, the initial guess $\mathbf{f}_J^{(0)}$ obtained from thin waveguides model optimization increase the efficiency of optimization procedure for the open waveguides via MMA even more.

Figure 48, left, shows the total transmission for a set of shifted humps (149) with the apex height $\mathrm{H_J} \in \{5, 6, \ldots, 55\}$ µm, L_x=100 µm, D=5 µm. The red line corresponds to the initial trajectories, and the blue line to optimized central curves via MMA with the parameters of the starting regularization $\rho \in (0, 1]$. Figure (48) on the right shows the transmission of the first and second modes of the optimized and initial trajectories. Our results are in good qualitative accordance with the work [49]. There the signal transmission in slab waveguides with constant thickness after optimization of the central trajectories is carried mostly by the fundamental mode as well. Thus, we can say that for (149), BFGS, with the application of the simplified methods for the open slab waveguide transmission computation, has acceptable behavior.

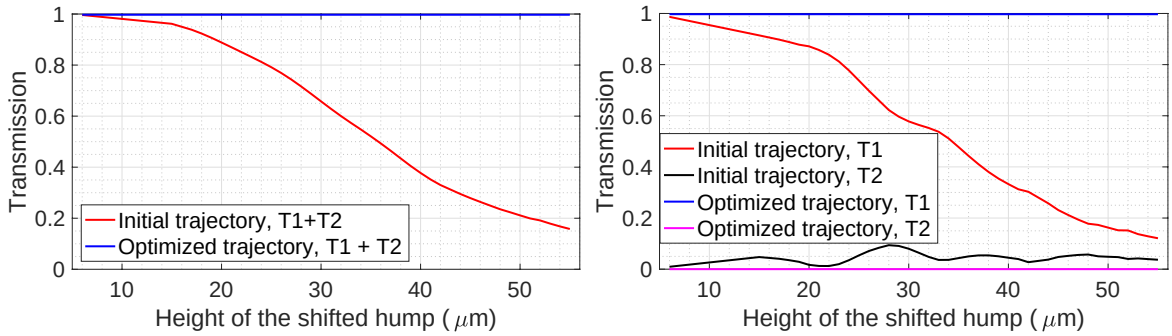

Figure 48: Transmitted energy computed with FEM pd $= 3$, $h = \lambda_0/10$ versus apex height of shifted humps (149) associated with the central trajectories before and after BFGS via MMA optimization, $\rho \in (0, 1]$. **Left**: total transmission; **Right**: 1st and 2nd modes.

A. Lamé coefficients

Lamé coefficients are a convenient tool for studying partial differential equations in various coordinate systems. If we know the form of the system in curvilinear orthogonal coordinates, it remains only to calculate the *scale factors.*

The expression for the gradient of a scalar function in a curvilinear orthogonal coordinate system (ξ, η) for the Lamé coefficients h_ξ, h_η is

$$\nabla u = \mathbf{e}_\xi \frac{1}{h_\xi} \cdot \frac{\partial u}{\partial \xi} + \mathbf{e}_\eta \frac{1}{h_\eta} \cdot \frac{\partial u}{\partial \eta},$$

where $\mathbf{e}_\xi, \mathbf{e}_\eta$ are unit vectors along the coordinate directions.

For a vector $\mathbf{a} = (a_\xi, a_\eta)^\top$ the divergence in curvilinear orthogonal coordinates is represented with

$$\operatorname{div} \mathbf{a} = \frac{1}{h_\xi h_\eta} \Big(\frac{\partial}{\partial \xi} (h_\eta a_\xi) + \frac{\partial}{\partial \eta} (h_\xi a_\eta) \Big).$$

Therefore, for the Laplacian applied to a scalar function, we have the following expression

$$\Delta u = \frac{1}{h_\xi h_\eta} \left(\frac{\partial}{\partial \xi} \left(h_\eta \Big(\frac{1}{h_\xi} \frac{\partial u}{\partial \xi} \Big) \right) + \frac{\partial}{\partial \eta} \left(h_\xi \Big(\frac{1}{h_\eta} \frac{\partial u}{\partial \eta} \Big) \right) \right). \tag{150}$$

For example, consider the problem in the geometric setting with cylindrical symmetry (15). Then, it will be helpful to consider it in cylindrical coordinates $\xi \to r$, $\eta \to \theta$. The corresponding Lamé coefficients are [30]

$$h_\xi = h_r = 1, \; h_\eta = h_\theta = r.$$

Nomenclature

Finite elements

cells The elements of an admissible mesh

h Mesh width, maximum cell diameter

pd Order of piecewise polynomial functions which form the finite element space over mesh

Ω_h Computational domain, polygonal approximation to the Ω

u_h Discrete approximation of a continuous function $u \in V$ defined in the finite-dimensional subspace $V_h \subset V$

Geometry notation

(x, y) Usual point in $\mathbb{R}^2$

Γ Plane curve, $\Gamma\colon I \to \mathbb{R}^2$ $s \mapsto \big(\Gamma_1(s), \Gamma_2(s)\big)$, where I is an open interval

$\mathbb{R}^+$ $x \in \mathbb{R} : x > 0$

$\mathbb{R}^n$ n-dimensional real Euclidean space

$\mathbb{R}^n_+$ Open half-space $\mathbf{x} \in \mathbb{R}^n : x_n > 0$

$\mathbf{x} = (x_1, \ldots, x_n)$ Point in $\mathbb{R}^n$

$\mathbf{x} = (x_1, \ldots, x_n)^\top$ Also a point in $\mathbb{R}^n$, depending on the context

Ω Open subset of $\mathbb{R}^n$

$\overline{\Omega}$ $\Omega \cup \partial\Omega$ is closure of Ω

$\partial\Omega$ Boundary of Ω

Number sets

$\mathbb{C}$ Complex numbers. Let $y \in \mathbb{C}$, then we denote $\mathfrak{Re}(z)$ the real part and $\mathfrak{Im}(z)$ the imaginary part of z

$\mathbb{N}$ Natural numbers

$\mathbb{R}$ Real numbers

$\overline{y}$ Conjugate of a complex number or function $y \in \mathbb{C}$

Other symbols

$\det A$ Determinant of the matrix A

$A^\top$ Transpose of the matrix A

Waveguide notation

λ_0 Vacuum wavelength

µm Micrometre, 10^{-6} metre

μ_0 Vacuum permeability

ω Angular frequency

R^+ Outer radius of curvature

ε_0 Vacuum permittivity

c_0 Speed of light in a vacuum

d Core thickness

k Wavenumber

k_0 Vacuum wavenumber

n_{cl} Cladding refractive index

n_{co} Core refractive index

T Transmittance

Functions

$\chi_I(x)$ Indicator function of I, $\chi_I(x) = 1$ for $x \in I$, $\chi_I(x) = 0$ for $x \notin I$

Δ Laplacian of u, $\Delta u = \sum_{i=1}^{n} \partial_{x_i}^2 u$

$\mathbf{u}\colon \Omega \to \mathbb{R}^n$ $\mathbf{u}(x) = \big(u^1(x),\, u^2(x),\, \ldots,\, u^m(x)\big)$, $x \in \Omega$

$\mathrm{supp}(u)$ Support of a function u

∇ Gradient of u, $\nabla u = (\partial_{x_1} u,\, \ldots, \partial_{x_n} u)^\top$

$\partial_x u$, $\dfrac{\partial u}{\partial x}$ Derivative of u with respect to x

References

[1] Milton Abramowitz and Irene A. Stegun. *Handbook of mathematical functions with formulas, graphs, and mathematical tables*. Dover publications, 1964.

[2] Sergio Albeverio, Claudio Cacciapuoti, and Domenico Finco. Coupling in the singular limit of thin quantum waveguides. *Journal of Mathematical Physics*, 48:032103, 2007. doi:10.1063/1.2710197.

[3] Donald E. Amos. A remark on algorithm 644: "A portable package for Bessel functions of a complex argument and nonnegative order". *ACM Trans. Math. Softw.*, 21:388–393, 1995. URL: https://api.semanticscholar.org/CorpusID:17933935.

[4] Meisam Bahadori, Mahdi Nikdast, Qixiang Cheng, and Keren Bergman. Universal design of waveguide bends in silicon-on-insulator photonics platform. *Journal of Lightwave Technology*, 37(13):3044–3054, 2019. doi:10.1109/JLT.2019.2909983.

[5] Alain Bamberger and Anne-Sophie Bonnet-Ben Dhia. Mathematical analysis of the guided modes of an optical fiber. *SIAM Journal on Mathematical Analysis*, 21(6):1487–1510, 1990. doi:10.1137/0521082.

[6] Carl M. Bender and Steven A. Orszag. *Advanced Mathematical Methods for Scientists and Engineers I. Asymptotic Methods and Perturbation Theory*. Springer New York, NY, 2013. doi:10.1007/978-1-4757-3069-2.

[7] Jean-Pierre Berenger. A perfectly matched layer for the absorption of electromagnetic waves. *Journal of Computational Physics*, 114(2):185–200, 1994. doi:10.1006/jcph.1994.1159.

[8] Enrico Bertolazzi and Marco Frego. g^1 fitting with clothoids. http://www.mathworks.com/matlabcentral/fileexchange/42113-g1-fitting-with-clothoids, 2013.

[9] Enrico Bertolazzi and Marco Frego. ig/isup1/sup fitting with clothoids. *Mathematical Methods in the Applied Sciences*, 38(5):881–897, mar 2014. doi:10.1002/mma.3114.

[10] Muhammad Rodlin Billah, Matthias Blaicher, Tobias Hoose, Philipp-Immanuel Dietrich, Pablo Marin-Palomo, Nicole Lindenmann, Aleksandar Nesic, Andreas Hofmann, Ute Troppenz, Martin Moehrle, Sebastian Randel, Wolfgang Freude, and Christian Koos. Hybrid integration of silicon photonics circuits and inp lasers by photonic wire bonding. *Optica*, 5(7):876–883, Jul 2018. doi:10.1364/OPTICA.5.000876.

[11] Adam Black, Ebru Toprak, Bruno Vergara Biggio, and Jiahua Zou. $l^1 \to l^\infty$ dispersive estimates for Coulomb waves. 2023. URL: https://api.semanticscholar.org/CorpusID:261530251.

[12] Anne-Sophie Bonnet-Ben Dhia, Simon N. Chandler-Wilde, Sonia Fliss, Christophe Hazard, Karl-Mikael Perfekt, and Yohanes Tjandrawidjaja. The complex-scaled half-space matching method. *SIAM Journal on Mathematical Analysis*, 54(1):512–557, 2022. doi:10.1137/20M1387122.

[13] Anne-Sophie Bonnet-Ben Dhia, Sonia Fliss, and Antoine Tonnoir. The halfspace matching method: A new method to solve scattering problems in infinite media. *Journal of Computational and Applied Mathematics*, 338:44–68, 2018. doi:10.1016/j.cam.2018.01.021.

[14] Guy Bouchitté, M. Luísa Mascarenhas, and Luís Trabucho. On the curvature and torsion effects in one dimensional waveguides. *ESAIM: Control, Optimisation and Calculus of Variations*, 13(4):793–808, 2007. doi:10.1051/cocv:2007042.

[15] Laurent Bourgeois, Sonia Fliss, Jean-François Fritsch, Christophe Hazard, and Arnaud Recoquillay. Scattering in a partially open waveguide: the forward problem. *IMA Journal of Applied Mathematics*, 88(1):102–151, 02 2023. doi:10.1093/imamat/hxad004.

[16] Dietrich Braess. *Finite Elemente: Theorie, schnelle Löser und Anwendungen in der Elastizitätstheorie*. Masterclass. Springer Berlin Heidelberg, 2013. doi:10.1007/978-3-642-34797-9.

[17] Haim Brezis. *Functional Analysis, Sobolev Spaces and Partial Differential Equations*. Universitext. Springer New York, NY, 2010. doi:10.1007/978-0-387-70914-7.

[18] Charles G. Broyden. The Convergence of a Class of Double-rank Minimization Algorithms 1. General Considerations. *IMA Journal of Applied Mathematics*, 6(1):76–90, 03 1970. doi:10.1093/imamat/6.1.76.

[19] Yves Capdeboscq, Roland Griesmaier, and Marvin Knöller. An asymptotic representation formula for scattering by thin tubular structures and an application in inverse scattering. *Multiscale Modeling & Simulation*, 19(2):846–885, 2021. doi:10.1137/20M1369907.

[20] Matteo Cherchi, Sami Ylinen, Mikko Harjanne, Markku Kapulainen, and Timo Aalto. Dramatic size reduction of waveguide bends on a micron-scale silicon photonic platform. *Opt. Express*, 21(15):17814–17823, Jul 2013. doi:10.1364/OE.21.017814.

[21] Weng Cho Chew and William H. Weedon. A 3D perfectly matched medium from modified Maxwell's equations with stretched coordinates. *Microwave and Optical Technology Letters*, 7(13):599–604, 1994. doi:10.1002/mop.4650071304.

[22] Giulio Ciraolo. A radiation condition for the 2D Helmholtz equation in stratified media. *Communications in Partial Differential Equations*, 34(12):1592–1606, 2009. doi:10.1080/03605300903328075.

[23] Giulio Ciraolo and Rolando Magnanini. Analytical results for 2D non-rectilinear waveguides based on a Green function. *Mathematical Methods in the Applied Sciences*, 31(13):1587–1606, 2008. doi:10.1002/mma.988.

[24] Giulio Ciraolo and Rolando Magnanini. A radiation condition for uniqueness in a wave propagation problem for 2D open waveguides. *Mathematical Methods in the Applied Sciences*, 32(10):1183–1206, 2009. doi:10.1002/mma.1084.

[25] Carl de Boor. *A Practical Guide to Splines*. Springer New York, NY, revised edition, 2001. URL: https://link.springer.com/book/9780387953663.

[26] John E. Dennis and Robert B. Schnabel. *Numerical Methods for Unconstrained Optimization and Nonlinear Equations*. Society for Industrial and Applied Mathematics, 1996. doi:10.1137/1.9781611971200.

[27] Anne-Sophie Bonnet-Ben Dhia, Ghania Dakhia, Christophe Hazard, and Lahcène Chorfi. Diffraction by a defect in an open waveguide: A mathematical analysis based on a modal radiation condition. *SIAM Journal on Applied Mathematics*, 70(3):677–693, 2009. doi:10.1137/080740155.

[28] Anne-Sophie Bonnet-Ben Dhia, Benjamin Goursaud, and Christophe Hazard. Mathematical analysis of the junction of two acoustic open waveguides. *SIAM Journal on Applied Mathematics*, 71(6):2048–2071, 2011. doi:10.1137/100811374.

[29] Lev Dolin. To the possibility of comparison of three-dimensional electromagnetic systems with non-uniform anisotropic filling. *Radiofizika*, 4(5):964–967, 1961.

[30] Boris Dubrovin, Sergei Novikov, and Anatoly Fomenko. *Modern Geometry - Methods and Applications: Part I. The Geometry of Surfaces, Transformation Groups, and Fields*. Graduate Texts in Mathematics. Springer New York, 2013. URL: https://books.google.de/books?id=ZEn0BwAAQBAJ.

[31] Pierre Duclos, Pavel Exner, and Pavel Šťovíček. Curvature-induced resonances in a two-dimensional Dirichlet tube. *Annales de l'I.H.P. Physique théorique*, 62(1):81–101, 1995. URL: http://www.numdam.org/item/AIHPA_1995__62_1_81_0/.

[32] David Edmunds and Des Evans. *Spectral Theory and Differential Operators*. Oxford University Press, Oxford, 1987.

[33] Lucas Gabrielli et al. On-chip transformation optics for multimode waveguide bends. *Nat. Commun.*, 3(1217), 2012. doi:10.1038/ncomms2232.

[34] Lawrence Evans. *Partial Differential Equations*. Graduate studies in mathematics. American Mathematical Society, 1998. URL: https://books.google.de/books?id=5Pv4LVB_m8AC.

[35] Pavel Exner and Petr Seba. Bound states in curved quantum waveguides. *Journal of Mathematical Physics*, 30(11):2574–2580, 11 1989. doi:10.1063/1.528538.

[36] Roger Fletcher. A new approach to variable metric algorithms. *The Computer Journal*, 13(3):317–322, 01 1970. doi:10.1093/comjnl/13.3.317.

[37] Roger Fletcher. *Practical Methods of Optimization*. Wiley Sons, Ltd, 200. doi:10.1002/9781118723203.

[38] Philip E. Gill, Walter Murray, and Margaret H. Wright. *Practical Optimization*. Society for Industrial and Applied Mathematics, Philadelphia, PA, 2019. doi:10.1137/1.9781611975604.

[39] Donald Goldfarb. A family of variable-metric methods derived by variational means. *Mathematics of Computation*, 24:23–26, 1970. doi:10.1090/S0025-5718-1970-0258249-6.

[40] Benjamin Goursaud. *Etude mathématique et numérique de guides d'ondes ouverts non uniformes, par approche modale*. Phd thesis, Ecole Polytechnique X, December 2010. URL: https://pastel.hal.science/pastel-00546093.

[41] Martin Halla. Analysis of radial complex scaling methods: Scalar resonance problems. *SIAM Journal on Numerical Analysis*, 59(4):2054–2074, 2021. doi:10.1137/20M1354234.

[42] Martin Hanke-Bourgeois. *Grundlagen der Numerischen Mathematik und des Wissenschaftlichen Rechnens*. Vieweg+Teubner Verlag Wiesbaden, third edition, 2009. doi:10.1007/978-3-8348-9309-3.

[43] Christophe Hazard. A distribution framework for the generalized Fourier transform associated with a Sturm–Liouville operator. Research Report RR-6885, INRIA, 2009. URL: https://inria.hal.science/inria-00371350.

[44] Mordehai Heiblum and Jay Harris. Analysis of curved optical waveguides by conformal transformation. *IEEE Journal of Quantum Electronics*, 11(2):75–83, 1975. doi:10.1109/JQE.1975.1068563.

[45] Jan S. Hesthaven and Tim Warburton. *Nodal Discontinuous Galerkin Methods*. Springer New York, 2008. doi:10.1007/978-0-387-72067-8.

[46] Kirankumar R. Hiremath, Manfred Hammer, Remco Stoffer, Ladislav Prkna, and Jiří Čtyroký. Analytic approach to dielectric optical bent slab waveguides. *Optical and Quantum Electronics*, 37(1-3):37–61, January 2005. doi:10.1007/s11082-005-1118-3.

[47] Kirankumar R. Hiremath, Remco Stoffer, and Manfred Hammer. Modeling of circular integrated optical microresonators by 2D frequency domain coupled mode theory. *Optics Communications*, 257(2):277–297, 2006. doi:10.1016/j.optcom.2005.07.057.

[48] Peter D. Hislop and Israel M. Sigal. *Theory of Quantum Resonances I: The Aguilar-Balslev-Combes-Simon Theorem*, pages 161–175. Springer New York, New York, NY, 1996. doi:10.1007/978-1-4612-0741-2_16.

[49] Zhen Hu and Ya Yan Lu. Computing optimal waveguide bends with constant width. *Journal of Lightwave Technology*, 25(10):3161–3167, 2007. doi:10.1109/JLT.2007.904033.

[50] Frank Ihlenburg and Ivo Babuška. Finite element solution of the Helmholtz equation with high wave number Part I: The h-version of the FEM. *Computers Mathematics with Applications*, 30(9):9–37, 1995. doi:10.1016/0898-1221(95)00144-N.

[51] Wolfram Research, Inc. Mathematica, Version 13.0. Champaign, IL, 2021.

[52] Xinru Ji, Junqiu Liu, Jijun He, Rui Ning Wang, Zheru Qiu, Johann Riemensberger, and Tobias J. Kippenberg. Compact, spatial-mode-interaction-free, ultralow-loss, nonlinear photonic integrated circuits. *Communications Physics*, 5(1):84, Apr 2022. doi:10.1038/s42005-022-00851-0.

[53] Patrick Joly and Christine Poirier. Mathematical analysis of electromagnetic open waveguides. *ESAIM: Mathematical Modelling and Numerical Analysis — Modélisation Mathématique et Analyse Numérique*, 29(5):505–575, 1995.

[54] Andreas Kirsch and Frank Hettlich. *The Mathematical Theory of Time-Harmonic Maxwell's Equations*. Springer International Publishing, 2015. doi:10.1007/978-3-319-11086-8.

[55] Christian Koos, Wolfgang Freude, Nicole Lindenmann, Sebastian Koeber, Tobias Hoose, and Muhammad Rodlin Billah. Three-dimensional two-photon lithography: an enabling technology for photonic wire bonding and multi-chip integration. In *Laser 3D Manufacturing*, volume 8970, page 897008. International Society for Optics and Photonics, SPIE, 2014. doi:10.1117/12.2044327.

[56] David Krejčiřík. *Mathematical aspects of quantum mechanics with non-self-adjoint operators*. Habilitation thesis, Charles University, Prague, 2017.

[57] David Krejčiřík and Helena Šediváková. The effective Hamiltonian in curved quantum waveguides under mild regularity assumptions. *Reviews in Mathematical Physics*, 24(07):1250018, 2012. doi:10.1142/S0129055X12500183.

[58] Lev Landau and Evgeny Lifshitz. *Quantum Mechanics. Non-Relativistic Theory (in Russian)*. Nauka, 3 edition, 1974.

[59] P. T. Leung, S. Y. Liu, and Kenneth Young. Completeness and orthogonality of quasinormal modes in leaky optical cavities. *Phys. Rev. A*, 49:3057–3067, Apr 1994. doi:10.1103/PhysRevA.49.3057.

[60] Rolando Magnanini and Fadil Santosa. Wave propagation in a 2D optical waveguide. *SIAM Journal on Applied Mathematics*, 61(4):1237–1252, 2001. doi:10.1137/S0036139999360489.

[61] Enrique A. J. Marcatili. Bends in optical dielectric guides. *The Bell System Technical Journal*, 48(7):2103–2132, 1969. doi:10.1002/j.1538-7305.1969.tb01167.x.

[62] Dietrich Marcuse. *Light Transmission Optics*. Van Nostrand Reinhold, New York, second edition, 1982.

[63] Dietrich Marcuse. *Theory of Dielectric Optical Waveguides*. Quantum Electronics Series. Academic Press, 1991. doi:10.1016/B978-0-12-470951-5.X5001-X.

[64] MATLAB. *version 9.14.0.2239454 (R2023a)*. The MathWorks Inc., Natick, Massachusetts, 2023.

[65] Andrea Melloni, Paolo Monguzzi, Raffaella Costa, and Mario Martinelli. Design of curved waveguides: the matched bend. *J. Opt. Soc. Am. A*, 20(1):130–137, Jan 2003. doi:10.1364/JOSAA.20.000130.

[66] Zoïs Moitier. zmoitier/bessel_complex_order: v1.0.1 compatibility with Matlab (v1.0.1). Zenodo, 2022. doi:10.5281/zenodo.6475751.

[67] Fernando Negredo, Matthias Blaicher, Aleksandar Nesic, Pascal Kraft, Julian Ott, Willy Dörfler, Christian Koos, and Carsten Rockstuhl. Fast and reliable method to estimate losses of single-mode waveguides with an arbitrary 2D trajectory. *J. Opt. Soc. Am. A*, 35(6):1063–1073, Jun 2018. doi:10.1364/JOSAA.35.001063.

[68] Aleksandar Nesic, Matthias Blaicher, Emilio Orlandini, Tudor Olariu, Maria Paszkiewicz, Fernando Negredo, Pascal Kraft, Mariia Sukhova, Andreas Hofmann, Willy Dörfler, Carsten Rockstuhl, Wolfgang Freude, and Christian Koos. Transformation-optics modeling of 3D-printed freeform waveguides. *Opt. Express*, 30(21):38856–38879, Oct 2022. doi:10.1364/OE.452243.

[69] Katsunari Okamoto. *Fundamentals of Optical Waveguides*. Academic Press, second edition, 2006. doi:10.1016/B978-0-12-525096-2.X5000-4.

[70] Frank W.J. Olver. *Asymptotics and Special Functions*. Academic Press, reprinted edition, 1997.

[71] Julian Ott. Domain optimization for an acoustic waveguide scattering problem. *Applied Mathematics & Optimization*, 72(1):101–146, 2015. doi:10.1007/s00245-014-9273-1.

[72] Julian Ott. *Halfspace matching: a domain decomposition method for scattering by 2D open waveguides*. PhD thesis, Karlsruhe Institute of Technology, 2017. doi:10.5445/IR/1000070898.

[73] Maria Paszkiewicz. Calculation of losses in freeform waveguides. Master thesis, KIT, Department of Physics Institute of Theoretical Solid State Physics, 2020.

[74] Maria Paszkiewicz, Mariia Sukhova, Willy Dörfler, and Carsten Rockstuhl. Approximation method for fast calculation of transmission in multi-mode waveguides. *J. Opt. Soc. Am. A*, 41(2):174–184, Feb 2024. doi:10.1364/JOSAA.504950.

[75] Michael Reed and Barry Simon. *Methods of Modern Mathematical Physics. Functional Analysis*. Academic Press, 1972. doi:10.1016/B978-0-12-585001-8.X5001-6.

[76] David F. Shanno. Conditioning of quasi-Newton methods for function minimization. *Mathematics of Computation*, 24:647–656, 1970. doi:10.1090/S0025-5718-1970-0274029-X.

[77] Allan W. Snyder and John Love. *Optical Waveguide Theory*. Springer New York, NY, 1 edition, 1983. doi:10.1007/978-1-4613-2813-1.

[78] Remco Stoffer, Kirankumar R. Hiremath, Manfred Hammer, Ladislav Prkna, and Jiří Čtyroký. Cylindrical integrated optical microresonators: Modeling by 3D vectorial coupled mode theory. *Optics Communications*, 256(1):46–67, 2005. doi:10.1016/j.optcom.2005.06.064.

[79] Nico Temme. Numerical algorithms for uniform Airy-type asymptotic expansions. *Numerical Algorithms*, 15:207–225, 09 1997. doi:10.1023/A:1019197921337.

[80] Edward C. Titchmarsh. *Eigenfunction Expansions Associated with Second-order Differential Equations*. Clarendon Press, 1962. URL: https://books.google.de/books?id=jv9QAAAAMAAJ.

[81] Vasily Vladimirov. Generalized functions. In *A Collection of Problems on the Equations of Mathematical Physics*. Springer Berlin Heidelberg, 1986.

[82] Florian Vogelbacher, Stefan Nevlacsil, Martin Sagmeister, Jochen Kraft, Karl Unterrainer, and Rainer Hainberger. Analysis of silicon nitride partial Euler waveguide bends. *Opt. Express*, 27(22):31394–31406, Oct 2019. doi:10.1364/OE.27.031394.

[83] Andrew J. Ward and John B. Pendry. Refraction and geometry in Maxwell's equations. *Journal of Modern Optics*, 43(4):773–793, 1996. doi:10.1080/09500349608232782.

[84] Calvin H. Wilcox. *Sound Propagation in Stratified Fluids*. Springer New York, NY, 1985. doi:10.1007/978-1-4612-1124-2.

[85] Yu Yang, Junchi Jia, Mingqing Zuo, Yuyang Gao, Zhangyuan Chen, Yongqi He, and Juhao Li. Suppression of modal crosstalk in laser-direct-writing weakly-guiding bending multimode waveguides. *Optics Communications*, 519:128421, 2022. doi:10.1016/j.optcom.2022.128421.